Master Thesis, Department of Geosciences

Reservoir quality of the Stø Formation in the Hoop Fault Complex and Fingerdjupet Sub-basin, SW Barents Sea

(The transition between the Stø and Fuglen Formations)

Niloufar Farazani

Master Thesis in Geosciences
60 credits

Faculty of Mathematics and Natural Sciences

UNIVERSITY OF OSLO
2017.12.01

Reservoir quality of the Stø Formation in the Hoop Fault Complex and Fingerdjupet Sub-basin, SW Barents Sea

(The transition between the Stø and Fuglen Formations)

Niloufar Farazani

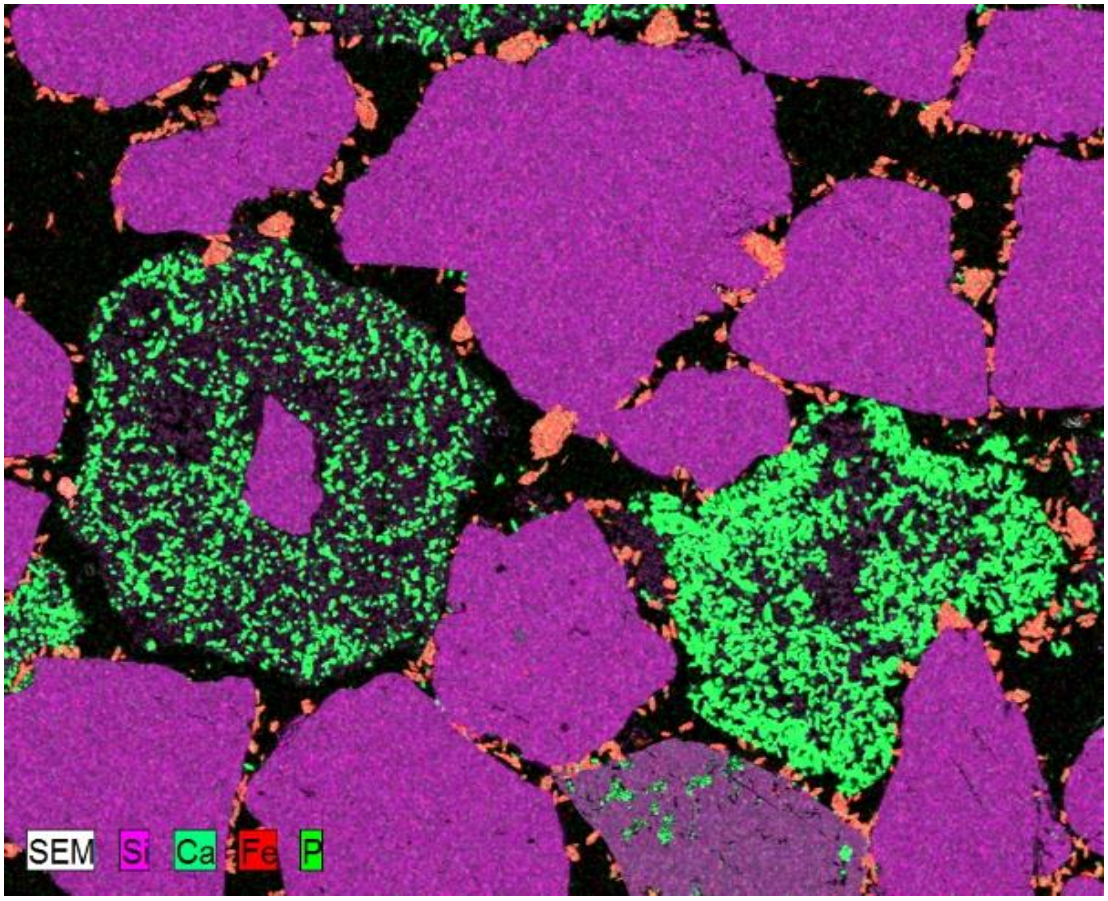

Master Thesis in Geosciences

60 credits

Faculty of Mathematics and Natural Sciences

UNIVERSITY OF OSLO
2017.12.01

Supervisor: Prof. Jens Jahren

Co-Supervisor: Ph.D. Lina Hedvig Line

This work is published digitally through DUO – Digitale Utgivelser ved UiO

http://www.duo.uio.no/

It is also catalogued in BIBSYS (http://www.bibsys.no/english)

Abstract

The Early to Middle Jurassic Stø Formation is the most commercially important sandstones reservoir in the Barents Sea. Stø Formation was deposited in a relatively shallow epicontinental sea in northern Pangea. One of the main objectives of this thesis is to evaluate and compare the reservoir quality of Stø Formation in Hoop Fault complex (well 7324/7-2) and Fingerdjupet Sub-Basin (well 7321/9-1). Six distinct facies describe sedimentological features of Stø Formation in Hoop area and Fingerdjupet Sub-Basin. Stø Formation in Hoop area was deposited in a fluvial system (floodplain, channel base and channel fill), while the sedimentary characteristics of Stø Formation in Fingerdjupet Sub-Basin indicate deposition in upper delta plain environments (upper delta plain deposits and minor distributary channel). Coarse conglomerates in both wells mark the transition from Stø Formation to underlying Fuglen Formation, indicating a transgressive event. The condensed section at the top of Stø Formation comprises of matrix, phosphate nodules and exotic clasts indicating three different sources. Factors such as rapid transgression, minimum net of sedimentation and high productivity are responsible for development of phosphate minerals which later eroded due to the subsequent regression and formed phosphate nodules within the unit. Matrix of the condensed section most likely only represent reworked material derived from Realgrunnen Subgroup (Tubåen, Nordmela, Fruholmen and Stø formations). The coarse-grained pebbly size clasts are only observed within the well 7321/9-1 in Fingurejupet Sub-basin and is absent in the other wells in the basin and also in Hoop Fault area. Loppa High could not be considered as a possible source for these exotic clasts. From the geological study, it is evident that during Jurassic time Loppa High has not been eroded to that depth at which these clasts are present. Accordingly, this hypothesis is discredited. The exact source of these exotic clasts is still ambiguous and requires further work and more investigations in this area. Petrophysical results show that Stø Formation intervals in well 7324/7-2 have the best reservoir quality compared to well 7321/9-1. The best reservoir quality intervals have been found in the fluvial deposits (channel base and channel fill) which were responsible for the deposition of clean sands. Relatively shallow depth of Stø Formation reservoir in Hoop area, despite significant exhumation of the study area, indicates that the formation has not experienced such high degree for diagenesis reactions. Furthermore, despite the fact that Stø Formation is thinly developed (21 m) in Hanssen, the reservoir intervals are hydrocarbon saturated and can be expected to have a high potential for hydrocarbon discoveries in Hoop Fault area.

ACKNOWLEDGEMENT

This Master Thesis is a part of a Master's Degree in Sedimentology at the University of Oslo. I would like to express my sincere gratitude to my supervisor Professor Jens Jahren and Co-supervisor Ph.D. student Lina Hedvig Line for their guidance and encouragement throughout the development of this project. I truly appreciate our highly educative meetings and their constructive feedbacks on this project. A special thanks to Mohammad Nooraiepour for his great supervision and discussions during petrophysical analysis.

I would like to thank OMV Norges AS and Norwegian Petroleum Directorate (NPD) for permission to view and log cores and collect samples. They kindly provided me with a great opportunity to build up my knowledge about the sandstone reservoirs found in the Hanssen and Fingerdjupet Sub-Basin wells.

I am grateful to Salahalldin Akhavan, Beyene Girma Haile and Berit Løken Berg for technical support with the samples preparation, X-ray diffraction analysis and in the SEM laboratory.

I owe thanks to a very special person, my husband Dr. Ehsan Rezapour for his continued and unfailing love, support and understanding my pursuit of the Master's degree that made the completion of the thesis possible.

Finally, I would like to thank my family for their love and encouragement, during my many years of studies without whom; I would not reach where I am today.

2017

Niloufar Farazani

Table of Contents

Chapter 1: Objectives and Geological background

1.1 Aims and objectives

Coarse conglomerates mark the transition between the Jurassic Stø Formation and the unconformable overlying Fuglen Formation, indicating a transgressive event. This event is also visible at the boundary between the Wilhelmøya Subgroup and Brentskardhaugen on Svalbard, indicating a regional influence. Stø/Fuglen Formations transition has been cored in two wells: 7324/7-2 (Hanssen) in the Hoop Fault Complex and 7321/9-1 in Fingerdjupet Sub-Basin. OMV Norge and Norwegian Petroleum Directorate (NPD) have provided access to core material from wells 7324/7-2 (Hanssen) and 7321/9-1, respectively. This project aims to improve our understanding of this transgression, how it affects the distribution of sediments and the processes responsible. Furthermore, the reservoir potential of Stø Formation at the selected locations within the Southwestern Barents Sea has also been investigated.

Investigations on reservoir quality of Stø Formation and this transgression event have been carried out based on the description and interpretation of sedimentological core logs, petrographic and petrophysical analyses. The combined results of these analyses are discussed in chapter 7 in order to evaluate the actual reservoir quality of Stø Formation in the selected wells.

1.2 Study area

The Barents Sea is a wide epicontinental sea that covers the north-western corner of the Eurasian continental shelf (Doré, 1995, Faleide et al., 1993). The Barents Sea has been bounded by Norwegian-Greenland Sea to the west, by the Svalbard and Franz Josef Land archipelagos to the north, by the Novaya Zemlya to the East and to the south by Norwegian and Russian mainland (Faleide et al., 2008)(Figure 1.1). Structural geology and the petroleum systems of Barents Sea are very complex compared to the North Sea and the Norwegian Sea. The Barents Sea has been affected by several phases of tectonism after the Caledonian orogeny terminated in the Late Silurian-Early Devonian (Gabrielsen et al., 1990, Smelror, 1994). There is also a significant difference between the tectonic and stratigraphic evolution of the western and eastern parts of the Barents Sea (Halland et al., 2014). During the Mesozoic and Cenozoic times, the western part of the Barents Sea was the most active sector and comprises of relatively thick sedimentary successions of Upper Palaeozoic to Cenozoic sediments (Faleide et al., 1984). The eastern and north-eastern parts of the Barents Sea is characterized by relatively stable platforms since Late Carboniferous with less noticeable tectonic activities (Hay, 1978, Gabrielsen et al., 1990). In terms of stratigraphy, “the continental shelf of the Barents Sea consists of sedimentary successions ranging from Late Palaeozoic to Quaternary, with lateral and vertical variations in thickness and facies”(Gudlaugsson et al., 1998, Faleide et al., 1993). These sediments comprise a mixture of carbonates and evaporate during Middle Carboniferous and Lower Permian, which is overlain by Mesozoic-Cenozoic clastic sedimentary rocks (Landrø, 2011). Several sedimentary basins

and platform areas make up the Norwegian sector of the Barents Sea. The areas of interest are the Hoop Fault Complex on the Bjarmeland Platform (well 7324/7-2) and Fingerdjupet Sub-basin on the northeastern part of Bjørnøya basin (well 7321/9-1). The locations of the two cores are shown in Figure 1.2.

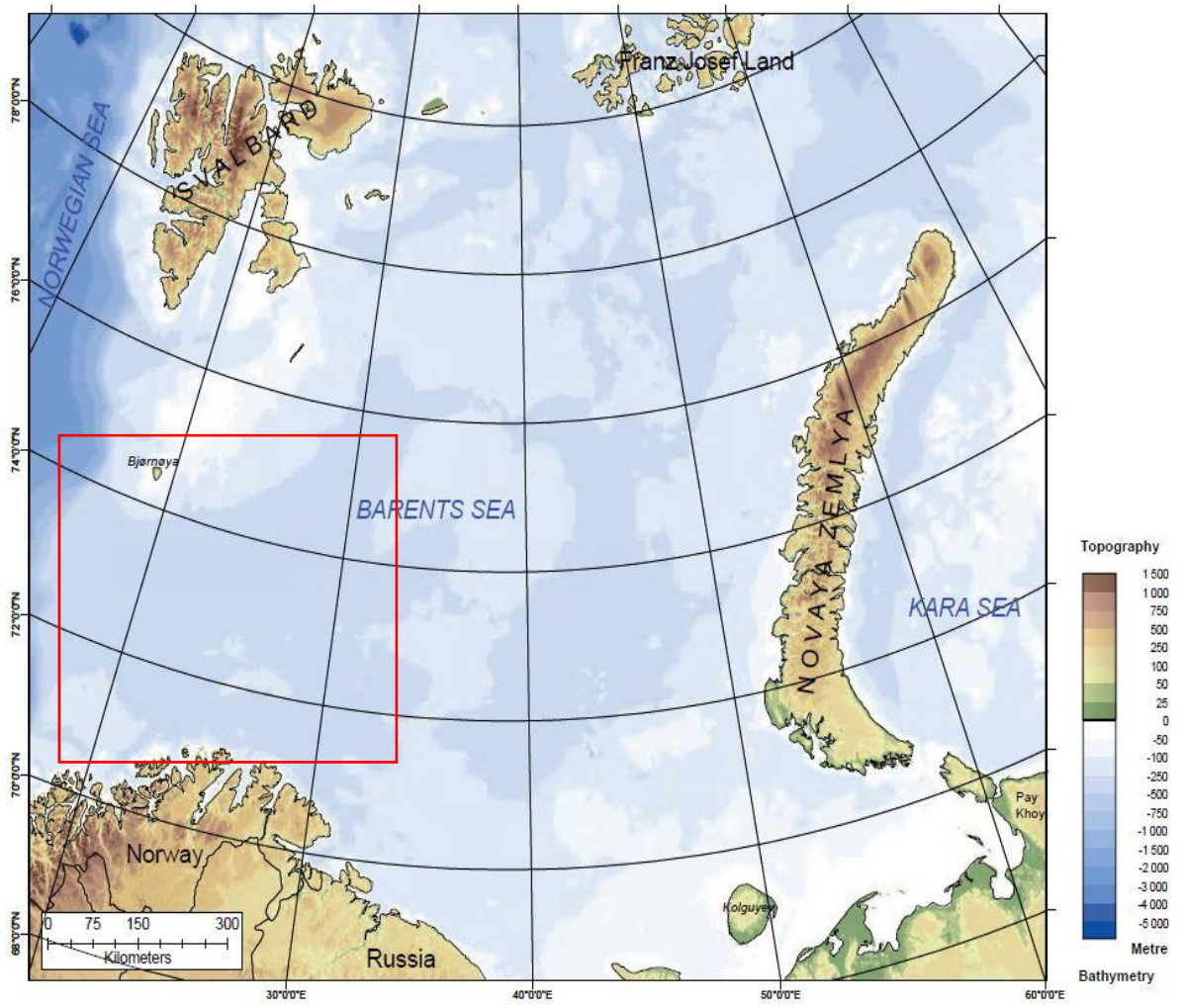

Figure 1.1: The map shows the geographical location of the Barents Sea (Smelror et al., 2009). Red box shows the location of Figure 1-2.

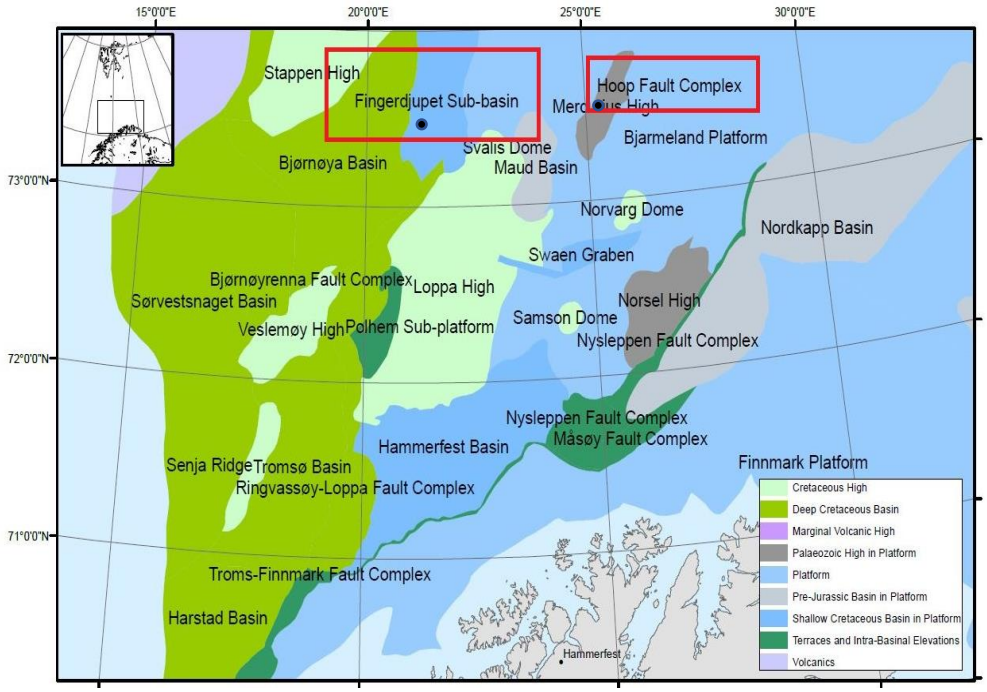

Figure 1.2: Map showing the structural elements of the Barents Sea. The black dots indicate the location of the well database, in this thesis, figure retrieved and modified from (Halland et al., 2013)

1.3 Geological background

1.3.1 Structural Geology of the Barents Sea

The western part of the Barents Sea was tectonically more active during Late Mesozoic and Cenozoic times, and this is characterized by enormous thick deposits of Cretaceous, Paleogene and Neogene sediments in the Harstad, Tromsø and Bjørnøya Basins (Landrø, 2011). Three major post- Caledonian rift phases have formed the main geological history of the western part of the Barents Sea since Late Paleozoic (Faleide et al., 1984)(Figure 1.3).

- First, Svalbardian Phase in the Late Devonian-Early Carboniferous
- Second, Mid and Late Kimmerian phases during Mid Jurassic to Early Cretaceous times
- Third, Cenozoic tectonism related to the progressive northward opening of the Norwegian-Greenland Sea in Early Tertiary.

Most parts of the Barents Sea has been affected by crustal extension during the Late Paleozoic time, and the main structural trends in the Barents Sea were established in Devonian times, especially during the Caledonian Orogeny (Steel and Worsley, 1984, Faleide et al., 1984). The later extension has been characterized by migration of the rifting towards the west, which caused the formation of well-defined rifts and distinct Basins in the southwest and growth of large-scale strike-slip faults in the North (Landrø, 2011). Except for radial movements which produced the current elevation differences the Svalbard Platform and eastern parts of the basin have been mostly stable since Late Paleozoic times (Landrø, 2011). The Caledonian basement was formed during the Caledonian orogeny in Late Silurian to Early Devonian.

During this time, the Caledonian basement was uplifted, eroded and deposited as red molasse sediments into the intermontane basins undergoing extensional collapse (Landrø, 2011).

Devonian

The tectonic regimes during the Devonian include both extensional and compressional regimes, which have only been observed on the Svalbard north-western of the Barents shelf (Landrø, 2011). Transgression and transaction during the Svalbardian phase resulted in the formation of half-grabens and intervening highs which controlled the depositional environment of source, reservoir and cap rocks (Gabrielsen et al., 1990, Dengo and Røssland, 2013).

Carboniferous

The Lower to Early Upper Carboniferous depositional basins were extensional basins (Faleide et al., 2015), comprising a mixture of clastics, carbonates and evaporates similar to the sediments of the same age in the Pechora Basin in the eastern part of the Barents Sea (Nalivkin, 1973, Gabrielsen et al., 1990). Throughout, the Early and Middle Carboniferous periods Svalbard and the Bjørnøya Basin were under the influence of a large-scale block fault close to the boundary between the Early to Middle Carboniferous (Brekke and Riis, 1987, Faleide et al., 1993). During the Late Carboniferous time, a widespread carbonate shelf of a regional extent became established in several large-scale basins including, the Nordkapp Basin of the south-western Barents Shelf, the Maud Basin, the Tromsø Basin and along the Billefjorden Fault (Gabrielsen et al., 1990). There is insufficient information regarding the basin development at this time, but the structural trend in the southern and eastern parts seems to be NE-SW and NNW-SSE trending in western and northwestern areas (Spitsbergen, Bjørnøya and western parts of the Loppa area).

Permian

The second episode of rifting in the Barents Sea (Norwegian-Greenland rift system) commenced during the Permian time and continued through to the Triassic (Smelror et al., 2009, Grøstad-Clark et al., 2010). Deposition of evaporites continued during the Early Permian, and resulted in vast, thick accumulations of evaporites in several basins, such as the Nordkapp Basin (4-5km), the Maud Basin close to the Hoop Fault complex (2-2 km) and the Ottar Basin (2 km) (Gudlaugsson et al., 1998). Climate change from sub-tropical and arid to more temperate during the Late Permian, led to the development of different depositional environment within the basins (Henriksen et al., 2011). This is seen in the Bajarmland and Tempelfjorden Groups where sedimentary successions start to change their composition from carbonate into more marine mudstone and chert deposits (Figure 1.4).

Geological background

Triassic

Examination of worldwide Triassic climates (Sellwood and Valdes, 2006) demonstrates that the continental positions between 40^0 N and 40^0 S were generally warm, with consisted of hot periods during which temperatures may have exceeded 30^0 C for most of the year. In terms of tectonic activities, the Triassic to Early Jurassic time scale is considered as a relatively quiet period. However, the Stappen High and Loppa High were affected by tilting (Gabrielsen et al., 1990). The Early to Middle Triassic time have been defined by subsidence toward the eastern area and sediment influx from the east (Gabrielsen et al., 1990). During this time, large amounts of clastic sediments were deposited in this area, which were supplied from the Uralian to the east, the Baltic Shield from the south and potentially from another local source (Landrø, 2011).The Triassic sequences comprise shales and sandstones with a complex vertical and lateral distribution (Landrø, 2011). Early Triassic times continued by shallowing and partial exposure of some area such that by Middle Triassic time most of the areas was dominated by the continental regimes. In the Late Triassic period, shoreline stepped back toward the southern and eastern borders of the south-eastern Barents Sea basin. The Triassic time terminated in conjunction with regression and erosional events (Landrø, 2011, Halland et al., 2014).

Jurassic

The Triassic to Jurassic boundary is associated with a more humid climate in the present NW European basin (Hallam, 1985). In terms of tectonic activities, the Middle Jurassic sandstones had been separated from Upper Jurassic shales as result of the Bathonian-Callovian hiatus which marked the onset of Cimmerian tectonic (Faleide et al., 1993). During Mid Jurassic time, block faulting started again (main phase of subsidence) and culminated during the period from Late Jurassic into Early Cretaceous (Aptian-Albian). It was terminated by the formation of the major Basins and Highs (Gabrielsen et al., 1990). The onset of rifting is observable within the sequence boundaries of the Middle Jurassic in the southwestern Barents Sea. However, the Upper Jurassic unconformities demonstrate the interplay between sea level fluctuations and continued faulting (Landrø, 2011). The Lower and Middle Jurassic interval is dominated by a large amount of sandstones which are present in the Hammerfest Basin and thickening into the Tromsø Basin (Faleide et al., 1993). These sandstone units are acting as the main reservoir in the Hammerfest Basin (Olaussen et al., 1984, Berglund et al., 1986, Olsen and Hanssen, 1987).

Geological background

Cretaceous

Generally, the Early Cretaceous structuring of the southwestern Barents Sea has been defined by extensional faulting such that the Harstad, Tromsø and western parts of the Bjørnøya basins experienced extreme rates of subsidence (Aptian to Albian) (Faleide et al., 1993). By the end of the Cretaceous time, a combination of the reverse faulting, folding and extensional faulting were more common in some areas and reached the highest level of inversion and folding during Eocene to Oligocene times (Gabrielsen et al., 1990).

Cenozoic

The Cenozoic structural development was related to two-main stages; firstly the opening of the Norwegian-Greenland Sea and second, the formation of the predominantly sheared western Barents Sea continental margin (Faleide et al., 1993). During this time, the main deformation took place during the initial break-up of the North Atlantic during the Eocene to Oligocene times and this introduced abounded magmatic activity in the western parts of the Barents Sea (Talwani and Eldholm, 1977, Myhre et al., 1982, Eldholm et al., 1987, Faleide et al., 1984). Most parts of the Barents Sea have been eroded and uplifted during the Neogene (Nyland et al., 1992, Berglund et al., 1986). According to Investigations conducted on Neogene wedge at the Senja Ridge, it is evident that an important part of the erosion occurred during the Late Pliocene and Pleistocene when the area was glaciated (Eidvin and Riis, 1989).

Geological background

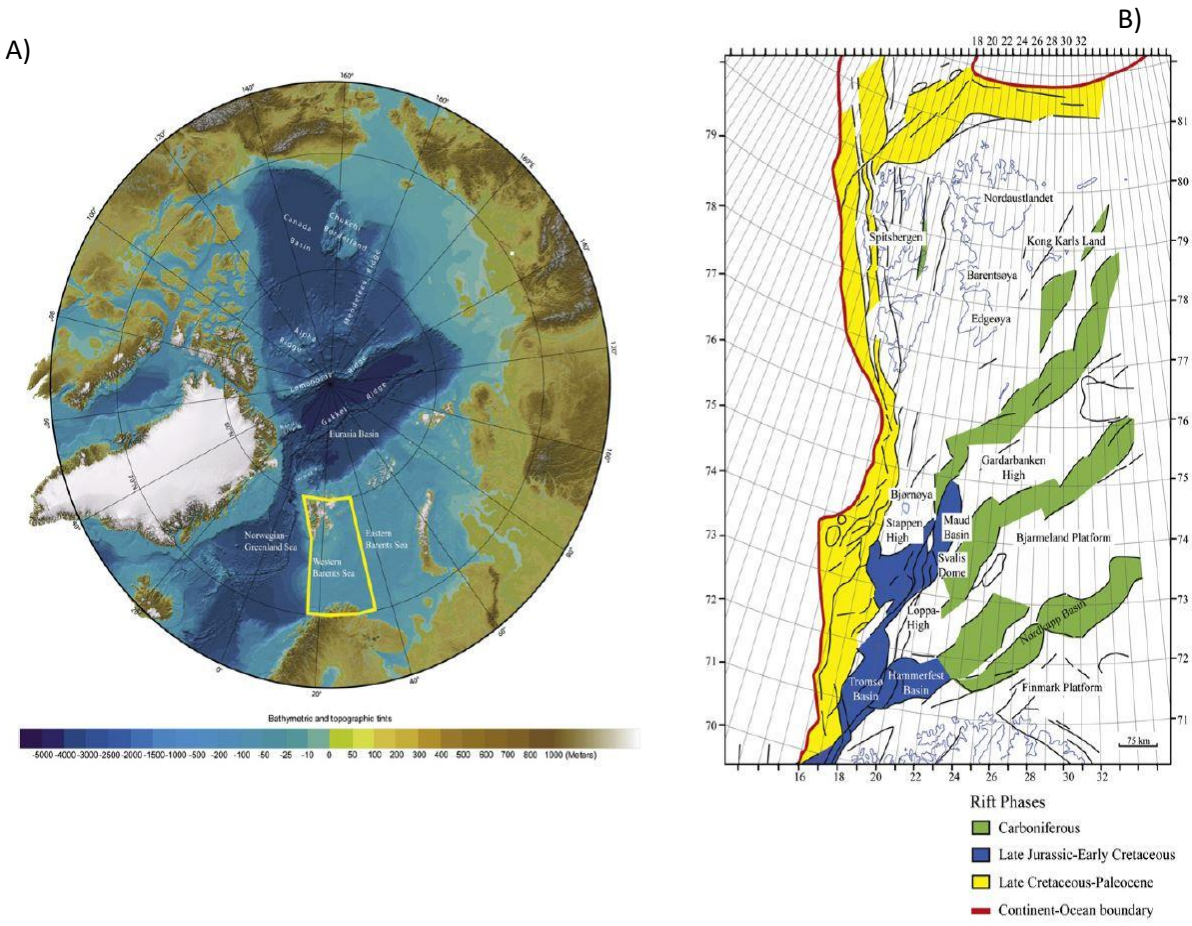

Figure 1.3: A) The regional setting of the study area shown by a yellow rectangle, Bathymetric map from Jakobssen et al. (2008). B) Main structural elements in the Barents, modified after Glørstad-Clark et al. (2010).

Geological background

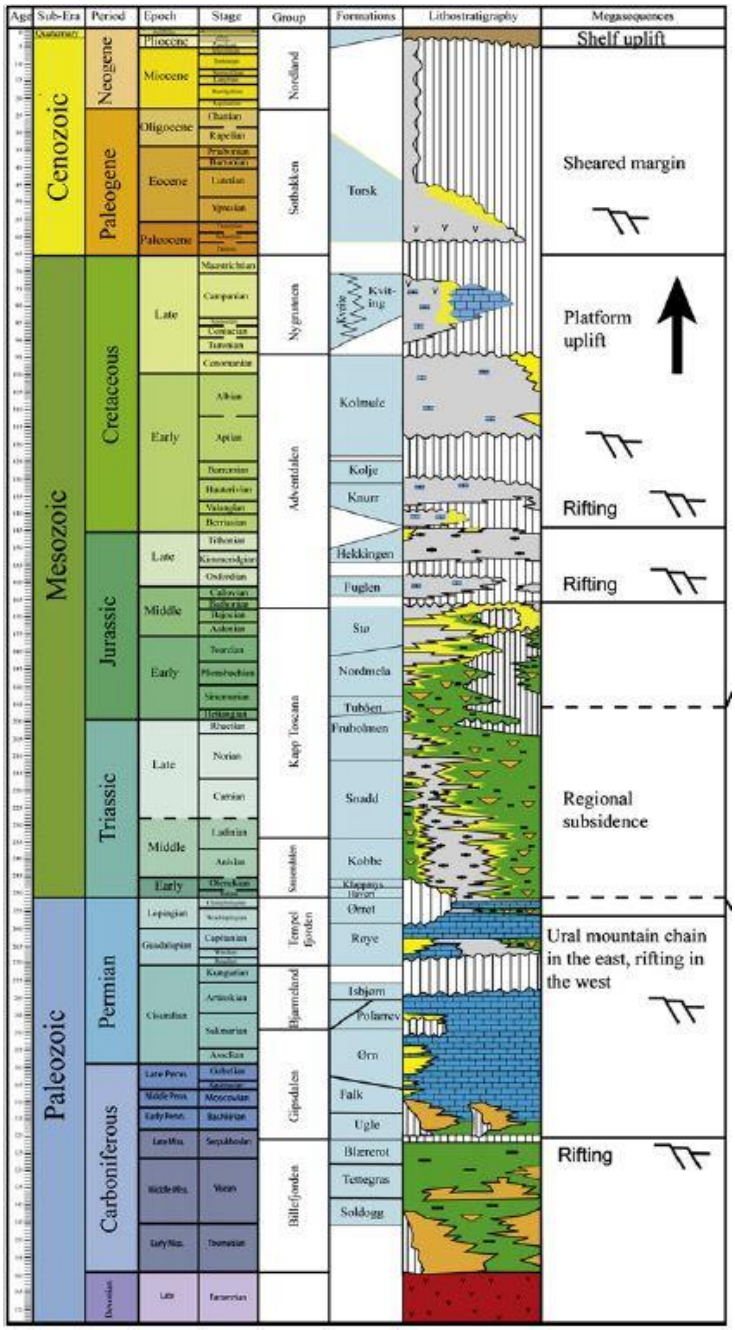

Figure 1.4: Schematic diagram of the lithostratigraphy and associated mega-sequences of the western Barents Sea (modified after Glørstad-Clark et al., 2010).

1.3.2 Geological Province

The structural elements of the western Barents Sea are comprised of three distinct regions which are covered by the Upper-Paleozoic to Cenozoic rocks (Faleide et al., 1984, Landrø, 2011): (1) a basin province between the Svalbard Platform and the Norwegian coast, which has been defined by a number of sub-basin and highs and presence of Jurassic–Cretaceous sediment as well as Paleocene-Eocene sediments in the west (2) Svalbard Platform, which is covered by a sedimentary succession of Upper Paleozoic and Mesozoic (mainly Triassic) sediments and (3) the western continental margin which consists of three segments (Landrø, 2011):

- A southern sheared margin along the Senja Fracture Zone.
- A central rifted complex southwest of Bjørnøya Basin associated with volcanism.
- A northern, initially sheared and later rifted margin along the Hornsund Fault Zone.

1.3.2.1 Main structural elements

The southern parts of the Barents Sea have been divided into several main structural elements such as the Hammerfest and Nordkapp Basins, the Finnmark and Bjarmeland Platforms and Loppa High (Halland et al., 2014). There are several smaller structural elements such as Norsel High, Veslemøy, Senja Ridge, Polheim Sub-platform, as well as a series of complex fault zones (e. g. the Troms-Finnmark, Ringvassøy-Loppa, Bjørnøyrenna, Måsøy, Nysleppen, Hoop Fault and Asterias Fault Complexes) (Halland et al., 2014). In the following sections, only the structural elements relevant for this study are discussed. For a regional geologic profile, see Figures 1.5 and 1.6.

Bjarmeland Platform

Description: The Bjarmland Platform is part of an extensive platform area between Hammerfest and Nordkapp Basins to the south and southeast, the Sentralbanken and Gardarbanken Highs to the north and the Fingerdjupet Subbasin and Loppa High to the west (Gabrielsen et al., 1990) (Figure 1.5). The Platform represents a structural element which has been relatively stable since the Late Palaeozoic times (Gabrielsen et al., 1990).

The Bajrmeland Platform includes minor highs and sub-basins which mostly formed by salt tectonics. As a result of Tertiary uplift, the platform sediments dip gently to the south with progressively older sediments sub cropping to the north at the base Quaternary unconformity (Gabrielsen et al., 1990, Halland et al., 2014).

Geological background

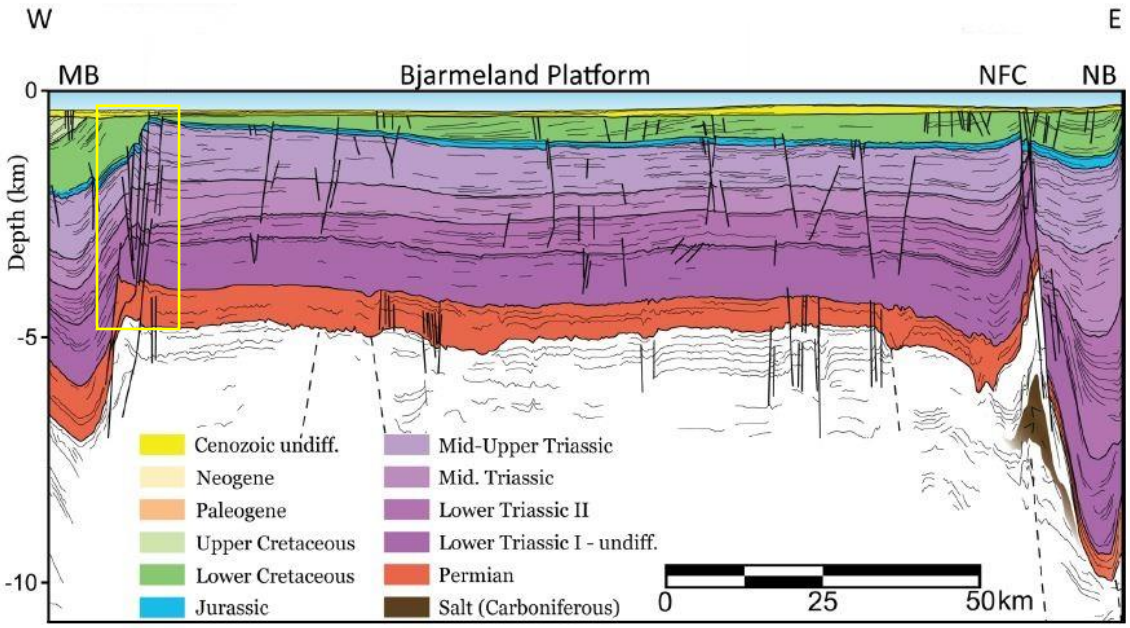

Figure. 1.5: Regional geologic profile across the southern part of the Bjarmeland Platform (modified from Smelror et al., 2009). MB – Maud Basin; NFC – Nysleppen Fault Complex; NB –Nordkapp Basin; Yellow rectangle – Hoop Fault Complex.

Hoop Fault Complex

Description: The Hoop Fault Complex cuts across the Loppa High and Bjarmland Platform between 21° 50 N, 21° 50 (Gabrielsen et al., 1990) (Figure 1.6). The northern parts of the Hoop Fault Complex consist of group of normal faults cutting the Bjarmeland Platform (Gjelberg, 1981). The Maud Basin and the Svalis Dome have developed in central parts of the Hoop Fault Complex while the southern part is a narrow graben on Loppa High (Gabrielsen et al., 1990). The Hoop Fault Complex has been under the influence of several faulting episodes. (Gabrielsen et al., 1990, Kjølhamar, 2012). "These faults and successions have formed the characteristic Hoop Graben" (Kjølhamar, 2012). The variation in the structural development of the Hoop Fault Complex have been regarded as the main reasons for migration and remigration of the hydrocarbons into the shallow structures (Kjølhamar, 2012). The Post-Eocene erosional events have removed lots of the Cretaceous and younger strata from Hoop Fault Complex and caused the older sedimentary succession of Permian and Carboniferous to be shallow and subsequently more accessible for hydrocarbon exploration (Kjølhamar, 2012).

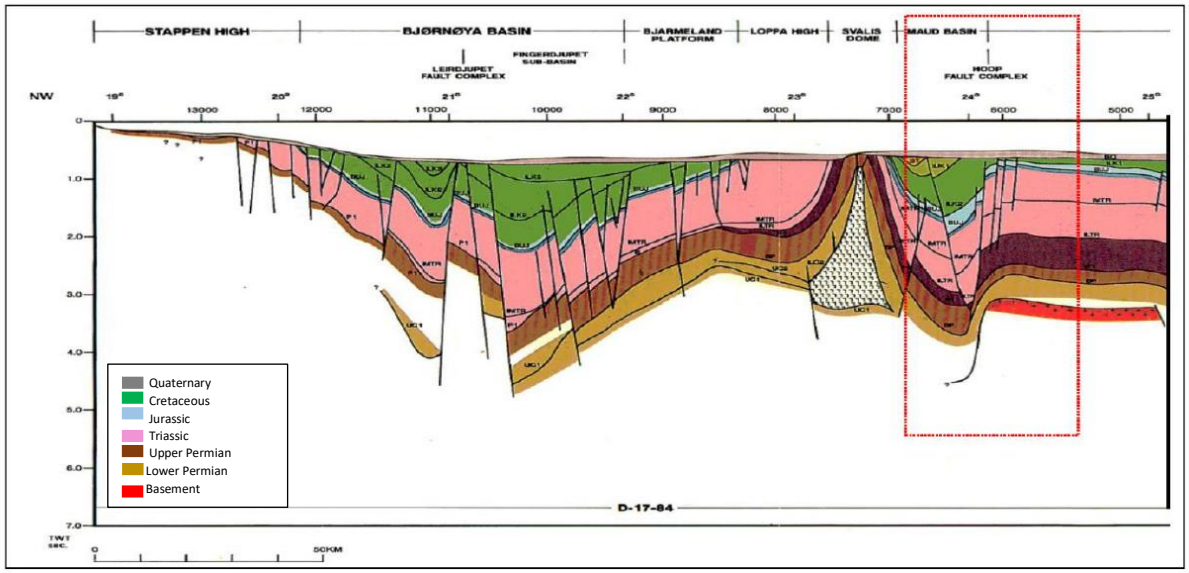

Figure 1.6: Profile line across the Hoop Fault Complex, D-17-84, modified from (Gabrielsen et al., 1990).

Fingerdjupet Sub-Basin

Description: The Fingerdjupet Sub-basin was formed during the Early Cretaceous time as a shallow northeastern part of Bjørnøya Basin (Gabrielsen et al., 1990).The Fingerdjupet Sub-basin subsided by Early Cretaceous time as result of an extensional tectonic episode which acted during the Late Jurassic to Early Cretaceous time (Gabrielsen et al., 1990). Further development of the basin occurred in response to tectonics and subsidence during Late Jurassic to Early Cretaceous. These rifting episodes caused formation of the shallower fan-shaped Fingerdjupet Sub-basin as a part of the Bjørnøya Basin (Faleide et al., 1984, Gabrielsen et al., 1990).

1.4 Jurassic stratigraphy and depositional systems

The Kapp Toscana Group is mainly dominated by shales, siltstones, and sandstones of Late Triassic to Middle Jurassic age (Dalland et al., 1988). The Kapp Toscana Group is divided into two subgroups: the Storfjorden and Realgrunnen Subgroups (Halland et al., 2014). The focus of this thesis will be on the Realgrunnen Subgroup (Early Norian to Bathonian). The Realgrunnen Subgroup is subdivided into four formations; Fruholmen, Tubåen, Normela, and Stø. The group is well developed throughout the Hammerfest basin and thinly developed on the Bjarmeland Platform, which makes the definition of various formations is unclear in this section (Halland et al., 2014) (Figure 1.7). The sediments of The Realgrunnen Subgroup have been deposited near-shore deltaic environments, and have been characterized as shallow marine, deltaic and fluviodeltaic deposits (Halland et al., 2014).

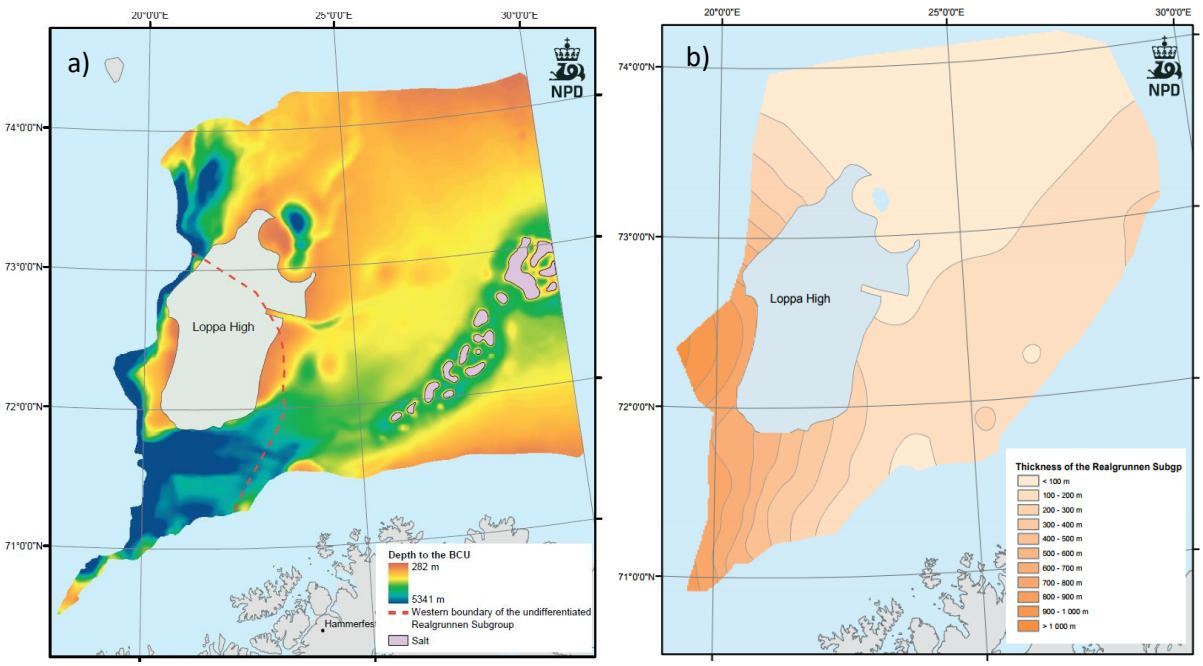

Figure 1.7: The thickness map (b) shows the Realgrunnen Sub-group well developed on Hammerfest basin and thinly developed on the Bjarmeland Platform. The Realgrunnen Subgroup were probably deposited on the Loppa High and the Troms-Finnmark Platform, but later Kimmerian movements removed them from these regions. Figure modified from (Halland et al., 2014).

1.4.1 Fruholmen Formation

The base of the Fruholmen Formation is Early Norian, whereas the top formation represents the Triassic-Jurassic Transition (Bergan and Knarud, 1993).
Fruholmen formation displays a general coarsening upwards trend, comprised of grey to dark shale that passes gradually upwards into interbedded sandstone, shale, and coals (Dalland et al., 1988, Halland et al., 2014, Ryseth, 2014). The boundary between Fruholmen Formation and underlying Snadd Formation is interpreted as major Early Norian transgression seen as organic marine shale deposits (Henriksen et al., 2011)(Figure 1.8).
Based on the lithological variations the Fruholmen Formation has been divided into three members including the shaly Akkar Member at the base, sandy Reke Member and shale-rich Krabbe Member (Dalland et al., 1988, Halland et al., 2014).
The interpreted depositional environment for the formation is open marine shales of Akker Member, passing upward into interbedded sandstones, shales and coals of Reke Member (Dalland et al., 1988, Halland et al., 2014).

1.4.2 Tubåen Formation

Tubåen Formation is absent in both Hanssen (7324/7-2) and Fingerdjupet Sub-Basin (7321/9-1) wells, indicating a prominent hiatus. The Tubåen Formation developed during the Late Rhaetian to Early Hettangian (Dalland et al., 1988, Halland et al., 2014). The formation has been divided into three parts, with lower and upper sand rich units separated by a more shale-

rich interval in between (NPD, 2014). The sandstone units of the Tubåen Formation have been deposited in high energy marginal marine conditions and have been interpreted as fluvial, deltaic origin, representing a variety of fluvial and distributary channel types (Ryseth, 2014). The marine shales reflect more distal environments, while the coals layers have been interpreted as protected back barrier lagoonal deposits (Halland et al., 2014).

1.4.3 Nordmela Formation

Nordmela Formation is Sinemurian to Late Pliensbachian in age. The formation comprising of interbedded siltstones, sandstones, shale, and claystone with minor coals. Sandstones units are more common toward the top of the Nordmela formation. The Nordmela Formation was deposited in a tidal flat to the flood-plain environment, with individual sandstone sequences representing estuarine and tidal channels (Dalland et al., 1988). Absence of Tubåen and Nordmela Formations in Hanssen (7324/7-2) and Fingerdjupet Sub-Basin (7321/9-1) indicate millions of years of missing data and could explain a vast change in mineral composition and depositional environment of Stø Formation.

1.4.4 Stø Formation

Stø Formation extends from Late Pliensbachian to Bajocian (Dalland et al., 1988). Stø Formation consists of moderately to well sorted and mineralogically mature sandstones, with thin units of shale and siltstone indicate regional markers (NPD, 2014). The sandstone maturity of Stø Formation could be a result of the extensive reworking of the sediment and chemical weathering in a temperate and humid climate in the source areas during the Jurassic time. The sandstone units of Stø Formation are interpreted to have been deposited in prograding coastal environments, while shale and siltstone intervals represent regional transgression in the southwestern Barents Sea such that the depositional environment changed from flood-plain to prograding coastal settings (Smelror et al., 2009).

1.5 Development of Realgrunnen Subgroup in Hoop Fault Complex

Recent discoveries in the Hoop fault area (Wisiting field) have triggered renewed interest in the reservoir quality and characterization in the area of the northern Hoop Fault Complex, with main interest of Jurassic intervals (Figure 1.8). The Fuglen Formation consists of mudstone in a marine flooding environment and acts as the cap rock above Stø Formation. By the Early Jurassic period, most parts of the Normela and almost the entire Tubåen Formation have been eroded from this area. As a result the boundary between Stø and Fruholmen Formation is marked by a clear unconformity between these two formations (Figure 1.9). Only the lower parts of the Fruholmen Formations is presented in the Hoop Fault Complex. The Triassic Reke Member implies a regression event and basinward shifts of the facies. It deposited in fluviodeltaic, heterolithic environments and is considered as a secondary reservoir. Triassic Akker member shows regional flooding and represents the start of the Realgrunnen subgroup. The member comprises marine mudstones and is considered

as the base of the reservoir as well as a cap rock for the Snadd Formation. In the Wisting field, the reservoir rock shows excellent quality and comprises Stø Formation and some part of the Fruholmen Formation. The Snadd Formation of the Upper Triassic shows poor reservoir quality.

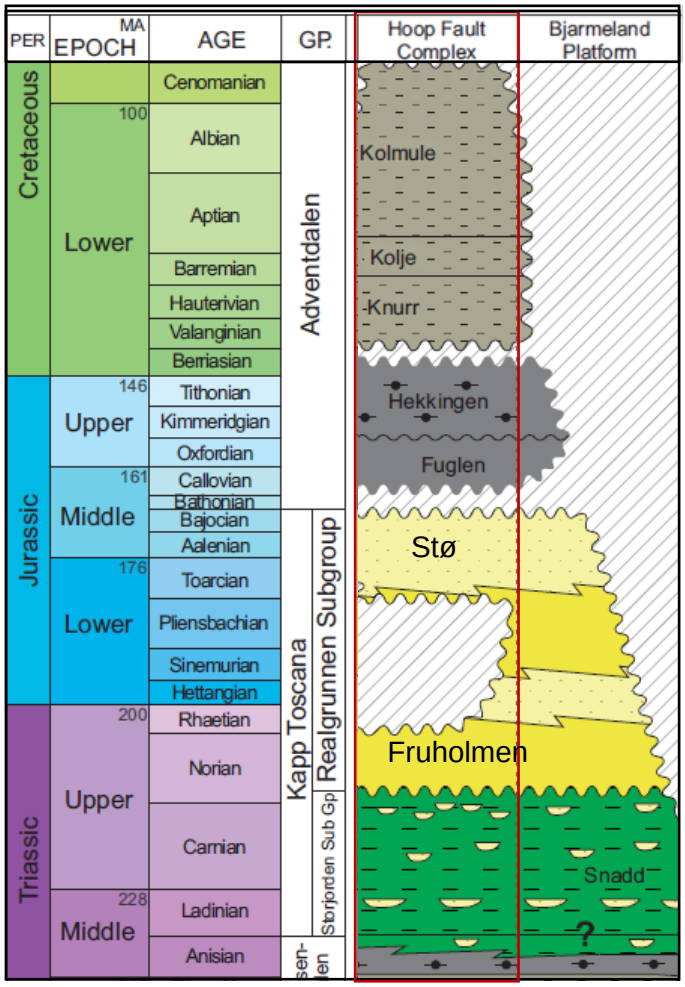

Figure 1.8: Stratigraphy and main plays in the Hoop Area, (after OMV Norge AS, 2016)

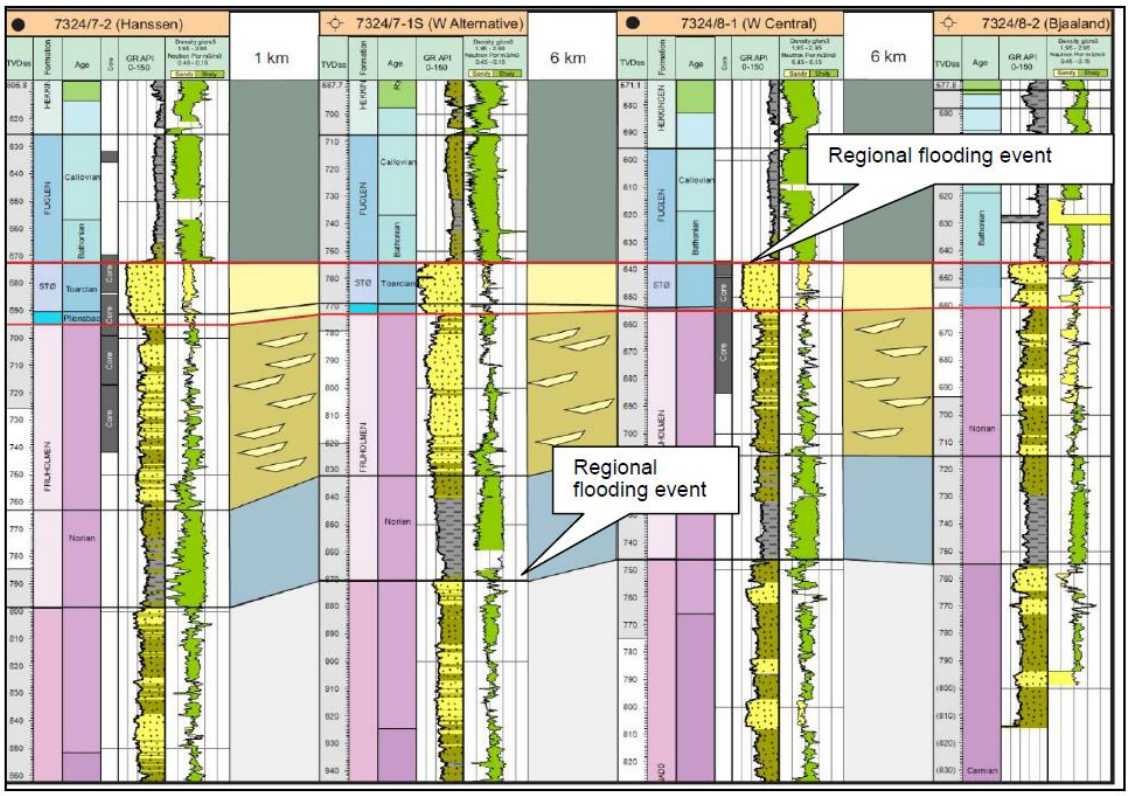

Figure 1.9: Well Correlation Realgrunnen Subgroup – Wisting wells (Photo was taken from, http://www.omv.com)

1.6 Climate change at the Triassic- Jurassic boundary

Examined wells in the Norwegian parts of the Barents Sea indicate an abrupt shift in framework mineralogy from plagioclase-rich, k-feldspar-poor and immature arenites in the Lower-Middle Triassic to mature quartz-rich sediments in the Uppermost Triassic-Jurassic period. According to Bergan and Knarud (1993) the reason for such a shift could be related to climatic changes, changes in palaeodrainage direction and thus provenance rocks and/or changes in the basin subsidence rate. Climate changes from semi-arid to semi-humid conditions play a vital role in the development of different mineralogical assemblies. Triassic climate change in the Barents Sea is evident in two zones: a hot and dry zone toward the south and a much more humid zone toward the north (Ryseth, 2014). This climate change has been related to north-ward plate tectonic drift combined with marine incursions (Frostick et al., 1992, Ahlberg et al., 2002). The arid climate condition caused intensive physical weathering and consequently deposition of significant amounts of detrital grains, plagioclase-rich and k-feldspar-poor and immature sandstone in Lower to Middle Triassic. The more humid climate condition in the latest Triassic and early Jurassic with higher annual precipitation and increase in the rate of chemical weathering caused generation of more mineralogically mature sandstone. In such a setting, the increase in precipitation leads to elevation of the groundwater table and a subsequent increase in the meteoric water flow

rate, resulting in a more pronounced mineral dissolution and leaching of feldspar (Bergan and Knarud, 1993). Also, during this time the uplifted Norwegian Caledonides changed the drainage direction of the major Fennoscandian river to other directions than northward. This regional change in drainage patterns of the Fennoscandian river allowed other potential provenance areas to supply clastic to the Barents Sea region by prohibiting the input of sediments from Fennoscandian river to Norwegian palaeocoast (Bergan and Knarud, 1993).

During the upper Triassic period the Caledonian and Precambrian metamorphic basements of the Fennoscandia were exposed and therefore led to denudation of Caledonian metamorphic and gabbroic rocks, which also led to deposition of immature arenites (Bergan and Knarud, 1993). After denudation of most of the Caledonides and the demise of the active easterly source the erosion and reworking of the unmetamorphosed sediments resting on the Fennoscandian Precambrian basement resulted in the deposition of mineralogically mature quartz-arenites during the Jurassic (Bergan and Knarud, 1993).

The mineralogical assembly of the Snadd and Fruholmen Formations have been documented in several published literatures. There is a significant difference between the mineralogical assembly of the Snadd and Fruholmen formations. The high levels of variation observed between the mineralogical assembly of these formations could not be explained by diagenetic processes as these formations have been deposited in a similar marine and continental setting thus experiencing similar diagenetic evolution (Bergan and Knarud, 1993). Diagenetic dissolution could not be the reason for the absence of plagioclase in Fruholmen and Stø formations. Plagioclase is usually the least stable of the feldspars therefor presence of plagioclase together with an absence of K-feldspar could not be explained by diagenetic reasons (Busenberg and Clemency, 1976, Bergan and Knarud, 1993). However, rapid subsidence during the Triassic may have caused deposition of the first generation of the sediment within Triassic succession where mineral alternation processes were minor (Bergan and Knarud, 1993). During this time basins and platforms in the south-west of the Barents Sea area were under the influence of significant subsidence and are characterized by vast clastic sediment accumulation (Riis et al., 2008). The rate of subsidence decreased significantly across the Triassic to Jurassic boundary and was accompanied by paleogeographic re-configurations and hinterland rejuvenation to the south (Bergan and Knarud, 1993, Ryseth, 2014). The significant reduction in the rate of subsidence during the latest Triassic and Jurassic led to the development of thinner successions, and to repeated resedimentation and erosion from the source area down to final accumulation basin (Bergan and Knarud, 1993, Ryseth, 2014). According to Bergan and Knarud (1993), transport time and exposure to groundwater are much higher in such a system than the older rapidly subsiding depositional regime which subsequently led to deposition of both texturally and mineralogically mature sediments during the Jurassic time (Stø Formation). Based on the discussion above it could be concluded that the humid climate (with more considerable annual precipitation), hinterland rejuvenation, and reduction in the rate of subsidence during the Jurassic are a likely

explanation to the increase in grain size and relative quartz content of Early Jurassic delta plain deposits, with respect to the late Triassic units in the Barents Sea.

1.7 Provenance (Stø Formation)

Analysis of detrital zircon U-Pb ages and signatures have been conducted by Pozer Bue & Andresen (2015) and Klausen et al. (2017) in order to determine the provenance area of Triassic-Jurassic depositional environments on Svalbard and the Barents Sea. These authors suggested three subdivisions based on the three different signatures (Figure 1.10). The first end member is sampled from Early and Middle Triassic, indicating a western Laurentian (North Greenland source). The provenance signature of samples of Vardebukta and Bravaiseberget formations from Early and Middle Triassic on Svalbard comprises of Proterozoic to Neoarchaen zircons and reflect the most likely sediments sources in northern Greenland and potentially Canada (Bue and Andresen, 2014). The provenance signature of the samples of De Greerdalen Formation from Late Triassic is dominated by Palaeozoic ages, indicating eastern sources, most likely from the Uralian Orogeny in the east with a minor input from the Timanides (Bue and Andresen, 2014). Late Triassic to Early and Middle Jurassic samples of Knorringfjellet, Svenskøya and Wilhelmøya formations (equivalent to Stø Formation), suggest mixing of zircons from both endmember groups. These sediments are interpreted to reflect reworking of older Mesozoic sediments, potentially together with the renewed input of the sediments from the west (northern Greenland). The increase in the maturity of the sandstones during the last Triassic to Early Jurassic, could be related to the extensive reworking of the sediments caused by regional transgression during this time.

Geological background

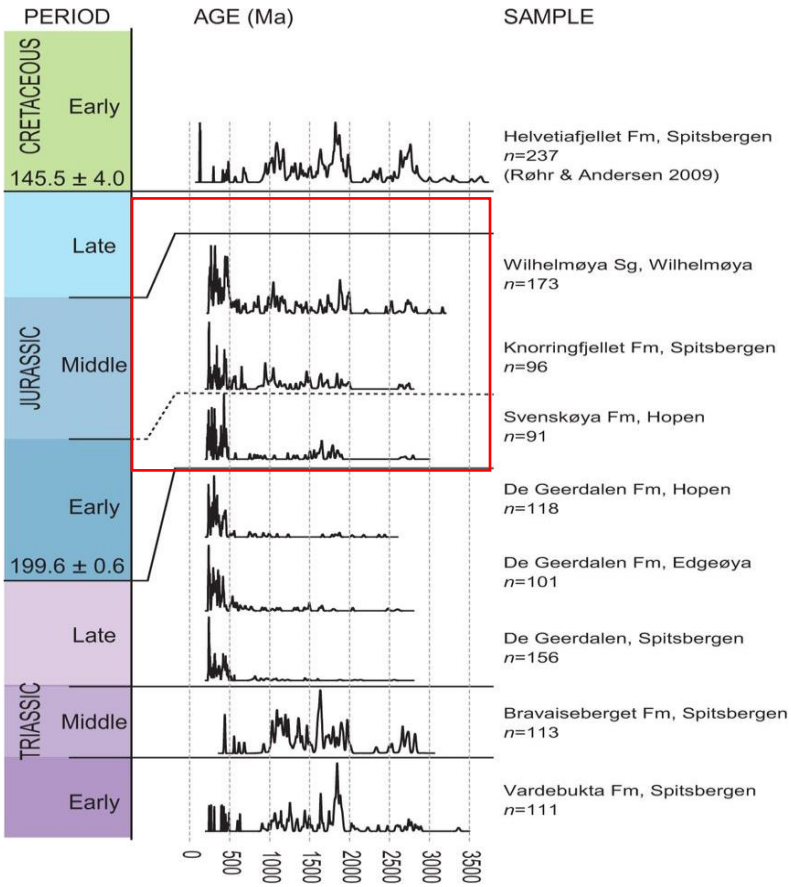

Figure 1.10: Provenance zircon age signatures of Mesozoic sands from Svalbard including three Early Cretaceous samples (Bue and Andresen, 2014). The red square indicates sample signatures of the time-equivalent of Stø Formation.

According to Pozer Bue & Andressen (2014), Early and Middle Jurassic sediments indicate either a new and different source area and/or mixing of the sediments from the previously described endmember groups, i.e.,The Early to Middle Triassic westerly source and Late Triassic easterly sources. Another possible theory was presented by Ryseth (2014), who concluded that rapid Late Triassic to Early Jurassic uplift and erosion of the Caledonides probably provided a new sediment input which along with erosion and reworking of the previously deposited sediments led to deposition of more quartz-rich sandstones deposits above the Snadd Formation (Figure 1.11). Paul et al. (2009) linked the increase in the rate of denudation during the Triassic-Early Jurassic to the rift shoulder uplift along the Atlantic rift system. These interpretations support the conclusion that hinterland rejuvenation played a major role in changing depositional trends at the Triassic to Jurassic boundary on the Norwegian shelf; from the North Sea to the Barents Sea areas (Ryseth, 2014). This hypothesis is also additionally supported by Smelror et al. (2009) who proposed that as result of the development of a major marine embayment in the South and North Barents basins, the supply of the sediment from the south-east (Uralides and Novaya Zemlya) to the western part of the Barents shelf ceased. Thus further enhance in petrographic characteristics induced by hinterland rejuvenations in Fennoscandia. This interpretation is later postulated by result of detrital zircon analysis on Jurassic Stø Formation samples obtained by Klausen et al. 2017 who

introduced southwest Caledonides and the southeast Fennoscandia as the major source for the reworked material and coarse-grained sediments on Southwestern margin of the Barents Sea. Based on climate and provenance studies, it could be concluded that the sandstone maturity of Stø Formation is a result of the extensive reworking of the sediment during the Jurassic time. This is in addition to the more effective chemical weathering in the temperate and humid climates, in the source areas. Establishment of a more humid climate and consequently high annual precipitation rate during the Jurassic time increased the rate of the dissolution of the unstable minerals, which subsequently led to a more pronounced leaching of the feldspars, and deposition of the more mineralogically mature sandstone of Stø Formation.

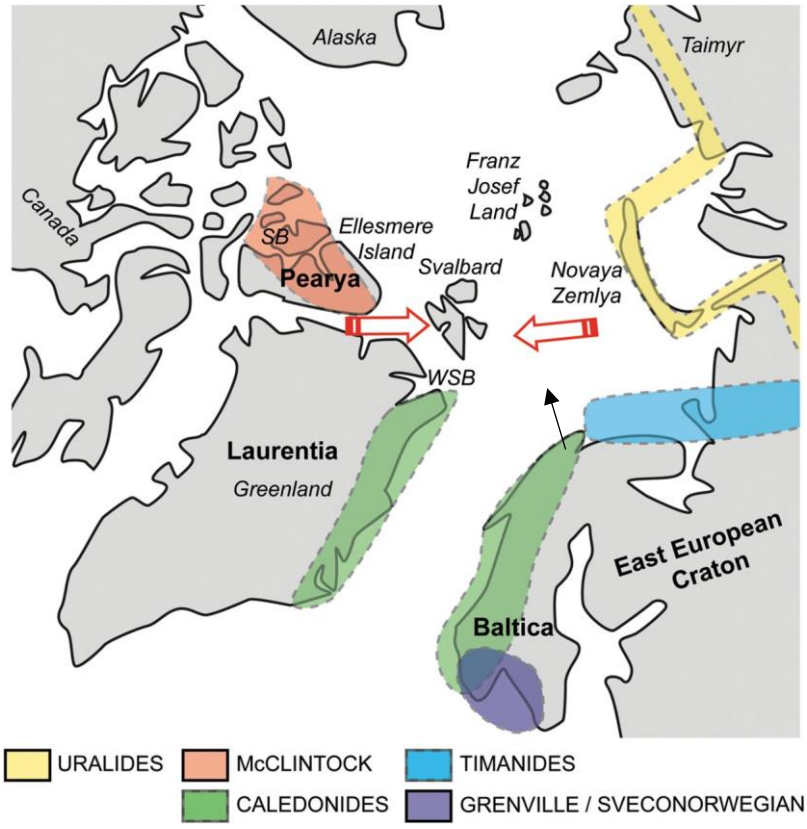

Figure 1.11: Red arrows are depicting main sediment transport directions and source areas during the Triassic. Early to Middle Triassic formation (Vardebukta and Bravaiseberget and De Geerdalen formations) supplied from a westerly source (Greenland and Artic Canada) and Late Triassic corresponding to an easterly source (Uralides). Early and Middle Jurassic sediments indicate a new source area from the Caledonies (black arrow) in addition to erosion and reworking of the previously deposited sediments (figure modified from Pozer Bue & Andresen, 2015)

1.8 Wilhelmøya Subgroup and Brentskardhaugen Bed on Svalbard

In Svalbard, the Kapp Toscana Group is subdivided into Storfjorden and Wilhelmøya subgroups. The Storfjorden Subgroup includes Tschermakfjellet, De Geerdalen, Skuld and Snadd formations. The Wilhelmøya Subgroup occurs in large parts of Svalbard and is time-equivalent of the Realgrunnen Subgroup on the southern Barents Sea Shelf (Mørk et al., 1999). The group includes Flatsalen, Svenskøya and Kongsøya formations. The upper boundary and lower boundary of the Wilhelmøya Subgroup have been bounded by Brentskardhaugen Bed and Slottet Bed, respectively. The Brentskardhaugen Bed is a thin conglomeratic unit rich in phosphatic nodules with fossils of different ages (Mørk et al., 1999). The Brentskardhaugen Bed documents an underlying unconformity, representing a hiatus (Mørk et al., 1999).

An explanation of the relationship between Wilhelmøya Subgroup and Realgrunnen Subgroup can be given as (Mørk et al., 1999): The De Greedalen Formation is Carnian to early Norian in age with Snadd formation as its offshore counterpart (Mork et al., 1982, Riis et al., 2008, Glørstad-Clark et al., 2010, Høy and Lundschien, 2011, Lundschien et al., 2014).The Flatsalen Formation is dated as Norian and is time equivalent to upper part of the Fruholmen and Tubåen formations of the Realgrunnen Subgroup (Worsley et al., 1988, Mørk et al., 1999).The Svenskøya Formation is Rhaetian in age, and its offshore counterpart is the Tubåen Formation in the south-western Barents Sea (Paterson et al., 2016, Paterson and Mangerud, 2015, Smith et al., 1976). The Kongsøya Formation has been only found in the Svalbard area and is time equivalent to Lower to Middle parts of Stø Formation in south-western Barents Sea (Lord et al., 2014). The Nordmela Formation is only defined for the south-western Barents Sea and does not have any time equivalent formation on the Sentralbanken and Svalbard areas. However, there are some facies in Kong Karls Land which correlate well to this formation (Gjelberg et al., 1987, Klausen et al., 2017). The Agardhfjellet Formation in Svalbard and Sentralbanken area is time equivalent to the Fuglen Formation in the Barents Sea. The base of Fuglen Formation is still unclear in the Barents Sea, therefore has been defined at the top of Stø Formation (Worsley, 2008) (Figure 1.12).

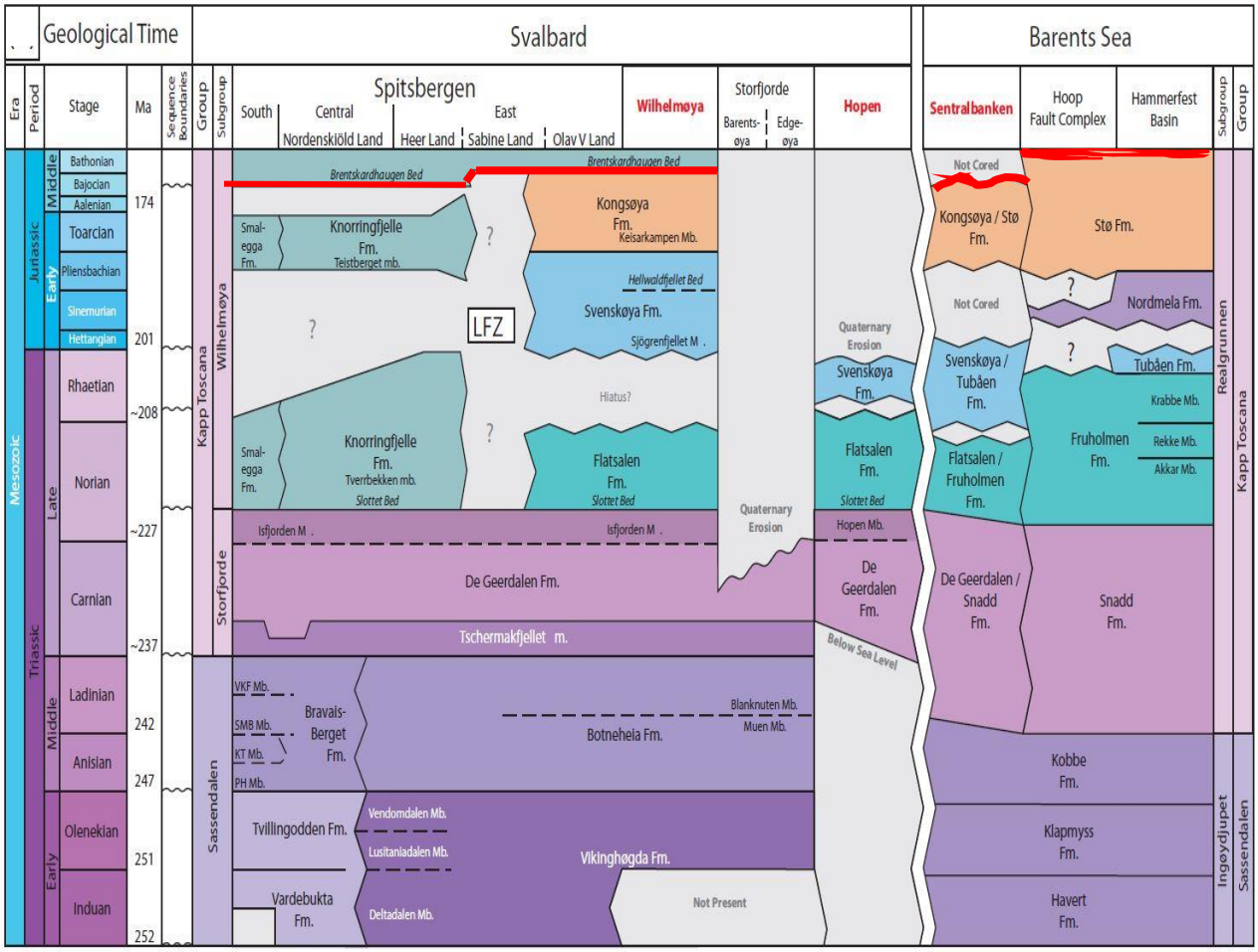

Figure 1.12: Modified stratigraphic chart after (Mørk et al., 2013) and Lord et al. (in press) showing the relationships between stratigraphic units in Svalbard and the Barents Sea.(red line indicates the position of the conglomerate unit).

1.9 Depositional history of the condensed section on Svalbard

During the Late Triassic-Early Jurassic time, large areas of the Barents Sea Shelf uplifted and eroded (Smelror et al., 2009). The Ladinian-Norian period in southwestern Barents Sea and Svalbard is dominated by delta influenced marginal marine to shallow marine conditions which led to deposition of the De Geerdalen formation in Svalbard. Shallow marine conditions were introduced to central Spitsbergen and the Barents Sea which probably started in Norian and culminated in the Rhaetian (Bäckström and Nagy, 1985). The lower parts of the Wilhelmøya Subgroup and Realgrunnen Subgroup (Tubåen, Nordmeal) have been deposited by this marine ingression as suggested by Bjærke & Dypvik (1977). Regression started during early Hettaningen and probably prevailed to the late Pliensbachian. During this time, the central parts of the Barents Sea including Loppa High, Svalbard, Frans Josef Land and Timan-Pechora areas were uplifted and eroded and also comprised a wide area of continental land (Smelror et al., 2009) (Figure 1.13a). As result of uplift and erosion, sedimentary rock from this time are absent over large parts of the region (Smelror et al., 2009). A new transgression started during Pliensbachina and reached its maximum by Toarcian (Bjærke and Dypvik,

1977). During this time, a global sea level rise introduced shallow-marine condition to Svalbard, western and eastern parts of the Barents Sea (Figure 1.13b). This transgressive event changed the depositional environments in this area from floodplain environment to prograding coastal settings with an extensive reworking of sediments. This resulted in the deposition of Stø Formation in the Hammerfest, Nordkapp, Bjørnoya Basins and also in Bajarmland Platform in the southwestern Barents Sea. On Svalbard, the shallow marine sandstone of Wilhelmøya subgroup was deposited in the similar prograding deltaic system (Smelror et al., 2009). This transgression even is also reflected by the fact that most of the ammonites found in the Brentskardhaugen belong to this age (Bäckström and Nagy, 1985). Presence of condensed conglomerate at the top of Stø and its correlation to Brentskardhaugen conglomerate Bed at the top of Kongsøya formation on Svalbard indicates a large regional extent of this transgression event. According to Bäckström and Nagy (1985), this marine ingression appears to be time correlative with the global Toarcian transgression which reached its maximum near the end of the stage. As a result of subsequent erosion and tectonic activity during the Middle Jurassic, the Toarcian deposits are unevenly preserved in the western Barents Sea, and nodules of the coarse conglomerate in these areas are commonly found preserved as remanie deposits of Brentskardhaugen bed (Smelror et al., 2009). The Middle Jurassic regression seems to have culminated in the Bathonian such that large parts of the Barents Shelf were exposed to erosion, resulting in a depositional gap over most of the western Barents Sea (Bäckström and Nagy, 1985, Smelror et al., 2009). This regression, resulted in coastal erosion of the shelf with energy high enough to break up parts of the Wilhelmøya Subgroup and concentrate coarse and resistant material, among conglomerate of Brentskardhaugen bed (Bäckström and Nagy, 1985, Maher Jr, 1989) (Figure 1.13c). A new transgression started probably near the end of the Bathonian simultaneous with global elevation of the sea level at the transition between Bathonian and Callovian (Bäckström and Nagy, 1985). This event led to the renewed reworking and final deposition of the Brentskardhaugen bed (Bäckström and Nagy, 1985). By the end of the Jurassic, the sea level reached its maximum, and an extensive marine shelf covered most of the Barents Sea and the Kara Sea. In the western Barents Sea, the Loppa High and the Stappen High, Sentral Banken High, the Hopen High and the Hjalmar Johansen Dome were uplifted and partly eroded due to initiation of Cimmerian movements during this time (Faleide et al., 1984, Faleide et al., 1993, Smelror et al., 2009, Faleide et al., 2008) (Figure 1.13d). On Svalbard, the Agredhfjellet Member deposited as energy decreased. Presence of a Kepplerites fauna of uppermost Bathonian-basal Callovian age in Agredhfjellet Member indicates deposition of Brentskardhuagen conglomerate and dark grey to black silty mudstone of Agardhfjellet Formation (equivalent to Fuglen Formation) during the same event (Bäckström and Nagy, 1985).

Geological background

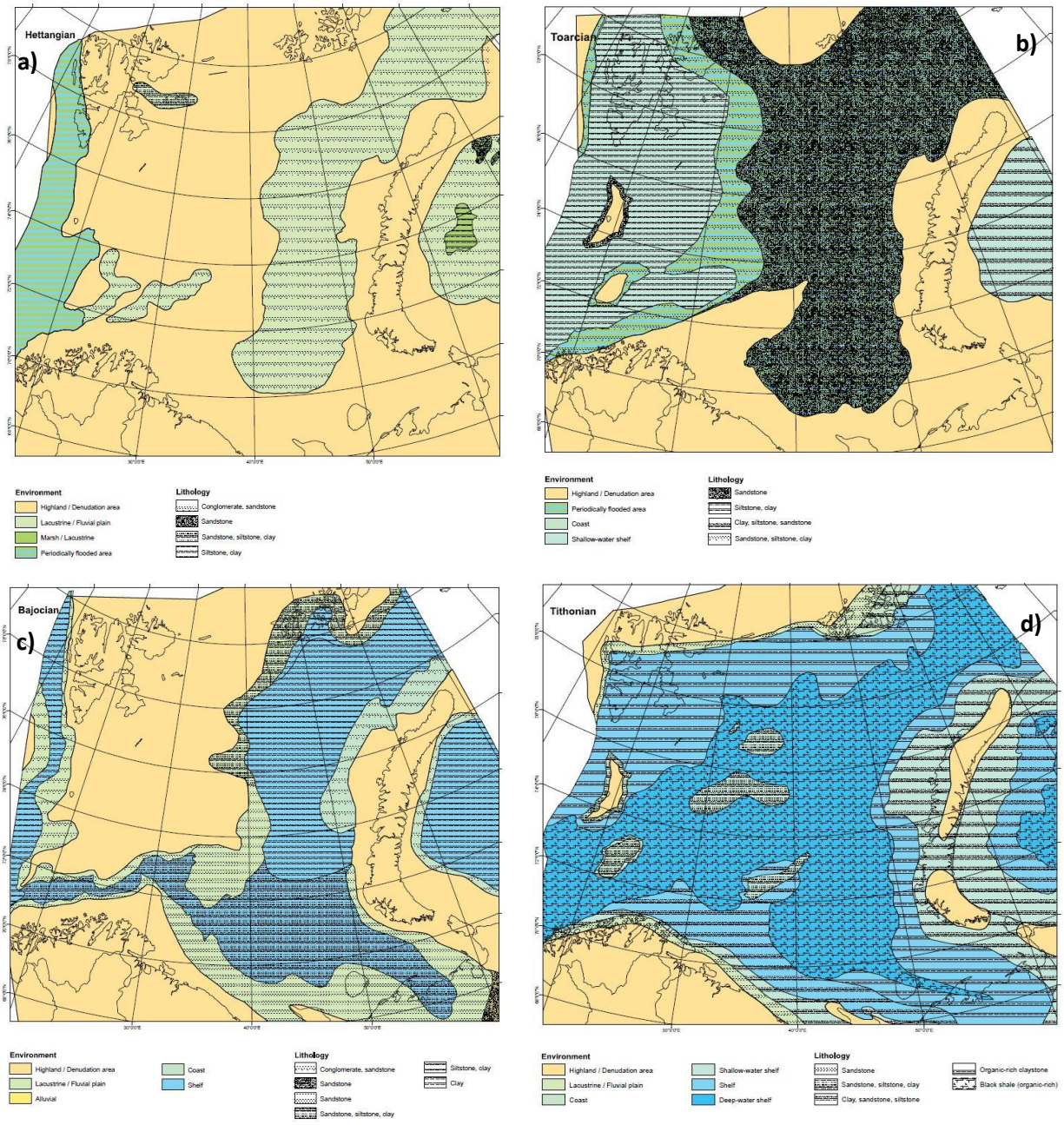

Figure 1.13: Stratigraphically development of the Barents Sea from Late Triassic to Late Jurassic (Smelror et al., 2009)

Chapter 2: Theoretical background

2.1 Introduction

Porosity and permeability are the most important factors when determining the reservoir quality of a sandstone reservoir, but other factors such as wetting properties of the mineral surfaces and pore geometry may also influence petroleum production (Bjørlykke and Jahren, 2015). The geological processes influencing the sandstone reservoir properties may divide into two regimes: 1) Primary composition of the sediments, which is closely related to the textural and mineral composition of the provenance and depositional environment and 2) post-depositional processes, which are controlled by the diagenetic processes near the surface and during burial. These processes control the reservoir quality and the chapter aims to explain them.

2.2 Sedimentological influence on reservoir quality

Primary sandstone composition is the most critical factor in predicting reservoir quality at depth. Primary composition of the sediments is a function of transport, provenance and depositional environment (Figure 2.1)(Bjørlykke and Jahren, 2015).

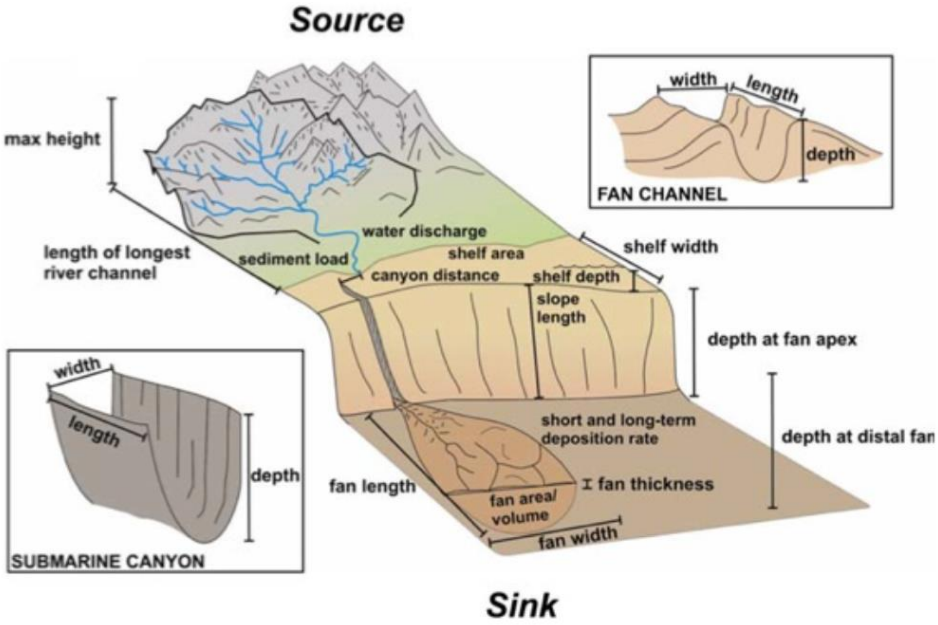

Figure 2.1: Illustration shows the processes on the sediment journey from the source to the basin (figure from Martinsen et al., 2010).

Grain size, sorting, textural and mineralogical composition are the most critical factors in order to determine the source area of the sediment as well as interpret the sequence of the diagenetic processes. These factors are controlled by provenance, transport and processes operating within the depositional environment (Bjørlykke and Jahren, 2015, Blatt et al., 2006) (Figure 2.1). Climate conditions also influence the reservoir quality by controlling the source

rock weathering, river discharge and post-depositional meteoric water flushing of the sediments. Also, type and distribution of clay-sized particles have an important role in the diagenetic evolution of sandstones. Clay minerals can be either deposited prior to deposition along with framework grains (allogenic) or, develop within the sand as consequence of mineral alternation (authigenic)(Nichols, 2009). Authigenic clays are produced within the basin where the sediments deposited while allogenic clay minerals have been transported from outside of the basin to the site of deposition and later became a part of pre-existing sedimentary rocks within the basin.

Allogenic, or detrital clays tend to occur in several modes within the sandstones depending on the source and depositional environment. Syndepositional clays are deposited as a dispersed matrix, lamina, mudstone/mud clasts, sand-sized floccules and biogenic pellets (Wilson and Pittman, 1977)(Figure 2.2). Infiltration residues clay and burrow fillings tend to form shortly after deposition (Wilson and Pittman, 1977). Allogenic clay minerals are carried by downward or laterally migrating pore waters and naturally accumulates in pore space of previously deposited sands (Ali et al., 2010). The accumulation of individual clay particles can form, tangential grain-coating and pore-bridging fabrics (Ali et al., 2010). Any type of clay mineral can occur as a detrital component, however typically chlorite, illite, smectite and mixed-layer clays occur as grain coatings (Ali et al., 2010). Clay coatings are important parameter during the further diagenesis, as these minerals postpone or inhibit quartz cementation (Ali et al., 2010).

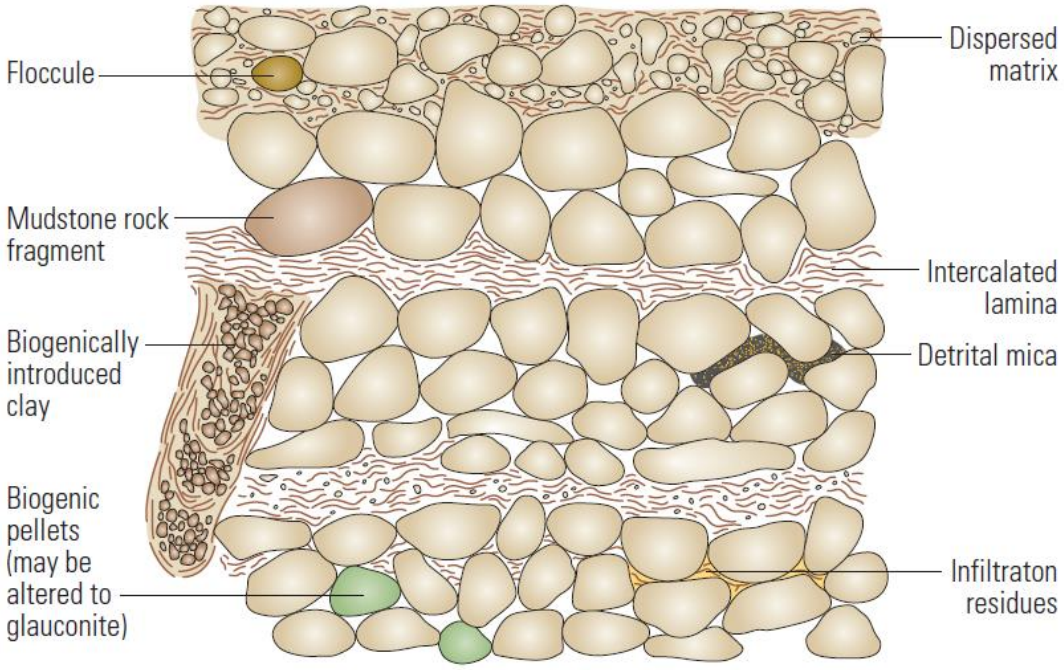

Figure 2.2: Modes of allogenic clays occurrences in sandstones (modified after Wilson and Pittman, 1977 in Ali et al., 2010).

Authigenic clays, unlike allogenic clays, develop subsequent to burial and are seen as pore linings, pore fillings, pseudomorphous replacements or fracture-fillings (Wilson and Pittman, 1977) (Figure 2.3). The factors such as pore-water chemistry and rock composition have a significant effect on the growth of authigenic clays (Ali et al., 2010).

Pore-lining clay minerals such as authigenic clay, detrital grains, bitumen, and micro-quartz could prevent quartz cementation by decreasing the necessary surface area for quartz nucleation, resulting in abnormal high porosity at great depth (Wilson and Pittman, 1977).

Pore filling authigenic clays and fractures-filling clays reduce the primary porosity of the sediment due to little net gain in pore space. Pore-filling authigenic clays reduce the permeability as the pores between the clay crystals are too small to be filled with oil (Bjørlykke and Jahren, 2015). Pseudomorphous replacement clays modify the primary mineralogical composition of the sedimentary rock by entirely or moderately replacement of grains but have an insignificant effect on reservoir quality (Wilson and Pittman, 1977).

By determining the primary composition of the sandstone, it would be possible to obtain useful information regarding provenance, palaeoclimate and tectonic stability during the time of deposition. Therefor understating the primary composition of the sandstone is the first vital step in order to understand a reservoir and diagenetic processes affecting the reservoir quality (Bjørlykke and Jahren, 2015).

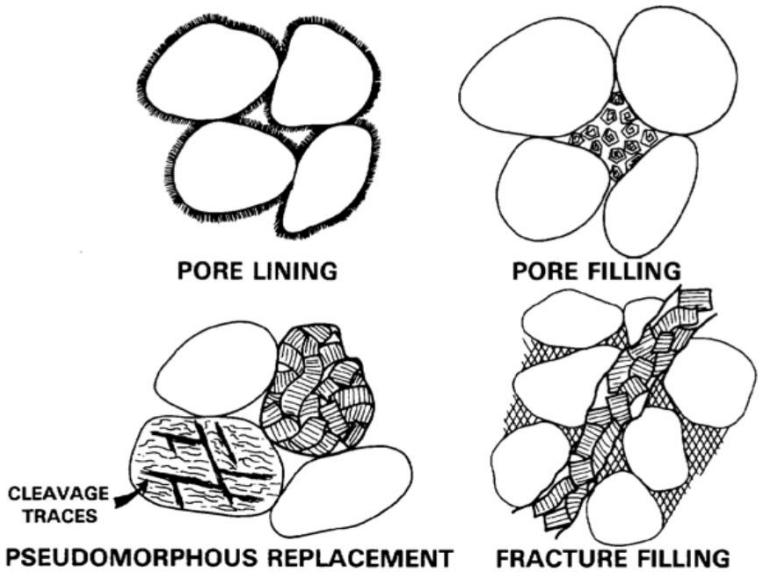

Figure 2.3: Occurrence of authigenic clays in sandstones from (Wilson and Pittman, 1977)

2.3 Diagenetic processes in sandstones

Diagenesis is an open /closed system which embraces all the processes that change the initial composition of the sediments after deposition and before metamorphism (Bjørlykke and Jahren, 2015). The starting point for the diagenetic processes is the initial composition of the sandstone, which is a function of the rocks eroded, transported and depositional environments. Therefore, the diagenetic models must be linked to the sedimentological processes (Bjørlykke and Jahren, 2015). The main diagenetic processes from surface conditions to deep burial are:

- Near-surface diagenesis
- Mechanical compaction
- Chemical compaction

2.4 Early diagenesis

A soon as the sediments buried at depth <1-10 m, the near-surface diagenetic reactions start to modify the initial composition of the sediments. At very shallow depth, sediments have the maximum potential to react with the atmosphere or meteoric water. Diagenesis in this stage operates within an open system and involves the addition and removal of solids in solution. The dissolved solids are transported by diffusion and fluid flow close to the surface, while diffusion takes place within about 1 m below seabed (Bjørlykke and Jahren, 2015). Sediments have maximum potential to change bulk composition after deposition at shallow depth than at greater depth, since the condition is oxidizing near the surface, while at greater depth the reducing conditions dominate. Therefore, the ability of the sediments to change their bulk composition after deposition tend to decrease gradually with burial (Bjørlykke and Jahren, 2015). In the earliest stage of diagenesis, the primary component of the sediments is under the influence of meteoric water flushing, biogenic activity, redox-driven processes and the precipitation of authigenic clay minerals (Bjørlykke and Jahren, 2015).

2.4.1 Redox reactions

The redox boundary is below the seafloor at a depth between 20 cm to 1 m. The redox boundary represents an equilibrium between the supply of the oxygen by diffusion and the consumption of the oxygen by oxidation of organic matter. The reducing conditions are mostly a result of biological decomposition of organic matter. The concentration of oxygen tends to decrease rapidly below the water/sediment interface, providing a concentration gradient for the diffusion of the oxygen downwards into the uppermost sediments (Bjørlykke and Jahren, 2010). The rate of downward diffusion of oxygen is controlled by the concentration gradient of oxygen within the porewater as well as the diffusion coefficient in the sediments (Bjørlykke and Jahren, 2015). The diffusion coefficient is higher in coarse-grained sand compare to mud deposits. Therefore, sand tends to have a deeper redox

boundary than mud. As result of the downward diffusion of oxygen, authigenic minerals such as hematite and goethite start to precipitate near the seabed in oxic environments, while at greater depths where the oxygen is absent within the porewater the reduction of sulphates by sulphate-reducing bacteria produces pyrite at the bottom of anoxic water(Bjørlykke and Jahren, 2015)

2.4.2 Biogenic activity

Biogenic activities play an important role in changing the textural composition of the sediments after deposition. The burrowing organisms consume mud and oxidize organic matter and physically destroy the primary sedimentary structures of the sediments. Bioturbation also plays an important role in reducing the porosity and permeability by mixing clay with clean sand. Bioturbation could increase the vertical permeability due to the destruction of thin intercalated clay lamina. The absence of bioturbation may be evidence of rather a rapid sedimentation giving little time for fauna to be established, or indicates a strongly reducing condition in which funna could not survive. Burrowing organisms eat mud and produce fecal material which may develop into smectite-rich clay, which later alters to chlorite coating, consequently improve reservoir quality (Bjørlykke and Jahren, 2010). The source of carbonate cement are mainly Calcareous organisms and sometimes also siliceous organisms, which cause a reduction in porosity at greater depth.

Marine organisms composed of aragonite which is very unstable at shallow burial depth thus dissolved and calcite will precipitate either as pseudomorphous replacements within the fossils or as pore-filling cement between the framework grains. Siliceous organisms composed of opal A. which may later develop into opal CT and quartz. Organic silica is an important source of grain coating micro-quartz, which could preserve porosity at greater depths (Bjørlykke and Jahren, 2015).

2.4.3 Meteoric water flow

Meteoric water is rainwater which penetrates into the ground, and as long as the groundwater table is above the sea level, it flows along the most permeable beds into the basin (Figure 2.4). Meteoric water is undersaturated with respect to all minerals (Bjørlykke and Jahren, 2015). The reaction between meteoric water and the land surface has been considered as the most critical part of weathering processes. Rainwater is slightly acidic since it contains carbon dioxide (CO_2) and sulphur dioxide (SO_2) from the air, producing carbonic acid (H_2CO_3) and sulphuric acid (H_2SO_4). Decaying organic matter also produces CO_2, which consequently causes the meteoric water to become more acidic. Humic acids caused by decaying plants also accelerate the weathering reactions. Meteoric water flushing first dissolves carbonates and then dissolve unstable minerals such as feldspar and mica and precipitates authigenic clay minerals, most commonly kaolinite (Bjørlykke and Jahren, 2015). Equation 2.1 shows the leaching reaction that dissolves feldspar and precipitates kaolinite, and Equestion 2.2 shows the dissolution of mica and precipitation of kaolinite. As is evident

from the reactions the low K+/H+ ratios drive the reactions to the right (Bjørlykke and Jahren, 2015).

Eq. 2.1 $2K(Na)AlSi_3O_8 + 2H^+ + 9H_2O = Al_2Si_2O_5(OH)_4 + 4H_4SiO_4 + 2K^+(2Na^+)$

Mica is dissolved, and kaolinite is precipitated as equation 2 shows:

Eq. 2.2 $2KAl_2Si_30_{10}(OH)_2 + 2H^+ + 3H_2O = 3Al_2Si_2O_5(OH)_4 + 2K^+$

Dissolution of feldspar and mica grains cause the development of holes which are secondary porosity, but due to precipitation of kaolinite in pore spaces, there is a little net gain in porosity. Authigenic kaolinite also reduces the permeability, since it tends to occur as pore-filling minerals. The pore space between the kaolinite crystals is too small to be filled with oil due to high capillary entry pressure. Thus the total water saturation would be higher in kaolinite-rich sandstone reservoirs.

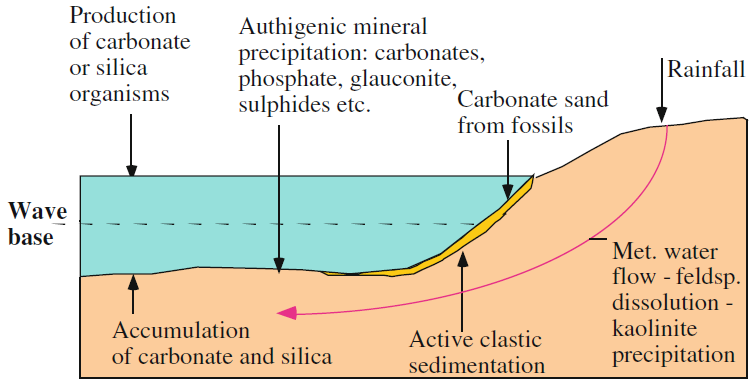

Figure 2.4: Meteoric water flushing and other diagenetic processes in shallow marine environments (Bjørlykke and Jahren, 2010).

2.5 Mechanical compaction

Mechanical compaction of sedimentary layers is a function of the effective vertical stress and compressibility of the grain framework (Chuhan et al., 2002) (Bjørlykke and Jahren 2012). The mechanical compaction process includes sliding, crushing, reorientation and repacking of the sediment grains. Mechanical compaction dominates in the shallow parts of the basin down to 2-4 km of burial depth depending on the geothermal gradient. Mechanical compaction is regarded as most effective porosity-reducing mechanism in shallow burial (Mondol et al., 2007, Lundergard, 1992, Paxton et al., 2002, Bjørlykke and Jahren, 2015) (Figure 2.5). The effective stress from the overburden reduces porosity by rearranging and packing the sediments. Crushing generates large relative motions between sand particles and increase the degree of deformation which lead to tighter grain packing and consequently reduction in

porosity (Chuhan et al., 2002). The main factors that have a significant effect on the degree of mechanical compaction include mineralogy, grain size, grain sorting and grain shape. Well sorted coarse-grained sand compacts more as compare to fine-grained sand due to grain crushing (Figure 2.6)(Chuhan et al., 2002, Chuhan et al., 2003). Likewise, grain shape, as well as the actual area of the contact surface, play an important role in terms of stress at a given grain contact. The porosity loss in fine-grained sandstone is mostly associated with reorientation and sliding of grains, while in coarse-grained sandstone deposits grain crushing will act as the main porosity reducing mechanism (Chuhan et al., 2002).

In sedimentary basin with normal geothermal gradients, little quartz cement (2-4%) strengthens the grain framework and will shut down further mechanical compaction in sandstones, so that further compaction is mainly controlled by the rate of mineral dissolution and precipitation in chemical compaction domain (Bjørlykke and Jahren, 2015). Understanding the degree of the porosity loss during the mechanical compaction window is essential, in order to determine the intergranular volume (IGV) which is the porosity before quartz cementation (Bjørlykke and Jahren, 2015).

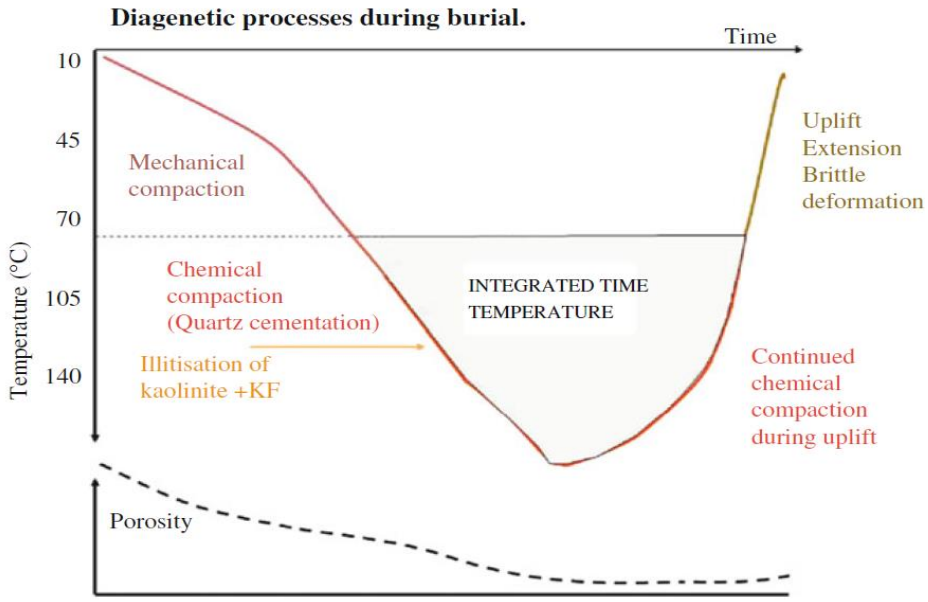

Figure 2.5: Mechanical and chemical compaction during the burial (Bjørlykke and Jahren, 2010).

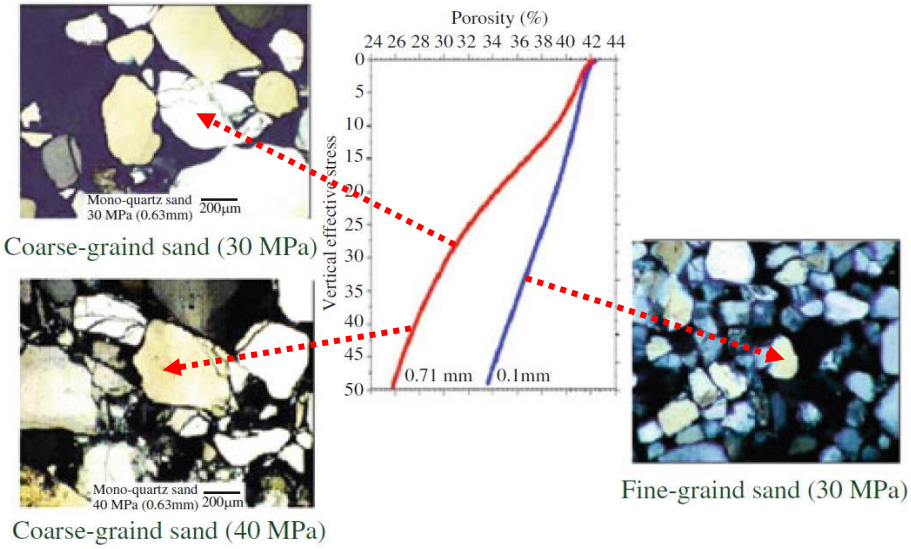

Figure 2.6: Experimental compaction of fine-grained and coarse-grained sand (Chuhan et al., 2002).

2.6 Chemical compaction

Chemical compaction dominates in the deeper parts of the basin at higher temperatures (>60-100^0 C) and involves dissolution and precipitation of minerals. Chemical compaction is considered as the main porosity reducing mechanism at greater depths. In this level, the time, temperature and factors such as detrital mineralogy and texture are controlling the quartz cementation in chemical compaction regime (Bjørkum et al., 1998, Walderhaug, 1996, Walderhaug and Rykkje, 2000). The amount of quartz cement is a function of available surface area for quartz precipitation and the time-temperature integral. Therefore, the geothermal gradient within the sedimentary basin and slow subsidence rates significantly increase the amount of quartz cement at a specific depth (Bjørlykke and Jahren, 2015).

2.6.1 Intermediate burial depth (2 - 3.5 km)

At intermediate burial depth both chemical and mechanical compaction act at the same time to reduce the porosity in sandstones. The transition from mechanical to chemical compaction is marked by the onset of quartz cementation at depth around 2 km and temperatures >60-80^{0}C, called transition zone. Mechanical compaction by fracturing and grain reorientation continues until initiation of quartz cement occurs around 70-80^{o}C. Quartz cementation efficiently prohibits further effect of mechanical compaction of sediments (Bjørlykke and Jahren, 2015). At this stage, further mechanical compaction would only be possible if coatings inhibit quartz cementation. Thus fracturing continues, and more fresh grain surfaces would be available for further quartz cementation and consequently more porosity reduction.

The process in which K-feldspar or plagioclase is replaced by albite is called albitization process. Albitization in sandstones tends to start at depth around 3 km. Albite is more stable than other feldspar minerals because sodium is normally the dominant cation within the pore water. During the albitization of plagioclase, dissolved Ca^{2+} start to precipitate as calcite

cement. It is worth to mention that the albitization does not have significant effect on reservoir quality of sandstone reservoirs (Bjørlykke and Jahren, 2010).

2.6.2 Deep burial (>3.5 – 4 km)

Quartz cementation starts at approximately 70^{0}C and proceeds until ambient temperatures are reduced below 70^{0}C. In this stage, the controlling factors are temperature and surface area available for quartz cementation. Thus the temperature history of the sandstone reservoirs is critical for modeling, predicting quartz cementation and evaluating the porosity in deep burial. Both porosity and permeability decrease sharply in deeply buried sandstones as result of quartz cementation and precipitation of illite (Bjørlykke and Jahren, 2015).

Illitization starts around a temperature range of 70-100^{o}C. The specific morphology of illite reduces the permeability of the reservoir. Since illitization requires a source of potassium, illite can form from feldspar, kaolinite, and smectite (Bjørlykke and Jahren, 2015).

Eq. 2.3 $KAlSi_3O_8 + Al_2Si_2O_5(OH)_4 = KAl_3Si_3O_{10}(OH)_2 + 2SiO_2 + H_2O$

At a temperature around 130^{0}C , feldspar and kaolinite are thermodynamically unstable.

Eq. 2.4 $KAlSi_3O_8 + Al_2Si_4O_{10}(OH)_2 = KAl_3Si_3O_{10}(OH)_2 + 4SiO_2$

The amount of illite at great depths depends on provenance through the supply of K-feldspar, as well as the intensity of leaching and kaolinite precipitation during the early stage of diagenesis.

2.7 Formation of overpressure

The development of overpressure at shallow depth reduces the effective stress, thus preserves the porosity (Bjørlykke and Jahren, 2010, Ramm and Bjørlykke, 1994). Overpressure develops as result of rapid burial of fluid-filled sediments which are covered by an effective seal. The pressure results from the fluids within the sediments will neutralize the effective stress from the overburden and subsequently preserve the intergranular porosity.

Chapter 3: Data and Method

3.1 Introduction

The primary objective of this chapter is to explain the methods which have been used in the present study. The research targets the evaluation of the reservoir quality of Stø Formation in the Hoop Fault Complex and Fingerdjupet Sub-basin in the southwestern Barents Sea along with the investigation of the transition from Stø to Fuglen formation, by employing several techniques such as sedimentological, petrographical and petrophysical analyses.

3.2 Wells used in this study

Stø/Fuglen formations transition is cored in two wells: 7324/7-2 (Hanssen) in the Hoop Fault Complex and 7321/9-1 in Fingerdjupet Sub-basin. OMV Norge provided access to Core material from well 7324/7-2 (Hanssen), and the Norwegian Petroleum Directorate (NPD) provided access to core data from the well 7321/9-1. The cores were logged, and samples were collected for the purpose of XRD, Optical Microscopy, and SEM analysis. Through this section, general information about the wells such as their geographical location and drilling history has been provided.

Well, 7324/7-2 (Hanssen) is located in the Hoop Fault Complex in the southwestern Barents Sea. The aim of this well was to prove the presence of the hydrocarbons in Realgrunnen Sub-group as well as in the Snadd formation. Stø Formation of the Realgrunnen Sub-group was encountered at 712 m depth and was an oil-bearing zone with relatively good reservoir rocks, whereas the secondary target Snadd Formation in deeper parts contains poor reservoir rocks (Figure 3.1).

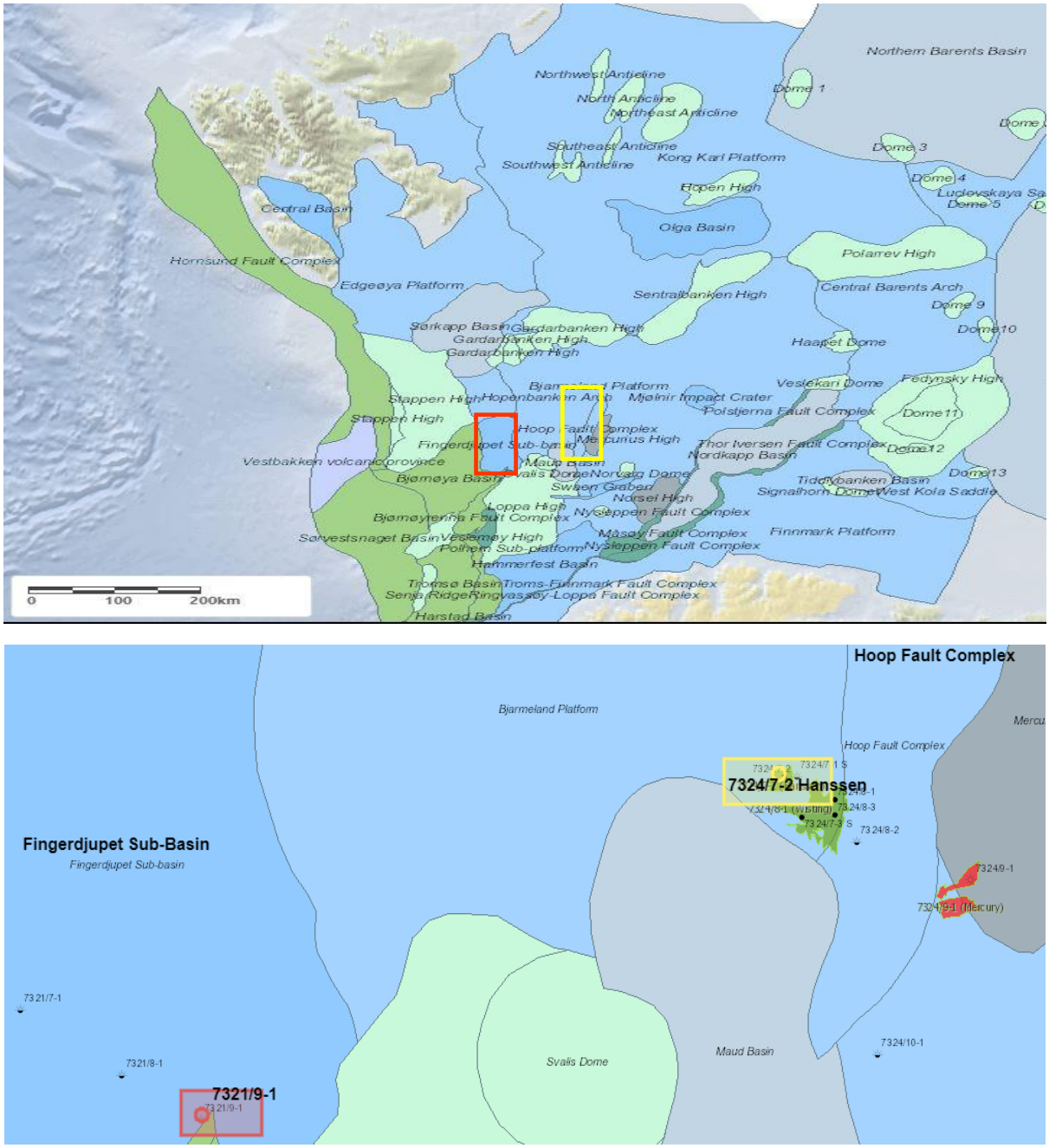

Figure 3.1: Position of wellbore 7324/7-2 in Hoop Fault Complex (yellow rectangle) and wellbore 7321/9-1 in the Fingerdjupet Sub-Basin (red rectangle) in the southwestern Barents Sea (http://www.npd.no/)

Well, 7321/9-1 belongs to the Fingerdjupet Sub-basin in the Bjørnøya East area (Figure 3.1). The primary target of the well was to evaluate the hydrocarbon potential of the Late Triassic to Middle Jurassic Sandstones of Stø, Nordmela, and Fruholmen Formations as well as Early Cretaceous to Triassic sandstones of the Snadd Formation. According to a report which has been published by the Norwegian Petroleum Directorate in 2005 about the operation result of the well 7321/9-1, the sandstone reservoirs of the Late to Middle Jurassic were water bearing with a weak indication of hydrocarbons. In this report, it is stated that the Snadd

Formation did not contain hydrocarbon shows nor gas and therefore was interpreted as water bearing.

3.3 Sedimentological Analysis

Core sampling and sedimentological logging of Stø and Fuglen formations were conducted in September and December 2016 at OMV and NPD, respectively. A Total of 21 m and 25 m core was logged for well 7324/7-2 and well 7321/9-1, respectively.

The cores were logged in several logging sheets with a vertical scale 1:50 for both Stø and Fuglen formations. Lithological description, grain size, color, boundaries, textures, sedimentary structures, and degree of bioturbation was investigated. The logging sheets were later digitalized using Adobe Illustrator CS6. The data derived from the core observation, core photos, and sedimentological logs were subsequently used in order to interpret facies description and depositional environments.

3.4 Mineralogical and Petrographical Analysis

Mineralogical and petrographical analyses have been carried out by using optical microscopy, Scanning Electron Microscopy (SEM) and bulk XRD analyses in order to evaluate the reservoir quality of Stø Formation.

3.4.1 Optical Microscopy

The collected core samples from the wells 7324/7-2 and 7321/9-1 were prepared at the Department of Geoscience, UiO. In total, 30 thin sections with 30µm thickness were made for the purpose of this study. The thin sections were analyzed using a Nikon Optical Microscope under both plane polarized light (PPL) and cross-polarized light (XPL) in order to describe grain characteristics, mineral content and diagenetic processes.

3.4.2 Mineralogical Analysis

In order to evaluate the reservoir quality, it is important to understand the petrographic characteristics such as mineral composition and sediment texture. This is due to the fact that these parameters provide valuable information about sediment provenance, climate, sediment transport, and type of depositional environments. These petrographic characteristics have been described based on the following features: mineral contents, grain size variation, the degree of grain sorting, the degree of grain roundness, sphericity, matrix content and grains contact. The study of mineralogical characterization has been conducted by using point counting technique and scanning electron microscope (SEM) analysis. Visual comparators such as "Atlas of Sedimentary rock (Adams et al., 1984)", "Color Guide to the Petrography of Sandstones, Siltstones, Shales and Associated Rocks (Ulmer-Scholle et al., 2014)" and XRD result were used to identify different types of minerals and cementation.
Quartz grains have high stability and were recognized by their extinction angles. Feldspar grains were identified by their characteristic twining effect.

The mineralogical assembly of quartz, feldspar and rock fragments, which were determined through point counting analysis were later classified according to Dott' classification scheme (Dott Jr, 1964) (Figure 3.2).

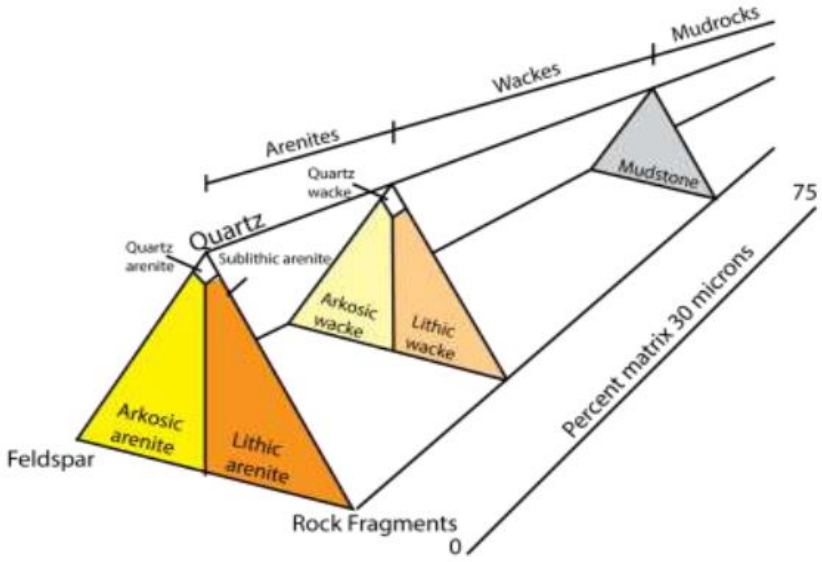

Figure 3.2: Scheme used for classification of sandstones, modified after (Dott Jr, 1964).

TEXTURAL ANALYSIS

Through the textural analysis, the following features of the grain have been measured: Average grain size, sorting, roundness, grain contacts, the degree of grain preservation, porosity and intergranular volume (IGV).

AVERAGE GRINE SIZE

Average grain sizes were determined in two ways first by visual observation during core logging and second by through the microscope measurements. Average grain size measured the longest axis of >100 grains per Sample. The measured average grain size was converted to phi scale by utilizing the Wentworth grain size scale (Eq. 3.1) (Figure 3.3).

Eq. 3.1: $$\Phi = -\log_2 d$$

where Φ denotes phi size, and d denotes grain diameter in millimetres.

Millimeters (mm)	Micrometers (μm)	Phi (ϕ)	Wentworth size class		Rock type
4096		-12.0	Boulder		
256		-8.0	Cobble	Gravel	Conglomerate/ breccia
64		-6.0	Pebble		
4		-2.0	Granule		
2.00		-1.0	Very coarse sand		
1.00		0.0	Coarse sand		
1/2 0.50	500.00	1.0	Medium sand	Sand	Sandstone
1/4 0.25	250.00	2.0	Fine sand		
1/8 0.125	125.00	3.0	Very fine sand		
1/16 0.0625	63.00	4.0	Coarse silt		
1/32 0.031	31.00	5.0	Medium silt		
1/64 0.0156	15.60	6.0	Fine silt	Silt	Siltstone
1/128 0.0078	7.80	7.0	Very fine silt		
1/256 0.0039	3.90	8.0			
0.00006	0.06	14.0	Clay	Mud	Claystone

Figure 3.3: Grain size classification (Wentworth, 1922)

GRAIN SIZE SORTING

Sorting was determined by using the standard deviation values given by Folk and Ward, (1957) (Eq. 3.2) and correlated with verbal terms (Folk, 1974) (Figure 3.4). The calculated sorting values were compared with the visual sorting estimation chart after (Harrell, 1984).

Eq. 3.2 $$\sigma = \frac{\Phi_{84}-\Phi_{16}}{4} + \frac{\Phi_{95}-\Phi_{5}}{6.6}$$

Where σ denotes standard deviation and Φ denotes phi size.

Standard deviation (Folk, 1974)		Visual comparators (Harrell, 1984)	
<0.35 Φ	Very well sorted	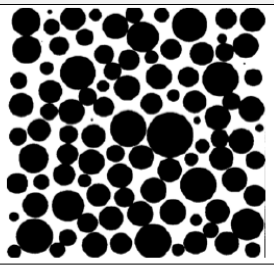	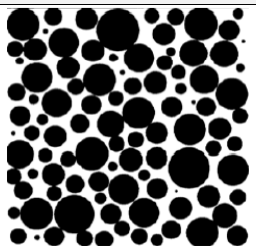
0.35 – 0.50 Φ	Well sorted		
0.50 – 0.71 Φ	Moderately well sorted	Well sorted (0.35ϕ)	Mod. – well sorted (0.50 ϕ)
0.71 – 1.00 Φ	Moderately sorted	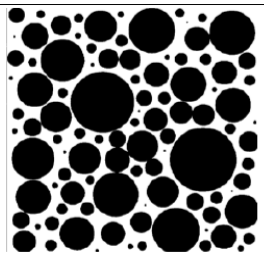	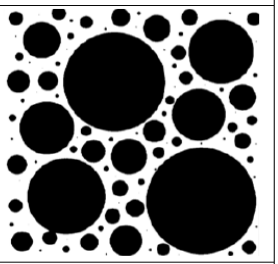
1.00 – 2.00 Φ	Poorly sorted		
2.00 – 4.00 Φ	Very poorly sorted		
> 4.00 Φ	Extremely poorly sorted	Poorly sorted (1.00 ϕ)	Very poorly sorted (2.00 ϕ)

Figure 3.4: Standard deviation values corresponding to terms of sorting (Folk, 1974) and visual comparators for grain size sorting after (Harrell, 1984)

GRAIN SHAPES

The grain roundness is the term to describe the shape of the corners on a particle, and grain sphericity is the term to explain how close a grain is to a sphere (Powers, 1953). The grain roundness and sphericity of 200 representative grains per thin section were determined based on their appearance compared to those in Powers, (1953) (Figure 3.5). The results were utilized to interpret sediment composition, transport process and distance and degree of reworking.

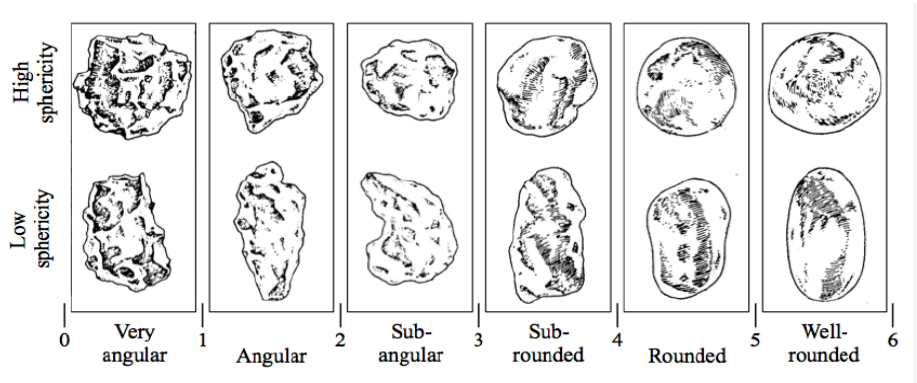

Figure 3.5: Determination of grain roundness and sphericity (Powers, 1953).

GRAIN CONTACTS

Development of mechanical compaction during the burial caused the creation of different types of grain contacts such as tangential, long, Concave-convex and sutured contacts (Figure 3.6).

Tangential and long grain contacts use to appear as a relatively straight-line contact between grains, while concave-convex contacts appear as curve lines. The presence of sutured grain contacts display stylolites pore spacing and along with concave-convex grain contacts indicate the highest degree of pressure solution during the mechanical regime before entering to transition zone and chemical compaction regime(Taylor, 1950, Boggs Jr and Krumbein, 1996).

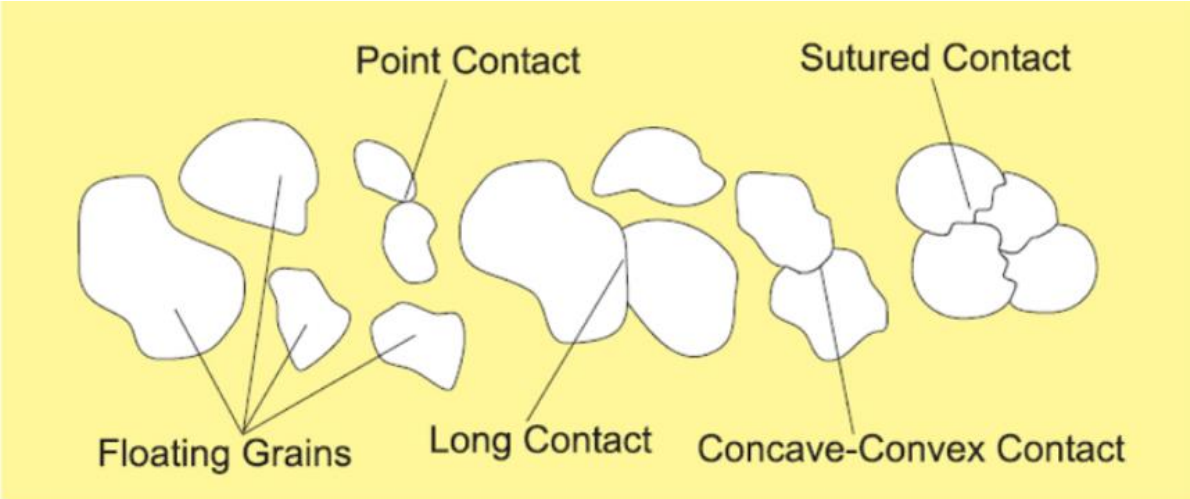

Figure 3.6: This figure shows the different type of grain contacts typically found in sandstones; tangential, long, Concave – convex and sutured contacts (figure from Santin et al., 2009).

INTERGRANULAR VOLUME (IGV)

Intergranular volume is defined as the sum of the intergranular pore space, intergranular cement and depositional matrix in a given volume of rock, where the depositional matrix is defined as clay and silt size particles which fill the space between framework grains (Paxton et al., 2002) (Eq. 3.3). IGV depends on grain composition and textural parameters such as sorting and grain size. Since IGV reflects the proximity of the framework grains, it has been considered as a valuable indicator of mechanical and chemical compaction (Paxton et al., 2002). The IGV value in the clean sand is around 40-42 % at the surface, but this amount decreases as a function of burial depth, effective pressure, the textural and mineralogical composition of the buried sediment (Paxton et al., 2002).

Eq. 3.3 $$IGV\ (\%) = V_{Porosity} + V_{cement} + V_{Matrix}$$

PRESERVATION OF DETRITAL GRAINS

The chemical instability of feldspar and mica grains has made these minerals decent indicators for weathering intensity in the depositional environment or the leaching intensity. These minerals tend to break down to clay minerals during the post-depositional processes. The preservation degree of the feldspar grains were determined based on the appearance of following features:

- Twins and cross-hatched characteristics.
- The surface texture of the feldspar grains.

Based on the degree of preservation, the feldspar grains have been classified into four groups. Group 1 represents the fresh grains without signs of weathering, such that twins are fully preserved. In group 2, grains have been under the influence of a slight degree of weathering but twins still well maintained. Group 3 represents grains with a relatively moderate degree of weathering, such that twins are blurry, and grain surfaces are rough. In group 4, due to an intense degree of weathering almost whole parts of the grains have been dissolved, but twins are still visible in the remaining parts (Table 3.1).

Table 3.1: Table classifying the degree of weathering from 1 to 4.

Preservation degree	*1= (Fresh grains)*	*2= (High)*	*3= (Intermediate)*	*4= (Low)*
Description	*Fresh grains, No sign of weathering. Twins well preserved*	*The presence of a slight degree of weathering. Twins still well preserved.*	*An intermediate degree of weathering. Twins are blurry, and grain surfaces are rough.*	*Most parts of the grains have been dissolved. However, twins are still visible in remaining parts.*

The preservation degree of mica grains were evaluated based on the intensity of deformation and alteration (Table 3.2). The degree of deformation and alternation of mica grains could provide information about leaching intensity, burial depth, and mechanical compaction. In this study, the observable mica grains have been classified into three groups such that group-1 shows well-preserved mica grains along with some sign of mechanical deformation, group-2 represents deformed grains which have been partly squeezed into intergranular pore space, and group-3 demonstrates completely dissolved and altered mica grains (Table 3.2).

Table 3.2: Table shows the classification of mica grains based on their preservation degree.

Preservation degree	*1= (Fresh)*	*2= (Intermediate)*	*3= (Low)*
Description	*Well preserved mica grains along with some sign of mechanical deformation.*	*Partly squeezed into intergranular pore space Deformed grains.*	*Completely dissolved and altered grains.*

The presence of completely dissolved grains has also been investigated as they reflect the post-depositional process. Post-depositional process alters the initial sediment composition and texture significantly, and consequently, causes the development of secondary porosity. The original composition of the grains could be determined through the SEM analysis provided that the remnants of the original grain could be found. Since primary and secondary porosity reflects different depositional processes, a distinction between them is valuable. Secondary porosity could have a positive effect on reservoir quality by increasing the total porosity as a result of grain dissolution. Although, this positive effect corresponds only to the surface and will quickly diminish by increasing the mechanical compaction during burial.

POINT COUNTING

The point counting analysis was performed in order to determine the relative portion of the minerals such as quartz, feldspar, rock fragments, cement (quartz cement, chlorite cement, illite cement, kaolinite cement), porosity and matrix in each thin section. 13 samples were chosen from well 7324/7-2 (Hanssen), and 17 samples from 7321/9-1 in Fingerdjupet Sub-basin. The thin sections were divided into ten equal parts using nine parallel lines, and within each part, 40 points have been counted (400 counts per slide). The spacing intervals varied between 2 to 4 depending on the sediment distribution within the thin section.

Uncertainties

The result of the point counting analysis commonly associates with several uncertainties. The following three principal sources of errors have been suggested by (Solomon, 1963): The operator error, counting error, and sampling error.

1. Operator error: depend on the experience different operators might give different results, especially when it comes to clay mineral identification and identification of the strongly altered minerals.
2. Counting error: Grain size variation, the area of counting and count length are common counting error thus the point-counting analysis may not be able to represent the exact composition of the sample. However, the stepping length is a controlling factor for variance in point counting results. In this study, 400 points per slide are chosen to limit this error. It is considered as the statistical representative number for the sandstone samples.
3. Sampling error: The third source of error is related to sampling error, such that the sample section could not represent the origin of parent rock accurately.

3.4.3 Bulk XRD

X-ray Powder Diffraction is a useful analytical technique primarily used for phases identification of crystalline materials which can provide detail information regarding the unit cell dimension.

Applications of Bulk XRD

X-ray powder diffraction can be used to order to identify unknown crystalline minerals (minerals and inorganic compounds) which are critical in geologic studies.

X-ray diffraction is based on constructive interference between monochromatic X-rays and a crystalline sample. X-rays are generated by a cathode ray tube and filtered to produce concentrated monochromatic radiation, directed toward the sample. The interplay between incident rays and the sample produces constructive interference and a diffracted ray which is expressed by Bragg's Law (Eq. 3.4).

Eq. 3.4 $$n\lambda = 2d_{hkl} Sin\ \theta$$

Where n is constant λ is the incident X-rays, d is the atom spacing in crystalline lattice and θ is the diffraction angle between the incident rays and atomic planes. Diffracted X-rays are detected, processed and counted. By scanning the sample through 2θ angles, all diffraction of the lattice should be detected at a 180^0 angle since the powder material has a random orientation. Since each mineral has a set of unique d-spacing thus the transformation of diffraction peaks to d-spacings allows identification of each mineral. Table 3.3 by Moore and Reynolds, 1989 shows a Characteristic peak for common mineral based on a comparison of d-spacing with the standard reference pattern.

Mineral	*d-spacing*	*Mineral*	*d-spacing*
Quartz	*3.34 Å*	*Kaolinit*	*7.0 Å, 3.58 Å*
Plagioclase	*3,19 Å*	*Chlorite*	*7.0 Å, 3.54 Å*
K-feldspar	*3.24 Å*	*Illite*	*10.0 Å*
Muscovite	*10.01 Å*	*Calcite*	*3.03 Å*

Table 3.3: Characteristic d-spacings used for identification of common minerals.

The XRD analysis has been carried out by utilizing the following software in order to achieve different goals:

- Diffrac EVA: To identify different type of minerals.
- BGMN Profex: To quantify the bulk mineralogy.

Sample preparation

40 samples were prepared for XRD analysis. The Crusher machine was used to crush the consolidated samples and separate the mineral grains from one another. By using the crusher machine, the grain size was reduced to less than 500 µm. Each sample was powderized once again using a McCrone micronizing mill. 3 grams of each sample were extracted and placed in the mill container with 9 ml of ethanol and 48 pieces of agate and micronized for 12 minutes. The samples dried overnight and were transferred onto pellets and run through the XRD.

Uncertainties

- The most significant uncertainty in XRD analysis is sample preparations.
- Lack of accurate adjustment of the instrument
- Preferred orientation of the surfaces of the samples

3.4.4 Scanning Electron Microscopy

The SEM allows the high-resolution study of the pores and identification and distribution of minerals within the pore space. In this study, five thin sections were selected for SEM analysis. A JEOL JSM-6460LV Scanning Electron Microscope with LINK INCA Energy 300 (EDS) was used for sample analysis. The thin sections were first cleaned and steamed with carbon before entering to the machine. The primary target of SEM analysis was to enhance the accuracy of the point counting results by identifying the smallest minerals and diagenetic cement which were difficult to recognize through point counting analysis. For this purpose, the Backscattered electrons (BEI) and secondary electrons (SEI) were used together in order to identify different elements in the samples. The achieved spectrum peaks through SEM analysis compared with those given in “SEM Petrology” (Welton, 1984).

Uncertainties

Uncertainties related to the result of the scanning electron microscopy are the possibility of the samples to be contaminated during the preparation process, which could be interpreted as natural features of the rock. Another source of mistake is related to the elemental analysis, particularly if the measured mineral is extremely small and is in a close contact with other minerals.

3.5 Petrophysical Analysis

Petrophysical analyses were carried out for both wells 7324/7-2 and 7321/9-1 based on the geophysical well logs. The evaluation of the compaction regime intervals, maximum burial-temperature, and uplift estimation were the aim of petrophysical analysis. The well logs used in this study are Gamma log (GR), neutron log, density log and sonic log. Summary of the wells database which have been utilized in this thesis is shown in (Appendix. A).

3.5.1 Compaction and Uplift estimates

Compaction in sandstones is divided into mechanical and chemical compaction regimes. Mechanical compaction is driven by the effective vertical stress created from the weight of the overburden and causes a reduction in bulk volume. The porosity generally decreases with depth due to reorientation and fracturing of the grains which is mainly in mechanical compaction window. Basically, the reduction in the bulk volume of the sediments in mechanical compaction window here is equal to the loss of porosity. The factors such as grain size, sorting and grain framework strength, have a straight effect on the loss of bulk volume during mechanical compaction such that well sorted and smaller grain size sands are more resistance to mechanical compaction compare to the coarse-grained sands. Unlike porosity, density and velocity tend to increase with depth. A sharp increase in the velocity and density log indicates the transition from mechanical to chemical compaction domain. The boundary between mechanical and chemical is called the transition zone and is marked by the onset of quartz cementation at temperatures around 70-80^{0}C. At temperatures higher than this level, the time, temperature and factors such as detrital mineralogy and texture are controlling the quartz cementation in chemical compaction regime (Bjørkum et al., 1998, Walderhaug, 1996, Walderhaug and Rykkje, 2000). The quartz cementation during the chemical compaction regime will strengthen the rock framework and consequently neutralize the further effect of mechanical compaction on sediments. In this study, the difference between calculated transition zone and observed transition zone has been used in order to estimate uplift for studied wells.

Uplift estimation

P-wave velocity and density tend to increase with burial depth. Thus, the well log data expected to follow a certain trend with increasing burial depth. The exception from this trend can occur due to variation in:

- Lithology, since coarse-grained rocks will compact more than fine-grained rocks due to higher effective vertical stress at grain contacts during the mechanical compaction regime (Mondol et al., 2008, Chuhan et al., 2003).
- Type of fluid in the formation (oil or water).
- pore pressure.

At the onset of chemical compaction (70-80^{0}C) a minor amount of quartz cement can prohibit the further effect mechanical compaction on sediments by stiffening grain framework (Dvorkin and Nur, 1996). The velocity/depth plot is able to demonstrate the transition from mechanical to chemical compaction regime as a sudden increase in velocity curve. Distinguishing the mechanical (MC) from chemical compaction (CC) regimes is essentially useful for the purpose of uplift estimation. The most common procedure for uplift estimation is plotting velocity versus depth together with one or several published compaction trends. The well, 7324/7-2 is selected for uplift estimation since high acoustic velocities in this well are encountered at shallow depth due to uplift. Many experimental compaction curves have been published, which show velocity/depth trends. In this thesis, uplift was estimated for well 7324/7-2 by comparing the observed velocity/depth trends with those published by (Storvoll et al., 2005); (Mondol et al., 2007), (Mondol, 2009); (Marcussen et al., 2010) and (Baig et al., 2016). Transition zone was estimated based on the entire velocity data set in well 7324/7-2, while uplift estimation was performed for data points which represent shaly intervals. The gamma-ray log was used as lithology indicator in order to determine the volume of shale in the formation. The shale boundary was set to 145 API for well 7324/7-2. Baig et al., 2016 has estimated the Cenozoic exhumation in the southwestern Barents Sea area based on well logs and thermal maturity data from more than 70 exploration wells together with widely distributed shot gather data along-offset seismic reflection lines (Figure 3.7). The suggested average net exhumation by (Baig et al., 2016) range from ~800 to 1400 m within the Hammerfest Basin, ~1150 – 1950 m on Loppa High, ~1200 – 1400 on the Finnmark Platform and ~1250 – 2400 on the Bajarmeland Platform.

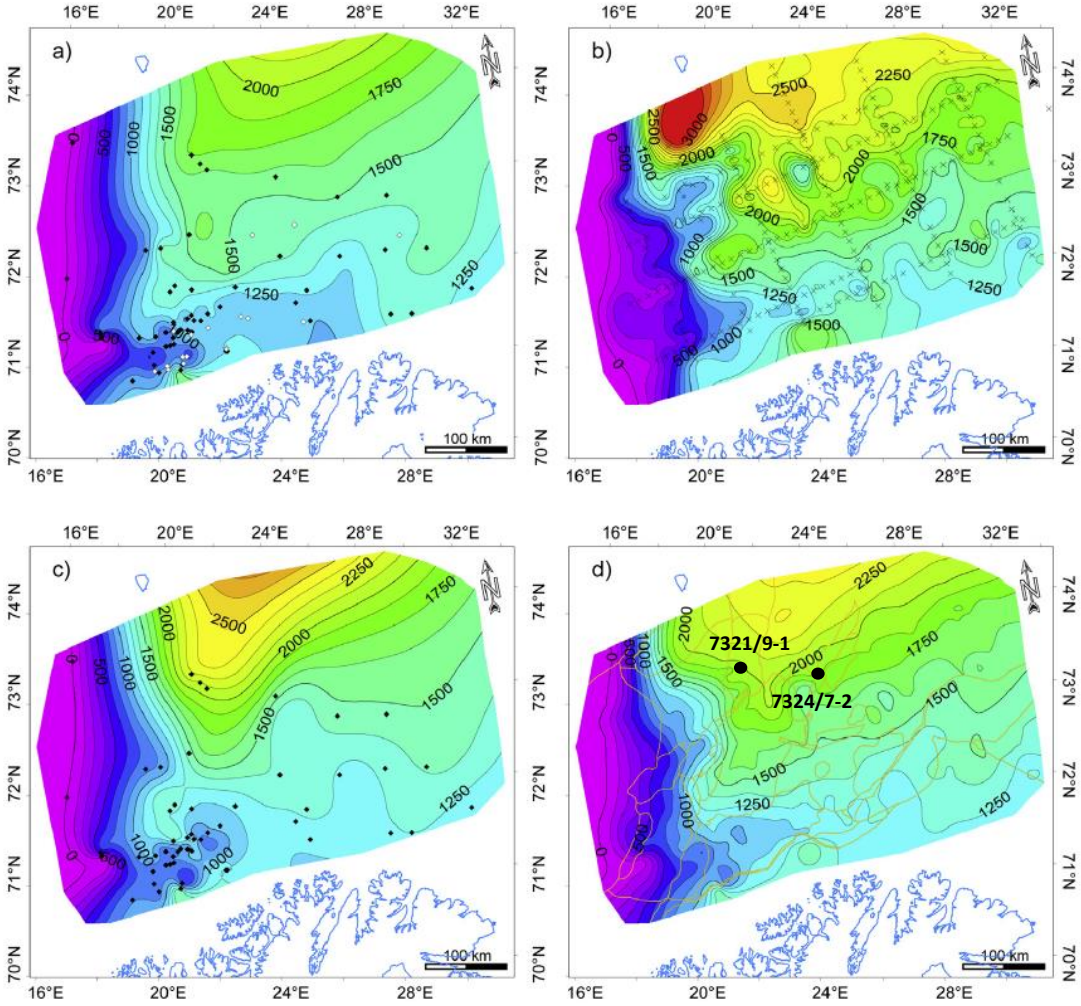

Figure 3.7: The net exhumation estimate maps a) from the sonic log, b) from shot gathers, c) from vitrinite reflectance and d) the arithmetic average net exhumation map of Southwestern Barents sea, modified figure after (Baig et al., 2016). The black circles show the approximate position of Hanssen (7324/7-2) and Fingerdjupet Sub-Basin (7321/9-1).

3.5.2 Geothermal gradients

The onset of quartz cementation occurs during the chemical compaction at temperatures above ~70°C which significantly accelerates the precipitation of quartz cement. 70^{0}C is the minimum temperature required for start of quartz cementation, and after the 80^{0}C significant volume of quartz, cement is expected. These limiting temperatures have been used in order to calculate the geothermal gradient and transition zone in wells which have been studied. The calculation of the geothermal gradient is an integrated part of compaction study. The following equation is used to calculate the geothermal gradient (Eq. 3.5):

Eq. 3-5 $$G = \frac{T_{bh} - T_{sf}}{D_{bh} - D_{sf}}$$

where T_{bh} is the bottom hole temperature (51 ^{0}C for well 7324/7-2 and 44 ^{0}C for well 7321/9-1), T_{sf} is the temperature at the sea floor (set as 4^{0}C), D_{bh} represents the maximum depth of the well (in m TVD), D_{sf} is the depth to sea floor from the sea level.

3.5.3 Gamma-ray log

The gamma-ray log measures the natural radioactivity emissions from formations. The radioactive elements present in sedimentary rocks are potassium (K40), uranium and thorium. Gamma log is especially useful and has been considered as a lithology indicator because of the facts that it will ideally indicate the volume of shale in porous reservoirs. Shales and sandstones have different signatures of GR which can be correlated readily between wells. Shales are more radioactive compared to sand and limestone due to their high content of radioactive elements. Thus shales tend to demonstrate high gamma-ray response compare to sandstones and limestone (Ellis and Singer, 2007). In this study, the gamma-ray log is used to discriminate the sand from the shale layers. Moreover, the gamma-ray log is also used to discriminated facies and depositional environments. Figure 3.8 and 3.9 show common gamma ray shapes and their potential application in the understanding of wireline facies and interpretation of depositional environments.

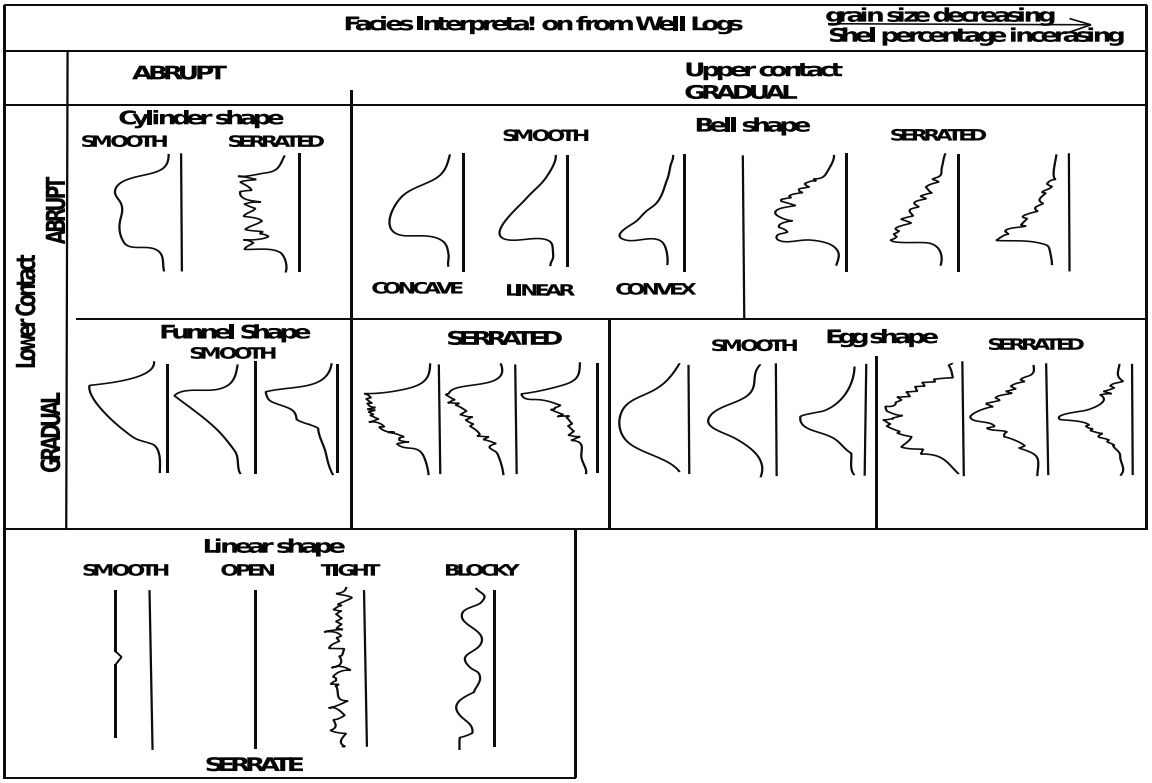

Figure 3.8: The gamma-ray shapes used in order interpret formations and depositional environments, modified after (Reading, 2009).

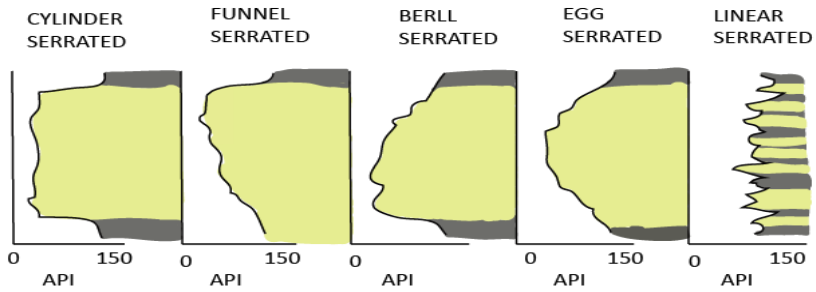

GAMMA SHAPE:	Log facies:	Interpretation of depositional environments:
CYLINDER SERRATED	Relatively thick coarser grained sandstones between finer argillaceous sediments.	Upward fining channel fills, Eoliansand, Evaporites, Beach
FUNNEL SERRATED	Upward coarsening sandstones capped by clay sediments.	Prograding systems: deltas, regressive shallow marine bars, island, submarine fan lobes, mouth bars, crevasse sandstone.
BELL SERRATED	Upward fining sandstones between argillaceous shale deposits above and below.	Channel fills, point bars, tidal creeks
EGG SERRATED	Upward coarsening to upward fining sandstones, between shale deposits	Upward fining channel fills, progradational and transgressive sands, submarine fan channel lobe.
LINEAR SERRATED	Thick mudstone deposits with interbedded sandstones	Floodpalin, tidal flats, marsh

Figure 3.9: General gamma-ray responses to variation in grain size (Emery and Myers). The sandstone and shale are shown by light green and gray color respectively.

3.5.4 Density log

Density log measures the bulk density of the formation including its solid matrix and fluid content. Density logging tools send gamma radiation into a formation and detect those that are scattered back. Density log could be utilized as a useful indicator of compaction trend since compaction reduces porosity and increase the density of the rock. The density log measures porosity Φ using (Eq. 3.6):

Eq. 3.6 $$\Phi = \frac{\rho_m - \rho_b}{\rho_m - \rho_{fluid}}$$

Where ρ_m denotes the density of the matrix which varies based on lithology (Table 3.4), ρ_b denotes the density driven by the log (bulk density) and ρ_{fluid} denotes the density of the pore filling fluid (Table 3.4).

Table 3.4: Table shows the most common densities of mineral found in sandstones.

Mineral/Fluid	Density [g/cm^3]	Mineral/Fluid	Density [g/cm^3]
Quartz	2.65	Kaolinite	2.59
Calcite	2.71	Illite	2.66
Dolomite	2.87	Smectite	2.1 – 2.6
Albite	2.61	Formation Water	1.025
Biotite	2.90	Oil	0.85
Muscovite	2.83	Drilling mud	1.35
Chlorite	2.80		

3.5.5 Neutron porosity log

The neutron logging tool measures hydrogen index in the formation. Pore space mostly occupied with fluids such as water and oil which are the primary source of the hydrogen within the formation thus the hydrogen index ideally reflects the amounts of the pore space in the formations. Although the neutron log is a useful tool for determining the porosity, however, it can lead to an overestimation in clay-rich formation. Clay minerals, especially smectite and kaolinite comprise of high amounts of hydrogen atoms which cause neutron porosity tools give significantly high values, called the shale effect. In gas-bearing formation, the neutron porosity will lead to underestimation of the porosity since gas comprises of fewer hydrogen atoms per unit of volume compared to oil and water, called the gas effect (Bjørlykke and Jahren, 2010).

3.5.6 Shale volume estimation

The gamma-ray log has both nonlinear relationship and linear relationship (Eq. 3.7). The volume of shale is expressed as a decimal fraction (V_{sh}). Calculation of the gamma ray index (IGR) is the initial step needed in order to determine the volume of shale from gamma ray log. The shale volume can be calculated from following equation (Rider, 1986):

Eq. 3.7: $linear\ response = I_{GR} = \frac{GR_{log} - GR_{min}}{GR_{max} - GR_{min}}$

Where I_{GR} donates gamma ray index, GR_{log} donates gamma ray log value in the area of the interest, GR_{min}donates minimum gamma ray reading (no shale), GR_{max}donates maximum gamma ray reading (pure shale).

Since the nonlinear responses are based on geographic area or formation, results of these relationships are more optimistic than that from the linear equation (Ghawar and Elburas, 2015). There are several nonlinear relationships, some of the commonly used relationships

have presented in Figure 3.10 and Table. 3-5. All of these relationships represent a lower shale volume compare to the linear method. In this study, the Larionov (1969) 'Old rock' relationship is used to estimate the shale volume in Stø Formation.

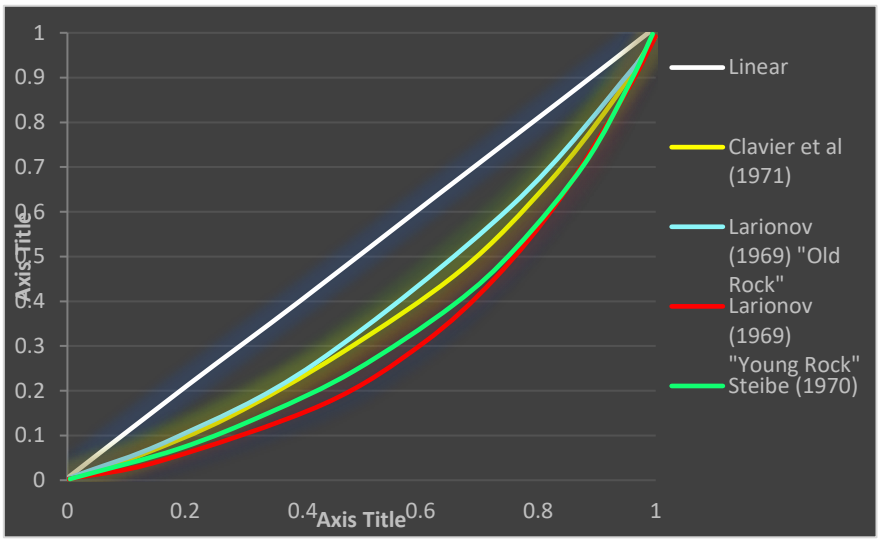

Figure 3.10: Chart shows commonly used shale volume estimation corrections (modified from Mondol, 2015).

Author(s) Equation

Table 3.5: Commonly used nonlinear equations for the estimation of shale volume from the gamma-ray log.

Larionov (1969) "Young Rock"	$V_{Sh} = 0.083 \times (2^{3.71_{\mathrm{IGR}}} - 1)$
Larionov (1969) "Old Rock"	$V_{Sh} = 0.33 \times (2^{I}_{GR} - 1)$
Steiber (1970)	$V_{sh} = I_{GR} \div (3 - 2 \times I_{GR})$
Clavier et al. (1971)	$V_{Sh} = 1.7[3.38 - (I_{GR} + 0.7)^2]^{1/2}$

3.5.7 Porosity from neutron-density combination

Both neutron and density log suffer from uncertainties related to the lithology. Therefore, an alternative approach is required for reliable porosity calculation. In industry practice, the combination of the neutron and density logs is the best method for evaluating the reservoir porosity since by averaging both results; the lithology effects could be cancel out (Kalani et al., 2015). The following equation is used in order to determine the porosity from the combination of density and neutron logs for Stø Formation.

Eq. 3.8 $$\Phi = \left(\frac{\Phi_N^2 + \Phi_D^2}{2}\right)^{1/2}$$

where Φ N and ΦD are neutron and density porosities, respectively.

3.5.8 Net-to-gross ratio and petrophysical cut-offs

Petrophysical cut-offs are defined as limiting values for expressing the NTG ratio (Worthington and Cosentino, 2005). The definitions of the net properties defined by (Worthington, 2005) are described in (Table 3.6), (Figure 3.11). In this study, the proposed cut-off values by Worthington and Cosentino (2005) have been used for calculating hydrocarbons in place of Stø Formation sandstones reservoir in well 7324/7-2 (Table 3.7).

Table 3.6: Definitions of Net properties. From Worthington and Cosentino (2005).

Term	Definition
Gross rock	All rocks within the evaluation interval.
Net sand	A lithologically clean sedimentary rock (commonly defines by a log-derived V_{sh} cut-off).
Net reservoir	Net sand intervals with reservoir properties (commonly defined by a log-derived porosity cut-off.
Net pay	comprises of those net reservoir intervals containing hydrocarbons (commonly defined by log dived water saturation (S_w=1-S_h) cut-off.
Net-to-gross	Generally, is a generic term that should always be defined with reference to the "net" terms above. It is the ratio of net thickness to the gross thickness and has a value between 0 and 1.

Table 3.7: Table shows the cut-off values proposed by (Worthington and Cosentino, 2005) for calculating hydrocarbons in place for sandstones.

Lithology	*Cut-off parameter*	*Range of values*
Sandstones	V_{SH}	*0.3 - 0.5*
	Φ	*0.06 – 0.08*
	S_w	*0.5 – 0.6*

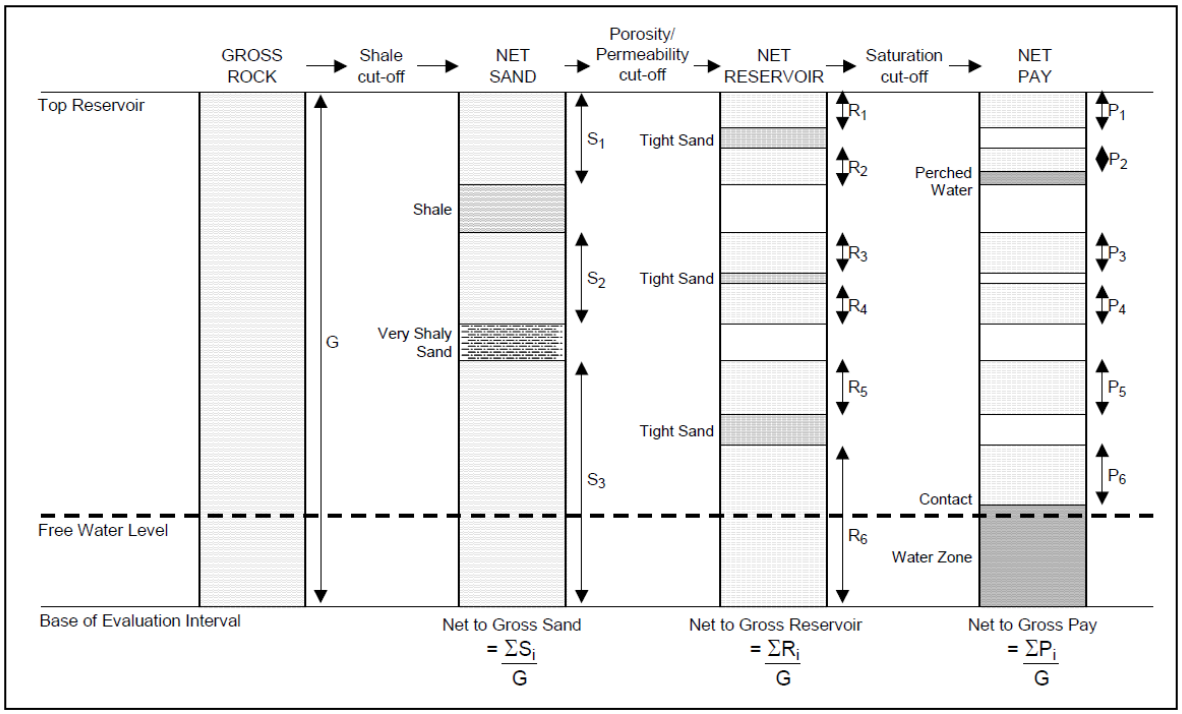

Figure 3.11: Figure shows the interrelationships of net parameters with cut-offs consecutively (modified after Worthington and Cosentino, 2005).

Chapter 4: Sedimentological Analysis

4.1 Introduction

The sedimentological analysis of Stø and Fuglen formations has been carried out based on observation from core data. Sedimentary facies of Stø and Fuglen formations were identified and characterized based on lithological as well as sedimentary structures. The degree of bioturbation has been determined using the bioturbation index defined by Taylor and Goldring (1993). The bioturbation index (BI) ranges from 0 (no trace of bioturbation) to 6 (intensively bioturbated). Seven facies are determined and categorized into three groups of facies associations. The detailed sedimentological description of Stø Formation is presented in Section 4.3, followed by the sedimentological result of the Fuglen Formation in Section 4.4.

4.2 Stø and Fuglen Formations

In this study wells 7324/7-2 in Hoop Fault complex and 7321/9-1 in Fingerdjupet Sub-basin provide the sedimentological and petrophysical dataset for Lower to Middle Jurassic Stø Formation and Middle to Upper Jurassic Fuglen Formation. The total core intervals for the well 73247/7-2 range from 710.00 to 735.00 m and for the well 7321/9-1 the core intervals range from 1372.00 to 1397.00 m.

4.3 Facies Description

Simplified versions of the logged sections of the wells 73247/7-2 and 7321/9-1 are presented in Figures 4.1 and 4.2. A summary of interpreted facies, facies association, and depositional environment interpretation is presented in Table 4.1. The legend for the logs is presented in Figure 4.3.

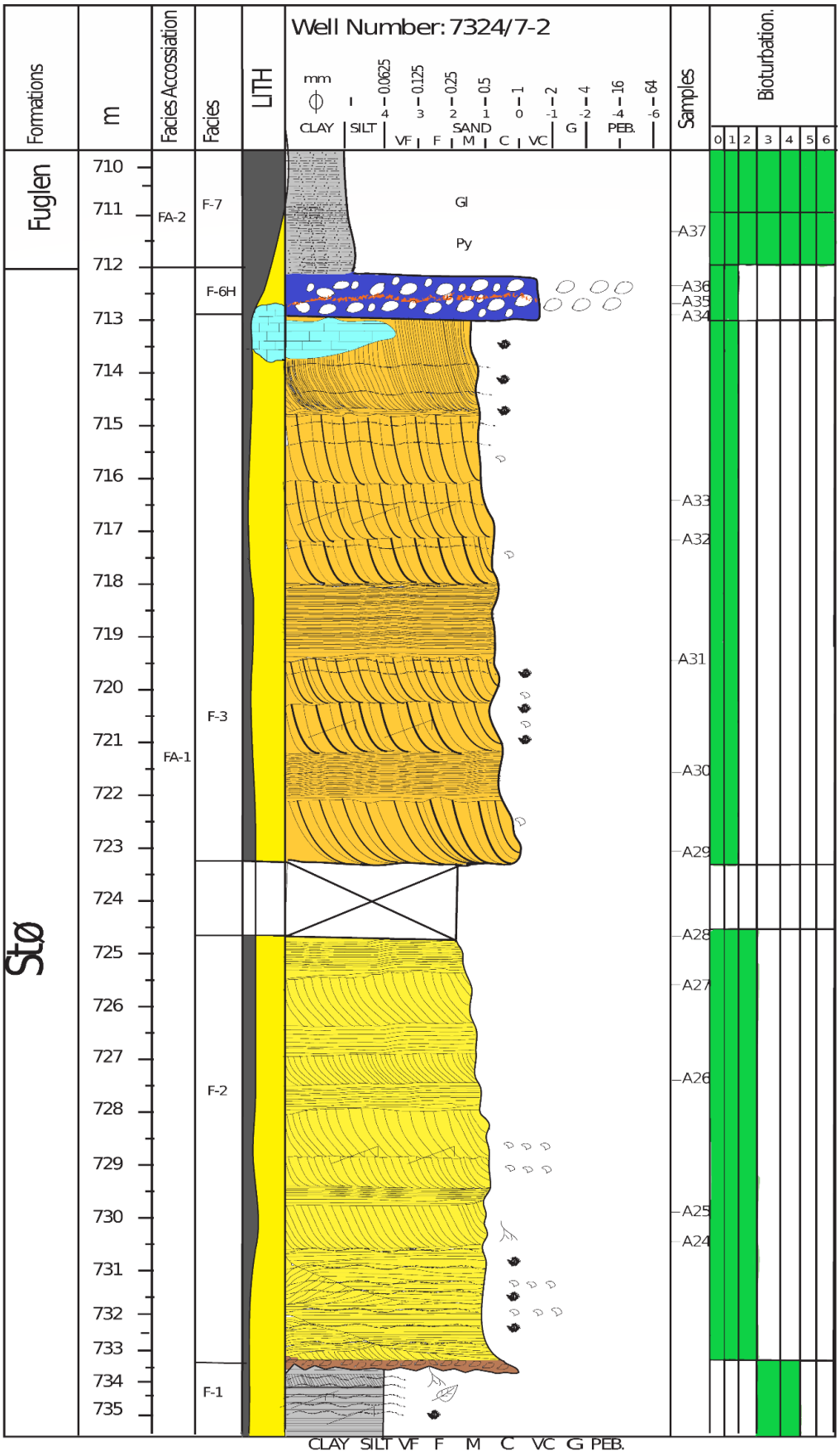

Figure 4.1: Lithological core log of well 7324/7-2 is illustrated. Different facies like flood plain, channel base, channel fill and transgressive lag facies are defined. The legend can be seen in Figure 4.3.

Sedimentological Analysis

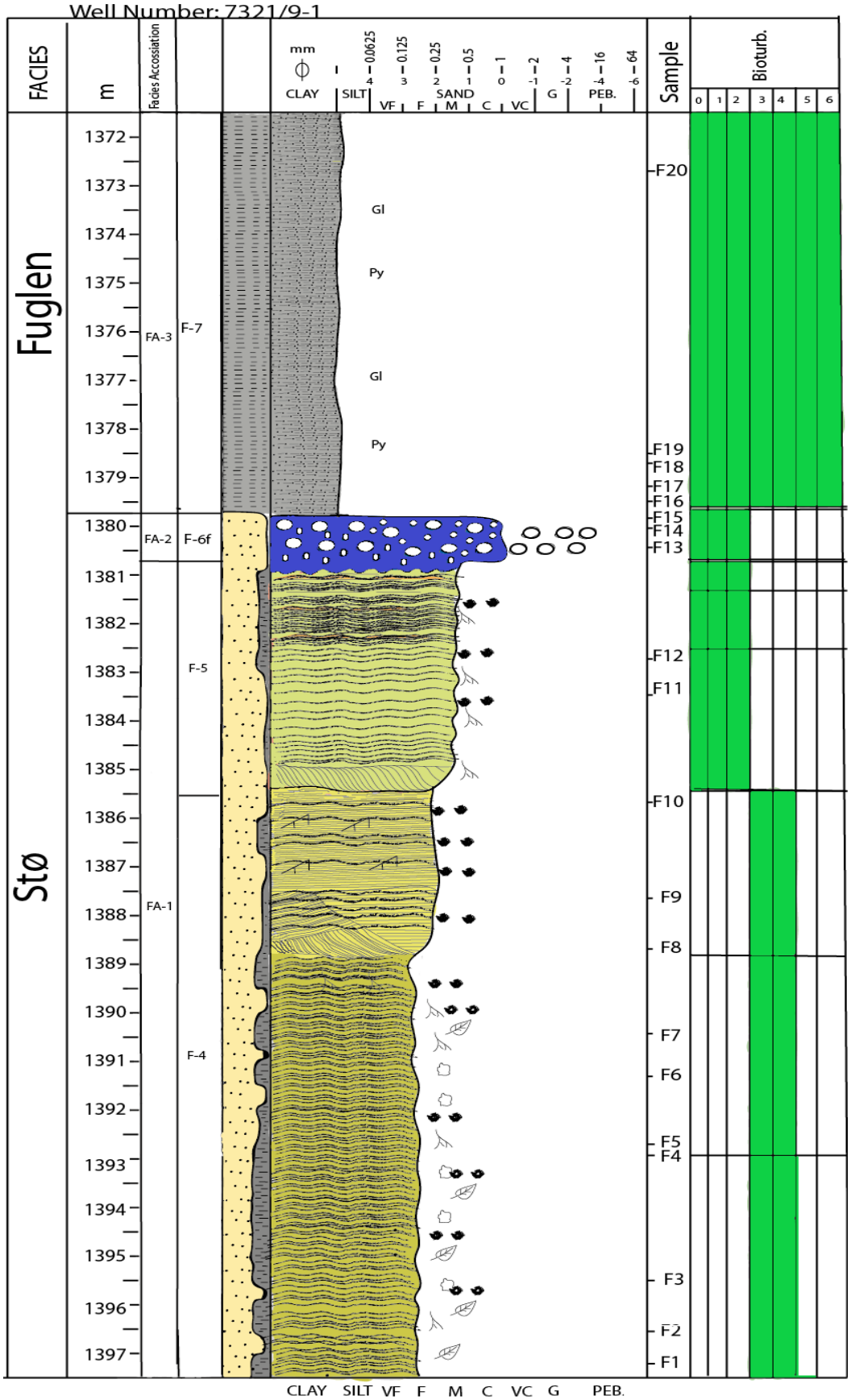

Figure 4.2: Lithological core log of well 7321/9-1 is illustrated. Different facies like Upper delta plain, distributary channel, transgressive lag facies are defined. The legend can be seen in Figure 4.3.

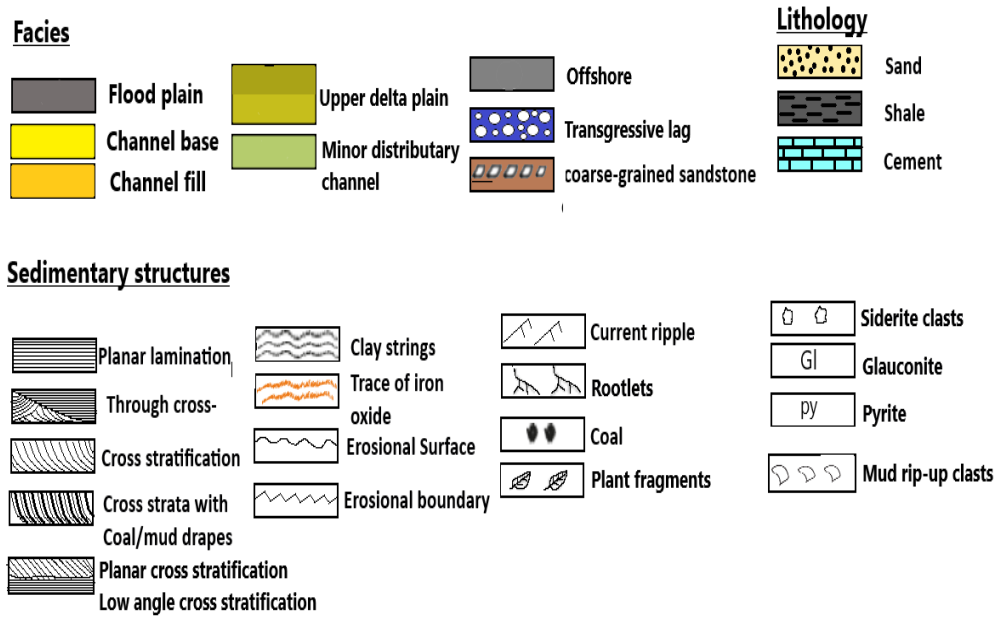

Figure 4.3: Lithological core legend used to describe the different facies characteristics.

4.3.1 Facies F-1: Floodplain

Description: Facies-1 consists of a high quantity of dark grey parallel-laminated clay stringers, interbedded with light grey and structureless siltstone. Thin layers of current ripple cross laminated, planar-parallel lamination of very fine-grained sandstone and several erosional surfaces have been found within this succession. Several traces of coal, plant fragments and rootlets are present within this unit. Trace fossils of animal origin are absent. This unit shows a high level of bioturbation with BI= 4-6. Facies F-1 is present only in well 7324/7-2 with an erosional boundary at the top (Figure 4.4).

4.3.2 Facies F-2: channel base

Description: Facies F-2 comprises of dark brown to light gray, coarse to medium grain sandstone intervals which preserve the primary sedimentary structures such as planar-parallel lamination and trough cross stratification. The boundary between facies F-2 and F-1 is erosive. Facies F-2 forms 8 m thick, fining-upward sandstone intervals in well 7324/7-2 (Figure 4.4). One of the characteristic features of the facies F-2 is the presence of relatively coarse-grained sandstones at the base of this unit. This coarse-grained sandstone unit forms 10 cm thick interval at the base of the unit and is structureless.

These deposits demonstrate a clear fining-upward trend from coarse sand to medium-fine sand toward the upper part of the succession. The typical sedimentary structures for facies F-2 are slightly low angled to planar parallel stratification, trough cross-stratification and cross-bedding with several internal erosive surfaces. This major sandstone body is otherwise characterized by mud flake conglomerates (mainly coal pieces and mudrock fragments). This succession shows a slight degree of bioturbation with BI= 1 to 2 and occurs only in well 7324/7-2 in conjunction with facies F-1(Figure 4.6).

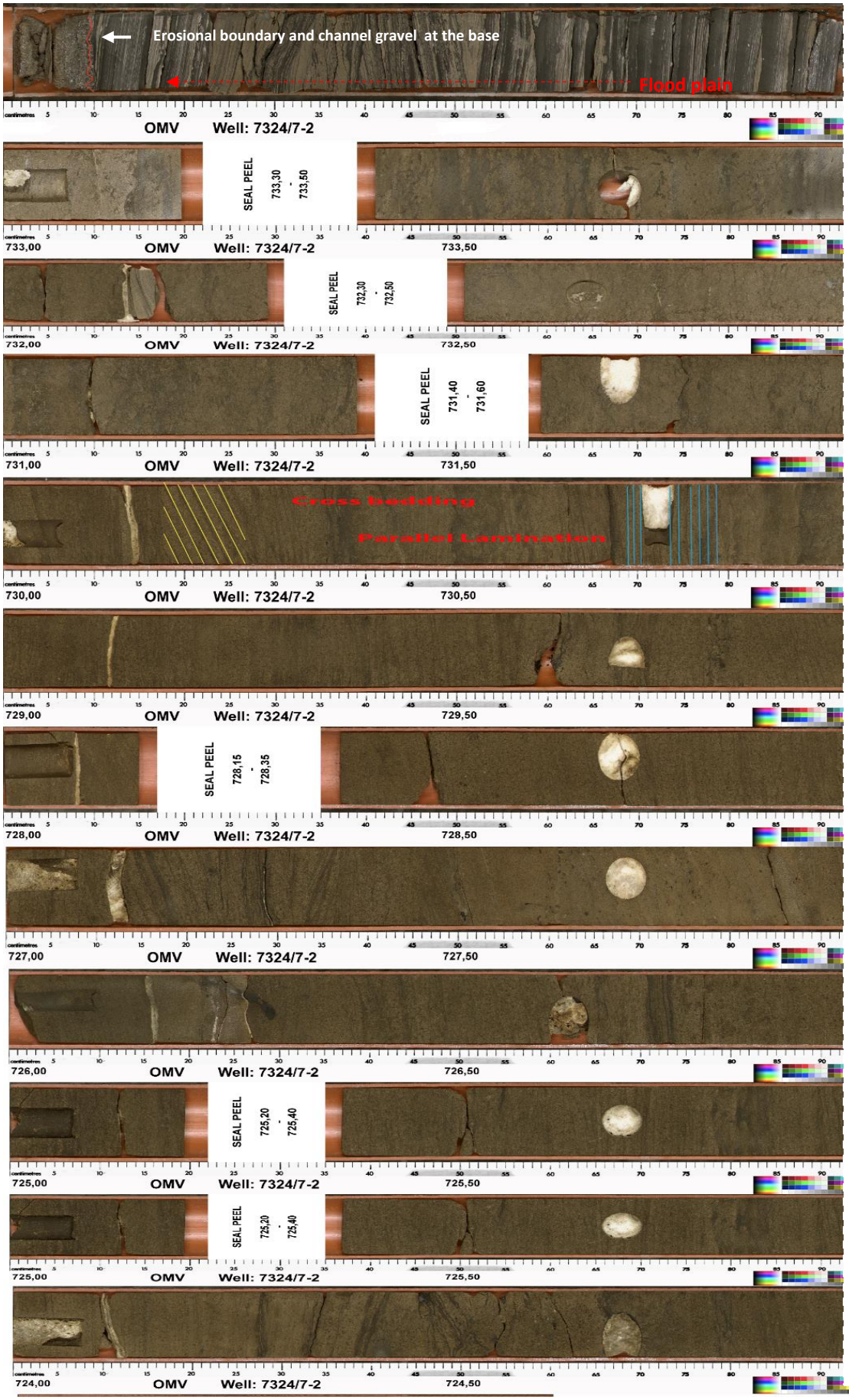

Figure 4.4: Parasequence set containing, Flood plain and Channel Base. Note a clear fining-upward trend from coarse sand to medium-fine sand toward the upper part of the succession of facies F-2. Well 7324/7-2. "734.00 -724.00".

4.3.3 Facies F-3: Channel fill

Facie-3 consists of light brown to dark brown, medium to locally coarse-grained sandstone (Figure 4.5). Individual sandstone units are ranging from 30 cm to 2 m thick, with several multiple and separate erosion surfaces. The overall thickness of the units is around 10m in well 7324/7-2. The dominant structures within the channel deposits are large-scale, high-angle planar cross-stratification with lamination of thin (1 mm) mud and cross lamination (Figures 4.7 and 4.8). Thin (<0.5 cm) mud drapes and mud rip-up clasts are commonly dispersed throughout this succession. The sandstone is commonly satured with oil. Different types of sedimentary structures such as cross-lamination and abundant mudstone drapes, wavy or lenticular bedding and flaser bedding have been observed within this unit (Figure 4.5). Finer-grained intervals occur in upper part of this section. In addition, calcite and siderite cementation are also common in the upper parts of the channel deposits. The channel deposits of facies-3 have been under the influence of a negligible degree of bioturbation (BI= 0 to 1).

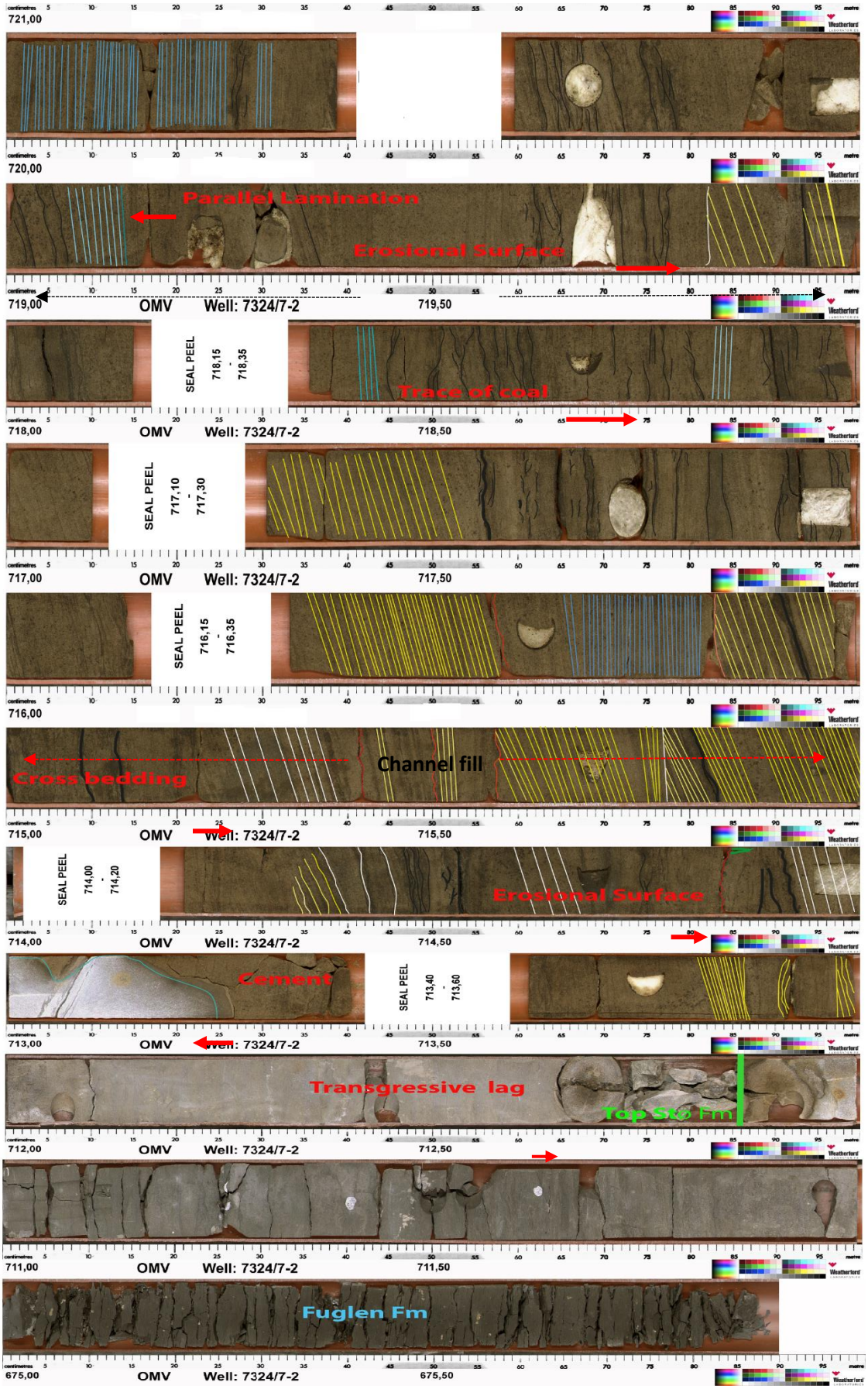

Figure 4.5: Parasequence set containing, Channel Fill and transgressive lag. Note the clear Fining upward trend. Well 7324/7-2. "675.50-723.00".

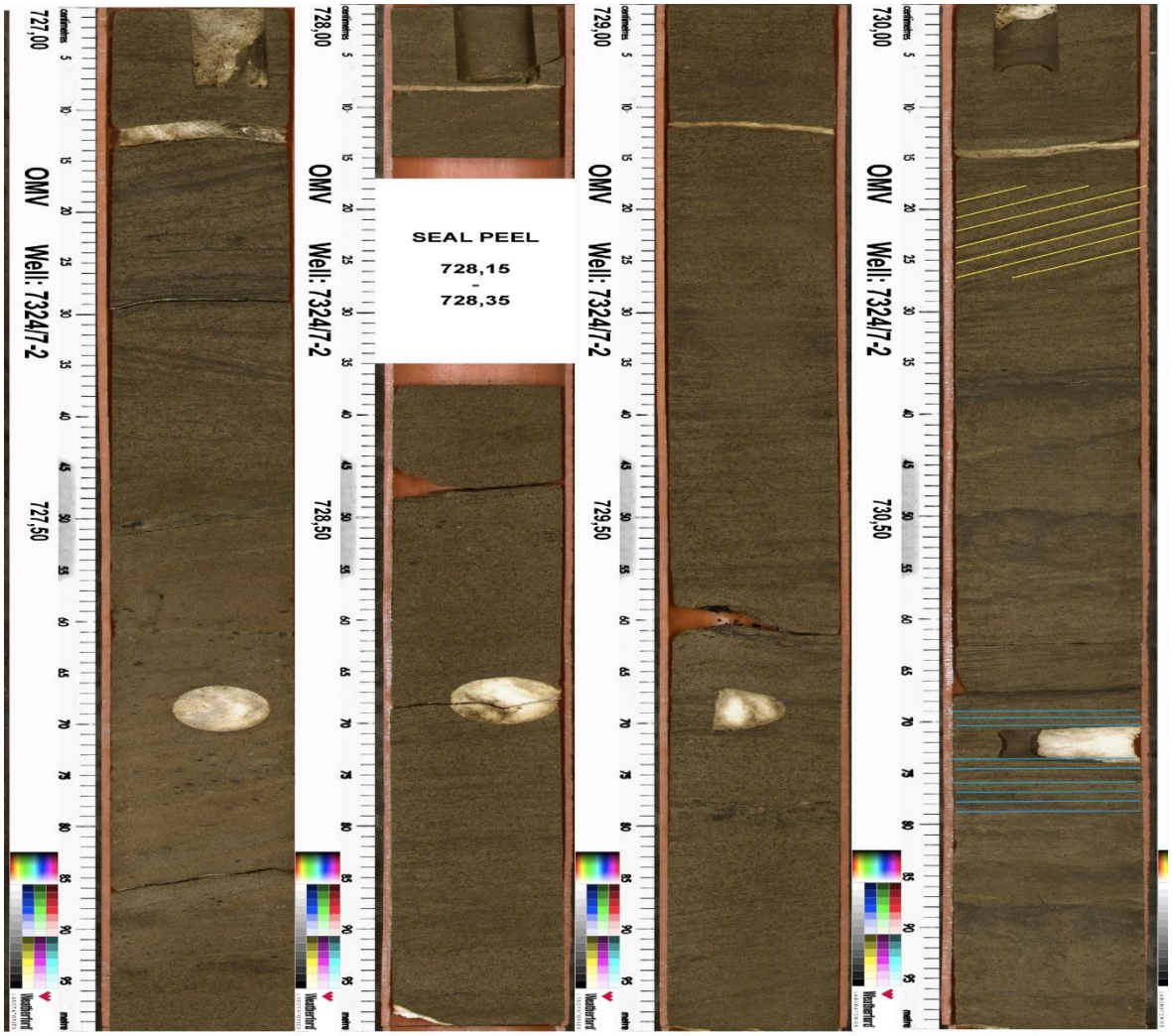

Figure 4.6: Channel base deposits with the degree of bioturbation ranging from (1 to 2 on BI). Well, 7324/7-2, intervals 727.50 to 739.50. Yellow lines show the cross-bedding.

4.3.4 Facies F-4: Upper delta plain

Facies-4 comprises fining upward fine to medium sands (Figure 4.9). The colour typically varies from light brown to grey colour, with the presence of some greenish and brownish intervals. This unit is argillaceous and has relatively high concentration of coal fragments and plant fragments. The section is moderately bioturbated (BI=2 to 3) and includes roots and a variety of burrows generated by reptiles, insects, and worms. However in some cases, even less bioturbated sandstone intervals (BI=1) with planar parallel stratification have also been observed (Figure 4.10). Common sedimentary structures within this unit are current-ripple lamination, trough and planar parallel stratification which frequently capped by coal layers. This unit has overall massive appearance in the well Fingerdjupet Sub-basin with thickness around 10.8 m. Facies F-4 has a gradual boundary with facie F-5 which show a slight transition from fine sand in facies F-4 to medium sand in facies F-5.

Sedimentological Analysis

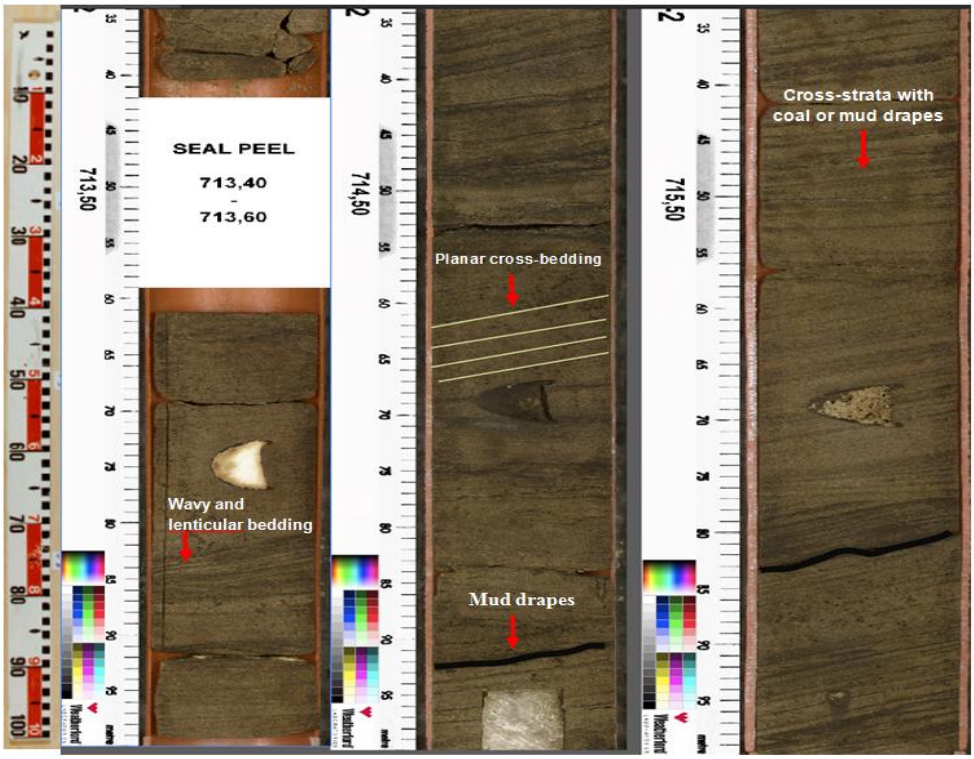

Figure 4.7: Thin mud drapes within a planar cross –stratified dune from facies F-3. The core interval is 715.15 m depth in well 7324/7-2 (Hanssen).

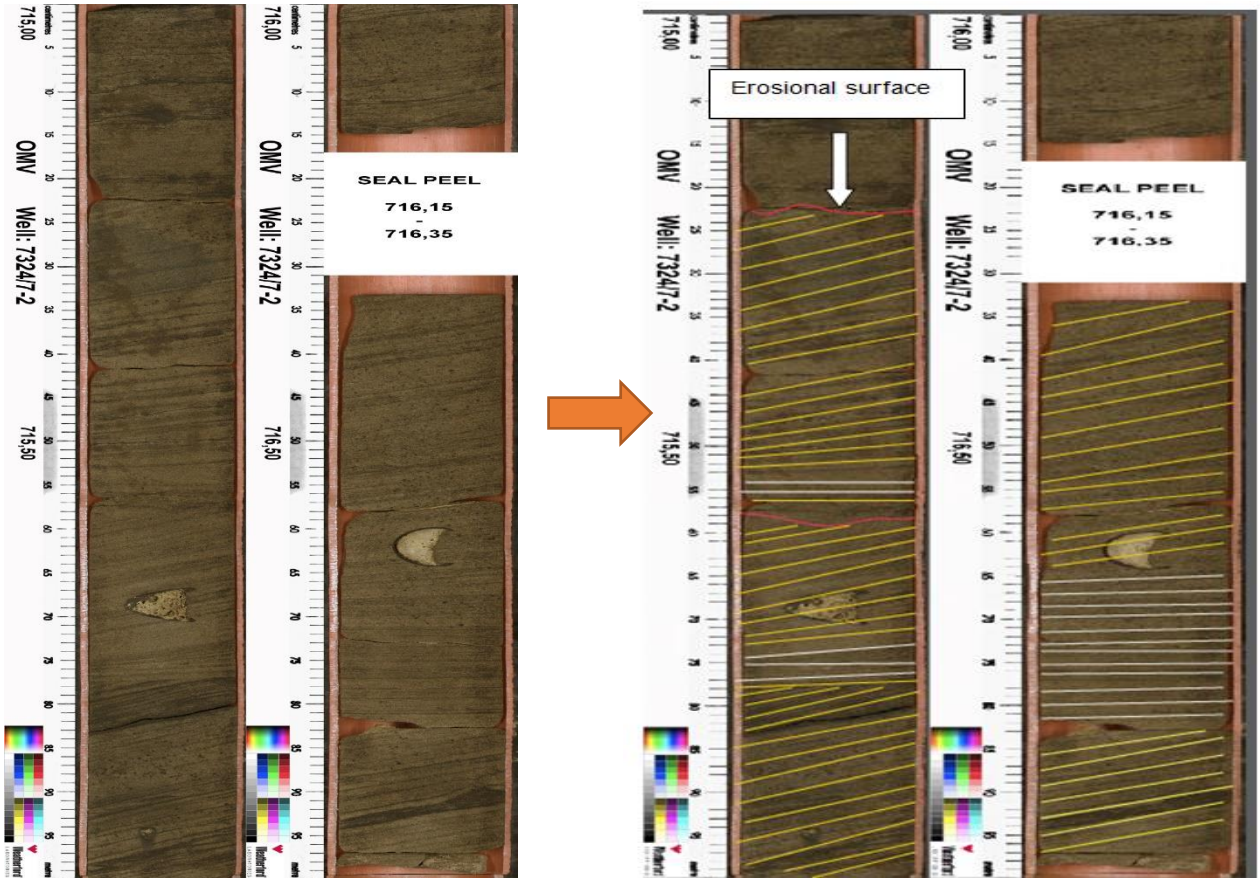

Figure 4.8: Theses picture shows presence of cross bedding with several internal erosive surfaces within the facies F-3.

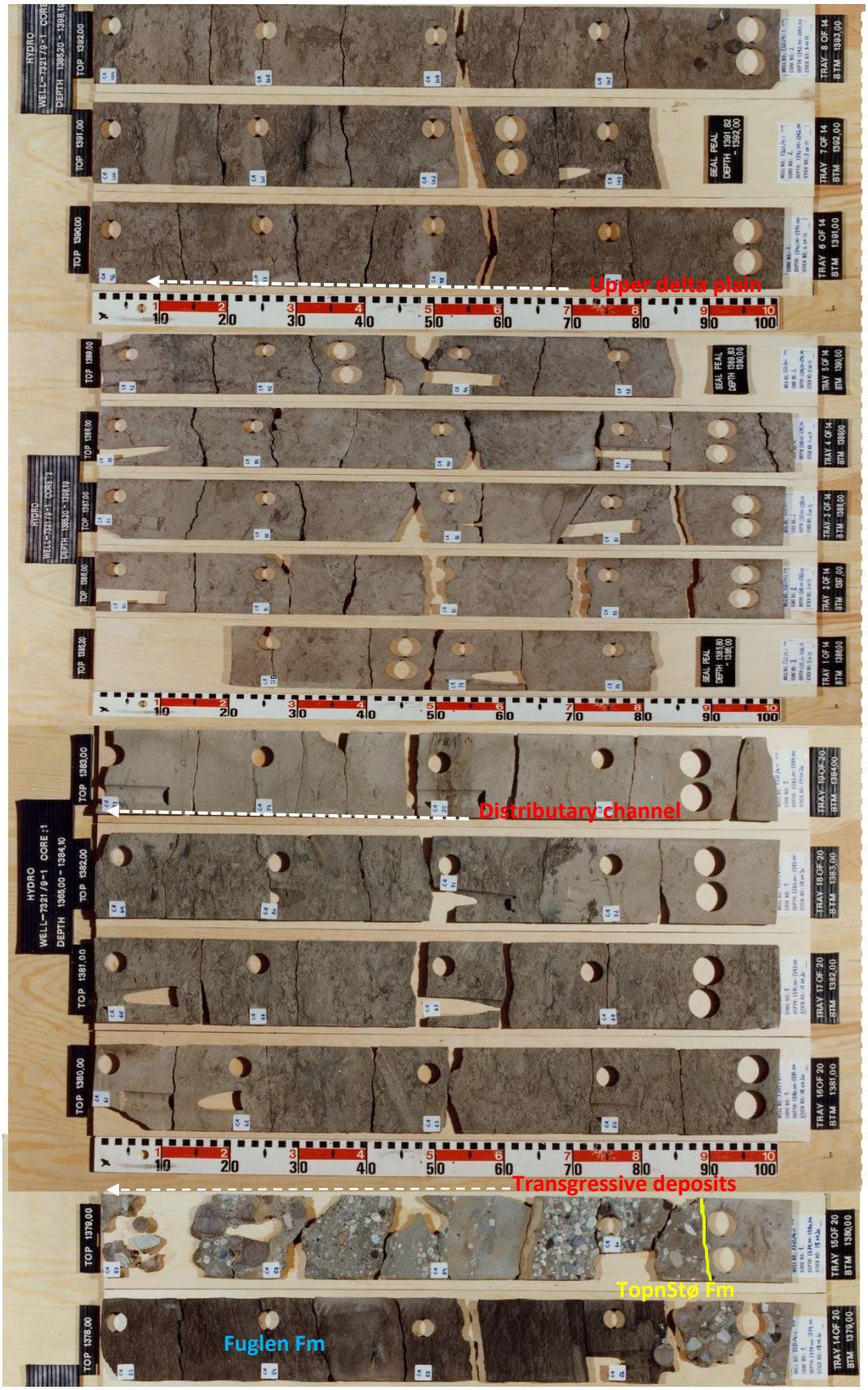

Figure 4.9: Parasequence set containing Transgresive Lag, distributary channel and upper delta plain. Well,7321/9-1. "1378 to 1392".

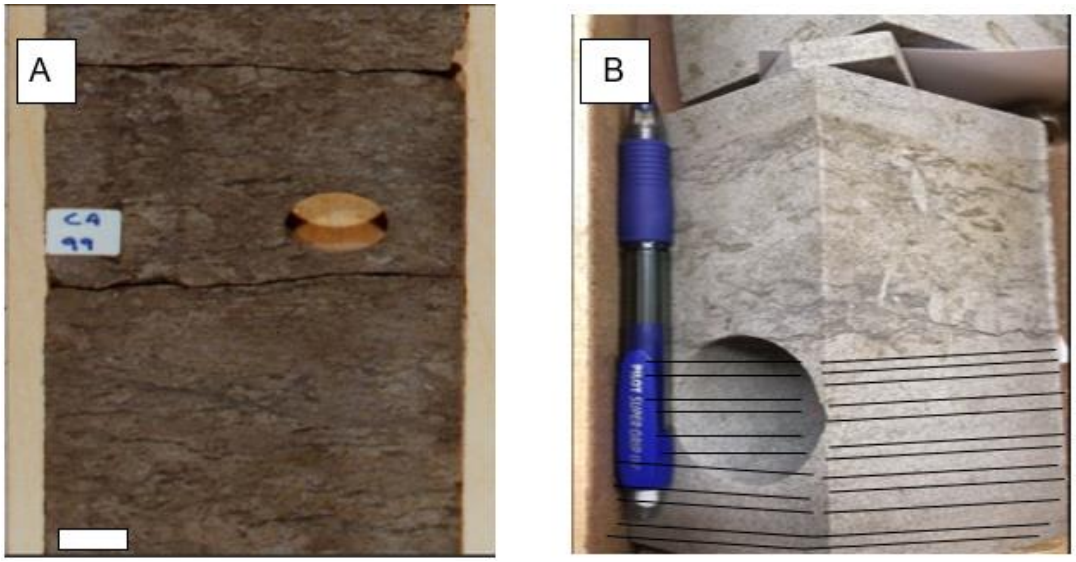

Figure 4.10: Facies F-4, clay-rich, and moderately bioturbated upper delta plain deposits. A) The core intervals is from the well 7321/9-1,"1390.70". B) Slightly bioturbation intervals, containing parallel to slightly inclined planar parallel stratified sandstone of the upper-delta plain deposits, from core interval 1396.75 – 1396.91 m depth of well 7321/9-1. All scale bars = 1 cm.

4.3.5 Facies F-5 Minor distributary channel

Facies F-5 is characterized by interbedded fine to medium-grained sandstone, grey siltstone, and claystone. Clay and silt content increase near the top of the succession and display predominantly flat laminated, micaceous and rich in carbonaceous debris. The sandstones are commonly structureless with a chaotic appearance which commonly mixed with clay. Coal fragments, plant stems are well preserved within this succession, but no other marine fossils have been found. Cross-bedding is the most characteristic feature of the facies F-5.

The measured thickness of facies F-5 is 4m in well 7321/9-1. This unit has a gradual lower boundary and sharp upper boundary. This succession is moderately bioturbated (BI=1 to 2). The concentration of iron oxide in upper parts of this unit is another characteristic feature of the facies F-5 (Figure 4.11). This unit also consists of siderite clasts which are well rounded and distributed sporadically throughout the core.

Figure 4.11: Facies F5: moderately bioturbated distributary channel deposits. The red and yellow arrows indicate the concentration of iron oxide and mud/coal fragments in this facies respectively.

4.3.6 Facies F-6 Transgressive lag

Facies F6 consists varying amount of quartz, light gray and moderately sorted pebbles, cobbles floating in a matrix of medium to coarse-grained sandstone. Facies F-6 units are correlated, meaning they occur at approximate the same time. Both cap a fluvial/deltaic sequence below and covered by marine. The thickness of the facies-6 varies between 1 to 1.5 m. This succession in Hanssen consists of coarse clast size in the lowest bed and more finer material at the highest, indicating fining-upward grading. Whereas, in Fingerdjupet Sub-Basin this unit demonstrates an inverse grading by the accumulation of coarse-grained pebble-sized clasts at the top and more coarse to the fine-grained material at the base. Facies F-6 is matrix-loading comprises of the medium sand to fine gravel fraction with changing admixture of quartz, chert pebbles, and glauconite which randomly oriented within the succession. The detrital grains are usually well- to very well rounded but vary considerably in size. The coarse-grained pebbly sized clasts are also well rounded and predominantly consisting of quartz grains.

The boundary at the top is sharp, indicating transition to massive shaly intervals of Fuglen Formation (Figure 4.12). Traces of iron oxide have been observed within this unit as in facies F-5. The degree of bioturbation is negligible (BI= 0-2) in this facies. Facies F-6 marks the transition from Stø to Fuglen formations, indicating an important time-stratigraphic boundary. The maximum flooding surface is found above Stø Formation which indicates transition from terrestrial (Stø Fm) to an open marine shelf environment (Fuglen Fm). Facies F-6 reflects the same depositional event in both wells, but in terms of sedimentary structures

and petrographic characteristics, this facies is entirely different in well 7324/7-2 from well 7321/9-1. Thus, this facies has been subdivided into facies F-6H in well 7324/7-2 and facies F-6f in well 7321/9-1.

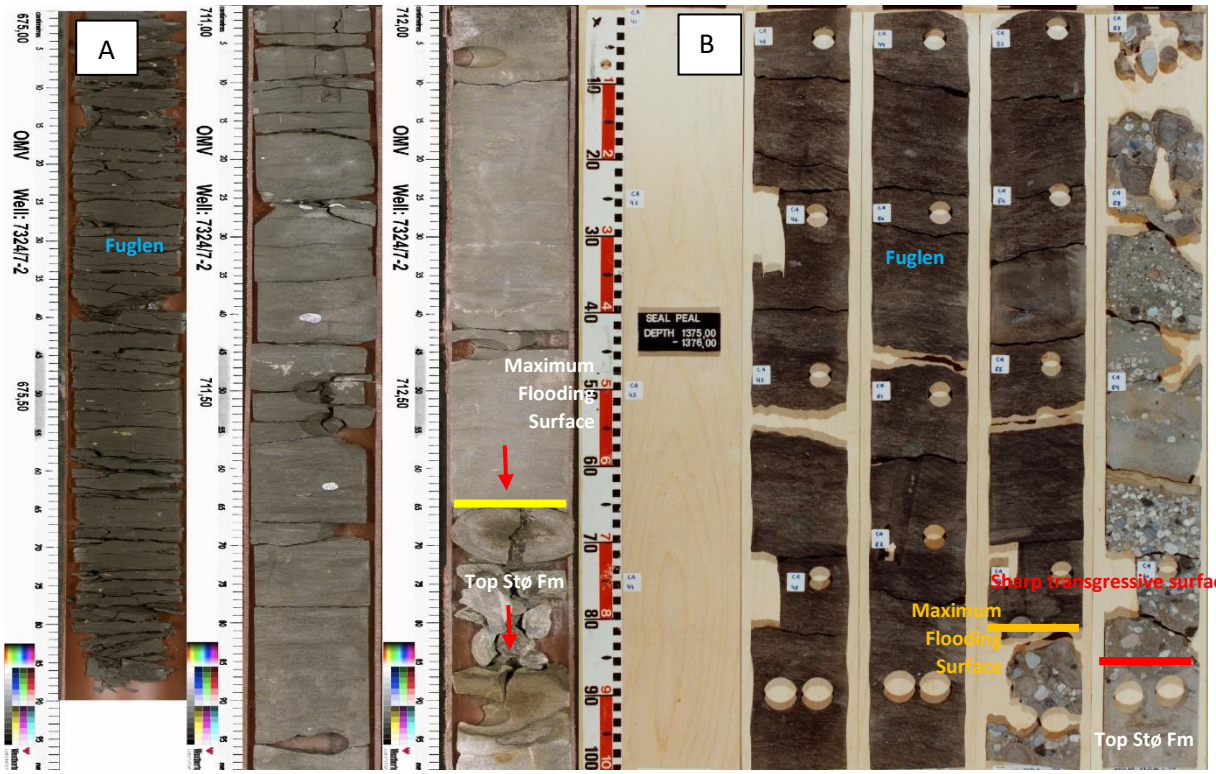

Figure 4.12: Conglomeratic lag deposits containing dominant quartz-pebbles. A) The core interval is 712 m depth of well 7324/7-2. B) The core interval is 1378.90 m depth of well 7321/9-1.

4.4 Fuglen Formation

Facies F-7 consists of brown-black mudstones and siltstones which are relatively consolidated. The siltstones are micaceous argillaceous and noncalcareous. F-7 has been extensively bioturbated (BI= 4 to 6). The main characteristics feature of facies F-7 is the presence of very thin layers of the sandstone between mudstone and siltstone intervals. These thin sandstone layers are more common in lower parts of the unit compare to upper parts of the succession. Sandstones show a low degree of bioturbation while mudstones intervals show an intense degree of bioturbation and entirely reworked by organisms. Another typical characteristic of facies-7 is the occurrence of abundant pyrite nodules and glauconite, which are dispersed throughout this succession.

4.5 Facies Associations

A facies association is often defined as a group of sedimentary facies which occur together and represents a particular sedimentary environment (Anderton, 1985, Nichols, 2009).The facies described in section 4-3 and section 4-4 are further assigned to 3 distinct facies association. Facies associations belonging to Stø Formation are deposited within fluvial to

deltaic environments, whereas the Fuglen facies association indicates deposition within an open marine environment.

4.5.1 Facies Association-1, Fluvial channel + Delta plain

Facies association-1 has been interpreted as a fluvial channel, and delta plain environment, based upon the corresponding facies grouping: Flood plain (F-1), Channel base (F-2), Channel fill (F-3), Upper delta plain (F-4) and distributary channel (F-5). FA-1 shows a moderate degree of bioturbation with relatively high concentration of terrestrial input, such as coal and plant fragments. In terms of sedimentary structures and other observed sedimentary features, the FA-1 contains coal/mud drops, erosional surface, cross-bedding, plane parallel stratification. Facies F2 and F3 with coarser grain size compare to facies F4 and F5 reflect deposition under a high energetic environment, whereas facies F4- and F-5 with higher degree of bioturbation and grain size variation between very fine to fine reflect deposition in a distal position relative to the main channel where the energy of the fluid decreases significantly. Another characteristic feature of the FA-1 is concentration of calcite cement and iron oxide in the upper core intervals. The sedimentary characteristic of facies F-1, 2 and 3 of the well 7324/7-2 indicate deposition in a fluvial channel. The channel base deposits of facies-2 undercut the bank comprised of floodplain material, forming a lag of channel gravels on an erosional base at the transition from F-1 to F-2. The channel fill deposits of facies F-3 indicate the initial loss of energy which allows coarse to medium sands to accumulate as trough cross-beds and large-scale high-angle planar cross-stratification with thin lamination of mud. Facies F-4 and F-5 of the well 7321/9-1 represent the transition from fluvial channel to the deltaic system (Figure 4.13). Delta is classified into three types based on the dominant energy (tide, wave, and river-dominated delta) (Nichols, 2009). The fining-upward succession of facies F-2, F-3, F-4 and F-5 and presence of terrestrial input such as trace of coal, plant root and cross-laminated bed and lack of tidal characteristic features, indicate a river-dominated delta. F-5 represents terrestrial minor distributary channel since there is no sign of tidal influence in this facies. Distributary channels on the upper delta plain are purely fluvial with limited marine influence(Coleman and Prior, 1982, Bhattacharya and Bhattacharya, 2010).

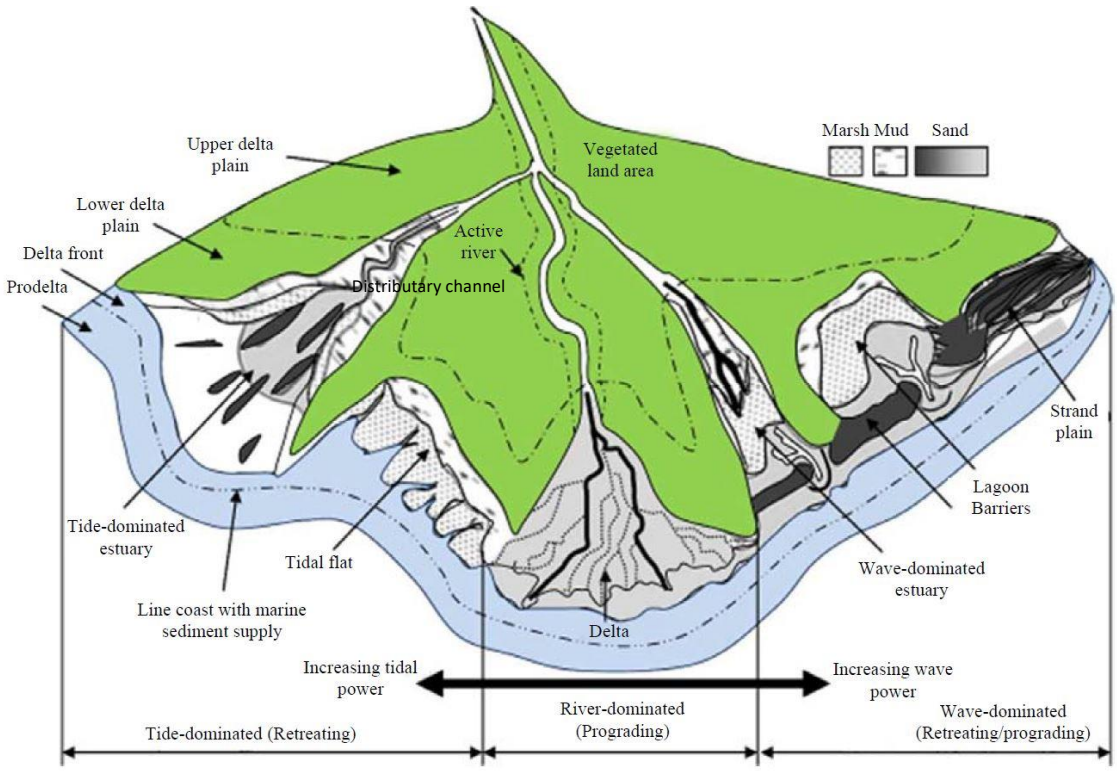

Figure 4.13: Schematic diagram of a fluvial system and associated deltas (Siddiqui et al., 2017).

4.5.2 Facies Association-2, Transgressive lag

This facies association has been characterized by the presence of angular to sub-angular conglomeratic intervals which predominantly consists of quartz grains with a negligible degree of bioturbation. The FA-2 marks the transition from terrestrial environment to fully marine environment, indicating a transgressive event.

4.5.3 Facies Association-3, Marine environment

Facies association-4 includes facies F7 with marine shale and siltstone. High degree of bioturbation reflects deposition below fair-weather wave base (above 100 m) where oxygen is sufficient for organisms to colonize. This condition led to deposition of highly bioturbated laminated pelagic and hemipelagic shale and siltstone of Fuglen Formation (Figure 4.14).

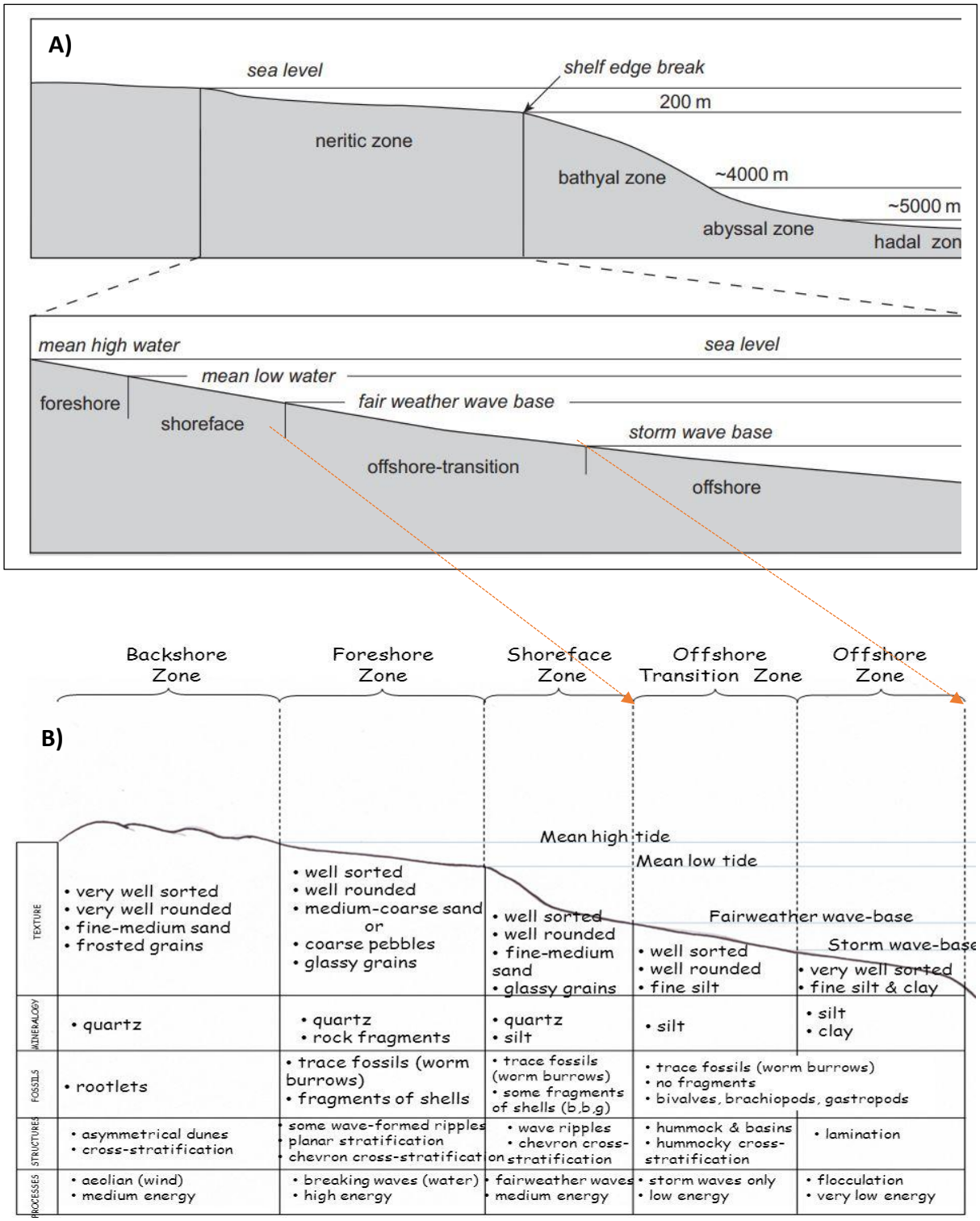

Figure 4.14 A) The shelf is described based on the depth to which different processes interact with the sea floor. B) the texture, sedimentary structures and processes, formed during fair weather and storm conditions within a siliciclastic continental depositional environment. This figure is modified after (Nichols, 2009)

Facies	Grain size	Description	Facies Association	Depositional Environments
F1	Very fine-grained sandstone	• Structure less and planar parallel cross stratification • Trace of coal and plant fragments • Highly bioturbated	Fluvial channel and Delta plain	Floodplain deposits
F2	Coarse to Medium-grained sandstone	• Planar parallel lamination and Cross stratification • Internal erosive surfaces and mud drops	Fluvial channel and Delta plain	Channel base
F3	Medium to locally coarse-grained sand	• planar cross stratification • Mud drops and mud rip-up clasts • Negligible degree of bioturbation	Fluvial channel and Delta plain	Channel fill
F4	Medium to very fine-grained sand	• Poorly sorted and planar parallel stratification • Plant fragments and several traces of coal • Moderately bioturbated	Fluvial channel and Delta plain	Upper delta plain
F5	Medium to fine - grained sand	• Concentration of iron oxide • Siderite clasts • Moderate degree of bioturbation	Fluvial channel and Delta plain	Minor distributary channel
F6	Pebbles, conglomeratic, coarse to medium grained sandstone	• Glauconitic • Carbonate cements • Trace of iron oxide • Negligible degree of bioturbation	Marine ravinement surface	Transgressive lag
F7	Mudstone	• Intensely bioturbated • High diversity of trace fossil • Abundance pyritic and glauconite	Offshore shelf	open marine

Table 4.1: Outline of the facies, facies association, and depositional environment interpretation.

Chapter 5: Results of Petrographic Analysis

5.1 Introduction

A detailed petrographic analysis was performed on 30 samples in order to deduce the mineralogical and textural properties of the different facies comprising Stø Formation. The results of petrographic analysis was used to interpret the diagenetic sequence and the corresponding changes in porosity and permeability of Stø Formation in different depositional environments.

Objectives for Mineralogical Analysis

- Determining and quantifying the mineral composition of the selected samples.

Objectives for Textural analysis

- Determine grain size, sorting, roundness, sphericity and grain contacts as described in Chapter 3.4.
- Estimation of mechanical compaction by grain contacts and determining the intergranular volume (IGV).

5.2 Stø Formation

5.2.1 Mineralogical Analysis

The calculated amount of the quartz, feldspar and rock fragments from the point counting analysis is represented in Table 5.3 and 5.5 in Appendix B and was plotted in a QRF- diagram (Figure 5.1).

The intergranular volume was calculated based on the total amounts of cement, depositional matrix, and intergranular porosity. The mineral distribution classifies the Jurassic Stø sandstones in studied wells as follows:

1. Well 7324/7-2: Quartz arenites, Sublithic arenites.
2. Well 7321/9-1: Quartz arenites, Sublithic arenites, and Lithic arenites.

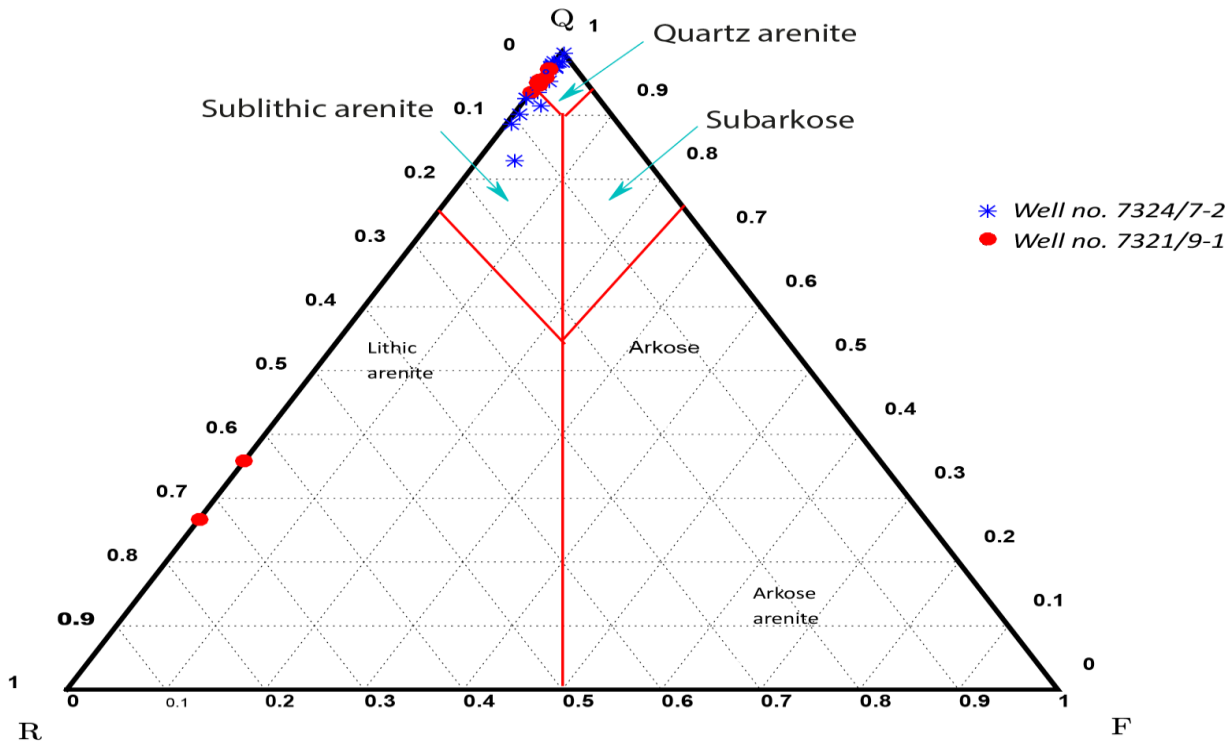

Figure 5.1: The QRF-diagram shows the mineral classification of Stø Formation in well 7324/7-2 and 7321/9-1.

The framework mineralogy of Stø Formation sandstones in both wells primarily consists of quartz grains ranging from 22% to 87% (Figures 5.3 and 5.4). Rock fragments, ranging from 2% to 6% with an average of 8% of rock volume in well 7324/-2 and 2% to 60% with an average of 10% of rock volume in well 7321/9-1 (Figures 5.2). Feldspar grains distributed in trace amounts in both wells and made up only 1% of the total rock volume. The matrix occupies on average 2% of the rock assembly in both wells. Facies F-6H and F-6f comprise the highest amount of matrix. Cement is recognized as calcite, kaolinite, illite, siderite and quartz cement. The highest amount of cement is registered within facies F3, F5 and F-6H. Kaolinite is most abundant (13.20%) in facies F-6f and facies F-6H (8.03%) (see Figure 5.2). Calcite is common in facies F-3 (5%), F-5 (1.64%), F-6H (15.64%) and F-6f (14.40%) (Figure 5-2). Siderite occurs in a significant amount around (9 %) in facies F-6H, less than 6% in facies F5 and in minor amounts in all facies except in facies F3 (Figure 5.2 and 5.3). An interesting observation in this study was the fluorapatite distribution, which is mostly in facies F2, F4, F-6f and in trace amounts in facies F5 while it is absent in facies F-3 and F-6H. Figure 5.3 and 5.4 illustrate the results of point counting and bulk XRD analyses (Table 5.4 and 5.6, Appendix B). There is a reasonable conformance between the obtained results from XRD and point counting analysis for each facies. All the facies contain the same mineral phases, but with a slight increase in calculated amounts of framework minerals, quartz, feldspar and rock fragments.

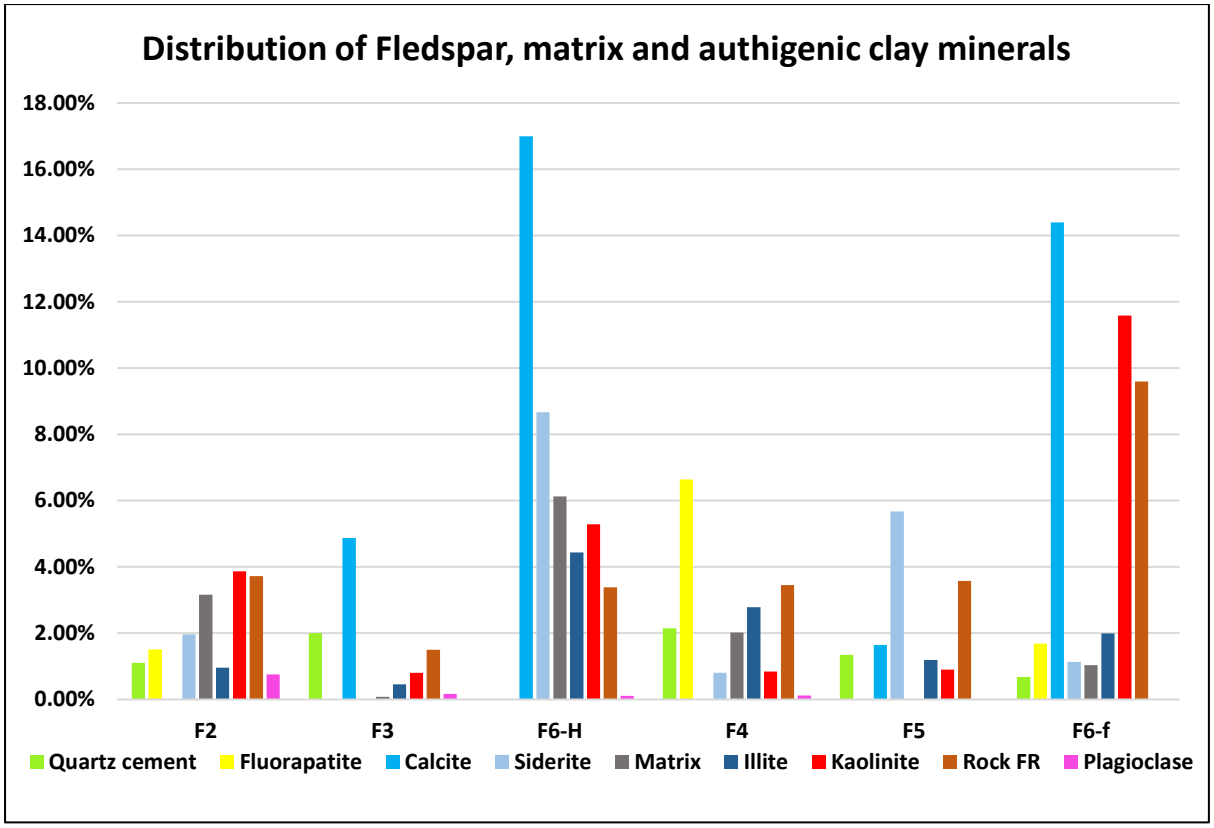

Figure 5.2: Distribution of feldspar, matrix and authigenic minerals in wells 7324/7-2 and 721/9-1 (point counting results).

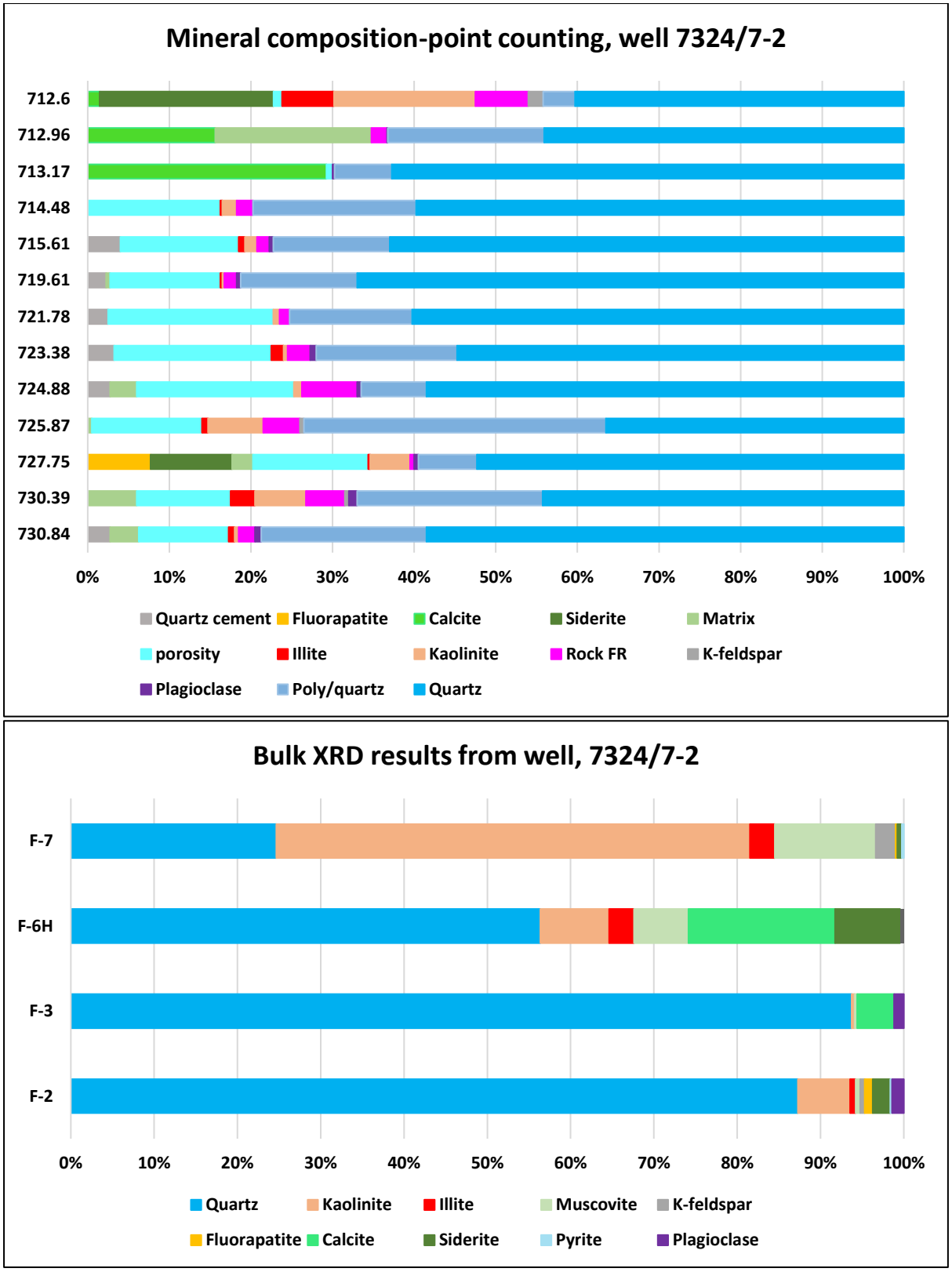

Figure 5.3: Graphs showing the mineral composition of the collected samples from the well 7324/7-2. A) Mineral composition from the point counting. B) The average result of the bulk XRD for the facies F2, F3, and F-6H.

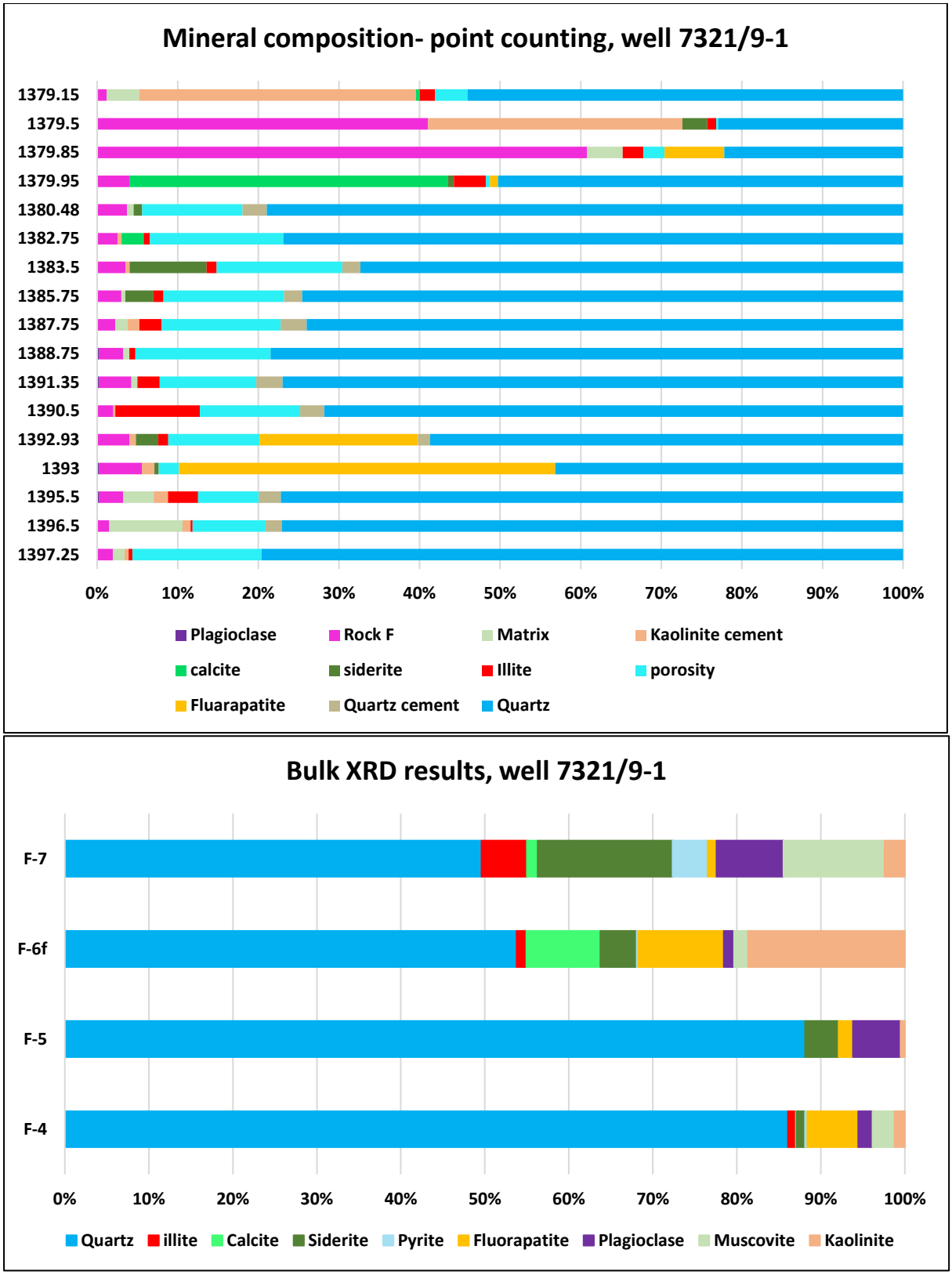

Figure 5.4: Graphs showing the mineral composition of the collected samples from the well 7321/9-1. A) Mineral composition from the point counting. B) The average result of the bulk XRD for the facies F4, F5, and F-6f.

5.2.1.1 Quartz

Quartz is the most abundant mineral in all the samples, and its volume varies between 41% to 87% and 22% to 79% in collected samples from wells 7324/7-2 and well 7321/9-1 respectively. Quartz is present in the form of monocrystalline (around 55%), polycrystalline (10% to 14%) grains and quartz cement (<10%). It also occurs as constituents in rock fragments and clays. The distribution of polycrystalline quartz is higher in the samples from facies F2, F3, and F4, while other facies contain less than 10% polycrystalline framework grains (Figure 5.5). The quartz cement is observed in trace amounts in some of the samples of Stø Formation, and its amount varies from 0% to 3.5 % in all facies.

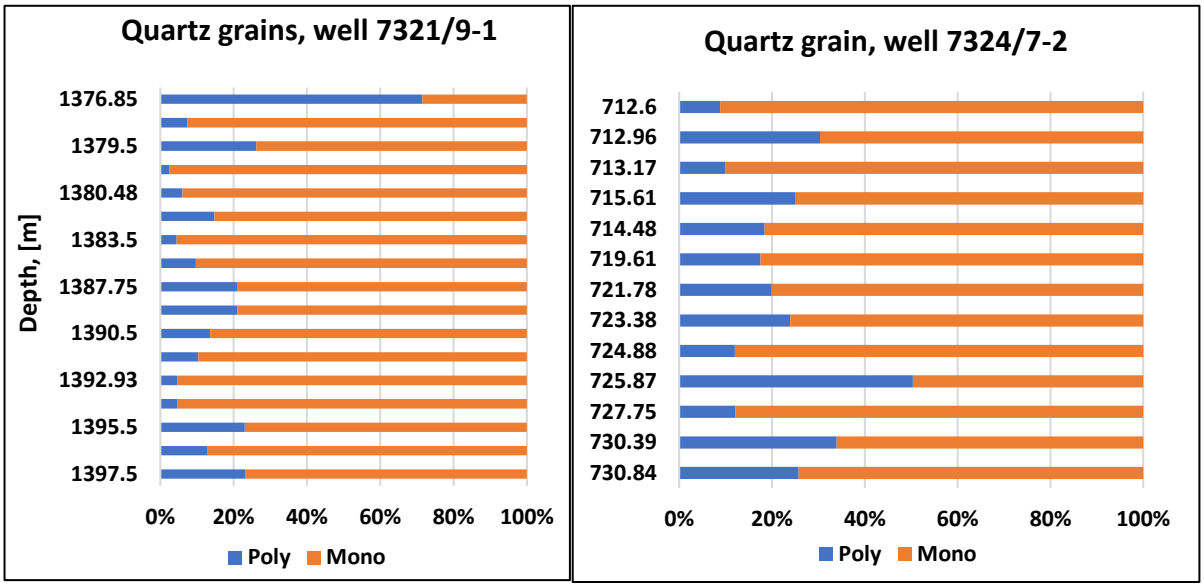

Figure 5.5: Distribution of monocrystalline and polycrystalline quartz grains with depth from the point counting. A and B: represent samples belonging to well 7324/7-2 and 7321/9-1, respectively.

5.2.1.2 Feldspar

The registered feldspar minerals are albite, oligoclase, orthoclase, and microcline which are present in trace amounts in a few samples. As a result of high degree of dissolution and alternation of detrital grains, it was difficult to specify the exact kind of feldspar grains either as microcline or plagioclase through microscopic analysis. However, bulk XRD analysis was able to differentiate between the different type of feldspar minerals. The bulk XRD estimated the total amounts of feldspar to around 3% in well 7321/9-1 and 2% in the well 7324/7-2. Based on the bulk XRD results, plagioclase was the dominant feldspar mineral in the studied samples, while K-feldspar was the least abundant feldspar mineral (Figure 5.6).

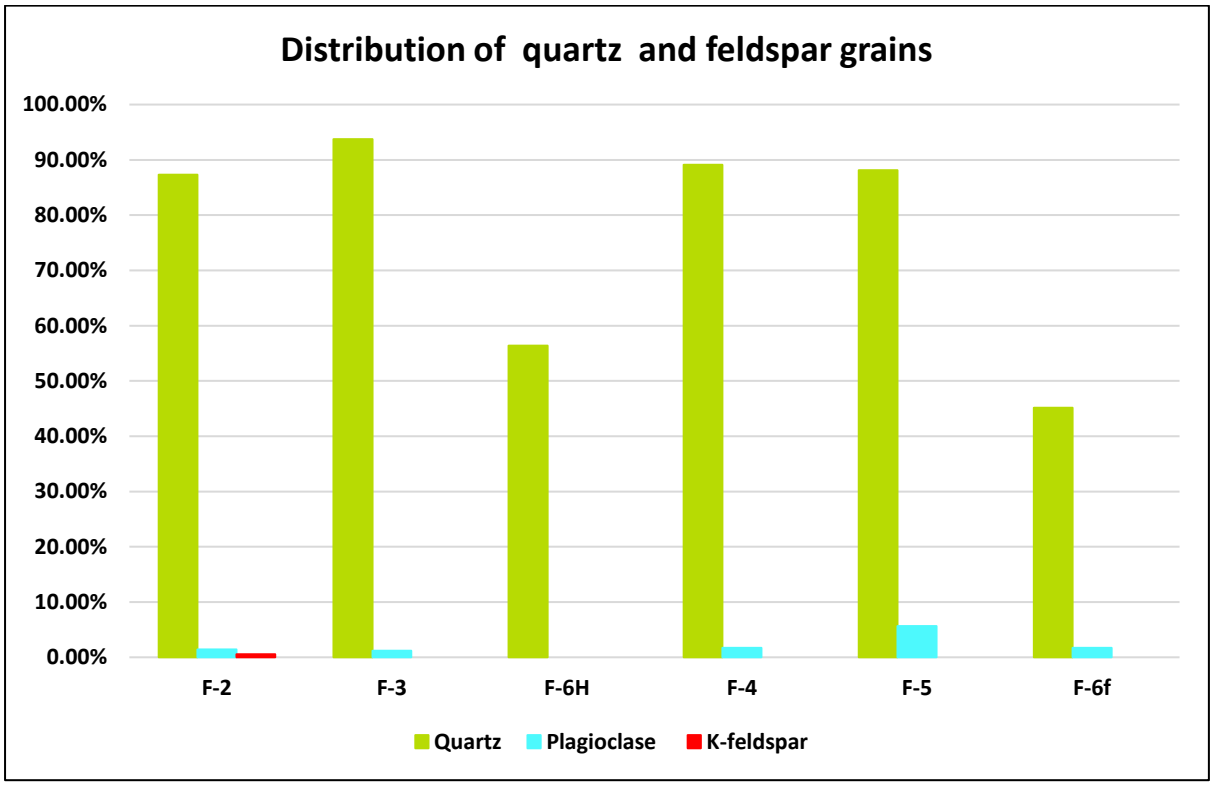

Figure 5.6: Distribution of feldspar grains according to the Bulk XRD results in each facies.

5.2.1.3 Rock Fragments

The rock fragments assembly in this study comprises chert, muscovite, igneous epiclasts, monogranular mica, lithic rock fragments and pseudomorph grains. In the present study, the secondary porosity is also considered as part of rock fragments assembly. The most frequently observed rock fragments in well 7324/7-2 are lithic rock fragments of weathered pre-existing consolidated rocks, muscovite and partly dissolved rock fragments that contain void space. The lithic rock fragments are the most abundant type of rock fragment in well 7324/7-2 which include 47% of the total amount of rock fragments while this amount reduces to 7% in well 7321/9-1. The highest amount of lithic rock fragments has been found in facies F-2 (61%) and F-3 (42%) (Figure 5.7). Partly dissolved grains (secondary porosity) is the second most abundant type of rock fragment within the facies F-2 (26%) and F-3 (42%). Muscovite is most abundant in facies F-6H (78%) while its amount decreases significantly within the facies F-2 (11%) and F-3 (14%). Chert grains constitute only 1.5% of total rock fragment assembly in well 7324/7-2 and has been found only in facies F-2. The chert grains are well preserved compared to the other framework grains.

The igneous epiclasts are mostly concentrated in facies F-6f of the well 7321/9-1 while it is absent in all the facies of well 7324/7-2. The igneous epiclasts, with an average 65% are the first most widespread type of rock fragments in well 7321/9-1. The highest concentration of the igneous epiclasts is mostly registered in facies F-6f (83%) (Figure 5.7). The clasts are well rounded and well preserved. The pseudomorph grains, muscovite schist, and lithic rock fragments are the second most abundant type of rock fragments in well 7321/9-1 and mostly distributed within facies F-4 and F-5. The total amount rock fragments assembly in facies F-4 and F-5 is around 3%. Muscovite is the most abundant rock fragments in facies F-4 (46%). The amounts of pseudomorph grains and lithic rock fragments within these facies are more and less the same (19%). Pseudomorph grains has the highest assembly in facies F-4 (19%) and F-5 (25%).

Facies F-2, F-3, F-4 and F-5 forming the Stø formation intervals in wells 7324/7-2 and 7321/9-1. The total amount of rock fragments in facies F-2, and F-3 (well 7324/7-2) is less than 3% while this amount increases up to around 4% in facies F-4 and F-5 (well 7321/9-1). Another diversity between the well 7324/7-2 and 7321/9-1 is related to the existence of igneous epiclasts in facies F-6f which caused the total amount of rock fragment in well 7321/9-1 increases from 4% in facies F-4 and F-5 to approximately 10% in facies F-6f (Figure 5.7).

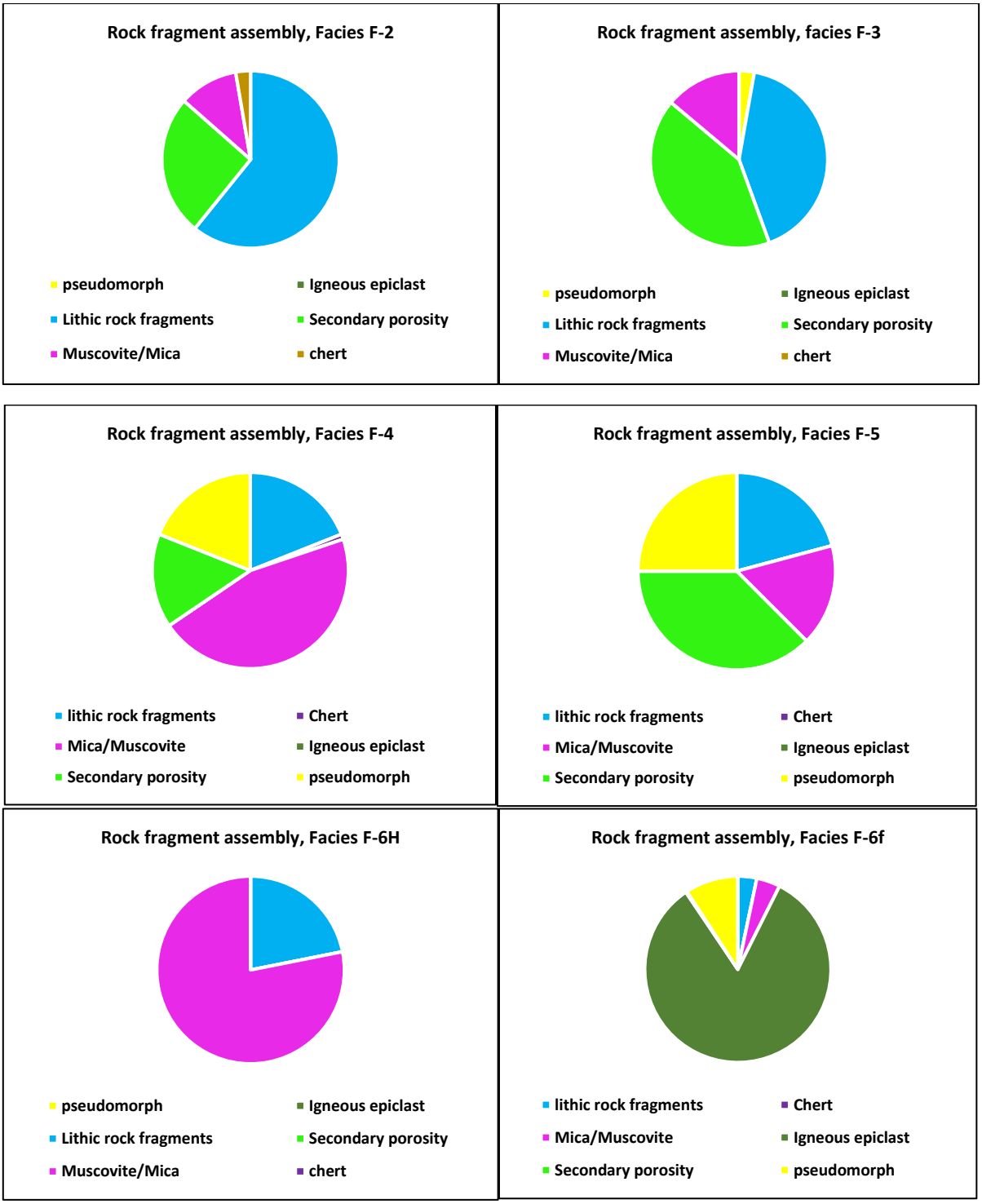

Figure 5.7: The average rock fragment assembly for the facies F-2, F-3, F-4, F-5, F-6H and F-6f. Lithic rock fragments are the most abundant type rock fragment in well 7322/7-2 whereas, in well 7321/9-1, Igneous epiclasts form a significant portion of the rack fragment assembly.

5.2.1.4 Clay minerals

Clay minerals make up 9% and 11% of the total rock volume in well 7324/7-2 and 7321/9-1, respectively. Kaolinite, illite, calcite, and siderite make up the clay minerals in well 7342/7-2 and well 7321/9-1 (see Figure 5.8).

Kaolinite

Kaolinite is the most abundant type of clay mineral in Stø Formation facies (F-2, F-3, F-4, F-5, F-6H, and F-6f). Kaolinite mostly distributes as pore filling and infilling secondary porosity. Kaolinite is commonly observed in conjunction with altered muscovite or feldspar (Figure 5.10). The highest concentration of kaolinite are found in facies F-2 (6.25%), F-6H (8%), F-6f (19%) compare to the other facies. The kaolinite constitutes 4% and 6% of the total rock volume of Stø Formation interval of the wells 7324/7-2 and 7321/9-1, respectively. Kaolinite well crystallized and occurs mostly in the form of booklets and vermicular in intergranular pore space close to the dissolved minerals (Figure 5.9).

Kaolinite is thermodynamically unstable at temperature above 90^0C and alters to dickite whereas at temperatures above 130^0C kaolinite replaced by illite depending on the availability of potassium (Bjørlykke et al., 1986). The chemical composition of the kaolinite and dickite is the same. However, the crystals of the dickte have thicker appearance comparing with kaolinite crystals.

According to the XRD result, Kaolinite is the most abundant type of clay mineral in the samples of the Fuglen formation in well 7324/7-2 compared to well 7321/9-1 (Figure 5.8) and includes 52.84% of the total rock volume of this formation. Kaolinite constitutes only 2.50% of the total rock volume of Fuglen Formation in well 7321/9-1.

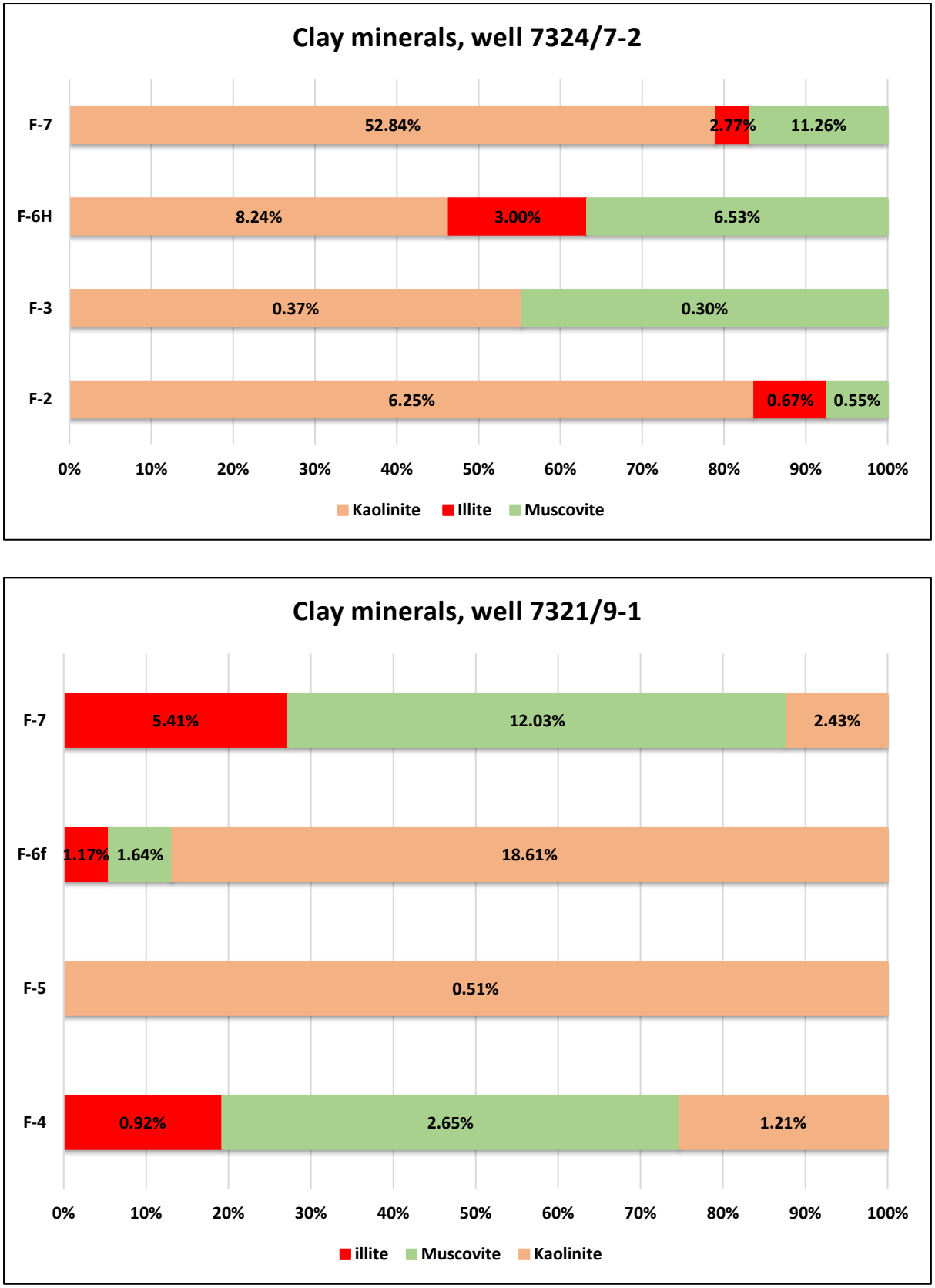

Figure 5.8: Distribution of clay minerals in each facies based on bulk XRD results. The point counting analysis could not provide an accurate estimation regarding the presence and distribution of different types of clay minerals within the samples. Only chlorite coating, kaolinite, and illite could be identified during point counting analysis owing to their characteristic mode of appearance.

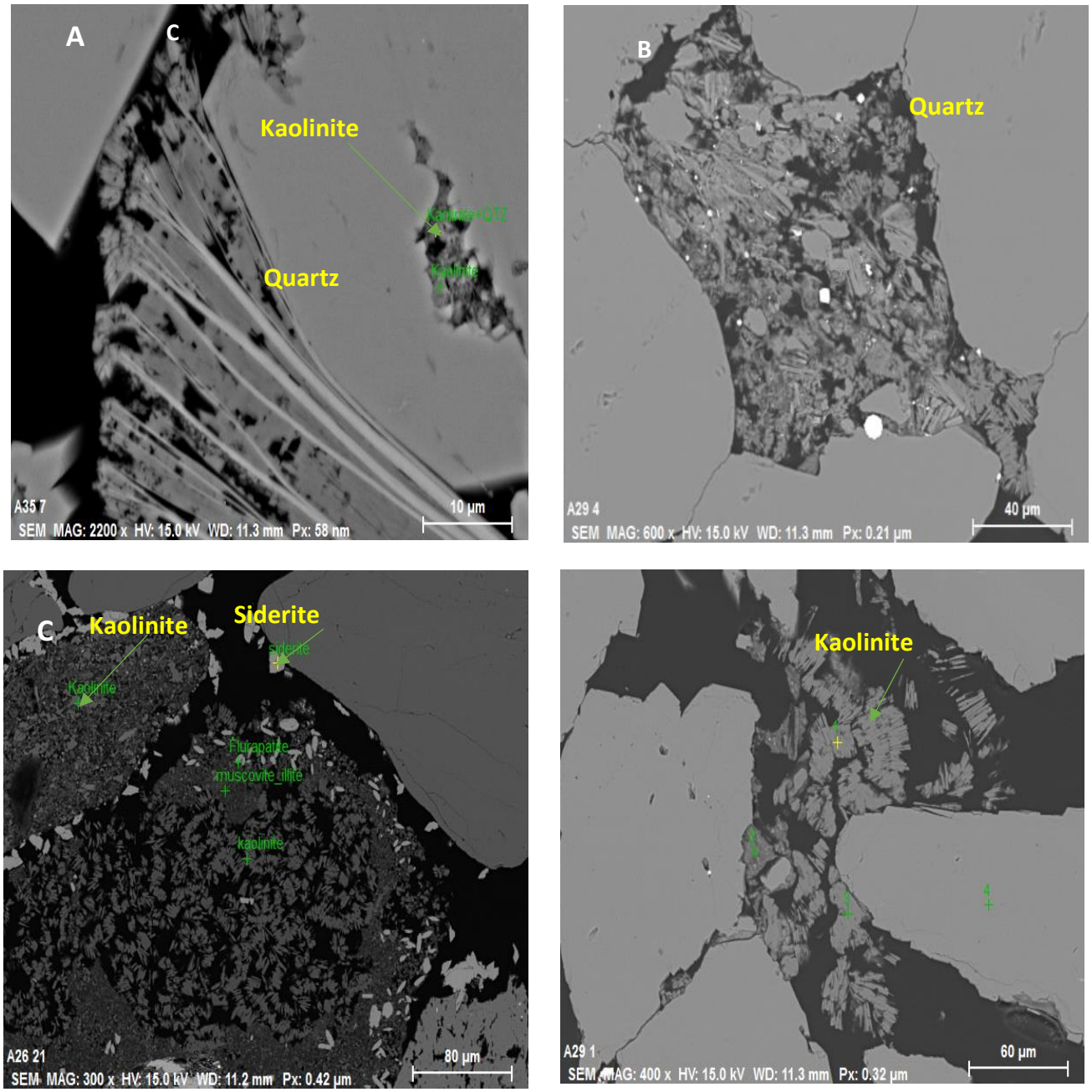

Figure 5.9: A, B) These pictures demonstrate the distribution of kaolinite mostly in pore space close to the dissolved minerals and filling secondary porosity (samples from facies F-6H, d= 712.96 m). C) This picture is taken from one of the samples of facies F-2 (d= 727.75), indicating distibution of the siderite around the grains and occasionally at grain surfaces. D) SEM image shows kaolinite crystals within the facies F-3 (d= 723.38 m).

Illite

Illite is found in samples belonging to facies F2, F4, F-6H, F-6f and F-7. According to XRD results, illite includes less than 1% of the total rock volume of Stø Formation in well 7324/7-2 and 7321/9-1. The highest amount of illite has been found within the facies F-6H (3%) and facies F-6f (1.17%). Typically, illite was found as pore-filling mineral in conjunction with kaolinite (Figure 5.10). Illite constitutes 3% and 5.50% of the total rock volume of Fuglen formation samples in wells 7324/7-2 and 7321/9-1, respectively.

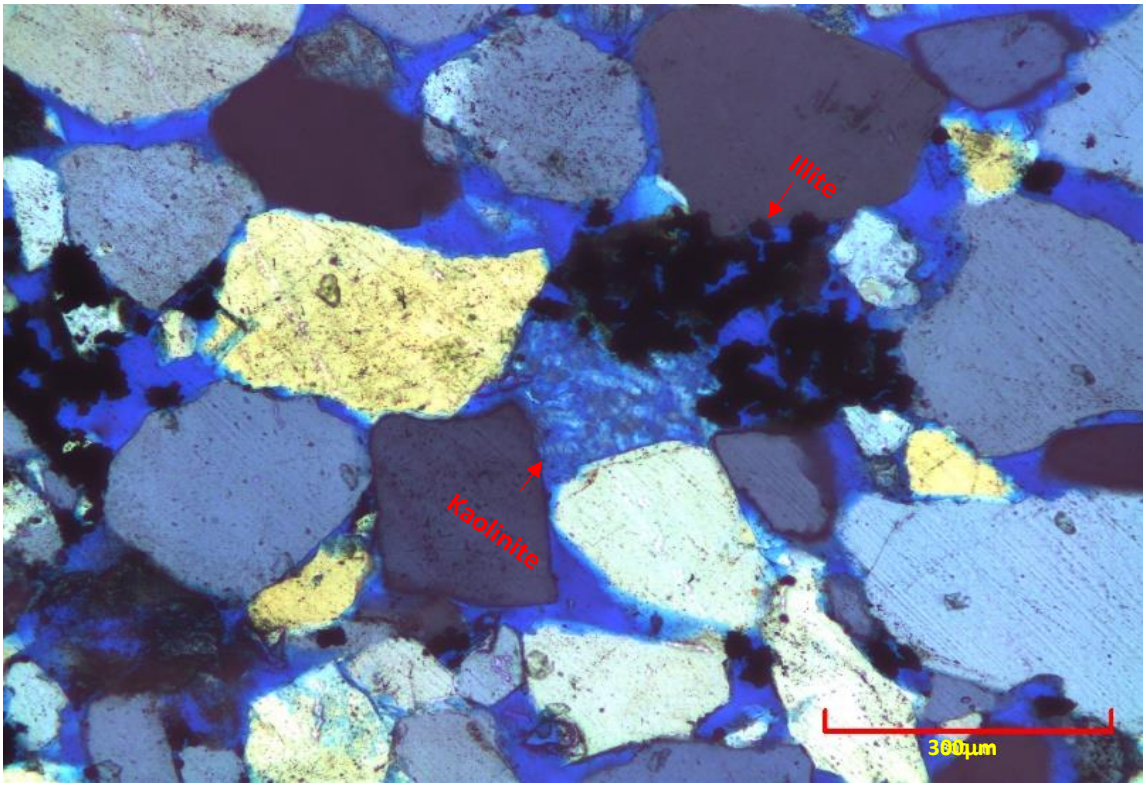

Figure 5.10: Illite and kaolinite as pore-filling minerals within facies F2.

Calcite and siderite

Calcite cement is present in a significant amount in two samples of the well 7324/7-2 and is registered in a trace amount in a few samples of the well 7321/9-1. Based on XRD results, the significant amounts of calcite cement concentrated in upper parts of facies F3 (4%), F-6H (18%) and F-6f (9%) (Figure 5.11). The total amount of calcite cement in Stø formation intervals of well 7342/7-2 and 7321/9-1 is estimated around 5% and 3%, respectively. Siderite occurs in samples belonging to facies F2, F4, F5, F-6H and F-6f. Siderite crystals are frequently observed around grains and occasionally at the grain surfaces (Figure 5.12). The highest concentration of siderite is found within facies F-6H (8%) and F-6f (4%). One of the samples of facies F-2 at the depth 727.75 m comprises a considerable amount of siderite as well as fluorapatite, Kaolinite, and muscovite (Figure 5.12).

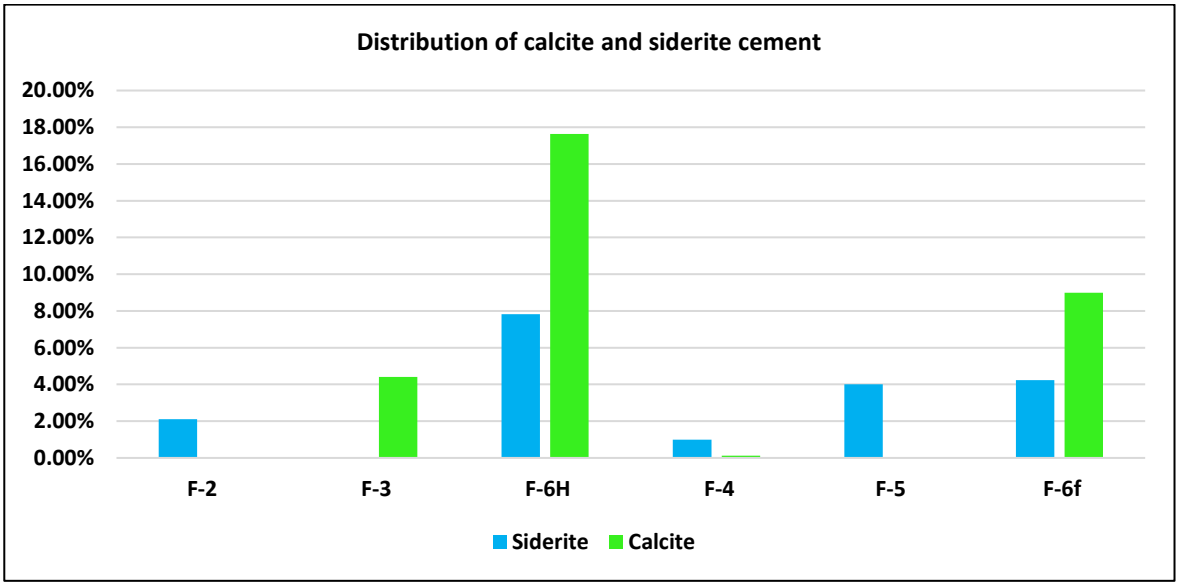

Figure 5.11: Distribution of Calcite and siderite cement within the facies F-2, F-3, F-4, F-5, F-6H, and F-6f, based on the XRD results.

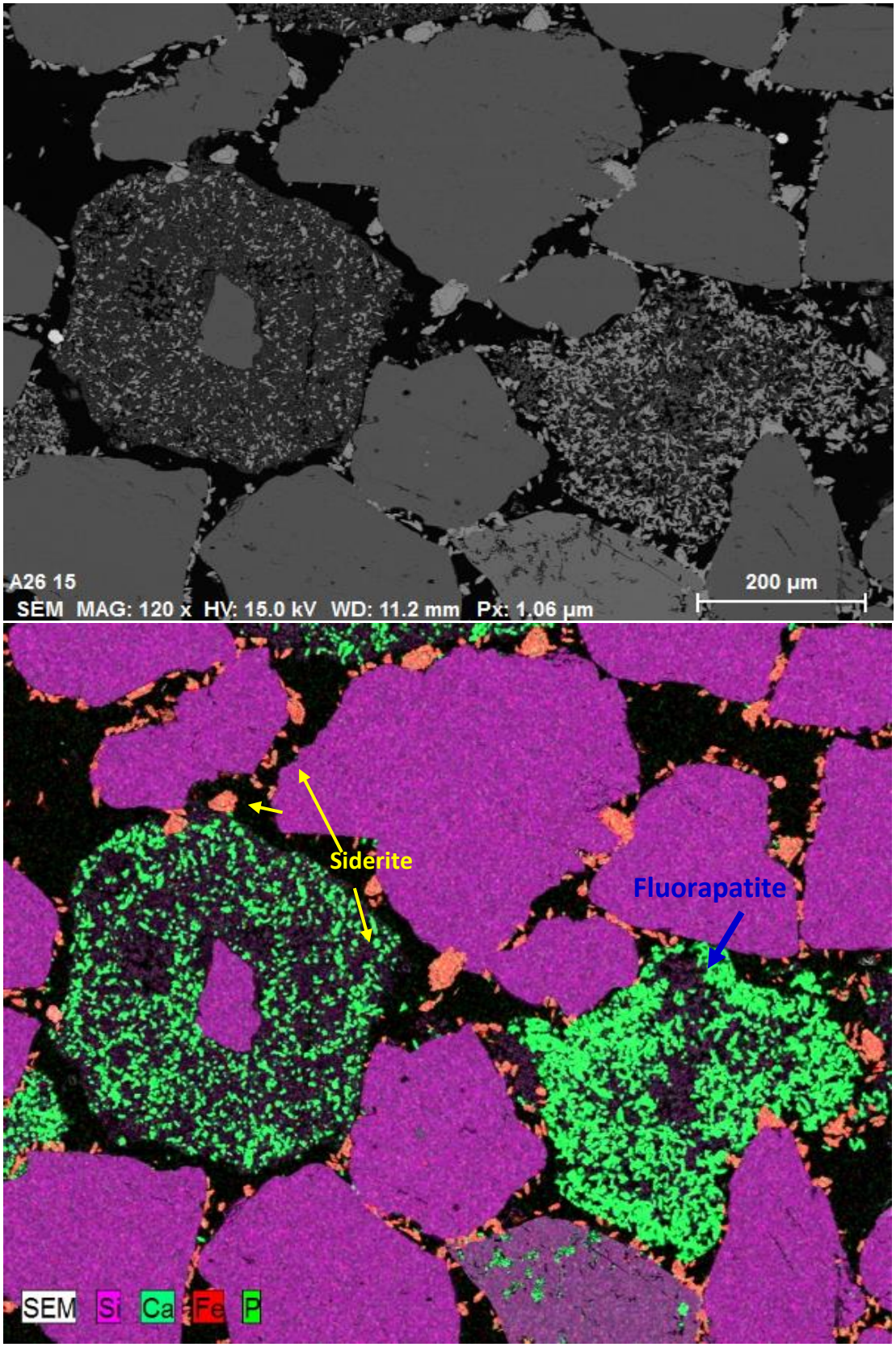

Figure 5.12: Pictures shows the distribution of siderite crystals around grains and occasionally at the grain surfaces. Fluorapatite has been observed significantly within one of the samples of the facies F-2 (d= 727.75 m). Fluorapatite probably formed from the remnants (skeleton) of dead reptile.

Quartz cement

Quartz cement is registered in trace amounts almost in all samples. Quartz cement value varies between 0 to 3.5% in all facies. Quartz cement tends to grow around the detrital quartz grains. It is worth to mention that it is not possible to make a precise differentiation between the quartz grains and quartz cement without the presence of dust rims during point counting analysis. Thus the possibility of over- or underestimating quartz cement is highly probable. (Figure 5.13).

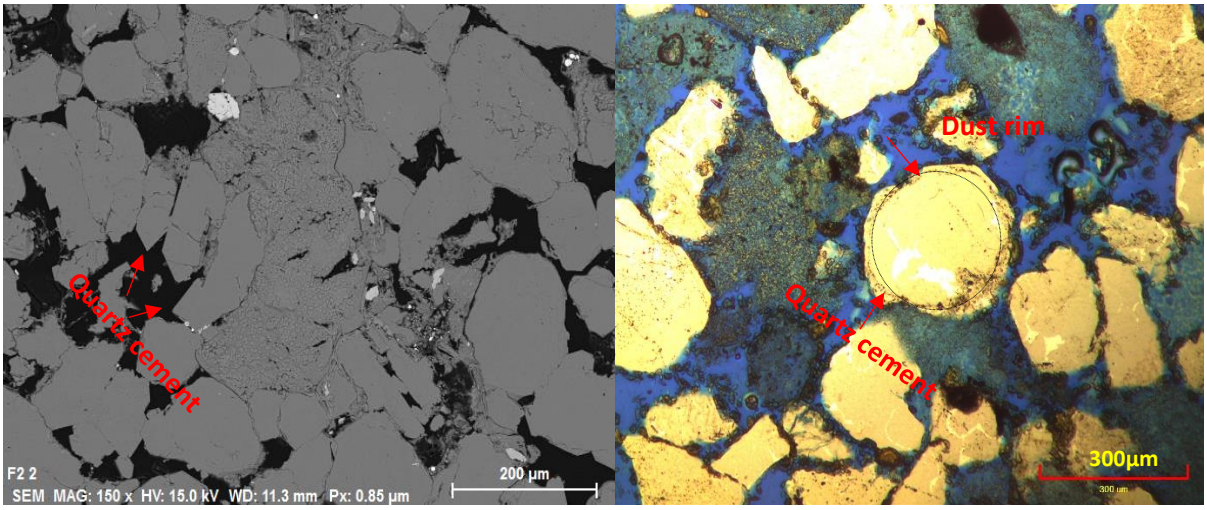

Figure 5.13: Quartz Cement within the sample of facies-4 (well 7321/9-1, d= 1396). Well 7321/9-1. Not the sharp edge around the quartz grains.

5.2.1.5 Trace Minerals

Pyrite

Pyrite was found in trace amounts in a few samples of facies F2 and F4. Through SEM analysis, small crystal clusters of pyrite have been observed. The total amount of pyrite is less than 1% in both wells. The pyrite crystals were observed as framboidal and blocky in the sandstone samples of Stø Formation (Figure 5.14)

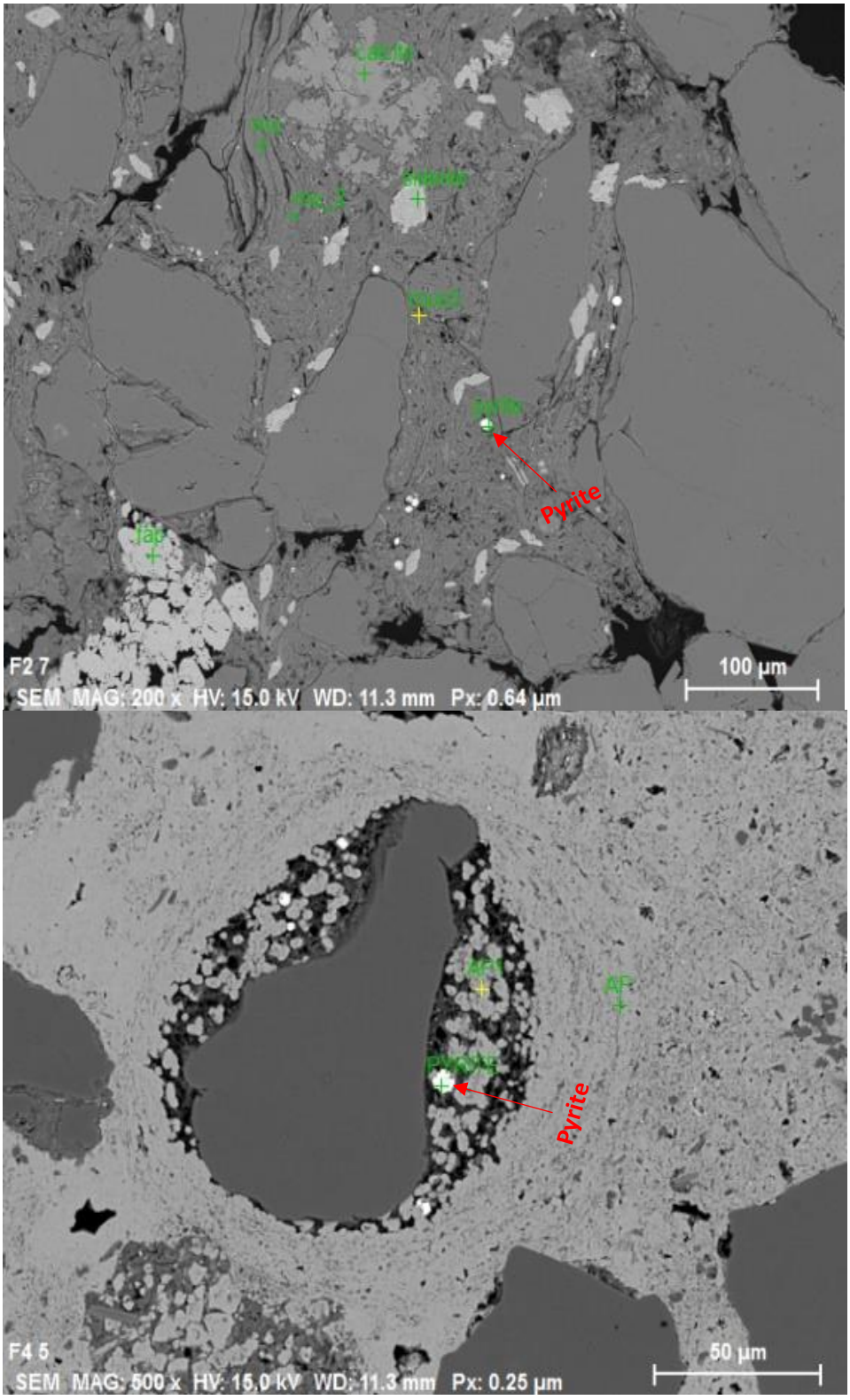

Figure 5.14: Pyrite in samples of facies F2 (well 7324/7-2, d= 725.50 m) and F4 (well 7321/9-1, d= 1393 m).

Fluorapatite

The highest amounts of fluorapatite were observed within a few of the samples in well 7321/9-1 and include around 6% of the total amount of rock volume. The highest concentration of fluorapatite has been observed in two samples of facies F4 (d=1393 m and 1392.80 m) and F-6f (d=1380.10 m) (Figure 5.15). Fluorapatite includes 10% and 6% of the total bulk mineralogy of the facies F-6f and F-4, respectively. Significant amount of fluorapatite has also been found in one of the samples of facies F2 (Figure 5.12).

Fluorapatite occurs within pore space of the samples of facies F2 and F4 as pore-filling cement (Figure 5.16).

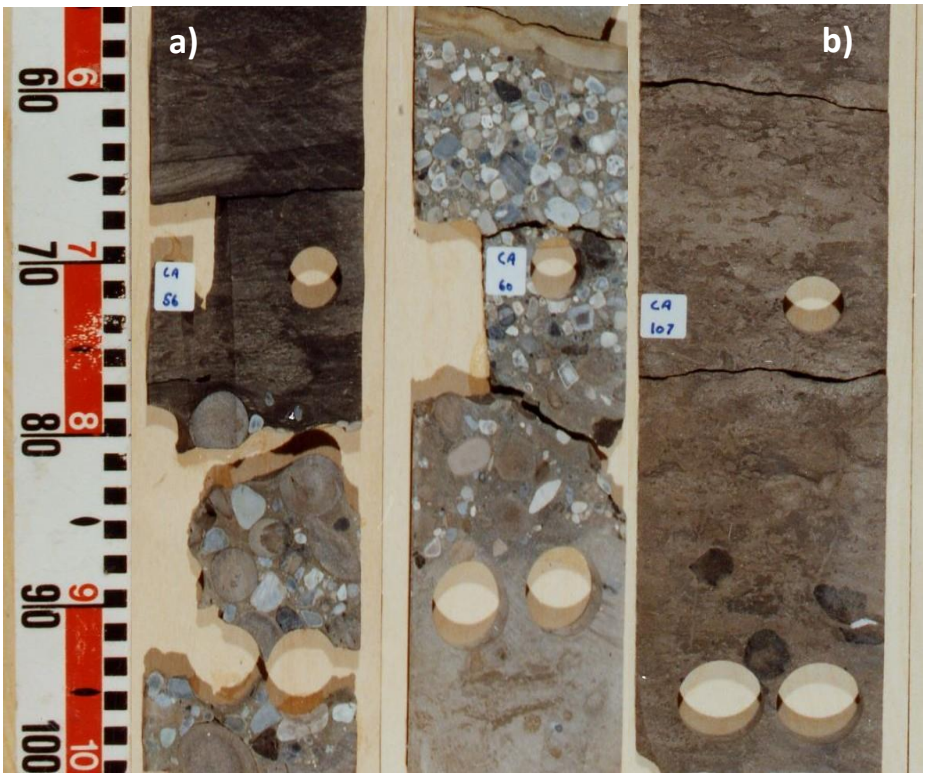

Figure 5.15a) core photos of the facies F-6f, indicating phosphate nodules associated which deposited during the transgressive event. Figure 5.14b) Demonstrates core photo of the facies F-4 (d= 1392.80 m). Fluorapatite within these facies is commonly formed from calcium phosphate present particularly in living organisms, e.g., bone mineral and tooth enamel.

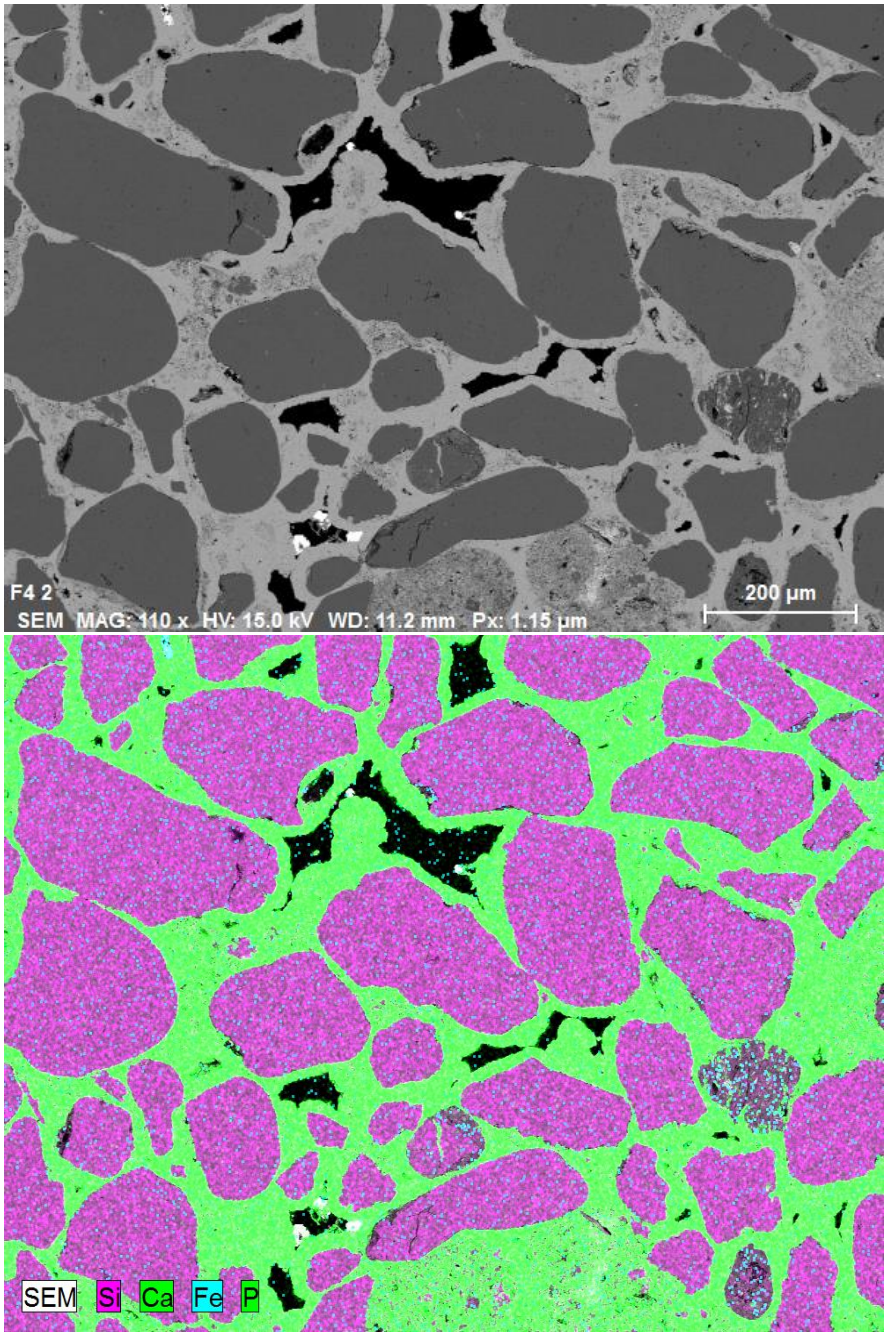

Figure 5.16: Distribution of fluorapatite in pore space a pore-filling cement (samples of facies-4, d= 1393.00). Fluorapatite within this facies is commonly formed from calcium phosphate present particularly in living organisms, e.g., bone mineral and tooth enamel.

5.2.1.6 Porosity and compaction

The porosity trend in the core intervals of the well 7324/7-2 and 7321/9-1 can be divided into three zones. In facies F-2 (730.84 -724.88m depth), the primary porosity varies between 11% to 19% and shows an increasing trend towards the upper parts of the facies. The average porosity in facies F-2 (Figure 5.17) is estimated around 15%, which is more and less the same as average porosity in facies F3. Facies F3 shows the higher volume of porosity (20%) in lower parts of this section compared to upper parts at the transition to facies F-6H. The transition from facies F-3 to F-6H can be observed from XRD and point counting results, where some samples of the facies F-3 comprise a significant amount of calcite cement, resulting in a remarkable drop in porosity trend from 20% in lower parts to 0.48% in upper parts of this succession. The last zone of porosity distribution in core 7324/7-2 belongs to facies F-6H in which porosity drops to 0.75% due to the existence of calcite and siderite cemented samples. The core intervals of the well 7321/9-1 are also divided into three parts. A sharp reduction in porosity is registered in lower parts of facies F-4, which could be related to the presence of more than 45% fluorapatite in pore space (d = 1393.00). The average porosity in this section is around 12 % and all the samples except one show more than 10% porosity. A slight increase in porosity is registered at the transition from facies F-4 to F-5 (d = 1383.75), where the samples demonstrate more than 15% porosity. The lowest amount of porosity is measured in uppermost parts of the well 7321/9-1 in facies F-6f. The porosity reduction in facies F-6f is related to the presence of high amounts of calcite cement (9%), siderite (4%) and Kaolinite (19%). This section has a higher porosity (4%) than its counterpart facies F-6H in well 7324/7-2. Based on the point counting results, the total amount of porosity in the well 7324/7-2 and 7321/9-1 is estimated 12% and 9%, respectively.

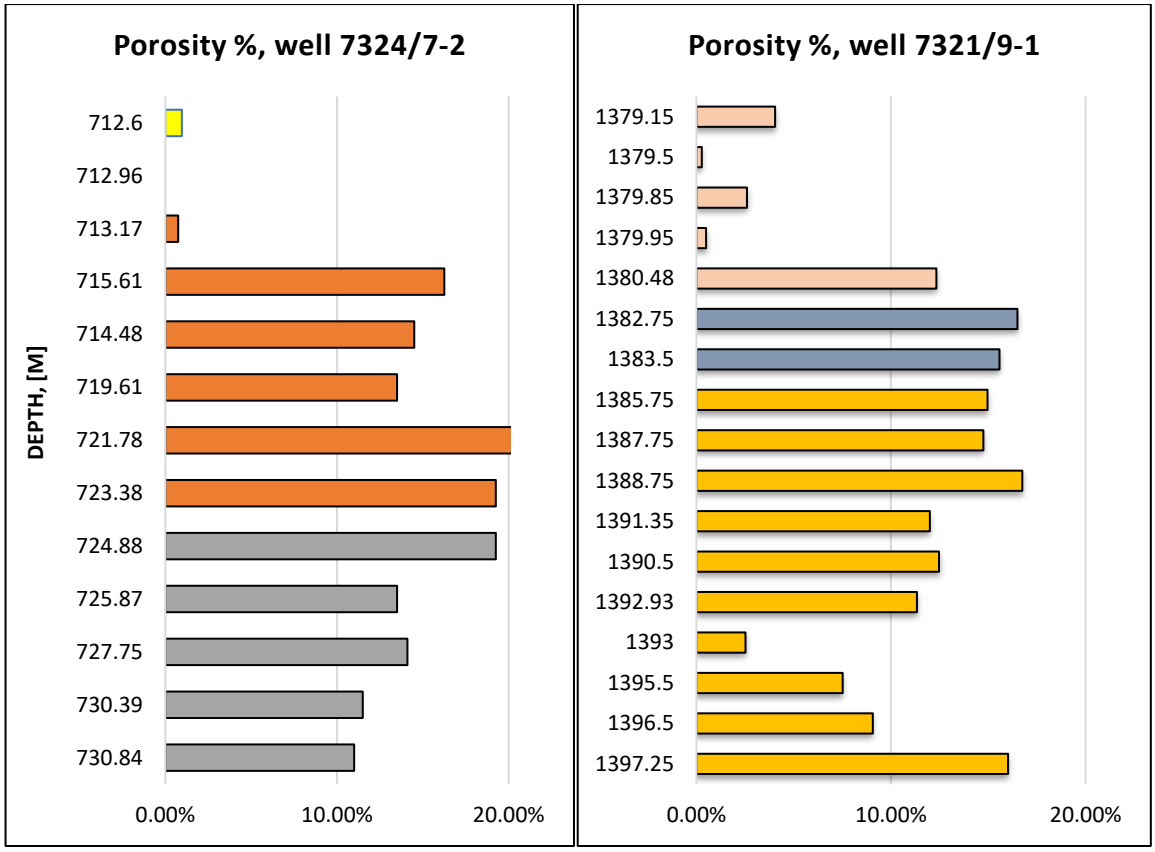

Figure 5.17: Porosity distribution (%) in well 7324/7-2 and 7321/9-1 from point counting. Facies F2 (green bars), F3 (red bars), F-6H (yellow bar), F-4 (orange bars), F-5 (blue bars) and F-6f (pink bars).

5.2.2 Textural analysis

Samples belonging to Stø Formation represent sandstones with possible reservoir potential. Thus, the textural analysis carried out based on the investigation of 200 grains per samples of these facies (in total 30 samples) are presented in this section.

Grain size

Cumulative frequency curves from the grain size distribution in facies F-2, F-3, F-4, F-5, F-6H, and F-6f are shown in (Figure 5.18). All the facies except facies F-6f show grain size variation between medium to very fine sand. Facies F-6f shows phi size variation between -4 to 2 due to the presence of high pebble-size particles in this facies (Figure 5.18). The grain size distribution in facies F-2 and F-3 are similar, but the abundance of fine sand is slightly higher in F-3. The grain size distribution in the samples of the facies F-4 and F-5 are more and less the same, and show variation between medium to fine sand. Facies F-6H consists of fine-grained sand, whereas its counterpart in well 7321/9-1 mostly consists of pebble size particles.

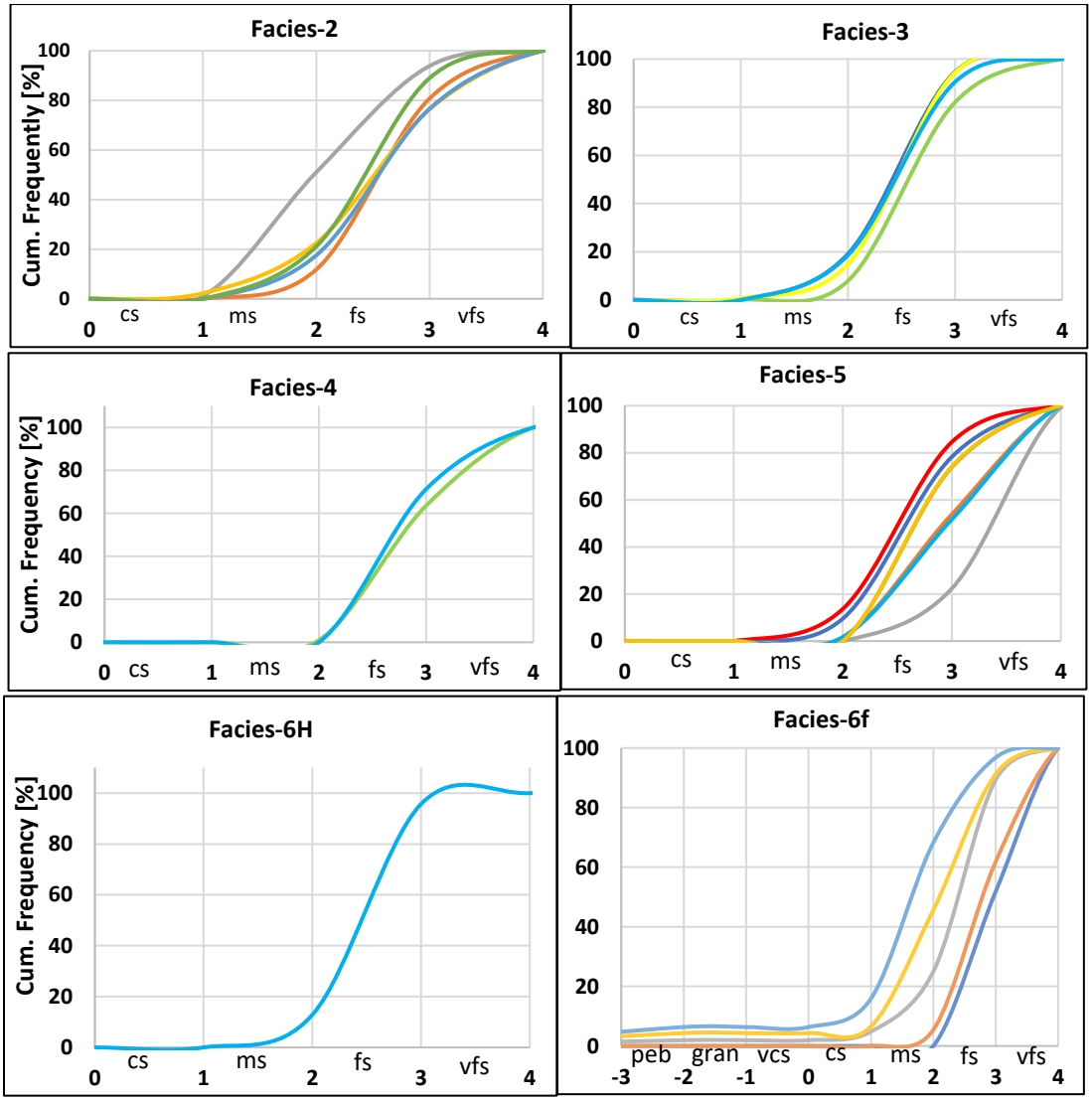

Figure 5.18: Grain size distribution in facies F2, F3, F4, F5, F-6H and F-6f in Stø Formation. Grain size presented as phi-values.

Sorting

The different degree of sorting in each facies is represented in Figure 5.19. It is evident from Figure 5.19 that most of the samples of facies F3, F4, F5 and F-6H plot in intervals of the well-sorted grains. Sorting degree in facies F2 varies from moderately to well-sorted grains. In contrast to all other facies, the samples of facies F-6f indicate moderately to poorly sorted degree due to the high quantity of the pebble size particles.

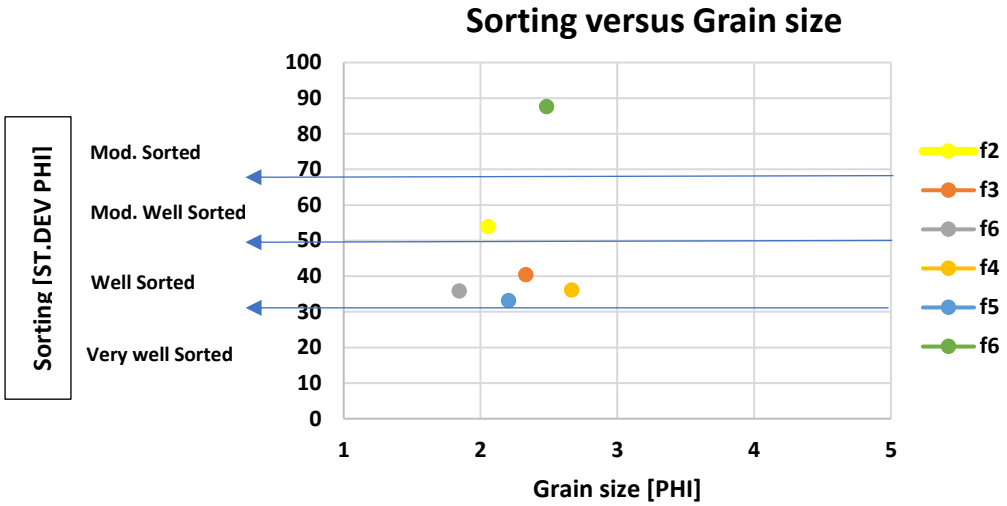

Figure 5.19: Sorting versus grain size for the facies F2, F3, F4, F5, F-6H and F-6f in Stø Formation. Sorting values were compared with the visual sorting estimation chart after Harrell, (1984).

Roundness and Sphericity

Figure 5.20 demonstrates the results of the particle shape analysis. The sphericity of the framework grains is also presented in Figure 5.20. Grains with low-sphericity are highly abundant in all facies but, the rate of grain distribution is slightly different among facies. The highest amount of low-sphericity grains is registered within facies F4, F5, and F-6f with a ratio 85/15. Facies F2, F3, and F-6H also consist of mostly grains with the low-sphericity framework, but the ratio between low- and high-sphericity is slightly lower (70/30).

Grain roundness analysis shows that most of the grains are angular to subrounded. The highest amounts of sub-angular grains are found in facies F5. In Facies F2 and F3, most of the grains are angular, and the distribution of sub-angular and sub-rounded grains are more and less the same in these two facies. Sub-angular grains are most common in facies F-6H and F-6f. Very-angular and very well-rounded grains are presented in small amounts in facies F2, F3 and F4.

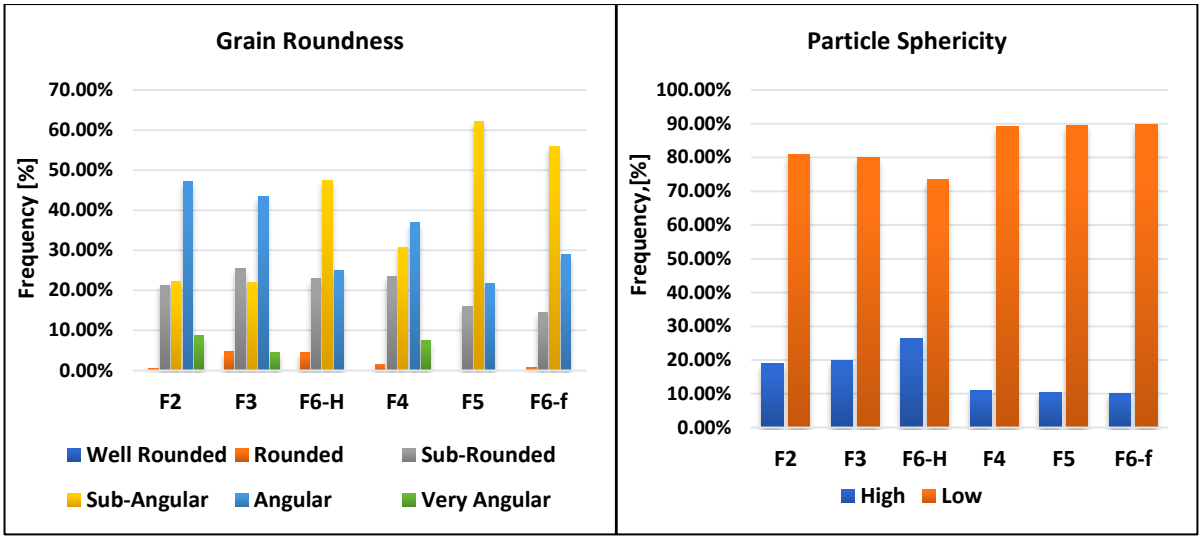

Figure 5.20: Frequency distribution histogram from the particle shape analysis of facies F2, F3, F4, F5, F-6H and F-6f in Stø Formation. Frequency (%) is displayed on the vertical axis. The particle shapes were qualitatively determined after the descriptions of Powers (1953).

Grain contacts

Figure 5.21 demonstrates the different type of grain contacts in all the samples of facies F-2, F-3, F-4, F-5, F-6H, and F-6f. The most common types of grain contacts in all the facies are Tangential. Facies F-5 deviates significantly from the other facies as it contains the highest concentration tangential grains (about 80%) and subsequently lowest concentration of long grains (6%). The long grain contacts are the second most common grain contact in all the facies, except facies-5 and facies-6f. In facies F-2, F-3, F-4 and F-6H 24% to 35% of all grain contacts are long. Floating grain contacts have been registered in all the facies with lowest amount (12%) in facies F-2 and with highest amount (36%) in facies F-6f. Concavo-convex and sutured contacts account for less than 5% of the grain contacts in facies F-2, F-3, F-4, and F-6H while these types of grain contacts are almost absent in facies F-5 and F-6f.

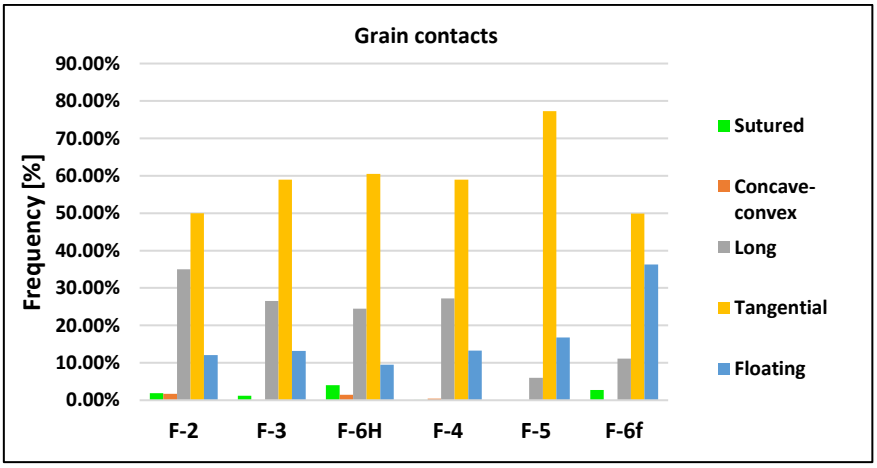

Figure 5.21: Frequency distribution histogram from the particle shape analysis of facies F2, F3, F4, F5, F-6H and F-6f in Stø Formation. The particle shapes were qualitatively determined after the descriptions of powers (1953).

Intergranular volume (IGV)

Intergranular volume was calculated based on point counting results by using the following formula:

Intergranular volume (IGV)= cement + depositional matrix + intergranular porosity

Figures 5.22 and 5.23 show the distribution of intergranular porosity, cement and depositional matrix in both respective wells.

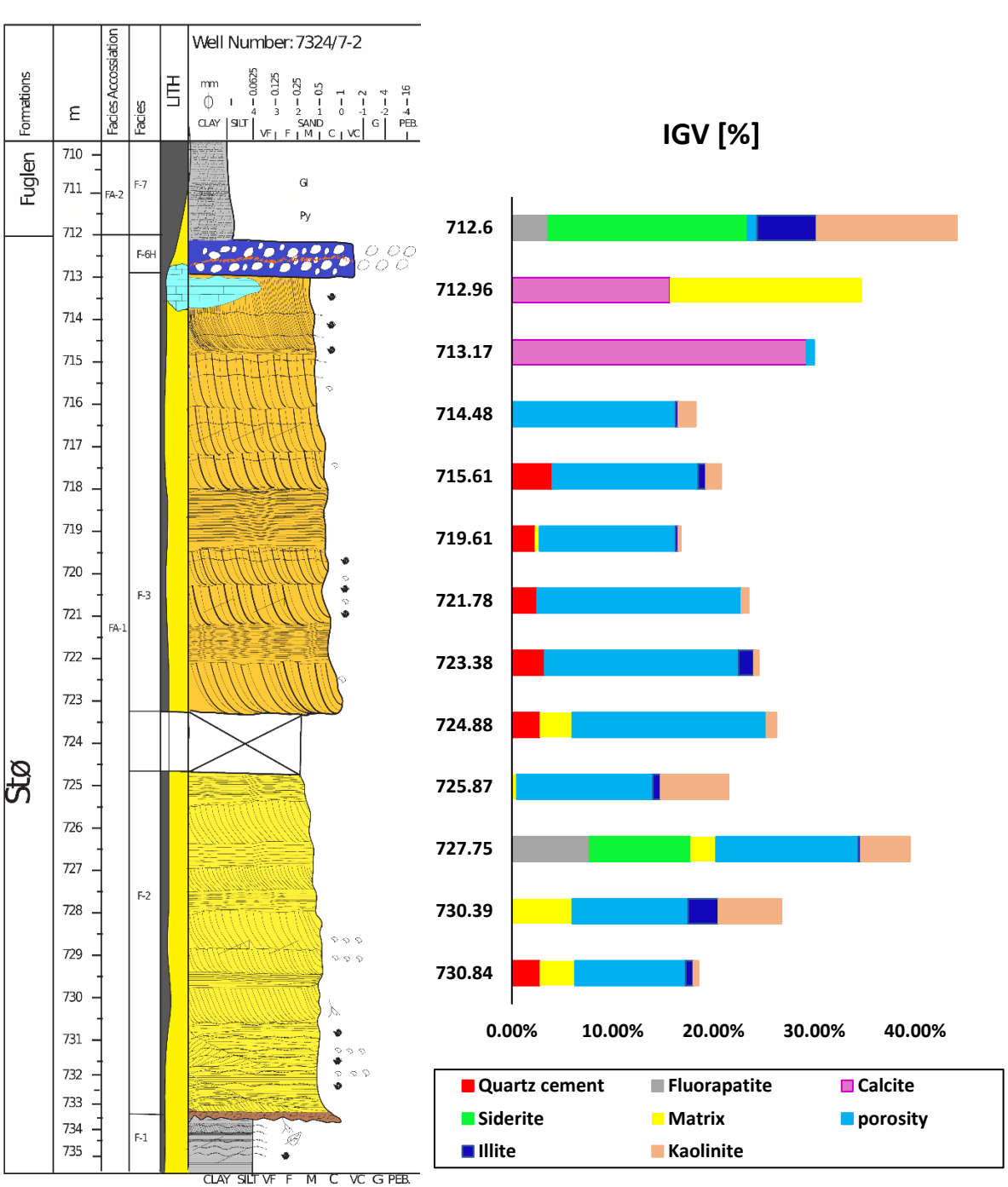

Figure 5.22: Intergranular volumes for analyzed samples in well 7324/7-2 (Hanssen). Stø Formation is depicting IGV range from 18% to 44%.

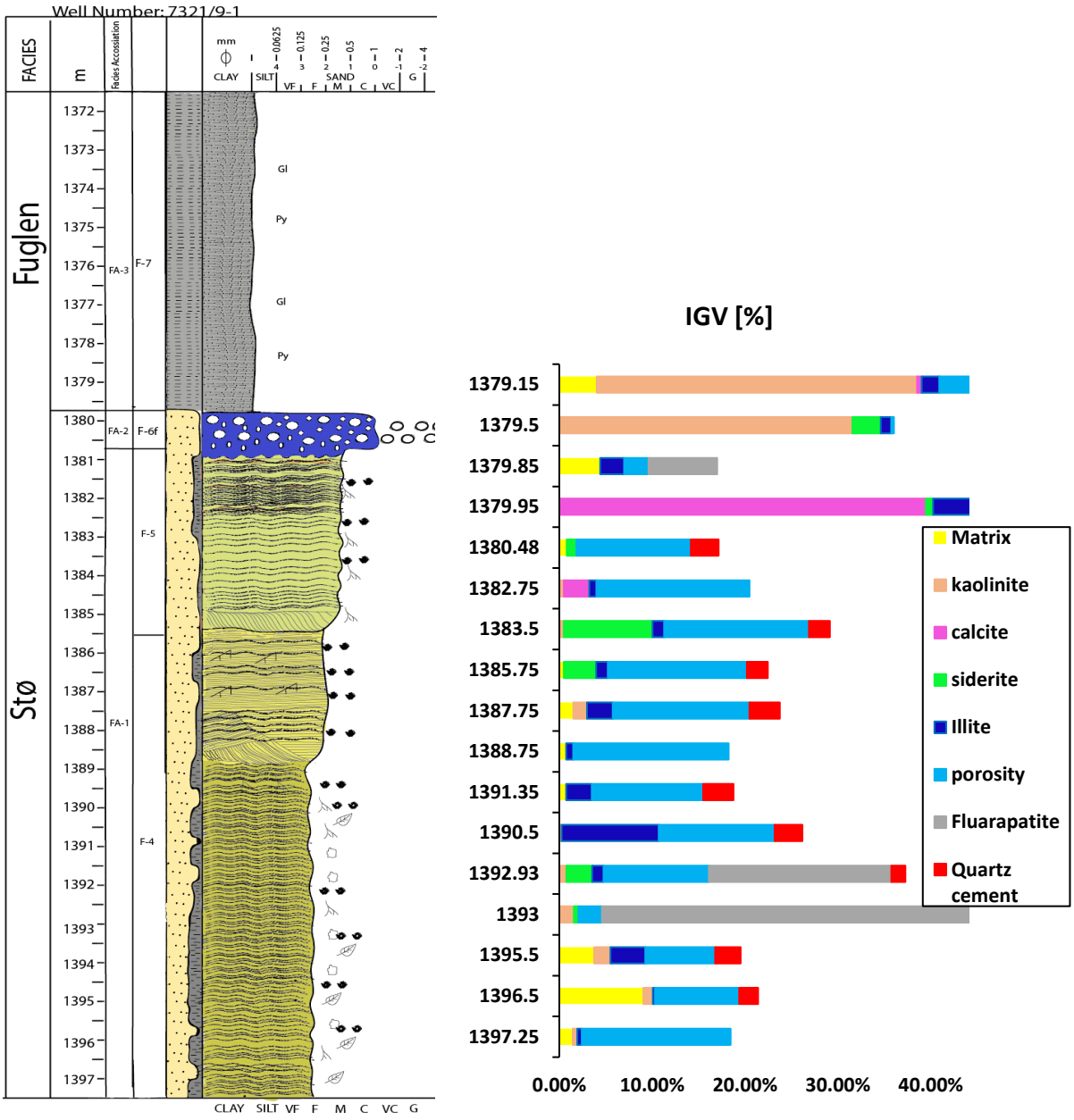

Figure 5.23: Intergranular volumes for analyzed samples in well 7321/9-1 (Fingerdjupet Sub-basin). Stø Formation is depicting IGV range from 17% to 45%.

Figure 5.24 shows the intergranular volume (IGV) and quartz cement of Stø Formation sandstones samples versus depth. The IGV ranges from 18.5% to 44% in well 7324/7-2 and from less than 17% to 45% in well 7321/9-1. The highest value of IGV (more than 40%) was found in the samples of the facies F-6H and F-6f. The High amount carbonate cements, secondary clay minerals (kaolinite + illite) and matrix are the main reasons for the grater IGV within these samples. Based on point counting results, IGV shows a reduction trend from the higher value in facies F-6H and F-6f in shallower depth toward a lower value in deeper depth in facies F-2, F-3, F-4, and F-5. In facies F-2, F-3, F-4, and F-5, the IGV is variable between 18% to 30%. It is worth mentioning that one of the samples of the F-2 (d= 727.75) and two samples of facies F-4 (d= 1393 and 1392.93) show IGV between 40 to 43% (Figure 5.22 and 5.23). The

reason for the high IGV value in these samples is related to the presence of high amounts of fluorapatite (8% to 46%) in pore space, resulted in significant increase in IGV value in deep burial. Quartz cementation value varies between 0% to 3.5 % in all facies (Figure 5.24). Porosity varies between 1% to 21 % in Stø Formation in well 7327/7-2 and between 0.50 to 17% in well 7321/9-1. The lowest porosity values (less than 4%) are within the samples of facies F-6H and F-6f, where a large portion of intergranular pore space is filled with early diagenesis cement including calcite, siderite and fluorapatite and clay minerals (kaolinite/illite). Matrix ranging from less than 1% to 6 % in samples of facies F-2 and from 1.5% to 9% in samples of facies F-4. The samples of the facies F-3 and F-5 are relatively clean in terms of matrix content (less than 0.5% on average). The Highest amount of matrix is found with the facies F-6H (19%) and F-6f (5%) which could be another reason for lower porosity within these facies.

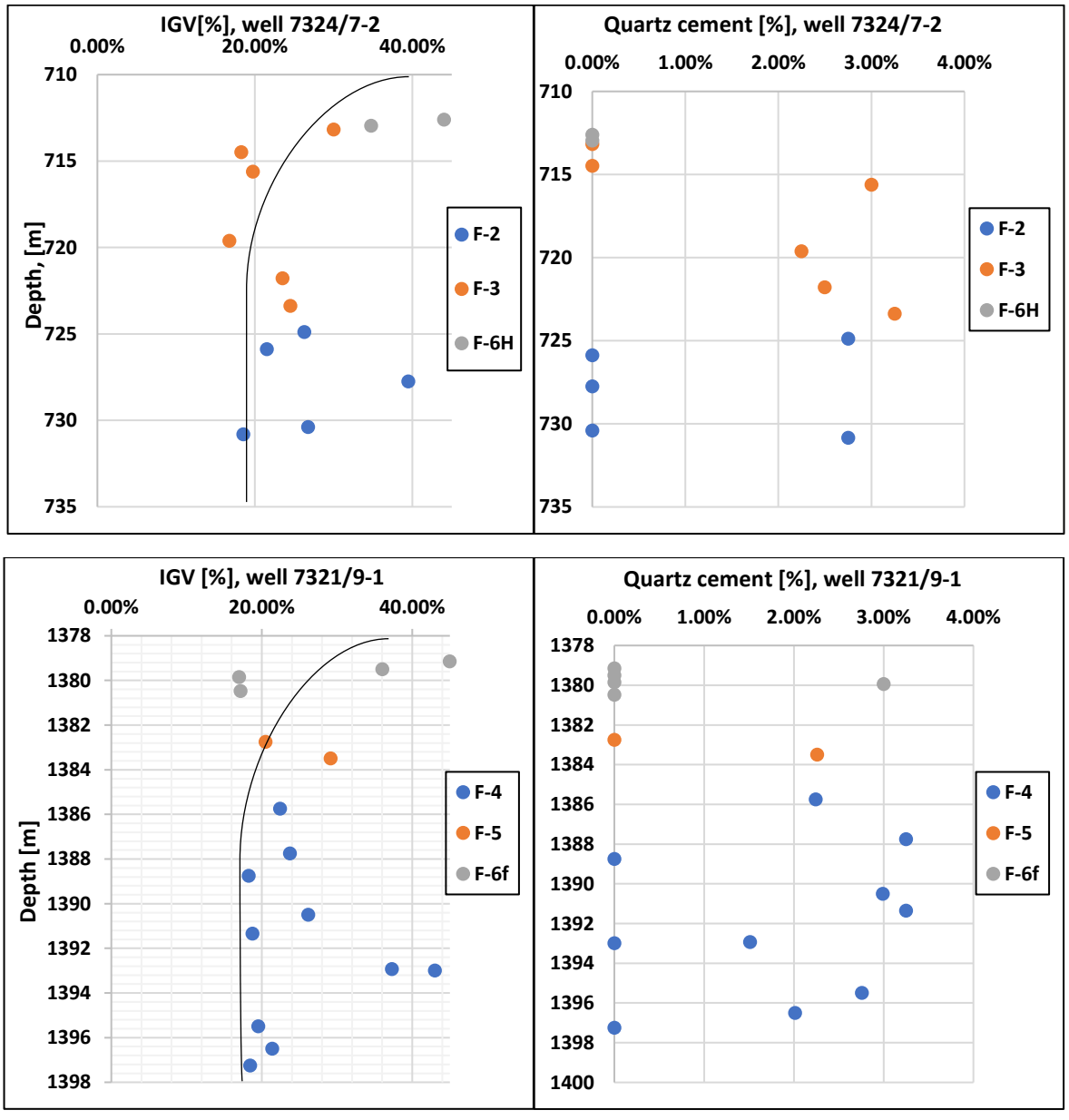

Figure 5.24: Calculated IGV and quartz cement vs. depth form well 7324/7-2 and 7321/9-1

Figure 5.25 shows IGV against grain size (phi). Most of the samples comprise of fine grained-size particles. The calculated average IGV value is almost the same within facies F-2, F-4 and F-5, ranging from 26%-25%. The average IGV value is slightly lower in facies F-3 (22%) compared to other facies. The highest calculated average IGV value has been found within the facies F-6H (42%) and F-6f (32%). From the Figure 5.25 it is evident that the IGV varies within the samples of the same facies. This variation is related to total amount of the carbonate cements within the samples. For example, two of the samples of the facies F-4 with more than 46% and 39% fluorapatite demonstrate higher IGV compared to rest of samples within the facies. Some of the samples of the facies F-6f show significantly lower IGV compared to other samples of this facies. This difference is related to the existence of a high amount of rock fragments within these samples (17%). Samples with more lithic rock fragments compact more readily thus IGV reduction within these samples is greater than samples with less amount of rock fragments.

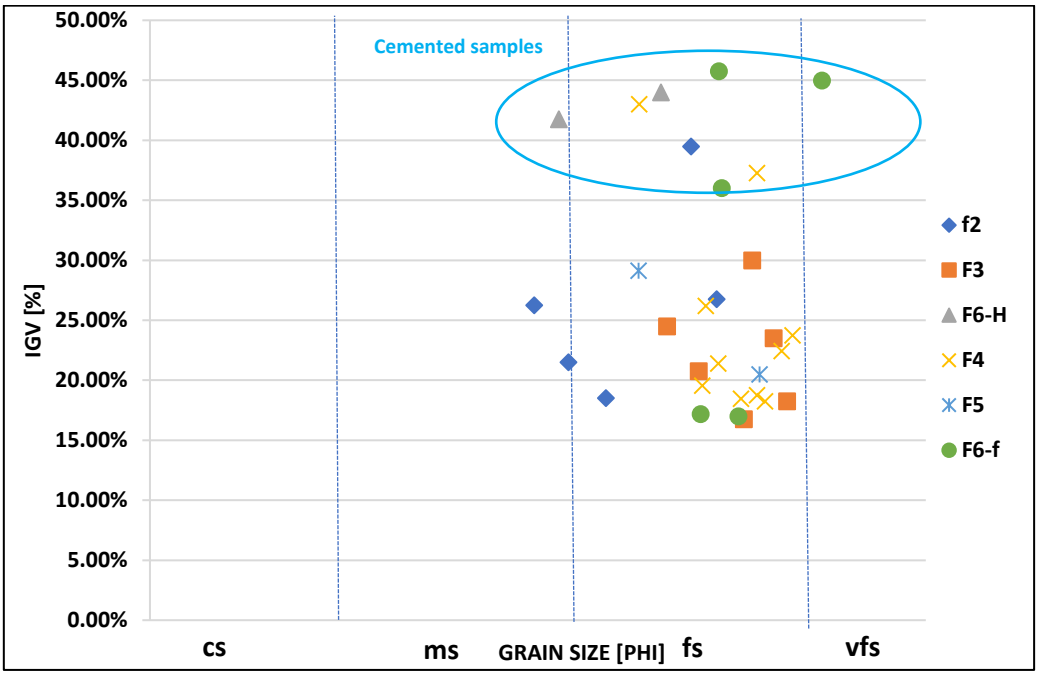

Figure 5.25: IGV versus grain size in Stø Formation sandstones facies.

Figure 5.26 displays a slight trend between IGV and sorting. Although, the samples of facies-6f are placed in moderately to poorly sorted intervals but still demonstrate a high amount of IGV, which could be related to the higher volume of cement in this facies.

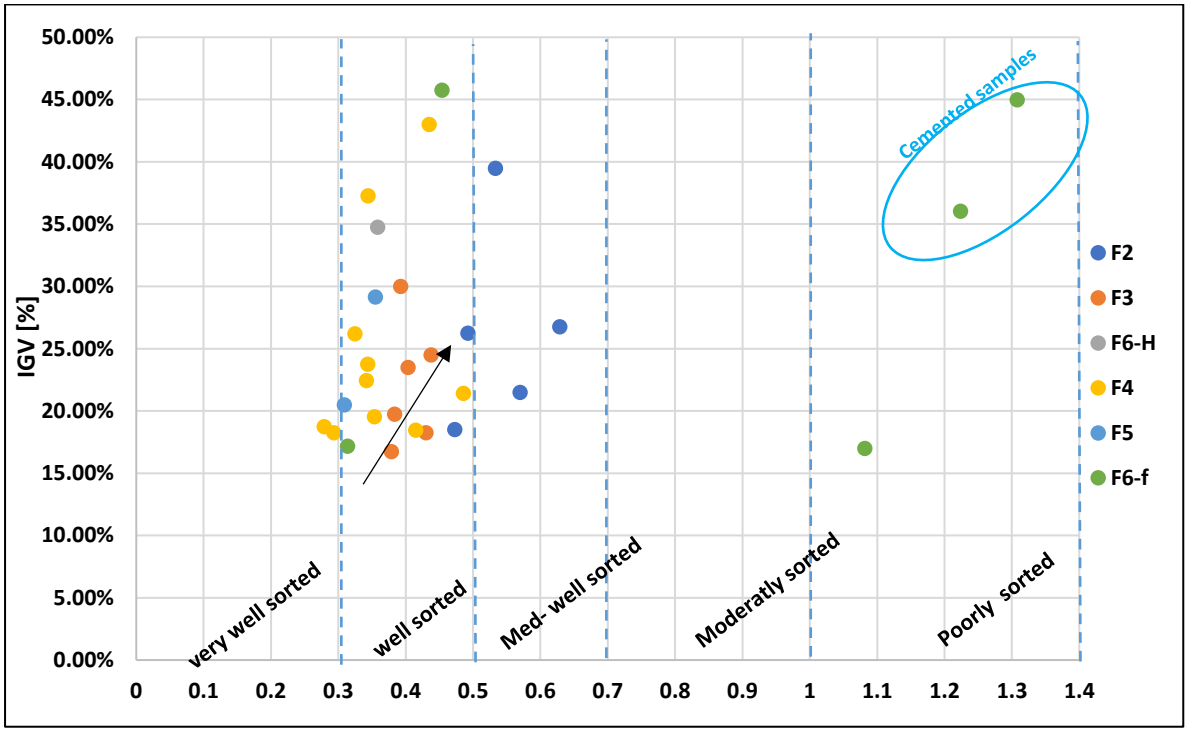

Figure 5.26: IGV versus sorting in Stø Formation sandstone facies

Preservation of detrital grains

Feldspar and mica grains have been observed in small amounts and made up only 1% and 2% of the total rock volume in well studied wells, respectively. Sector diagrams represent the preservation of feldspars and micas in Stø Formation (well 7324/7-2 and 7321/9-1) (Figure 5.27). Most of the feldspar grains (65%) show low preservation degree in well 7324/7-2 such that most parts of the grains have been dissolved, but, twins are still visible in the remaining parts. Around 35% of the feldspar grains in well 7324/7-2 have blurry twins and rough surfaces. The majority of mica grains in well 7234/7- 2 have been under the influence of an intense degree of alteration and deformation, resulting in completely dissolved and altered grains. In well 7321/9-1, feldspar and mica grains show a better preservation degree. Around 64% of the mica grains in well 7321/9-1 show intermediate preservation degree, which are partly squeezed into intergranular pore space.

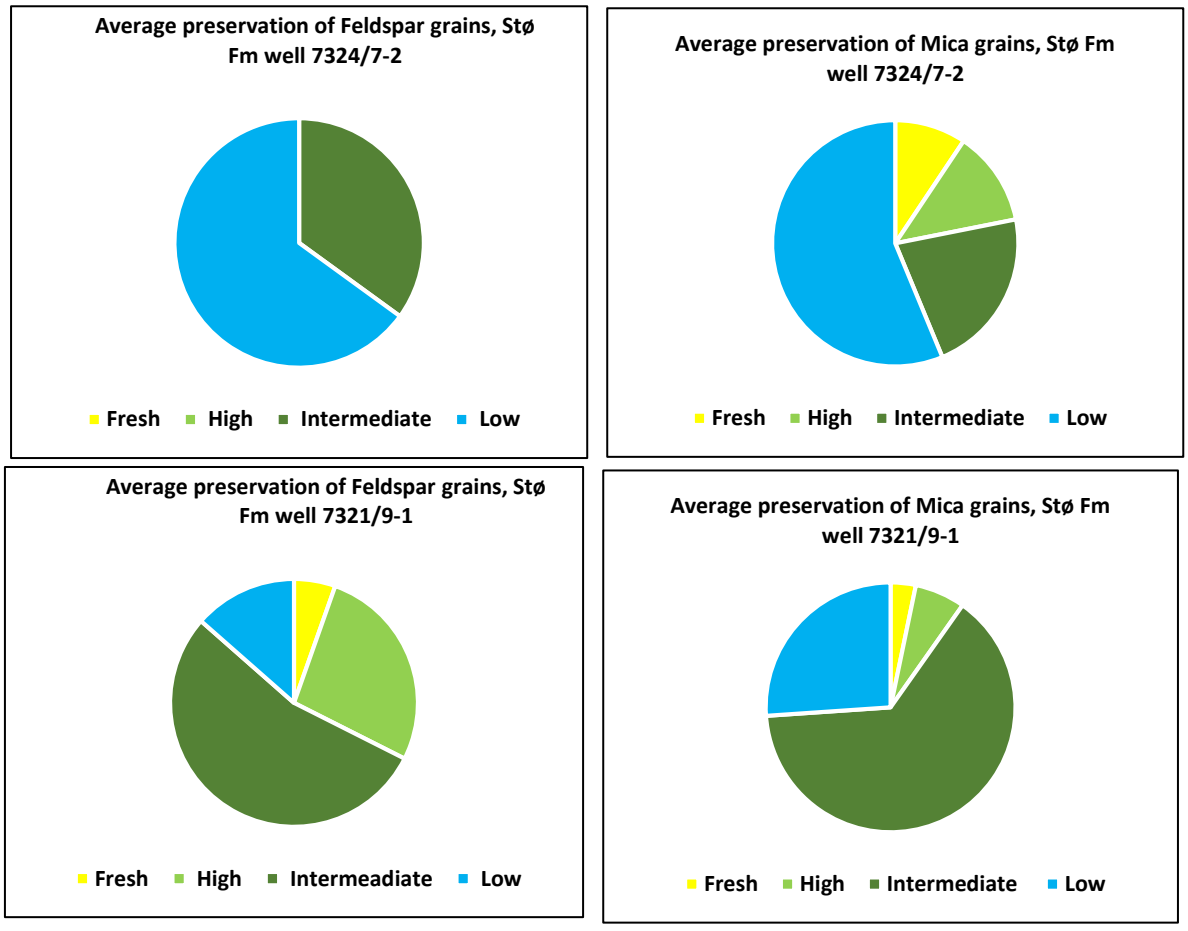

Figure 5.27: Sector diagrams presenting the average degree of preservation of feldspar grains and mica grains in Stø Formation, well 7324/7-2 and 7321/9-1.

Evidence of dissolved grains is registered in several samples. Dissolved grains make up 1.50% and 3.50% of all investigated samples in well 7324/7-2 and 7321/9-1, respectively. Observed dissolved grains are recognized as pseudomorphous replacements and secondary porosity.

Chapter 6: Results of Petrophysical Analysis

6.1 Introduction

The well 7324/7-2 and 7321/9-1 from Hoop fault complex and Fingerjupt Sub-basin in southwestern Barents Sea were analyzed with respect to petrophysical properties such as velocity, density, gamma ray and neutron porosity. The intervals belonging to Stø Formation were analyzed in both wells. The depths to Stø formation were taken from data found at the Norwegian Petroleum Directorates fact pages. Lithologies outside Stø Formation and intervals of the Fuglen Formation and other formations were determined in each well based on lithological core description and petrophysical well logs data which also have been provided by NPD. All depths refer to true vertical depth (TVD) below the seafloor.

The aim of the petrophysical analysis is to obtain information about porosity, depositional environments, compaction and burial-temperature history of the cored sections. The geothermal gradient is calculated using bottom hole temperature in order to determine which temperature sediments exposed to at maximum burial. These parameters are essential for deducing the diagenetic history of the sediments. Porosity and permeability are the most important reservoir properties and have been considered as vital factors for extracting hydrocarbons and consequently determining reservoir quality. There are two factor which have a direct effect on porosity and permeability. The first one is sedimentological conditions (provenance, climate, transport, depositional environments and mineralogical composition), and the second one is the diagenetic processes occurring both near the surface and during burial (Xi et al., 2015).
The study area has been subjected to a significant uplift and erosion during Cenozoic. This means the reservoirs were buried much deeper than the present depth and reservoir properties, (porosity and permeability) have been under the influence of burial processes such as compaction and consolidation. It is worth to mention that due to lack of petrophysical data from well 7321/9-1, the petrophysical analysis has been carried out based on the available petrophysical data from well 7324/7-2.

This chapter is divided into two sections as follows:

- Section one discusses the compaction trends and petrophysical analysis.

- Section two discusses the effects of burial on velocity-trends (uplift estimation) in the study area, based on the published literature on uplift and erosion in the SW Barents Sea.

6.2 Gamma-ray log response

Lithology has a significant effect on the rock response to compaction. Well, 7324/7-2 covers formations from lower Jurassic (Realgrunnen Sub-group) to lower Cretaceous (Adventdalen Group). The gamma log response shows values between 30 to 250 API for the well 7324/7-2 and 30 to 300 API for the well 7321/9-1 (Figure 6.1). The lithology shows a significant difference in upper well (Adeventdalen Group) from the lower well (Realgrunnen Sub-Group). The lower Jurassic to Middle Jurassic intervals comprise of the shale, siltstone, and sandstone of the Realgrounnen Sub-group, whereas the upper Jurassic to lower Cretaceous intervals include shale, claystone, and limestone of the Adventadalen Group.

The gamma reading is relatively high in upper parts of both wells, indicating the open marine shale of the Kolmule, Kolje, Knurr, Hekkingen and Fuglen formations. The gamma-ray responses in the Kolmule, Kolje and Knurr Formations of Adventdalen Group increase with depth (coarsening upward trend). An explanation for this is the presence of high amount of organic matter as well as potassium-rich deposits in these intervals which caused high gamma-ray reading. The gamma-ray log follows an analogous trend in Kolmule, Kolje, Knurr and Hekkingen Formations in both wells, although the gamma-ray reading is slightly higher in these formations in well 7324/7-2 compared to well 7321/9-1. Intervals of major decrease in gamma-ray responses at depth 250 m (BSF) in well 7324/7-2 and 900 m (BSF) in well 7321/9-1 indicate the transition from Fuglen to Stø Formation. Stø Formation mainly comprises of moderately to well-sorted sandstones which caused low gamma-ray reading. The gamma-ray pattern in Stø Formation in wells 7324/7-2 and 7321/9-1 is slightly different. In well 7324/7-2 gamma-ray shows blocky to smooth cylinder patterns, representing relatively thick coarse grain sandstone between finer argillaceous sediments while in well 7321/9-1 the base of Stø Formation is marked by a gradual transition from Nordmela to Stø Formation and the gamma-ray log demonstrates a serrated bell pattern, representing upward fining sandstones between argillaceous shale deposits above and below (Figure 6.2 and 6.3). The lower zone includes the Fruholmen and Snadd formations with a wide range of gamma-ray readings in both wells. Suggested depositional environments for different facies are as follows:

- Floodplain, channel base and channel fill for facies F1, F2 and F3, respectively, well 7324/7-2.
- Upper delta plain, minor distributary channel for facies F4 and F5, respectively, well 7321/9-1.

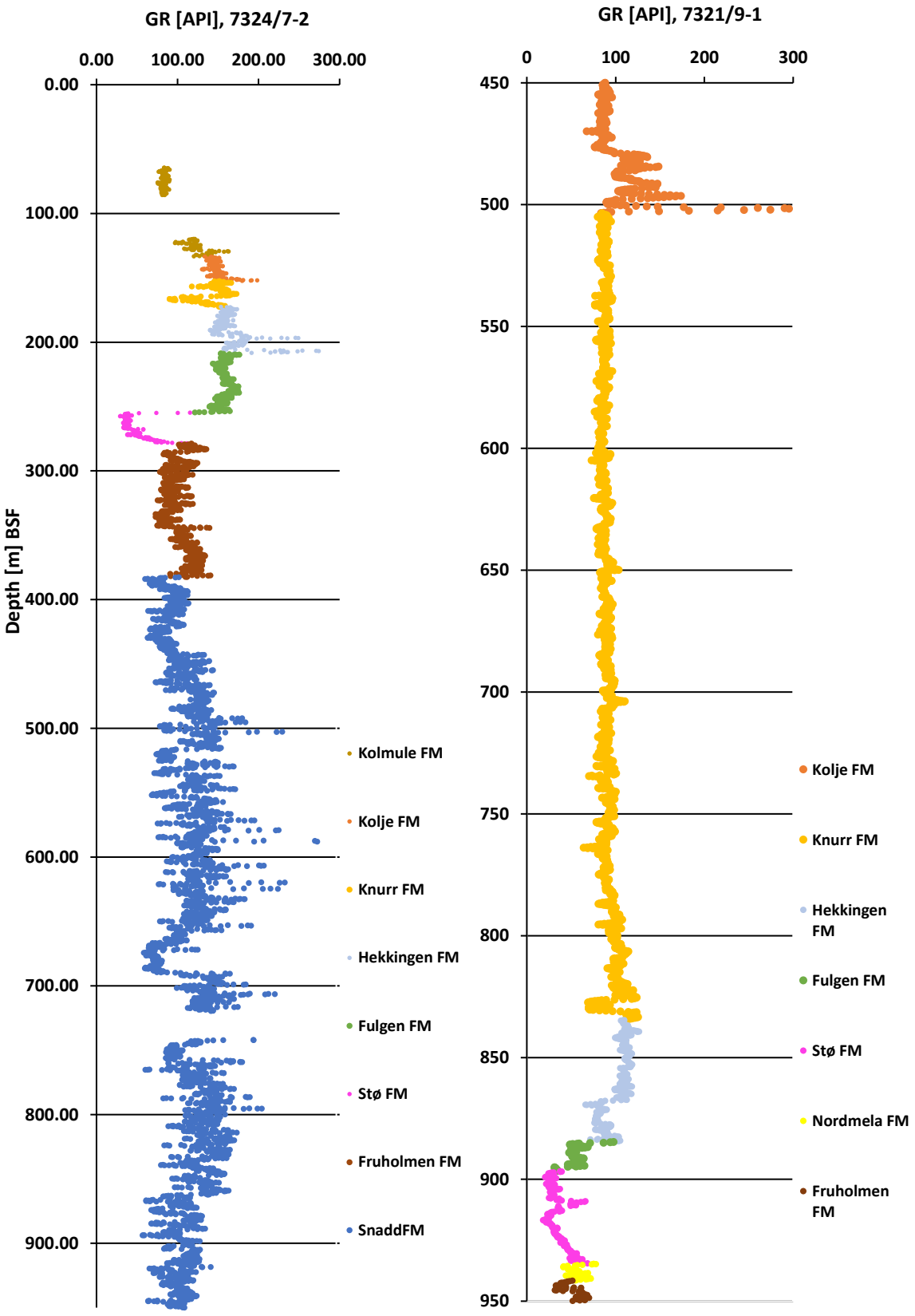

Figure 6.1: Gamma-ray log responses for well 7324/7-2 and well 7321/9-1.

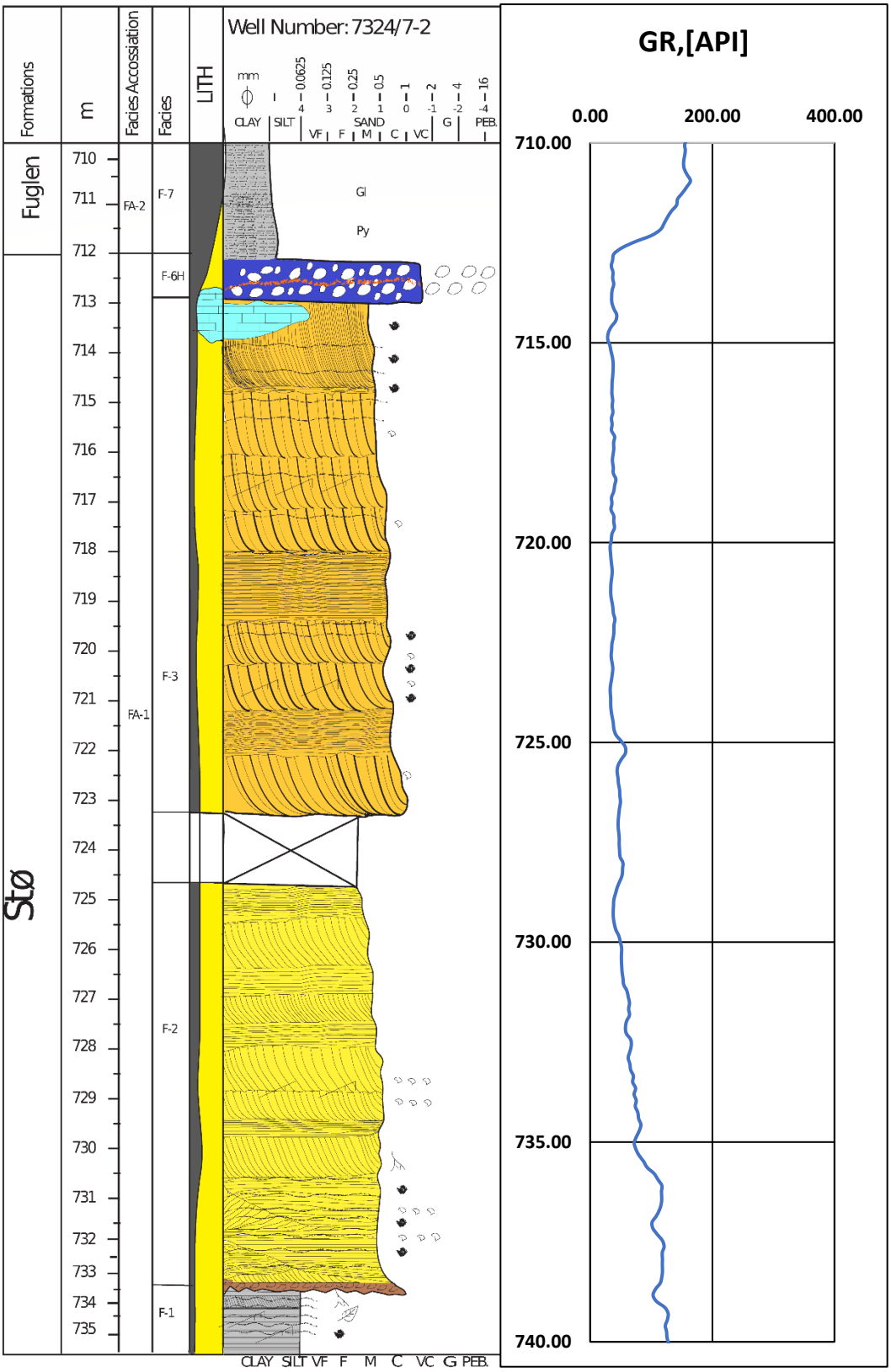

Figure 6.2: Gamma-ray in well 7234/7-2 indicate, upward fining sandstones of Stø Formation capped by the clay sediments of Fuglen Formation.

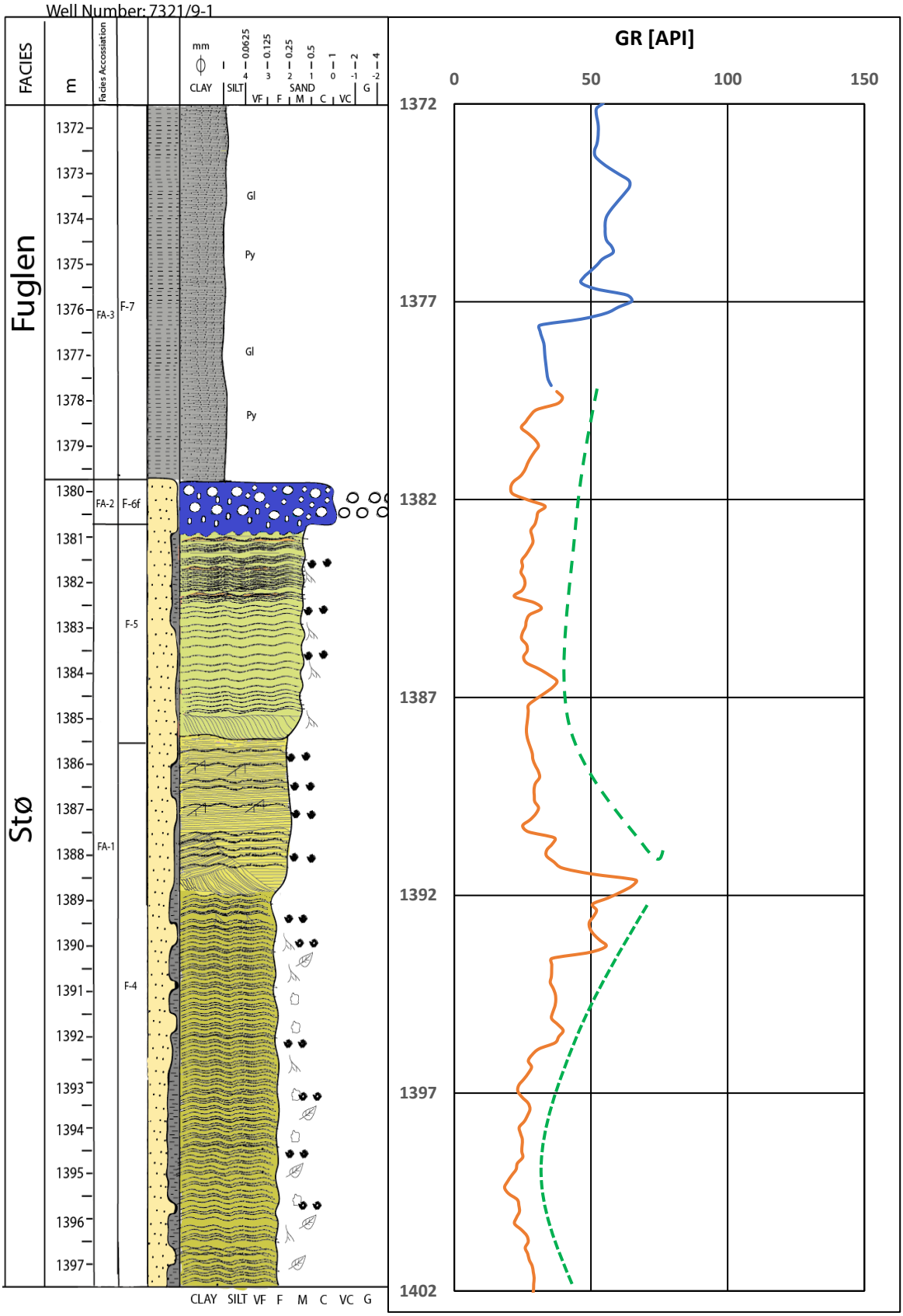

Figure 6.3: The bell (green dash line) shape of the gamma ray for the well 7231/9-1 indicates an upward increase in argillaceous content, between the sandstone deposits.

6.3 Acoustic velocity log and Density Log Response in Well 7324/7-2

The velocity-depth trends in the well 7234/7-2 show two distinct compaction domains; a mechanical compaction regime (MC) controlled by vertical effective stress from the weight of the overburden and a chemical compaction regime (CC) controlled by mineral reactions (Figure 6.4A). The velocity curve may be interpreted to increase linearly with depth. However, careful observation shows that there is a break in the trend at about 120 m with velocity 2000 (m/s), after this depth there is an abrupt increase in the VP-log, indicating the transition from mechanical compaction to chemical compaction. The transition zone (TZ) from MC to CC is clearly revealed by a cross plot of density versus velocity (Figure 6.5). The transition zone between two compaction regimes occurs at a depth of about 135m in well 7324/7-2, which was identified by the point of significant and abrupt increase in the velocity and density curves, resulting from grain framework stiffening. The TZ occurs within the Kolje Formation, and thus, Knurr, Hekkingen, Fuglen, Stø, Fruholmen and Snadd Formations are placed within the present chemical compaction regime.

6.4 Bulk Density Log Response

Density log shows increase with depth in well 7324/7-2 (Figure 6.4B). The exceptions from this trend are located within Stø Formation, where the density decreased from 2.5 g/cm^3 in Fuglen Formation to 2.3 g/cm^3 in Stø Formation. Velocity versus bulk density cross plot is also used for identifying the transition zone (Figure 6.5). At shallow burial depth, (60 m, BSF) density log increased gradually from 2.2 to 2.5 g/cm^3 at 120 m burial depth below the sea floor, however, after this depth, there is a sharp increase in density curve which implies the transition zone from MC to CC. A maximum density is registered in greater depth and appears to have been reached at 2.7 g/cm^3. This could be either related to the stability of grain framework structure at greater depth or related to the presence of more amount of quartz cement which has neutralized the further effect of mechanical compaction on sediments.

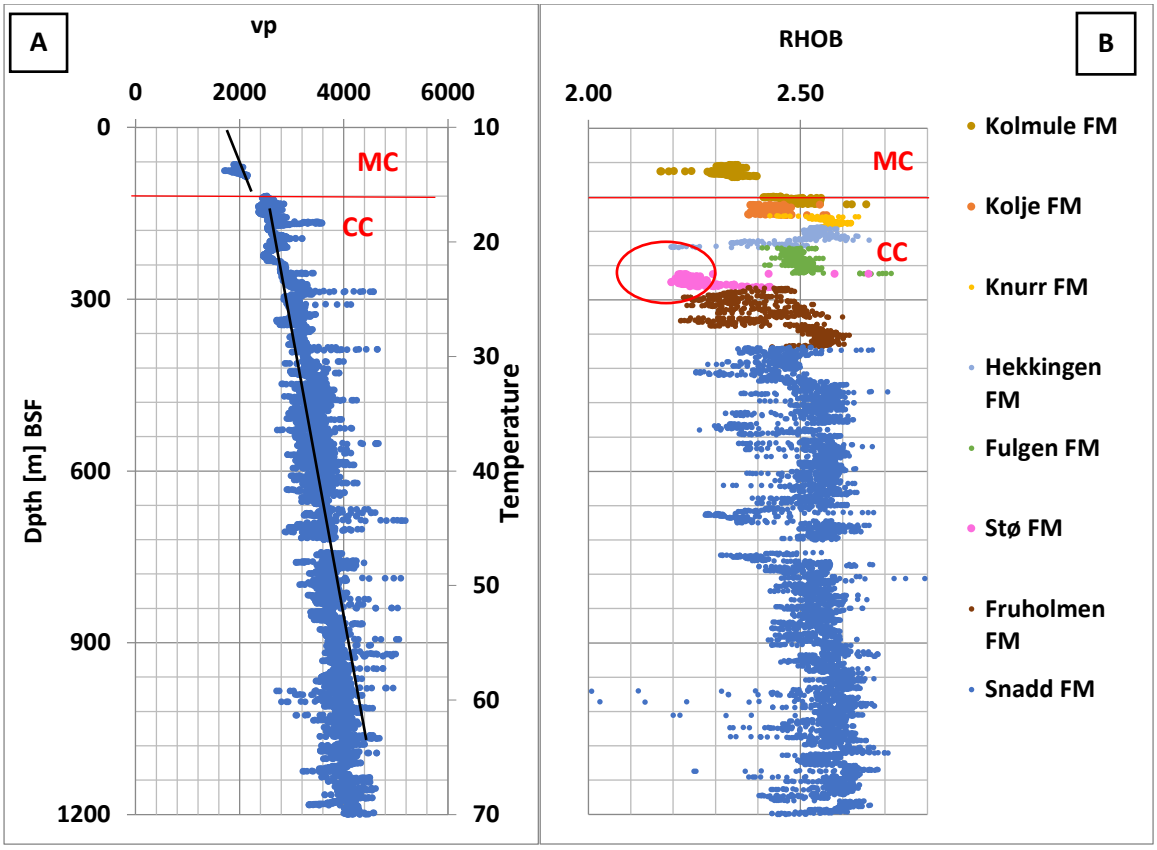

Figure 6.4: A) velocity/depth for well 7324/7-2 at present burial depth below sea floor (BSF). The general trend line (in black) is not for a particular lithology but for the entire well data. B) density/depth for well 7324/7-2, red circle indicates decrease in density log within Stø Formation.

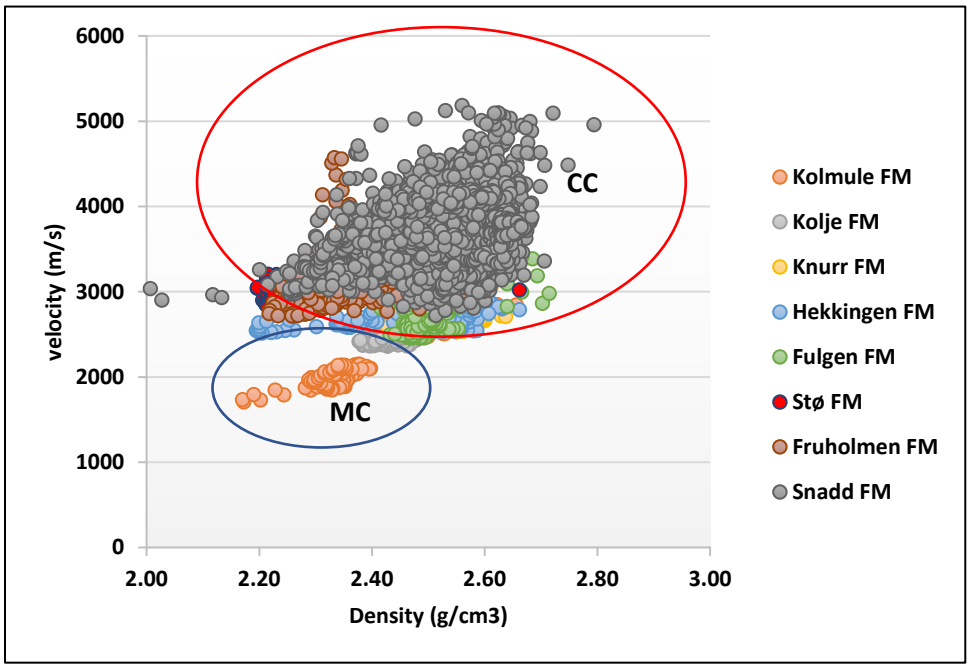

Figure 6.5: Velocity-density cross-plot. The blue circle shows the Kolmule Formation in mechanical compaction (MC) regime, whereas the red circle highlights the Formations in chemical compaction (CC) zone.

6.5 Neutron Log Response

The neutron log is sensitive to the hydrogen content in the formation and loses its energy when colliding with hydrogen atom nucleus (Bjørlykke, 2010). The neutron porosity logs in well 7324/7-2 show an inverse, linear relationship with the corresponding bulk density log (Figure 6.6). Neutron and bulk porosity responses are significantly high (40% and 2.6 respectively) in clay, rich formations such as Kolmule, Kolje, Knurr, Hekkingen and Fuglen formations. Whereas, at the transition from Fuglen to Stø Formation a remarkable decrease in both neutron and bulk density log (25% and 2.30 respectively) is registered which implies the presence of hydrogen in these intervals either water or oil.

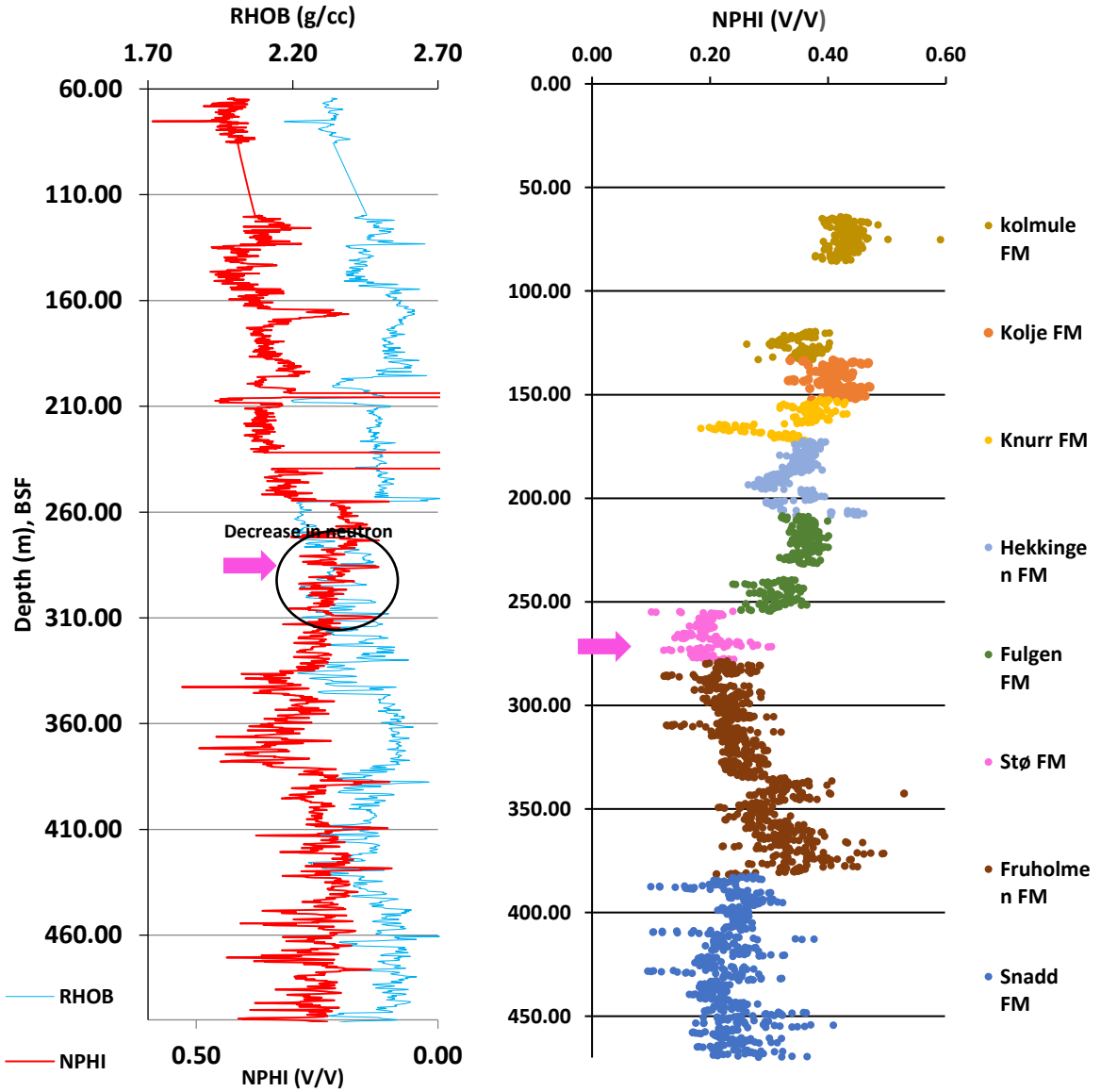

Figure 6.6: Neutron porosity and bulk density trend versus depth in well 7324/7-2. Abrupt decrease is registered in neutron porosity log response at the transition from marine Fuglen Formation to Stø Formation (pink arrows).

6.6 Depth and Temperature of Transition Zone

The transition zone represents the transition from mechanical to chemical compaction. In well 7324/7-2 the estimated transition zone is placed at 594 m burial depth with relatively low temperature which are significantly lower than the standard depth and temperature at which onset of quartz cementation would be possible (Figure 6.7).

Table 6.1: Transition depths and associated temperatures (at present) for the well 7324/7-2.

WELL	Transition depth (m TVDSS)	Transition depth below seafloor (m)
7324/7-2	594	135

The well, 7324/7-2 is selected for uplift estimation since high acoustic velocities in this well are encountered at shallow depth due to uplift. In this well, velocity and density logs increase significantly at a certain depth, indicating the possible transition from mechanical to chemical compaction zone. Many experimental compaction curves have been published, which show velocity/depth trends. In this thesis, uplift was estimated for well 7324/7-2 by comparing the observed velocity/depth trends with those published by (Storvoll et al., 2005); (Mondol et al., 2007), (Mondol, 2009); (Marcussen et al., 2010) and (Baig et al., 2016) (Figure 6.7). Transition zone was estimated based on the entire velocity data set in well 7324/7-2, while uplift estimation was performed for data points which represent shaly intervals. The gamma-ray log was used as lithology indicator in order to determine the volume of shale in the formation. The shale boundary was set to 145 API for well 7324/7-2. Approximate amount of uplift in well 7324/7-2 is estimated around 1800m and have the best fit with the empirical compaction curve published by Baig et al. (2016) (Figure 6.8). Baig et al., 2016 has estimated the Cenozoic exhumation in the southwestern Barents Sea area based on well logs and thermal maturity data from more than 70 exploration wells together with widely distributed shot gather data along-offset seismic reflection lines (Figure 3.7). The suggested average net exhumation by Baig et al. (2016) range from ~800 to 1400 m within the Hammerfest Basin, ~1150 – 1950 m on Loppa High, ~1200 – 1400 on the Finnmark Platform and ~1250 – 2400 on the Bajarmeland Platform.

After correcting for exhumation, the zone of transition between mechanical and chemical compacted sediments in well 7324/7-2 is found to correspond to a depth of 1935 m (BSF) and at temperature 76^0c. The maximal burial depth (m) of Stø Formation is estimated between 2060-2090 m [MD] with temperature variation between 80-81^0C. Due to lack of petrophysical data for the well 7231/9-1, the suggested average net exhumation by Baig et al., (2016) on Fingerdjupet Sub-Basin (1500-1900) has been used as the amount of uplift for this well. The estimated net exhumation for well 7321/9-1 according to the approximate position of the well on Fingerdjupet Sub-Basin is 1600m.

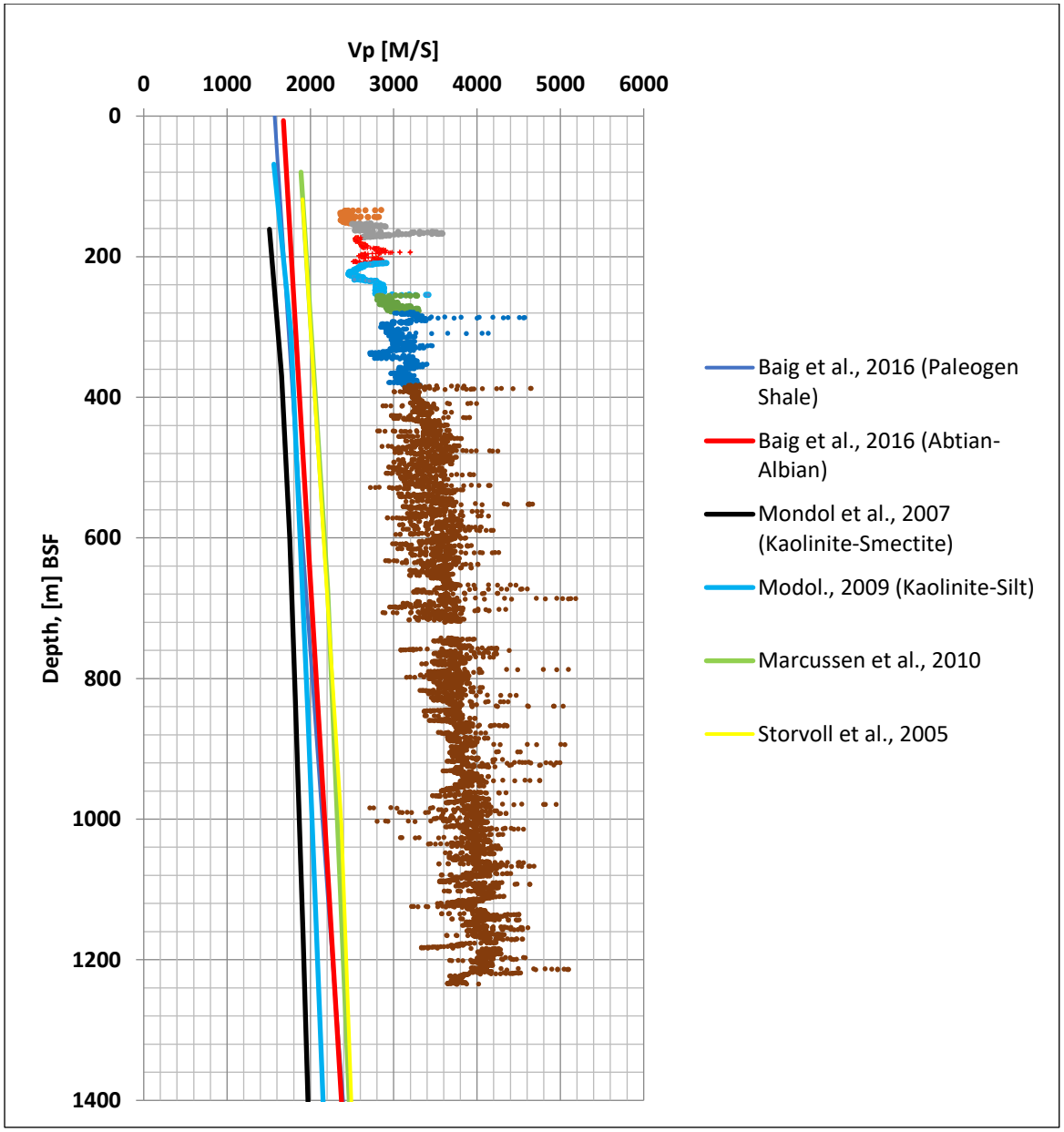

Figure 6.7: Transition zone and uplift estimation for the well 7324/7-2.Transition zone estimation was performed using the velocity data while uplift estimations were performed for data points that were considered to represent shale.

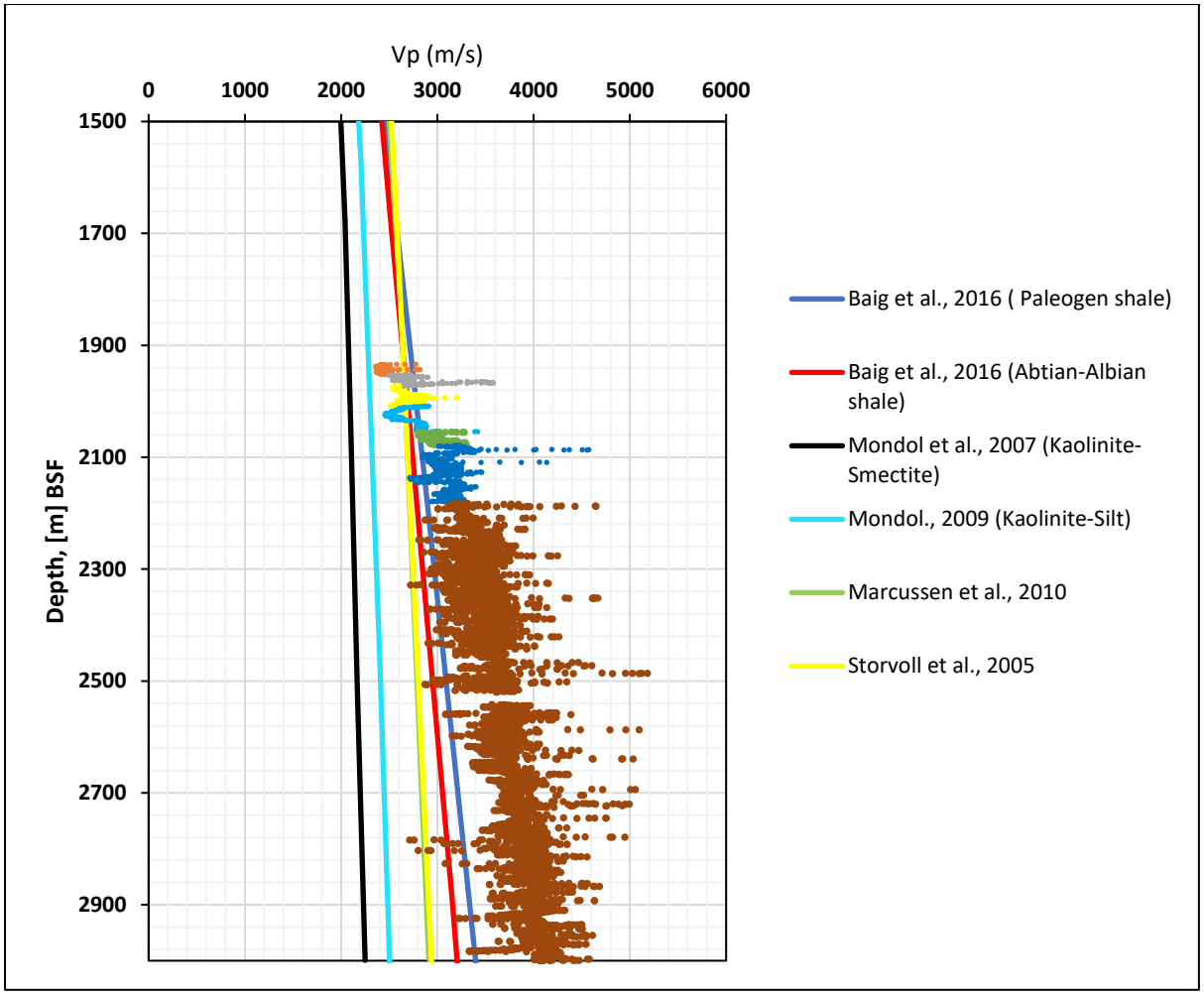

Figure 6.8: Vp/depth plot, experimental compaction curves after (Storvoll et al., 2005), (Mondol et al., 2007);(Mondol, 2009); (Marcussen et al., 2010)) and (Baig et al., 2016) for the well 7324/7-2. The total exhumation in well 7324/7-2 was estimated to 1800 m based on comparing with the experimental compaction curve of Paleogene shales and Aptian-Albian shales published by (Baig et al., 2016).

As mentioned earlier, the chemical compaction in well 7324/7-2 started at a temperature around 76^0c (Figure 6.9). The result of uplift estimation along with the calculated geothermal gradient of the well 7324/7-2 and 7321/9-1 were used to predict the maximal burial depth. The results are presented in Table 6.2.

Based on the results it could be concluded that the Hoop area and Fingerdjupet Sub-Basin have been subjected to significant uplift and erosion and Stø Formation reservoir was buried much deeper than at which it is presently found.

Table 6.2: Approximate uplift by comparison with the compaction curve by Baig et al. (2016). Geothermal gradient calculated using bottom hole temperature.

Well	Uplift estimation [m]	Geothermal gradient [°C]	Maximal Burial depth (m) of Stø Formation	Temperature at Maximal burial depth(^{0}c)
7324/7-2	1800	37.25	2060-2090	80^{0}C
7321/9-1	1600	30.36	2495-2635	80^{0}C

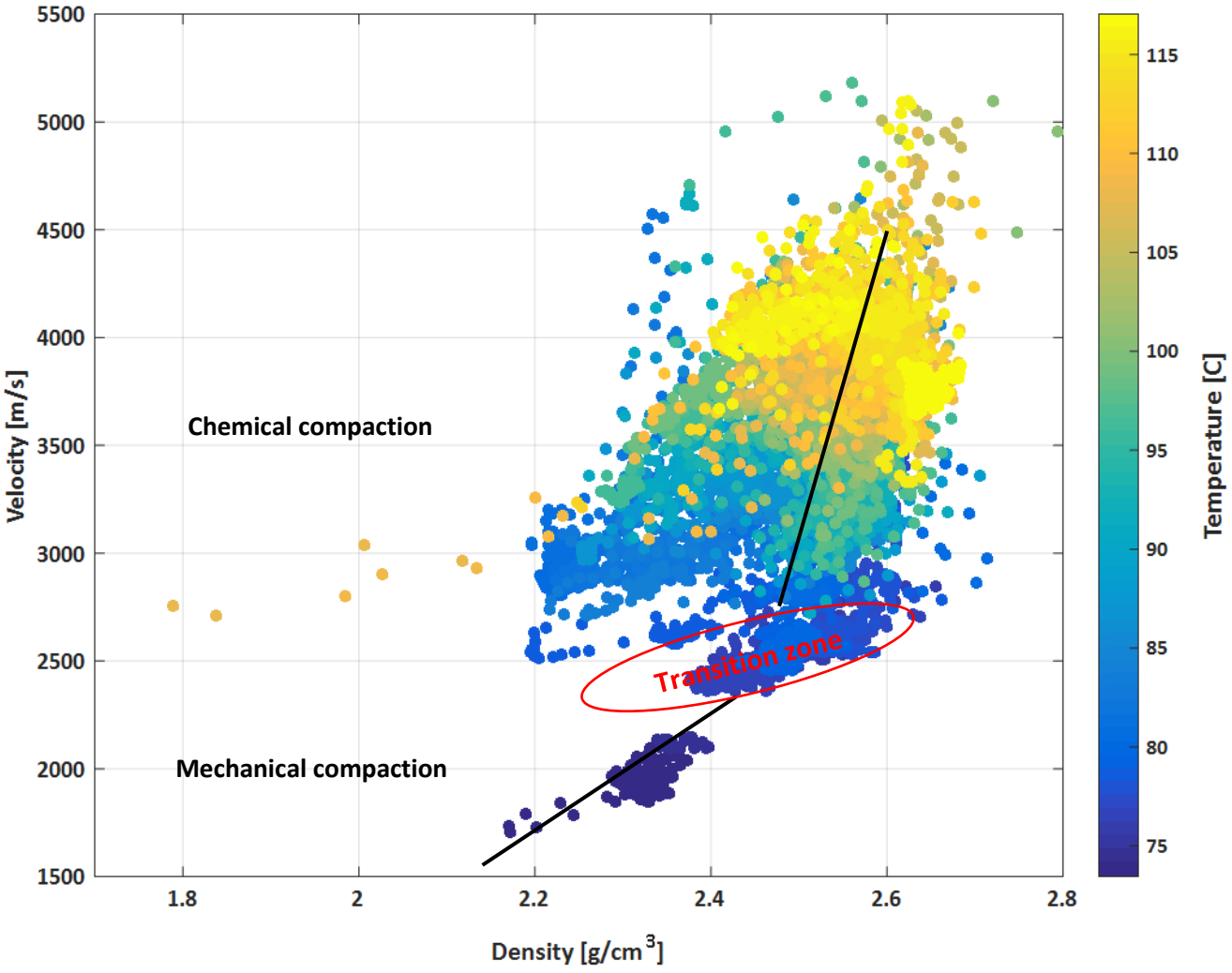

Figure 6.9: Velocity/density cross plot along with temperature variation shows a higher temperature at greater burial depths compares to shallower intervals. In well 7324/7-2 the onset of chemical compaction regime is registered at temperatures around 76^{0}C.

6.7 Porosity Estimation in Stø Formation

In well 7324/7-2 the porosity was calculated for Stø Formation using the following methods, and the result are shown in table 6.3 and Figure 6.10.

- Density Porosity
- Porosity from Neutron-Density Combination

Table 6.3: Average formation porosities, estimated using the various methods. Φ_D-Simple density porosity (assumes matrix density of 2.65 g/cm3 and fluid density of 1.025 g/cm3); Φ_N- neutron porosity reading; Φ_{ND}- porosity from the neutron-density combination.

well	Formation	Φ_D	Φ_N	Φ_{ND}
7324/7-2	Stø	24 %	20%	22%

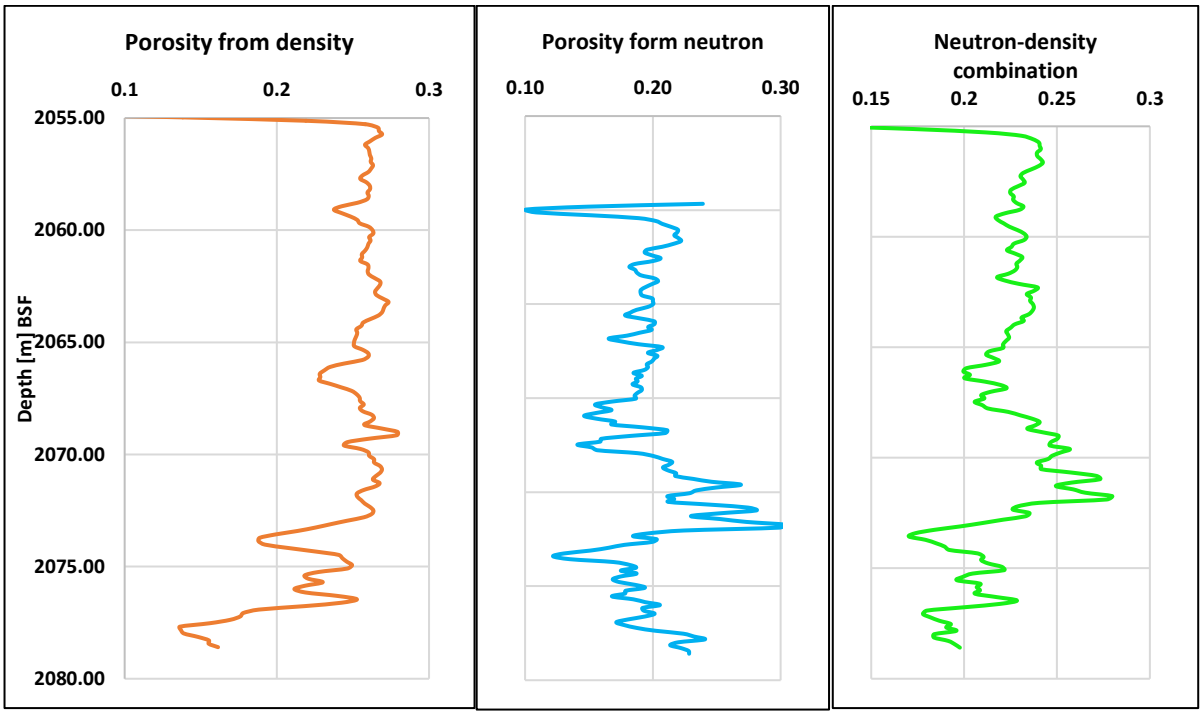

Figure 6.10: Porosity/depth distribution derived from log density, neutron porosity and combination neutron-density in Stø Formation. As is evident from the plots the Neutron-density combination suggests a more accurate value for porosity compare to porosity values derived *from density and neutron logs.*

6.8 Net-to-Gross Ratio and Petrophysical Cut-offs

'Petrophysical cutoffs' are simply limiting values used in expressing the NTG ratio (Worthington, 2005). In this study, the proposed cut-off values by Worthington (2005) has been used in order to determine the petrophysical cut-offs in well 7324/7-2 (Table 6.4). The Net properties and three petrophysical cut- offs such as shale volume V_{sh} cut-off, porosity Φ cut-off, and water saturation (Sw) cut-off have been determined through three steps and have been discussed in following sections:

Table 6.4: Table shows the cut-off values proposed by (Worthington, 2005) for calculating hydrocarbons in place for sandstones.

Lithology	Cut-off parameter	Range of values
Sandstones	V_{sh}	0.3 - 0.5
	Φ	0.06 – 0.08
	S_w	0.5 – 0.6

6.8.1 First Step: Determining the Net Sand Cut off for Stø Formation

The net sand cut-off has been determined based on shale volume with cut off value 30%. The cut-off is applied to the values above the V_{sh} cut-off (30%). This means that all values above this threshold could economically not be profitable for hydrocarbon extraction. V_{sh} versus Φ cross plot represents the core plug samples for both wells which are being studied. According to the cross plot it can be observed that almost all the samples are below the V_{SH} threshold. However, two samples of the well 7324/7-2 represent shale volume between 48 and 60%. (Figure 6.11).

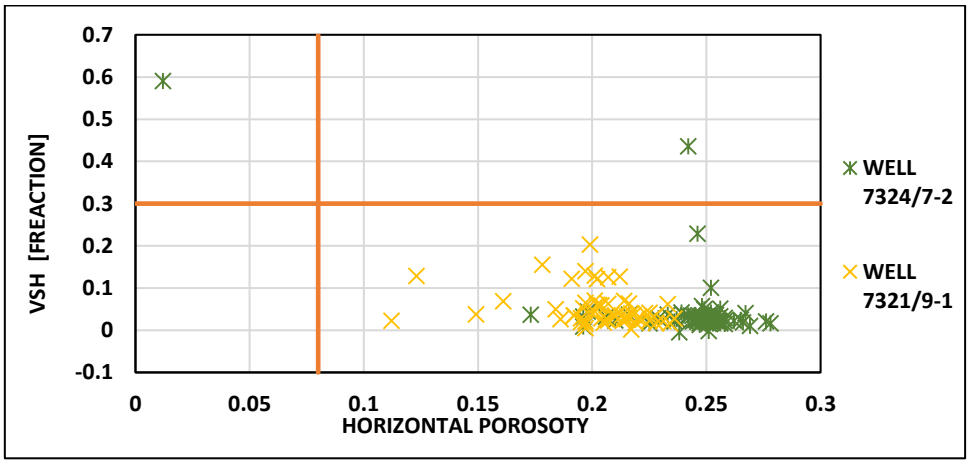

Figure 6.11: V_{sh} versus Pc cross plot represents all the core plug samples for the well 7324/7-2 and 7321/9-1. In this case the V_{sh} cut-off has been set to 30%, which captures more than 90% of the hydrocarbon and Samples with V_{sh}> V_{sh} cut-off is rejected since there is no reservoir containing both hydrocarbons and more than 50% V_{sh}.

6.8.2 Second Step: Determining Net Reservoir Cut-off for Stø Formation

The net reservoir cut-off is usually defined in terms of log-derived fractional porosity being greater than or equal to porosity cut-off value (P_c) (Worthington, 2005). Permeability versus porosity cut-off cross plot (Figure 6.12) is used to identify the best value for P_c and consequently to determine the reservoir quality of Stø Formation in both wells. The minimum P_c value in this study has been set to 8% (Worthington, 2005) (Table 6.4). Based on the permeability/porosity cross plot, the fair reservoir quality, good reservoir quality and very good reservoir quality have been identified (Figure 6.12). From the Figure 6.12, it could be assumed that the reservoir quality in well 7324/7-2 is very good owing to very good porosity as well as permeability while in well 7321/9-1 the reservoir quality varies from fair to good. The reservoir quality of Stø Formation in well 7324/7-2 and 7321/9-1 has also been discussed based on matrix content and intergranular volume (IGV). Figure 6.13 demonstrates the reservoir quality versus matrix content. High matrix content corresponds to poor permeability, and consequently lower reservoir quality in well 7321/9-1 compare to well 7324/7-2. The lowest amount of the matrix has been observed in the samples of the well 7324/7-2. Although, some samples of the well 7321/9-1 contain minor amounts of the matrix (less than 5%) but still demonstrate poor reservoir quality which is due to carbonate cementation. Figure 6.14 shows the reservoir quality versus IGV. IGV varies between 10 to more than 20 % within the samples of the well 7324/7-2 whereas in well 7321/9-1 most of the samples comprise less than 5 to 20% IGV. Presence of cement corresponds to poor permeability and high IGV in few samples of Stø Formation in well 7321/9-1.

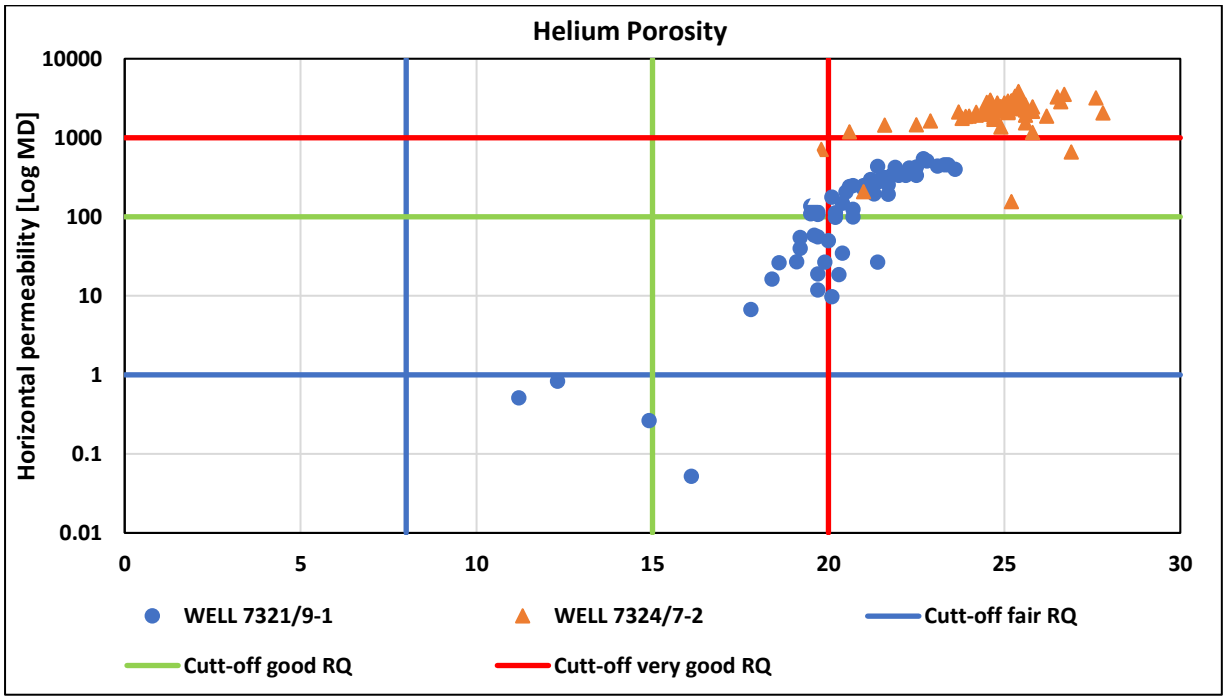

Figure 6.12: Horizontal permeability/Helium porosity cross plot represent all the core plug data belonging to wells which are being studied. The results suggest a very good reservoir quality for the 7324/7-2 and fair- good for the 7321/9-1.

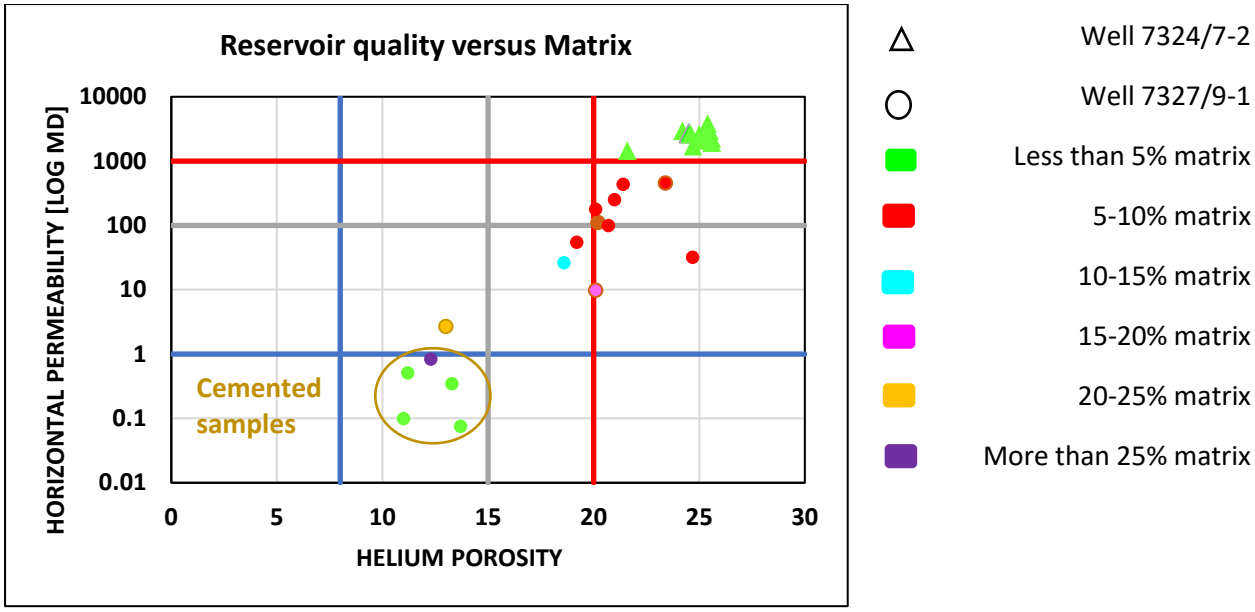

Figure 6.13: Reservoir quality versus Matrix for the wells 7324/7-2 and 7321/9-1.

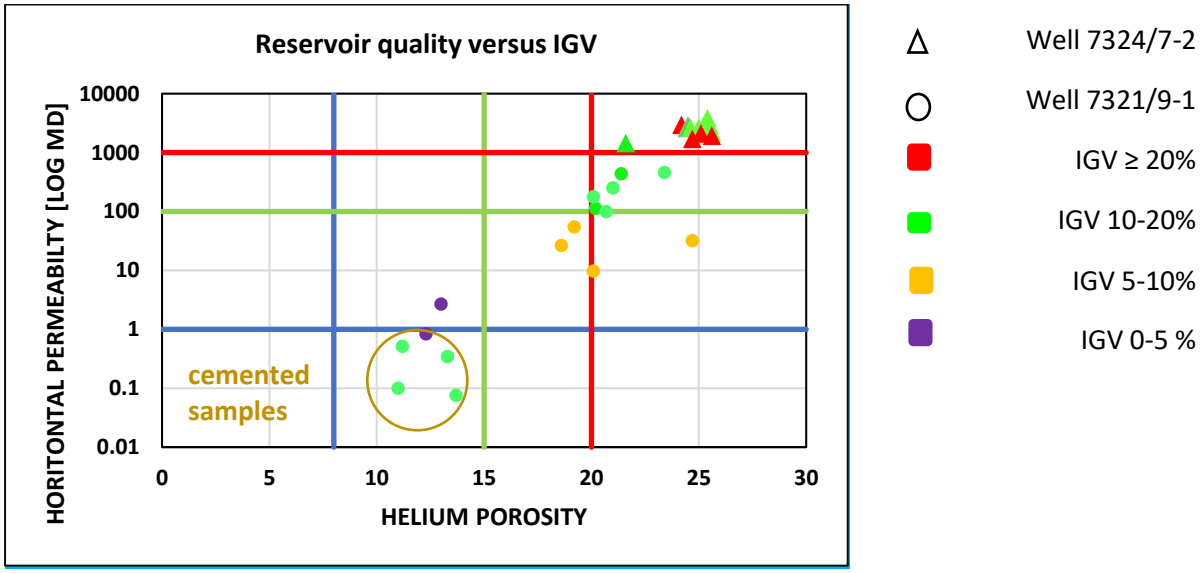

Figure 6.14: Reservoir quality versus intergranular volume for the wells 7324/7-2 and 7321/9-1.

6.8.3 Third Step: Determining Net Pay Reservoir Cut-off for Stø Formation

Net pay is commonly defined by log derived water saturation cut-off (S_w=1-Sh) (Worthington, 2005). Water saturation/helium porosity cross plot is used to determine the S_w Cut-off value (Figure 6.15). In this study, the S_w Cut-off has been defined based on the values which proposed by (Worthington, 2005). After calculating the $V_{sh,}$ and porosity cut-off then the S_w cut-off has been applied and only those samples with ($V_{sh,} \leq V_{sh}$ Cut-off) and (PHIE ≥ $PHIE_C$) and ($S_w < S_w$ Cut-off) has been accepted. From the Figure 6.15, it is evident that all the samples of the well 7324/7-2 have the water saturation below the defined S_w cut-off (50%), whereas almost half of the samples of the well 7321/9-1 are above this threshold and comprise of more than 50% water. The result of petrophysical cut-off of Stø Formation is presented in (Table 6.5).

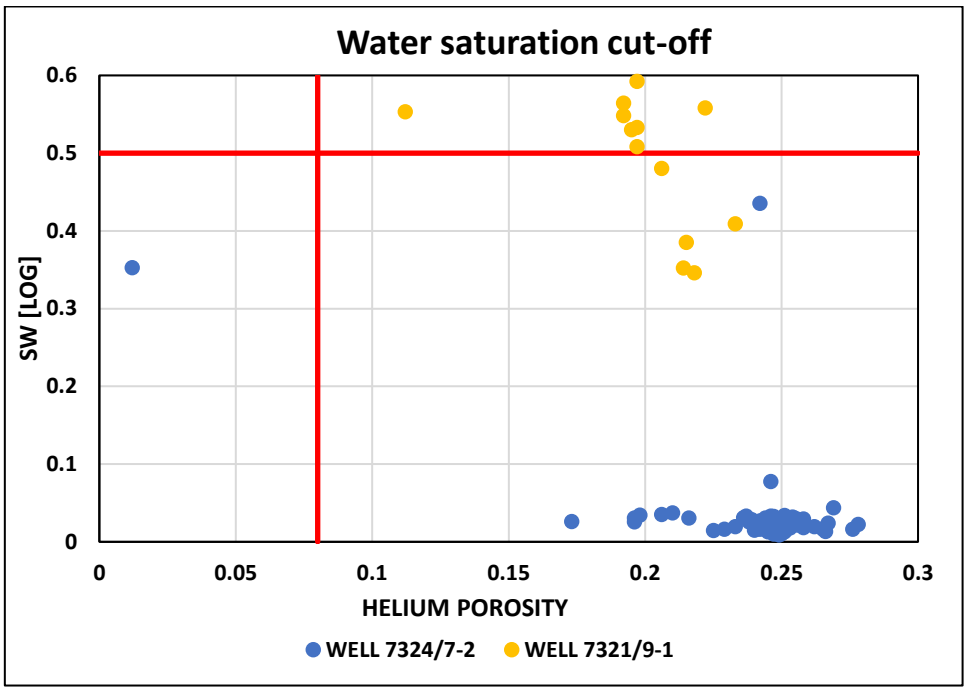

Figure 6.15: water saturation cut-off for well 7324/7-2 and 7321/9-1.

Table 6.5 show Various net-to-gross fractions for Stø Formation.

Well	Formation	Gross	Net sand	Net reservoir	Net pay	N_s/G	N_R/G	N_p/G
7324/7-2	Stø	158	152	155	154	0.96	0.98	0.97
7321/9-1	Stø	263	263	------	-----	1	-----	-----

Chapter 7: Discussion

7.1 Introduction

Condensed coarse conglomerates have occurred at the base of the Jurassic transgressive shelf succession. This condensed section has also been found at the transition from Jurassic Stø Formation to the unconformable overlying Fuglen Formation in wells 7324/7-2 (Hanssen) in Hoop area and 7321/9-1 in Fingerjupt Sub-basin in the southwestern Barents Sea. This event is also visible at the boundary between Wilhelmøya Subgroup and Brentskardhaugen on Svalbard, indicating a regional influence.

This chapter aims to discuss:

Firstly the depositional environment of Stø Formation, secondly the diagenetic evolution and reservoir quality of Stø Formation through the sedimentological, petrographical and petrophysical analysis and third, the transgression event which led to deposition of condensed coarse conglomerates at the top of the formation.

A precise prediction of the reservoir quality would be more likely if the processes that affect the sandstone parameters are well understood (Bjørlykke, 2010). Porosity and permeability are the most important reservoir properties which in turn are function of provenance, climate, erosion, transport, deposition, and burial diagenesis (Reading, 1996). The results of the sedimentological, petrographical and petrophysical analyses are discussed in chronological order from the provenance area to deep burial, in order to interpret the geological evolution that has prompted the current observations.

7.2 Stø Formation

7.2.1 Climate, Provenance and Depositional Environment

The mineral distribution classifies the Jurassic Stø sandstones in the studied wells as Quartz arenites, Sublithic arenites and Lithic arenites (Figure 7.1). The framework mineralogy of Stø Formation in both wells comprises of predominantly quartz. However, the high content of rock fragments in well 7321/9-1 classify some of the Jurassic sandstones as Sublithic arenites. The difference in petrographic characteristics of Stø Formation in the two wells could be related to the different geographical position of the wells. The results of petrographic analysis suggest moderately to well sorted, mineralogically mature sandstones composition for Stø Formation. This maturation could be related to paleoclimate, provenance and depositional environment which are critical factors, affecting the sandstone composition. Based on the review of the previous works which were presented in chapter 1 of this thesis it was concluded that:

- Humid climate (more considerable annual precipitation), hinterland rejuvenation and reduction in the rate of subsidence during the Jurassic likely explain the increase in grain size and relative quartz content of Early Jurassic delta plain deposits with respect to the Late Triassic units in the Barents Sea.

- In such a setting, the increase in precipitation caused elevation of the groundwater table and subsequently increase in meteoric water flow rate, therefor more pronounced mineral dissolution and leaching of feldspar (Bergan and Knarud, 1993).

- The provenance signature of the samples of Wilhelmøya Formation (equivalent to Stø Formation), suggest mixing of zircons ages from: 1) Early and Middle Triassic, indicating a western Laurentian (North Greenland source) and 2) Late Triassic, indicating eastern sources Uralian Orogeny (Bue and Andresen, 2014).

- Stø Formation sediments are interpreted to reflect reworking of older Mesozoic sediments, potentially together with the renewed input of the sediments from the west (northern Greenland).

- The increase in the maturity of the sandstones during the Late Triassic to Early Jurassic, could be related to the extensive reworking of the sediments caused by regional transgression during this time.

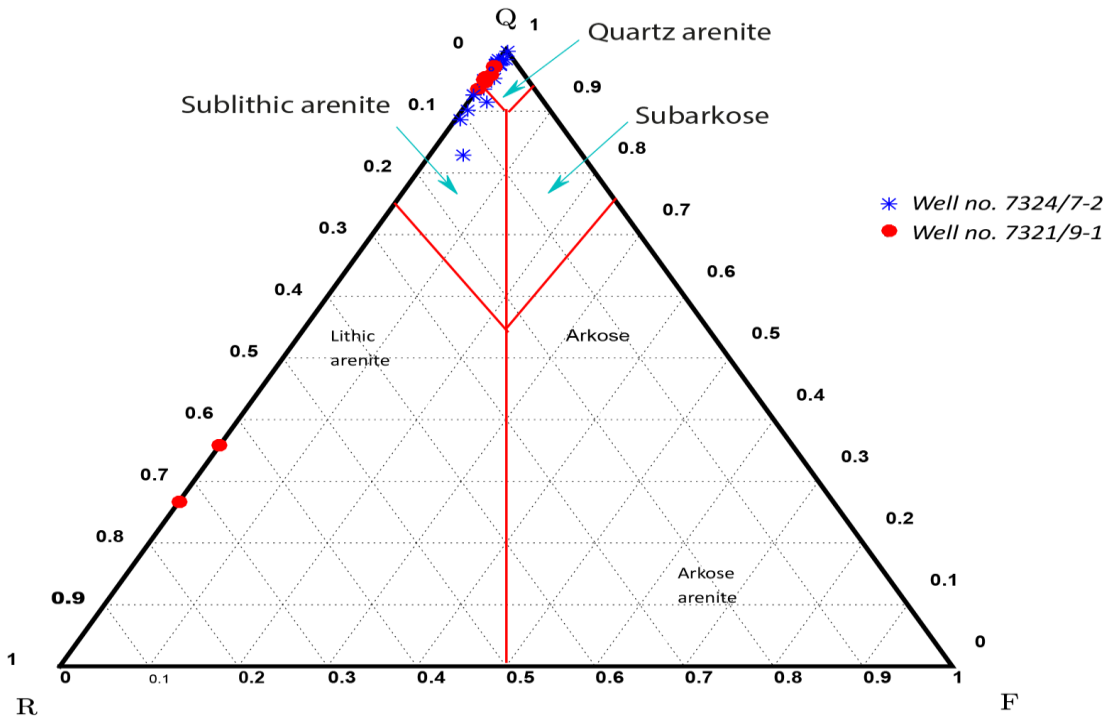

Figure 7.1: *The QRF-diagram shows the mineral classification of Stø Formation in well 7324/7-2 and 7321/9-1.*

7.2.2 Depositional environment

Aims and objectives of this section are to discuss the depositional environment and related processes of Stø Formation in Hoop area and Fingerdjupt Sub-basin based on newly defined facies.

7.2.2.1 Facies F-1: Floodplain

Interpretation: Facies F-1 was formed in a floodplain environment. Fine-grained material such as silt and clay indicate suspension fall-out under low-energy conditions. Thin layers of current ripple cross laminated and planar-parallel lamination of very fine-grained sandstone indicate high-velocity flooding events during which the water spreads out from the main channel over the floodplain areas (Buatois et al., 2012, Nichols, 2009). Reduction in flow velocity led to the formation of current ripples and climbing ripples, indicating equilibrium between the rate of sedimentation and ripple migration (Nichols, 2009). The absence of marine trace fossils and other tidal characteristics indicate deposition above the tidal limit, in subaerial delta plain (Li et al., 2011). This interpretation is also supported by the presence of terrestrially derived palynomorphs and the absence of marine plankton (Buatois et al., 2012) (Figure 7.2 and 7.3).

7.2.2.2 Facies F-2: Channel base

"Erosive bases and fining-upward trends are the most obvious characteristics of channel deposits" (Buatois et al., 2012). The occurrence of conglomerate lags, planar and through cross-stratification, suggest a high energy environment and uni-directional flow regimes which caused rapid deposition of the sediments and consequently formation of these sedimentary structures (Reading, 1996, Fielding, 2006). Planar cross-stratification within the unit indicates the migration of two-dimensional dunes whereas through cross-stratification implies migration of three-dimensional dunes. Migration of three-dimensional dunes without separation at the dune crests resulted in the formation of trough cross stratification in uni-directional flow regimes (Reading, 1996, Fielding, 2006). Trough cross bedding structures probably formed in the central parts of the channel where the flow energy is high enough for the formation of subaqueous dunes and consequently the development of trough or planar cross bedding within the succession (Nichols, 2009). The lower parts of this unit comprised of coal pieces and mud-rock fragments which probably derived from erosion of facies F-1. This succession represents channel base deposits (Figure 7.2 and 7.3).

7.2.2.3 Facies F-3: Channel fill

The relatively coarse nature of the sandstones together with the presence of primary sedimentary structures, such as cross-lamination and abundant mudstone drapes suggest deposition in high energy conditions in a channelized setting (Collinson, 1969). Cross-lamination sedimentary structures suggest deposition in the inner bank where the flow is slower and caused development of ripples in the finer sand, producing cross lamination (Allen, 1970). This succession exhibits a graduation from coarser material at the base, to finer at the top, indicating a fining upward trend which is a characteristic of point bar deposits of a meandering river (Nichols, 2009).The facies association is interpreted as channel fill deposits. The occurrence of thin layers of mud drapes and erosional surfaces between sandstone units indicate periods of non-deposition on point bar which are known as lateral accretion surfaces or epsilon cross-stratification. This is interpreted as the product of meandering river (Allen, 1965, Nichols, 2009). Furthermore, erosional surfaces indicate strong flood events, during which water flowed over the bank streams toward the next bend and eroding the channel. Deposition in a high energy fluvial setting is inferred for this succession. Well-defined fining upward channel fill successions and lack of marine influence in this unit indicate deposition in upper delta plain environment and meandering is the dominant channel pattern (Elliott, 1976, Cherven, 1978, Fielding, 1987, Miall, 1985)(Figure 7.2 and 7.3).

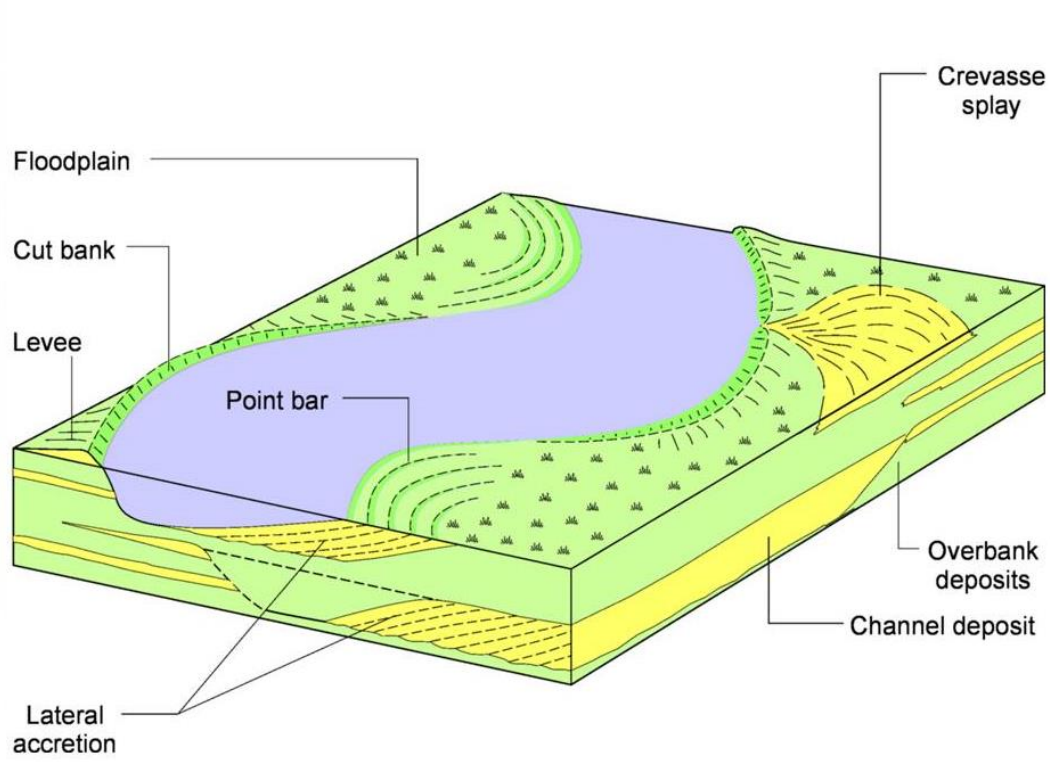

Figure 7.2: Main morphological feature of a meandering river (Nichols, 2009).

7.2.2.4 Facies Association-1 Fluvial channel: Facies F-1, F-2 and F-3

The observed sedimentary structures within the facies F-1, F-2, and F-3 suggest deposition in a meandering system. The occurrence of conglomerate lags, planar and through cross-stratification within Facies-2, suggest deposition in a high-energy environment such as central parts of the channel. Flow velocity is significantly high in the central parts of the channel and causes formation of subaqueous dunes and consequently led to development of observed sedimentary structures.

The lower parts of this unit has comprised of several pieces of coal and mud-rock fragments which probably derived from the facies F-1. Facies F-3 interpreted as the channel fill deposits in the inner bank where the flow is slow enough for formation cross lamination sedimentary structure. The well-defined fining upward trend of the facies F-1, F-2, F-3, and presence of sedimentary structures such as planar/through cross-stratification, cross-lamination, epsilon cross-stratification and lack of marine influence indicate deposition in a meandering river in upper delta plain environments (Elliott, 1976, Cherven, 1978, Fielding, 1987, Miall, 1985). Based on the sedimentological observations facies association-1 has been interpreted as a fluvial channel (Figure 7.3).

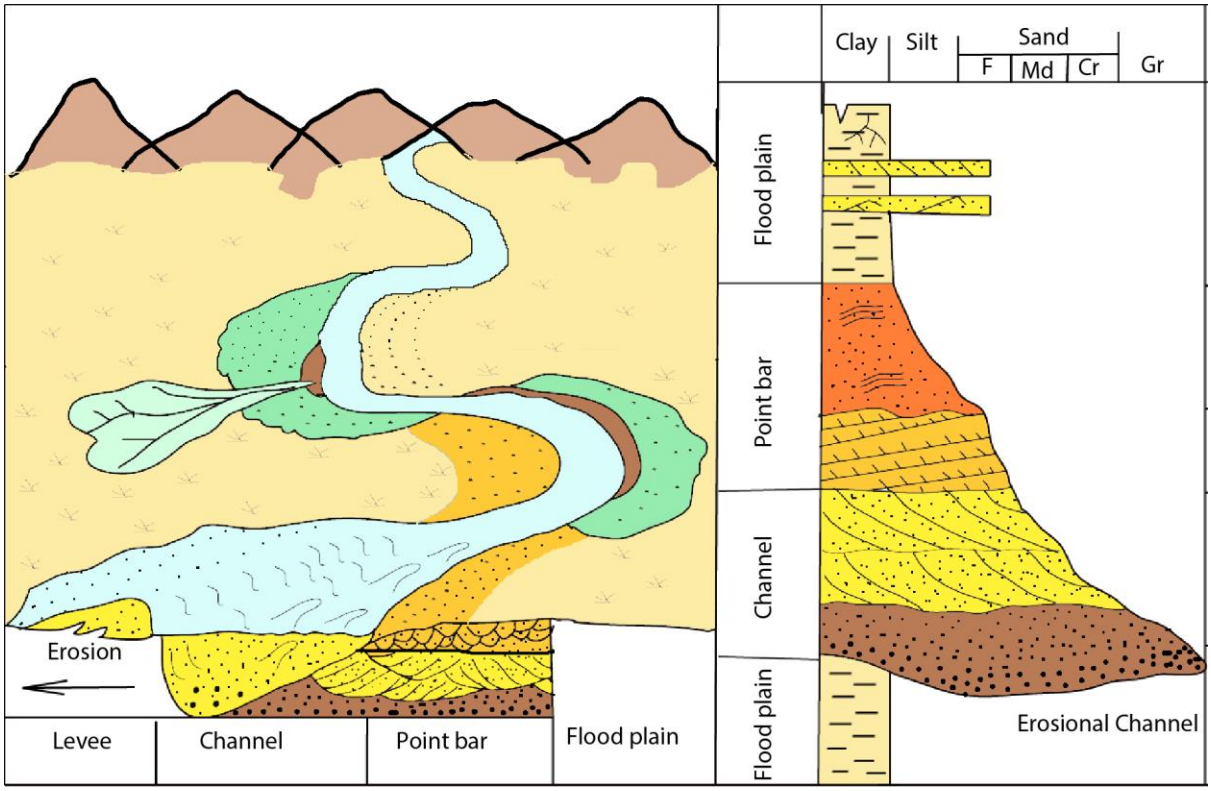

Figure 7.3: Figure illustrates the typical meandering facies sequence and facies association-1. The figure is drawn by author and inspired by Miall, Andrew D., (1982).

7.2.2.5 Facies F-4: Upper delta plain

The distribution and characteristics of the sedimentary structures within the facies F-4 suggest an upper delta plain setting. Upper delta plain deposits of facies F-4 consists levee, overbank and crevasse splays. Fine-grained sandstone with interbedded claystone and siltstone which are commonly structureless are interpreted as channel-levee deposits indicating occasional flooding events. Also, the relatively coarse-grain sandstone units in the upper part of the succession with primary sedimentary structures such as current-ripple lamination, trough and planar parallel stratification containing coal layers and clay stringers have been interpreted as crevasse splay deposits which formed during high-energy flooding events (Elliott, 1974, Fielding, 1984, Fielding, 1986). Siderite nodules are commonly observed in conjunction with abundant clay stringers, plant stems. These nodules were scattered through the siltstone layers of levee deposits and have been interpreted as the overbank deposits. Based on the above interpretation and also absence of tidal influence indicators and marine trace fossils it is interpreted that this unit deposited above the tide limit, in upper delta plain (Buatois et al., 2012).

7.2.2.6 Facies F-5: Minor distributary channel

Minor distributary channel deposits of facies F-5 are interpreted to have formed as a result of channel bank-breaching of main distributaries, followed by prolonged flooding events (Fielding, 1986). These processes formed a permanent crevasse channel and transported sediments across the interdistributary area over previously deposited crevasse splay toward the delta front. The chaotic appearance of the sandstone units of facies F-5 indicates rapid sediment discharge, as a result of high-energy flows. Such flows were capable of carrying and entering a large amount of plant stems, peat, and clay from channel banks to the channel. The interbedded nature of the channel deposits suggests that the discharge was variable during the time (Elliott, 1974, Fielding, 1986). Occasional coarse-grained sandstones and siderite clast are interpreted as overbank deposits which were deposited during periods of flood stage (Figure 7.4).

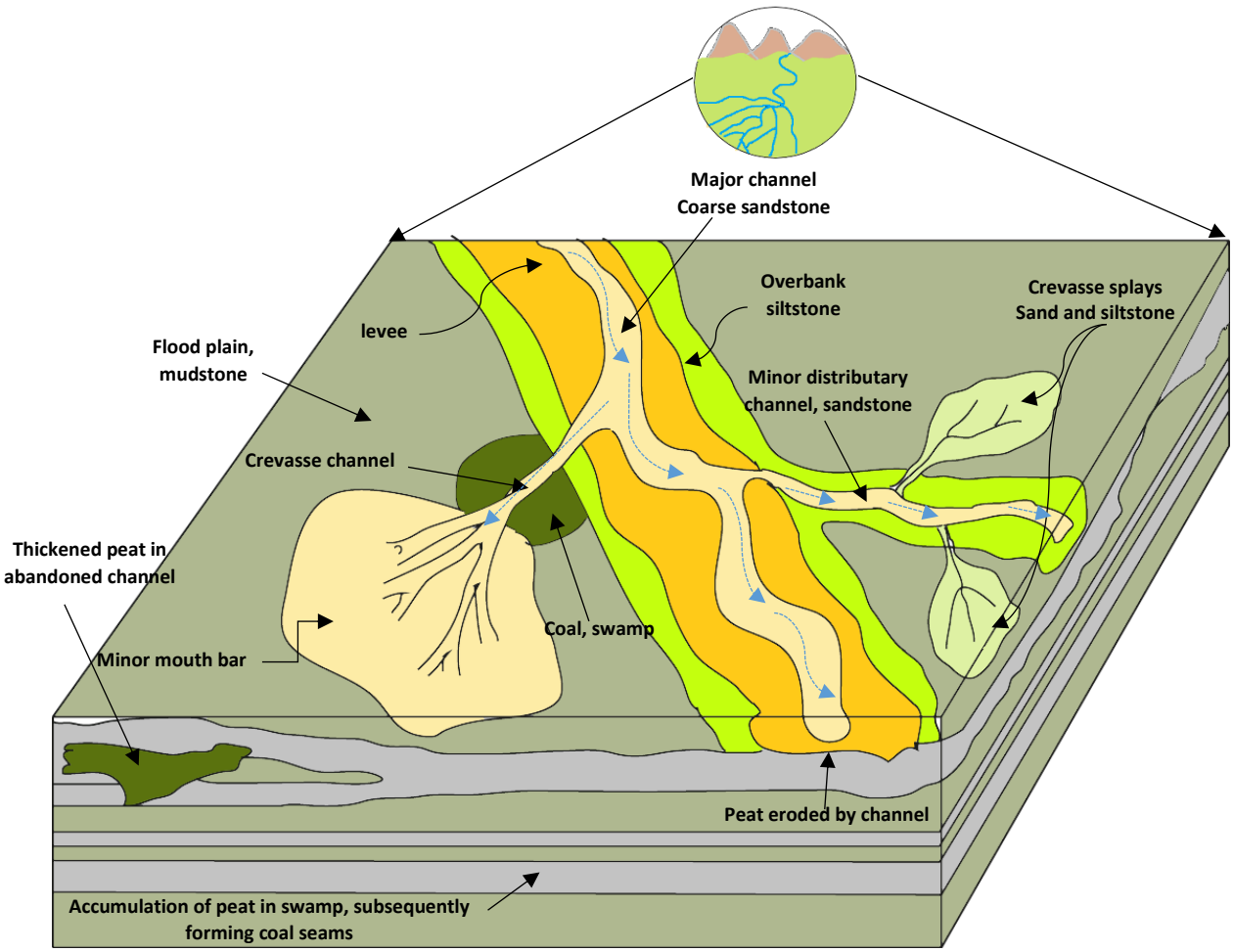

Figure 7.4: Schematic illustration of facies variation in upper delta plain depositional environment. The figure is drawn by author and inspired by Guion et al., (1995).

7.2.2.7 Facies Association-1 delta Palin, facies F-4 and F-5

A delta is regarded as a river-dominated delta where the effect of tide and wave are minor (Nichols, 2009). A river-dominated delta is also controlled by fluvial processes of transport and sedimentation. A characteristic feature of these deltas is channel instability which leads to frequent avulsion of the major and minor channels. These newly formed channels are called distributary channels, leaving the formal channel, its levees, and overbank deposits behind. A river-dominated delta has a well-developed delta plain facies, consisting of channels and overbank sediments. Presence of siderite nodules, plant stems, and abundant clay stringers in faceis F-4 indicate deposition in the overbank areas of a delta plain which is the site of sedimentation from the suspended load during the flooding events. The existence of coal, peat and high amount of clay stringers within this intervals suggest growth and vegetation under appropriate climate conditions in a hot/wet tropical region, resulted in a formation of peat and eventually coal within the sediments (Nichols, 2009). Accumulation of the sand close to the channel edge leads to the development of the levee which is a site of fine grain and suspended load deposition.Thus, fine-grained sandstone with interbedded claystone and siltstone deposits of the facies F-4 could be interpreted as channel-levee deposits, indicating occasional flooding events.

The relatively coarse-grain sandstone interval in the upper part of the succession which shows the coarsening upward trend is interpreted as crevasse splay deposits.

The crevasse splay deposits in facies F-4 includes sedimentary structures such as current-ripple lamination, trough and planar parallel stratification containing coal layers and clay stringers which accumulated during high-energy flooding events (Elliott, 1974, Fielding, 1984, Fielding, 1986, Elliott, 1986). Facies F-5 is interpreted as minor distributary channel which developed as result of avulsion of major channel, followed by prolonged flooding events. The difference in petrographic characteristics of Stø Formation in the two wells could be related to the different geographical position of the wells. The newly defined facies model for Stø formation in wells 7324/7-2 and 7321/9-1 has been used in order to produce a facies distribution map (Figure 7.5). As discussed in the previous section, Stø Formation in well 7324/7-2 was deposited in a fluvial system and comprises of relatively coarser grained sand, indicating deposition in proximal part relative to the main channel, while in well 7321/9-1 Stø Formation comprises of very fine to fine sand and suggest deposition in a distal position relative to the main channel probably in minor distributary channel where the energy of the flow decreases significantly. Absence of marine trace fossils and indicators of tidal influence within the facies of Stø Formation also suggest deposition above the tide limit, in upper delta plain environment (Buatois et al., 2012).

Figure 7.5 demonstrates the approximate position of the wells. The significant difference in petrographic characteristics of Stø Formation in two wells could be related to the supply of the sediment from different sources. Geographic position of the well 7321/9-1 is close to Loppa High. Loppa high during the Early to Middle Triassic mostly comprised of very fine to fine sand similar to those which have been observed in Stø Formation intervals in

Fingerdjupet Sub-Basin (well 7321/9-1). Loppa High was uplifted and eroded during the Jurassic time. Thus, the eroded sediments from the Loppa High have been deposited in Stø Formation to a great extent. Stø Formation comprises of coarser grain size particles in well 7324/7-2 which is located further north. It is difficult to specify the exact source of the sandstones of Stø Formation in Hanssen. However, the erosion of Maud basin and Mercurhigh high at the time of deposition could be considered as another possible source of the sediments.

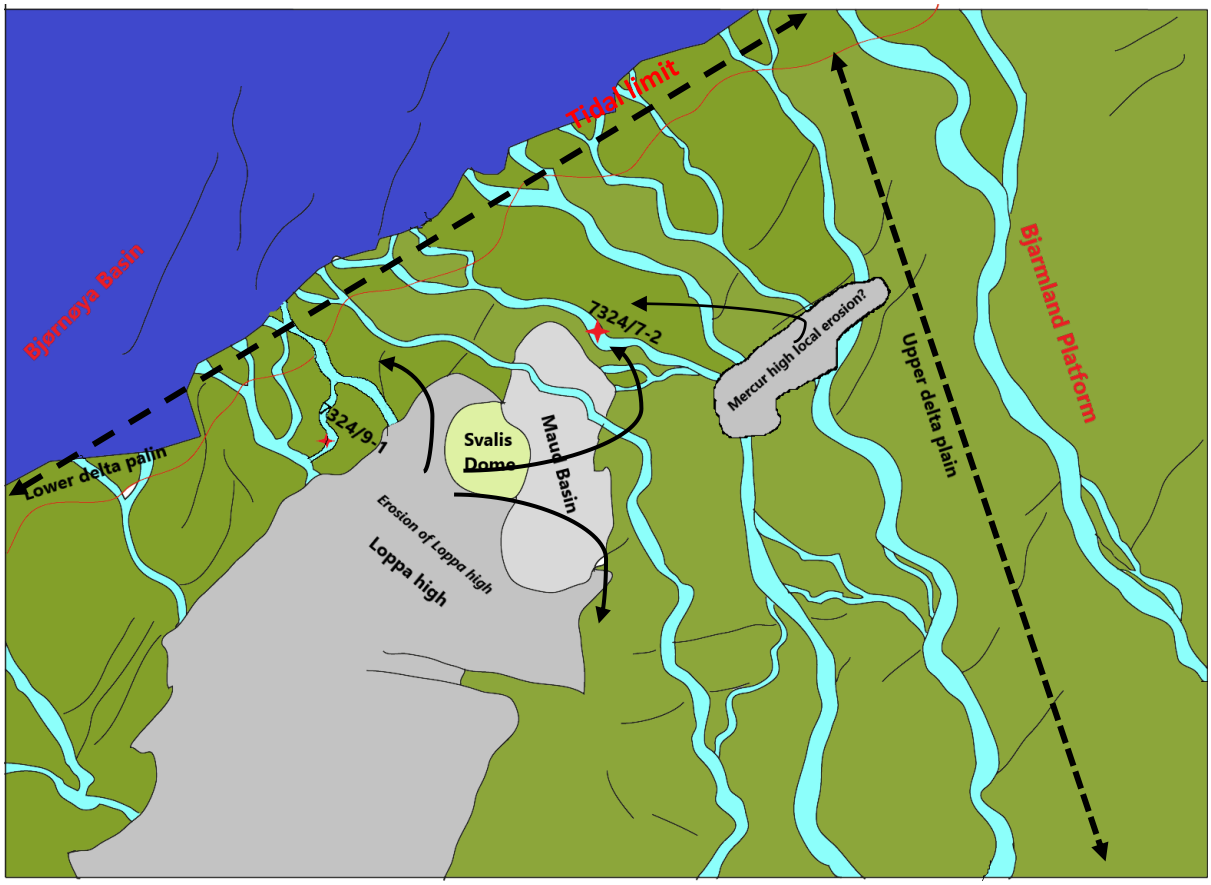

Figure 7.5: Facies distribution map of the wells 7324/7-2 and 7321/9-1 based on the newly defined facies model for Stø Formation.

7.2.3 Diagenetic evolution

7.2.3.1 Uplift estimation

Maximal burial depth in Hoop Fault complex and Fingerdjupet Sub-Basin is estimated around 1800m and 1600m, respectively. The estimated uplift in Hoop Fault complex and Fingerdjupet Sub-Basin corresponds to an approximate maximum burial depth of 2.06 km in well 7324/7-2 and 2.5 km in well 7321/9-1. The maximal burial depth (m) of Stø Formation is estimated between 2060-2090 m [MD]. Due to lack of petrophysical data for the well 7231/9-1, the exhumation estimate maps from the Barents Sea provided by Baig et al. (2016) has been used in order to estimate the amount of uplift for this well (Figure 7.6). The geothermal gradient in this study is calculated using the recorded bottom hole temperature of the wells and is

equivalent to 37.25^{0}C for Hanssen (7324/7-2) and 30.36^{0}C for Fingerdjupet Sub-Basin (7321/9-1). The result of uplift estimation along with the calculated geothermal gradient of the well 7324/7-2 and 7321/9-1 were used to predict the maximal burial depth and temperatures. The maximal temperature for both well is calculated 80^{0}C. The results are presented in Table 7.1. Based on the results it could be concluded that the Hoop Fault complex area and Fingerdjupet Sub-Basin have been subjected to significant uplift and erosion and Stø Formation reservoir was buried much deeper than at which it is presently found. Temperature reactions such as quartz cementation which initiates in temperatures above 70 ^{0}C and Kaolinite to dickite transformation (90^{0}C) have been considered in order to improve our understanding about the minimum temperatures at which sediments are sustained. Presence of small amount of quartz cement (0% to 3.5 % in all facies) in Stø Formation could be related to the duration of exposure to temperatures at which quartz cementation initiated (quartz cementation window). From the uplift estimation results, it is evident that Stø Formation intervals were exposed to the temperature of 80 ^{0}C for a short time and then uplifted, and thus the time for quartz cementation was probably very short resulted in the precipitation of considerably less amount of quartz cement within these intervals. Also, the amounts of quartz cement might be underestimated due to difficulties in differentiating detrital quartz cement from quartz grains during point counting analysis.

Table 7.1: Estimated uplift, Geothermal gradient, maximal burial depth and temperatures for the well 7324/7-2 for wells 7324/7-2 and 7321/79-1. Uplift has been estimated using the selected reference literature.

Well	Location	Uplift estimate [m]	Geothermal gradient [°C]	Maximal Burial depth (m) of Stø Formation	Temperature at Maximal burial depth(^{0}c)	Baig et al. (2016) (Estimated uplift in meters)
7324/7-2 **7321/9-1**	**Hoop Fault** **Fingerdjupet Sub-Basin**	**1800** **1600**	**37.25** **30.36**	**2060-2090** **2495-2635**	**80 ^{0}C** **80 ^{0}C**	**1750-2000** **1500-1900**

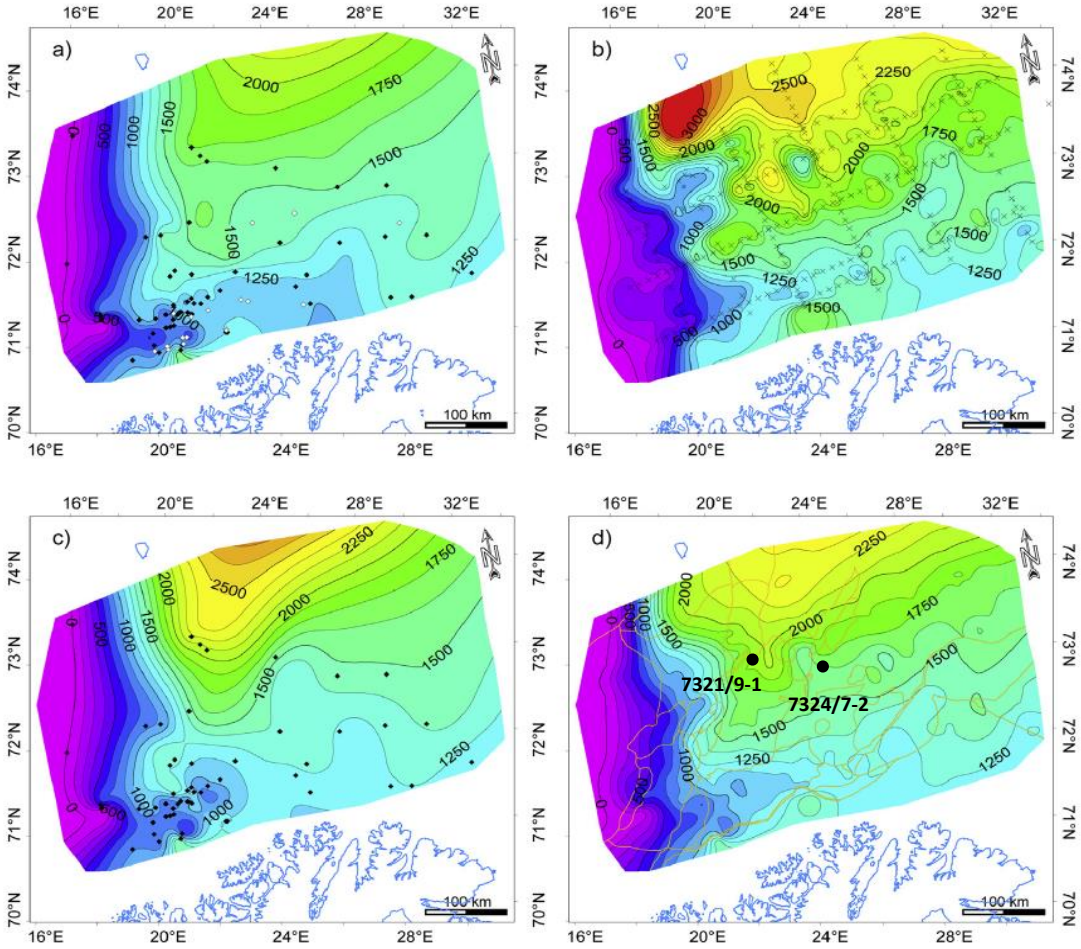

Figure 7.6: The net exhumation estimate maps a) from the sonic log, b) from shot gathers, c) from vitrinite reflectance and d) the arithmetic average net exhumation map of Southwestern Barents sea, modified figure after (Baig et al., 2016). The black circles show the approximate position of Hanssen (7324/7-2) and Fingerdjupet Sub-Basin (7321/9-1).

7.2.3.2 Early Diagenesis

Early diagenesis of sandstones usually occurs immediately after deposition of the sediments at depth <1-10 m. In the earliest stage of diagenesis, the primary component of the sediments is under the influence of meteoric water flushing, biogenic activity, redox-driven processes and the precipitation of authigenic clay minerals (Bjørlykke and Jahren, 2015). The early diagenetic minerals observed in the wells which have been studied include carbonate cement (siderite and calcite), phosphate and Kaolinite pore-fills.

7.2.3.3 Meteoric leaching

Meteoric water leaching has a significant impact on the reservoir properties by changing the initial composition of the sediment. Meteoric water flushing first dissolves carbonates and then dissolves unstable minerals such as feldspar and mica and precipitates authigenic clay minerals within the pore space, most commonly pore-filling authigenic kaolinite (Bjørlykke and Jahren, 2015). Dissolution of unstable minerals during the leaching reaction lead to the development of secondary porosity which is later filled by precipitation of authigenic clays in the pore space. According to petrographic data of studied samples, the main early diagenesis reaction in studied samples is leaching of unstable minerals such as feldspar and muscovite and precipitation of pore filling authigenic kaolinite. Stø Formation consists of considerably low amounts of feldspathic minerals. This is probably due to extensive reworking of underlying sediments, potentially together with the renewed input of the sediments source area, containing less feldspathic minerals. The effect of kaolinite on reservoir potential is negligible since it is observed in a small amount in both wells. However, it may have a minor effect on permeability. The highest concentrations of kaolinite have been registered within the facies F-6H and F-6f which were associated with low feldspar content and secondary porosity (Figure 7.7). A more likely interpretation is that as result of the significant flux of water almost all the feldspar minerals have dissolved and formed authigenic clay minerals mostly kaolinite. Kaolinite in these facies is mostly concentrated as pore filling kaolinite which caused a significant reduction in primary and secondary porosity. The pore space between the kaolinite crystals is too small to be filled with oil due to high capillary entry pressure thus there is a little net gain in porosity (Bjørlykke and Jahren, 2015). In general, Stø Formation intervals in well 7324/7-2 comprises of lower quantity of Kaolinite 4% compared to its counterpart in well 7321/9-1 (6%). The majority of mica grains in well 7324/7-2 have been under the influence of an intense degree of alternation and deformation indicating an intensive degree of meteoric water leaching. This process probably occured at shallow burial depth during the early stage of diagenesis where the meteoric water leaching is more efficient and sediments have the maximum potential to change their bulk composition (Bjørlykke and Jahren, 2015). Samples belonging to the Fuglen Formation indicate the highest concentration of kaolinite compared to Stø Formation samples. The highest amount of kaolinite is concentrated within the facies F-7 in well 7324/7-2 (53%) while this amount decrease to less than 3 % in well 7321/9-1.

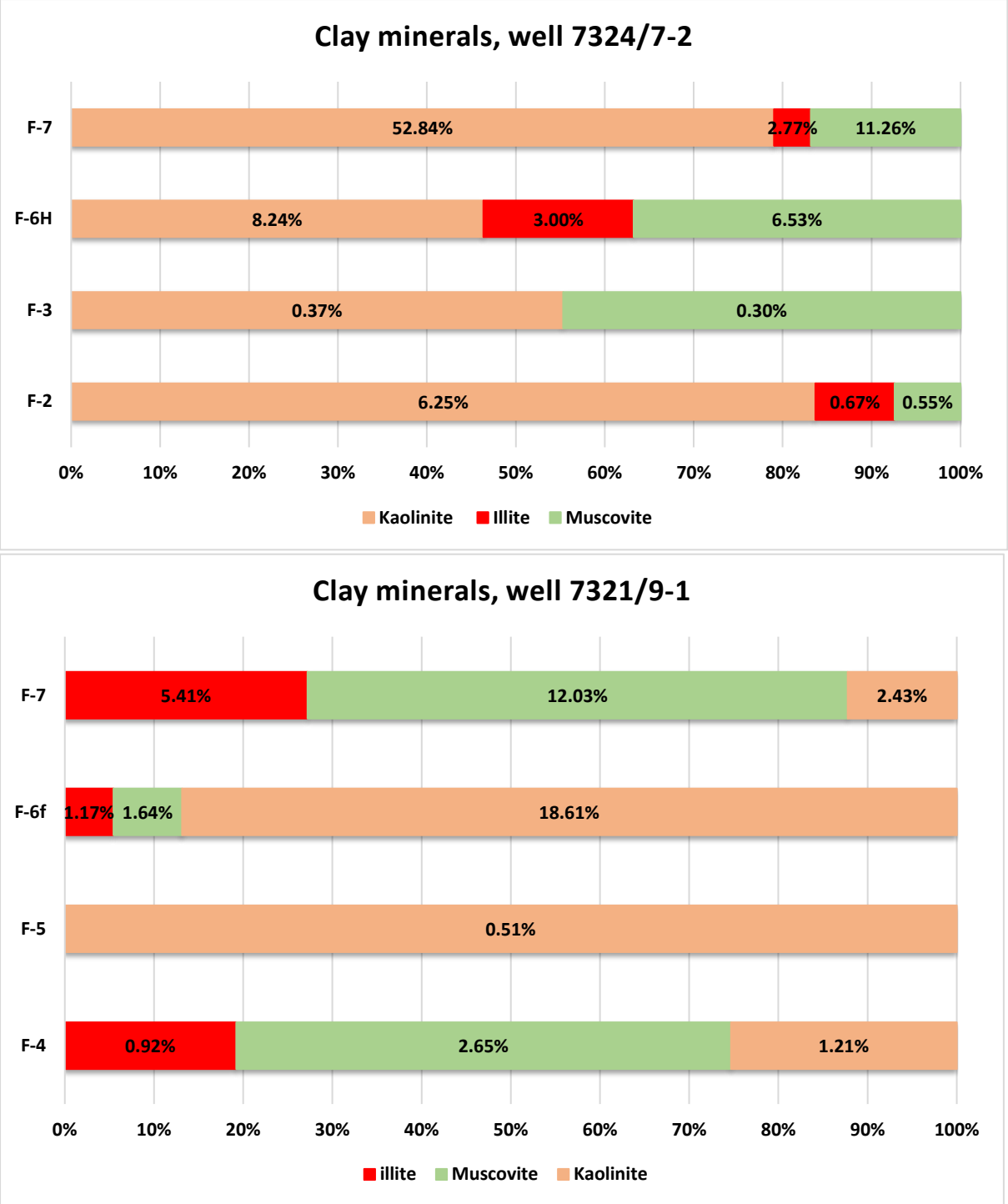

Figure 7.7: Distribution of clay minerals in each facies based on bulk XRD results. Alternation of feldspar and muscovite and precipitation of kaolinite indicate the early diagenetic processes related to meteoric water leaching.

7.2.3.4 Carbonate cementation

Carbonate cement is an early diagenetic process during which the biogenic calcite is dissolved, and carbonate cements such as calcite and siderite are precipitated. Precipitation of carbonate cement usually occurs at a shallow burial depth (Bjørkum et al., 1998, Olaussen et al., 1984). Precipitation of early calcite cement severely affects the reservoir properties of sandstones (Maast, 2013). The highest concentration of calcite cement is observed within the facies F-6H (18%) and F-6f (9%). These facies also consist of more than 8% and 4% siderite, respectively. The volume of the calcite cement show reduction by increasing the burial depth. Presence of calcite cement is still evident in some samples below the cemented intervals of the facies F-6H and F-6f, indicating the reduction in pore filling calcite cement vertically from shallower depth toward the deep burial. From the textural analysis, it is manifest that grains are floating in calcite cement and mostly exhibit the tangential contact. This observation indicates the precipitation of calcite cement prior to the mechanical compaction, preventing reorientation and fracturing of the grains (Figure 7.8).

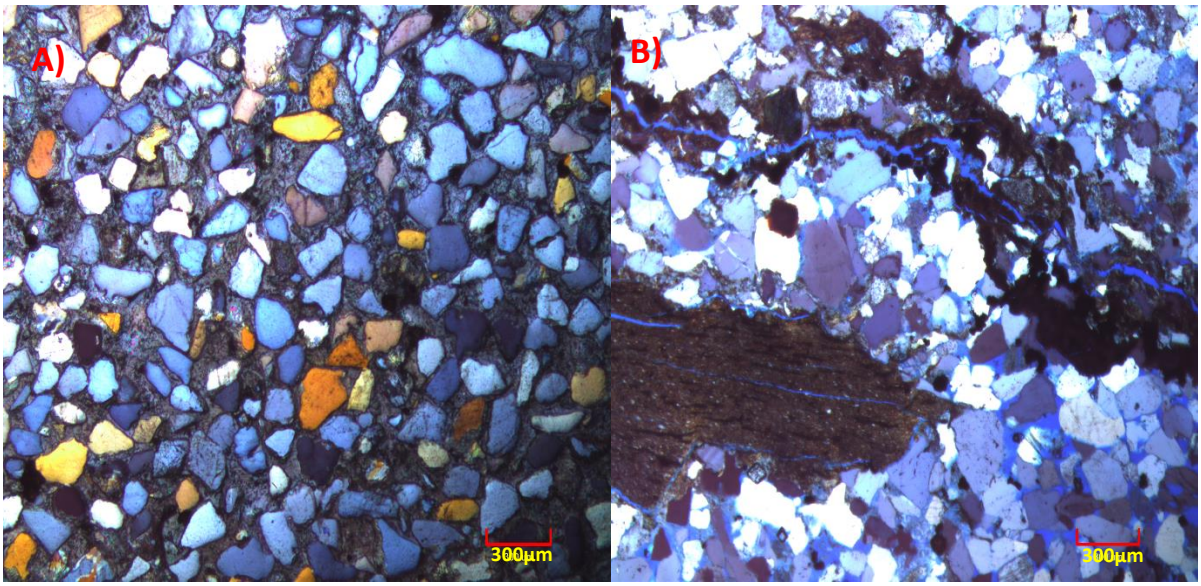

Figure 7.8: A) Calcite cemented intervals of the facies F-6H (d= 712.96 m) showing floating and tangential grains contact. B) Non-cemented sample of the facies F-2 (d= 730.39) showing reorientation and fracturing of the grains caused by mechanical compaction. Note the grains contact in picture B which are mostly long and tangential. The most significant consequence of the precipitation of the calcite cement within the sedimentary intervals is the development of impermeable barriers which severely affect the reservoir quality (Maast, 2013).

7.2.3.5 Phosphate

According to Bjørlykke and Jahren, there are several prerequisites for preservation and formation of the phosphate deposits such as:

- The lower rate of sedimentation and limited or no input of clastic sediment. Therefore, the occurrence of phosphate beds or signatures indicates the period of major or minor breaks in sedimentation in addition to periods of very slow sedimentation.

- High organic productivity. It has long been known that phosphate tends to form in an area with strong upwelling and consequently higher organic productivity. In such a setting the nutrients are consumed by organisms (plant plankton) and provide a high primary production.

- Phosphate deposits are sensitive to erosion and will be easily eroded even as a result of minor regressions and form conglomerates phosphate mudstone.

- Transgression plays a vital role in the deposition of phosphate minerals by holding clastic sediment back for a while and consequently providing a favorable environment for the biogenic matter to be concentrated.

Fluorapatite is the most commonly observed type of phosphate within Stø Formation. The observed fluorapatite is to a great extent is derived from remnants of the dead organisms with a phosphate skeleton which later disintegrated and liberates phosphate minerals (apatite) within the sediment (Bjørlykke and Jahren, 2015). Fluorapatite is commonly formed from calcium phosphate present particularly in living organisms, e.g., bone mineral and tooth enamel. Presence of the fluorapatite indicates weathering of the phosphate sediments which caused dissolution of carbonate and carbonate containing apatite and precipitation of fluorapatite (Bjørlykke and Jahren, 2015, Leroy et al., 2001).

7.2.3.6 Intermediate Diagenesis

Mechanical compaction

Mechanical compaction is driven by the effective vertical stress created from the weight of the overburden and causes a reduction in bulk volume (Marcussen et al., 2010). Mechanical compaction typically includes reorientation and fracturing of the grains which leads to significant reduction in porosity.

Intergranular volume (IGV)

The initial predicted IGV is around 44%-45% in the samples of the facies F-6H and F-6f which shows a reduction proportional to the increase of burial depth. From Figure 7.9, it is evident that the effective loss of porosity is caused by mechanical compaction prior to quartz cementation and reaches to 21% and 20% in well 7324/7-2 and 7321/9-1, respectively. The results of thin section analysis confirm this interpretation as most of the grains within the Stø Formation intervals display tangential grain contacts with neighboring grains.

From the petrographical results, it is evident that high abundance of early diagenesis cements (carbonate and phosphate cements), secondary clay minerals (kaolinite + illite) and matrix material correspond to high IGV value within the samples of facies F-6. IGV shows a significant reduction in the samples of facies F-6H and F-6f by increasing the burial depth. However, this reduction is more evident within the facies F-6f where IGV drops from initial value 44% to 17%.

Empirical studies (Figure 2.6) suggest that coarse-grained sands compact more readily compared to fine-grained sands due to grain crushing. Poorly sorted sandstones containing an abundance of the matrix and lithic rock fragments show a higher loss of porosity due to ductile deformation and reduced fraction between grains which lead to more efficient grain packing and consequently higher loss of porosity. Monocrystalline grains (e.g., quartz) have a higher internal strength compared to polycrystalline fragments (e.g., lithic rock fragments), meaning that they tend to deform more easily under mechanical stress (Pittman and Larese, 1991).

Facies F-6f comprises of moderately sorted pebbles, cobbles floating in a matrix of medium to coarse-grained sandstone. Therefore it could be concluded that the existence of coarse-grained size particles containing an abundance of lithic rock fragments are the main reason for greater IGV reduction in this facies which led to more efficient grain packing and consequently more loss of intergranular volume.

From the textural analysis, it is evident that a majority of the grain contents are mostly tangential indicating the loss of porosity as a result of compaction processes in contrast with cementation processes. Based on the grain size analysis, it could be observed that well sorted and very fine-grained sand intervals of Stø formation have the best potential for preserving the porosity before initiation of chemical compaction compared to samples with poorly

sorted coarse-grained size particles. The described trends match well with the reference literature regarding the experimental compaction studies, e.g., Masst (2013), Marcussen (2010) and Bjørlykke and Jahren (2015). All the facies except F-6H and F-6f show porosity values more than 10% and display grain size variations between medium to very fine sand.

Chemical compaction

Chemical compaction is occurring at deeper burial in a chemically closed system. Governed by time, temperature and factors such as detrital mineralogy (Bjørkum et al., 1998, Walderhaug, 1996, Walderhaug and Rykkje, 2000, Marcussen et al., 2010). At the onset of chemical compaction (70-80 ^{0}C) a minor amount of quartz cement can prohibit the further effect of mechanical compaction on sediments by grain framework stiffening (Dvorkin and Nur, 1996). The transition zone (TZ) from MC to CC is revealed by a cross plot of density versus velocity (Figure 6.5). In well 7324/7-2 the transition from mechanical to chemical compaction regime is registered at temperatures around 76 ^{0}C. From Table 7.1 and Figure 7.9 it could be concluded that Stø Formation intervals are mostly placed in chemical compaction regime as the maximum burial depth of Stø formation is above 2 km with a temperature of 80 ^{0}C. Initiation of quartz cementation is registered within the samples of facies F-3 and F-5. Quartz cementation value varies between 0% to 3.5 % in all facies (Figure 7.9). Although this amount is relatively low but still is in a sufficient range for shutting down the mechanical compaction (Bjørlykke and Jahren, 2010). Precipitation of quartz cement in Stø Formation mainly depends on the factors such as available surface areas for nucliation and the time-temperature integral.

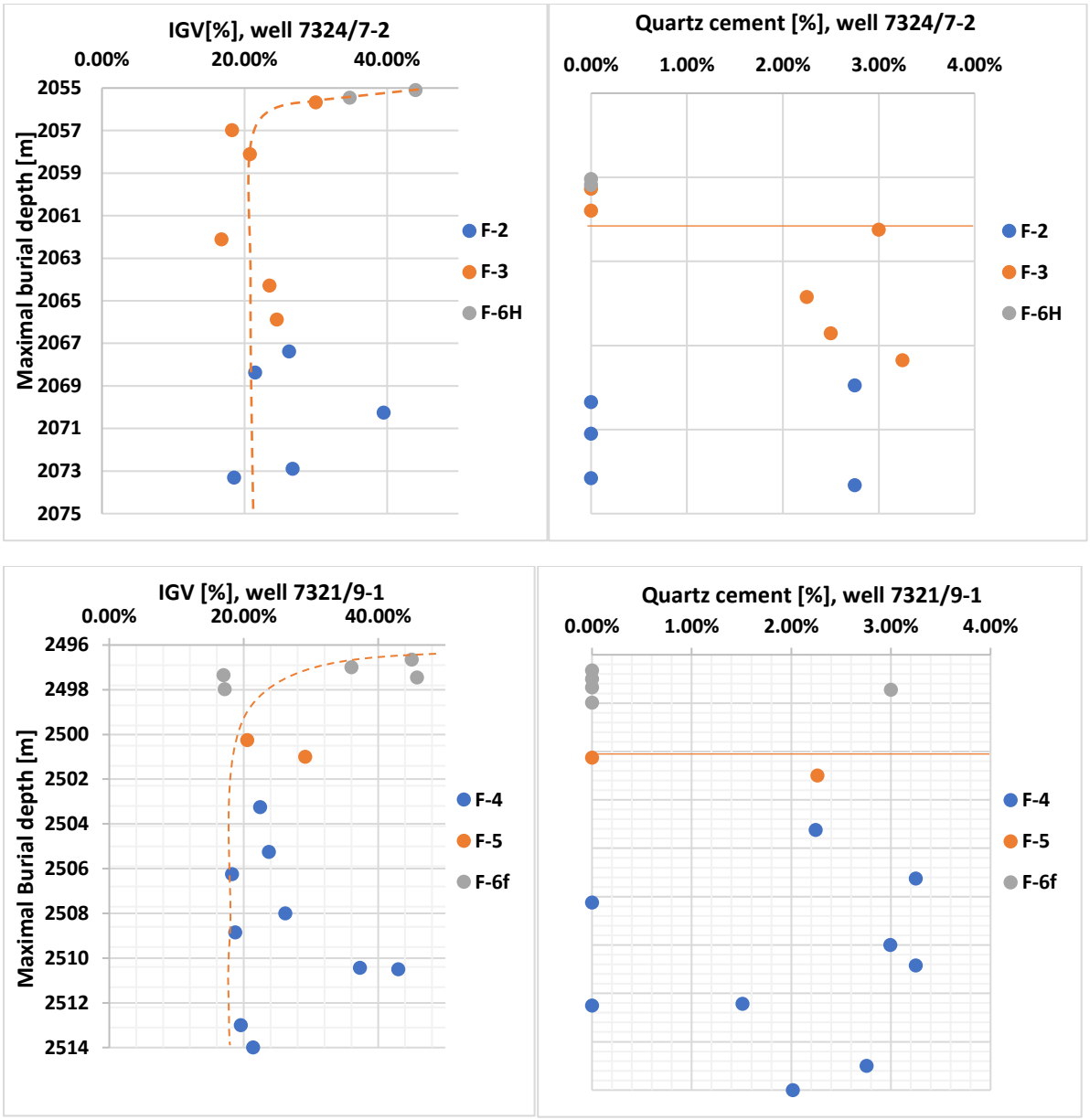

Figure 7.9: Calculated IGV and quartz cement vs. depth form well 7324/7-2 and 7321/9-1.

Illitization

Illite is found in trace amounts in almost samples and includes less than 1% of the total rock volume of Stø Formation in well 7324/7-2 and 7321/9-1. The highest amount of illite has been found within the facies F-6H (3%) and facies F-6f (1.17%). Infiltration residues clay and burrow fillings tend to form shortly after deposition as result of water containing suspended clay particles (Wilson and Pittman, 1977). Allogenic clay minerals are carried by downward or laterally migrating pore waters and naturally accumulates in pore space of previously deposited sands (Ali et al., 2010). Observed, illite in Stø Formation probably deposited as parts of infiltrated material which later due to diagenetic reaction altered to illite.

Any type of clay can occur as a detrital component, however typically chlorite, illite, smectite and mixed-layer clays occur as grain coatings (Ali et al., 2010). If the observed illite is deposited at the time of deposition as part of the infiltrated material, then no further chemical alteration will occur during diagenesis processes. The formation of illite from smectite via mixed layered minerals at temperatures from about 70 to 80 ^{0}C is well known (Bjørlykke and Jahren, 2015). At this temperature, a thin hair plate-like minerals of authigenic illite will form which have a detrimental effect on reservoir quality by reducing the permeability (Bjørlykke and Jahren, 2015). Smectite may be presented in some muddy, mainly volcanic, sandstones which have flushed with a limited amount of meteoric water (Bjørlykke and Jahren, 2015). Smectite is stable at temperatures below 70^0 C and at temperatures above this level (between 70–80^0 C) is dissolved and replaced by illite (Bjørlykke and Jahren, 2010). This theory can potentially explain the absence of smectite within the samples of Stø Formation provided that completed alteration has taken place. The reaction between K-feldspar and Kaolinite at temperature about 130^{0}C is another possible source of illite since above this temperature these minerals are no longer thermodynamically stable and replaced by illite (Bjørlykke. 1988). However, calculated maximum burial temperatures from Stø Formation in both wells are less than 130^{0}C. Therefore this diagenetic reaction could not be considered as the possible source for precipitation of illite in Stø Formation.

7.2.4 Reservoir quality

As described in chapter 2, Porosity and permeability are critical factors in order to determine the reservoir quality of a sandstone reservoir since these parameters control the total hydrocarbon storage capacity and the fluid flow within the reservoir. (Bjørlykke and Jahren, 2015). Based on core plug data, sedimentological logging and thin section analyses, Facies F-2, F-3, F-4, and F-5 can be discussed concerning reservoir quality. Heavily cemented intervals of the facies F-6H and F-6f where associated with high amount of clay (Kaolinite + illite), cement (calcite, siderite, and fluorapatite) and the highest volume of IGV, indicating poor or negligible reservoirs quality thus these facies have been excluded from further discussion. According to point counting results, the porosity varies between 1% to 21 % in Stø Formation in well 7327/7-2 and between 0.50 to 17% in well 7321/9-1.

Facies F-2: Channel base

This facies is a relatively clean, medium to fine-grained, moderately to well-sorted sandstone. According to point counting results, the primary porosity varies between 11% to 19% in facies F-2 and shows an increasing trend towards the upper parts of the facies. The average porosity is estimated around 15% which later characterized this facies in terms of reservoir quality as good. This facies shows little depositional matrix on average (3%) and quartz cement (1%). However, one of the samples of this facies shows more than 6% kaolinite, fluorapatite (8%) and siderite (10%) which caused a significant increase in IGV in deep burial(Figure 5.22).

Facies F-3: Channel fill

This facies consists of medium to fine-grained, well-sorted sandstone. Sandstone intervals of the facies F-3 are commonly saturated with oil. According to point counting results, the average porosity in facies F-3 is more and less the same as average porosity in facies F-2. Facies F-3 shows the higher volume of porosity (20%) in lower parts of this section compared to upper parts at the transition to facies F-6H. Facies F-3 consists of the relatively negligible amount of matrix (less than 1%), kaolinite and illite. However, some samples in upper parts of the unit at the transition to facies F-6 H are partially cemented, resulting in a remarkable drop in porosity trend from 20% in lower parts to 0.48% in upper parts of this succession. These cemented samples may, however, reduced the permeability by generating impermeable vertical barriers subsequently negatively effect on reservoir quality.

Facies F-4: Upper delta plain

Facies F-4 comprised of medium to fine-grained, well-sorted sandstone. The average porosity in this section is around 12 % and all the samples except one show more than 10% porosity (Figure 5.17). This facies shows on average around 3% illite and 2% matrix material. Two samples of this facies comprise of significant amounts of fluorapatite which caused a sharp reduction in estimated average porosity in lower parts of facies F-4. The section is moderately bioturbated (BI=2 to 3) and includes roots and a variety of burrows generated by reptiles, insects, and worms. The porosity and permeability of this facies could have negatively been affected by bioturbation activities which mixed clay with clean sand.

Facies F-5: Minor distributary channel

Facies F-5 is characterized by interbedded fine to locally medium-grained sandstone, grey siltstone, and claystone. According to sedimentological observations, this unit is moderately bioturbated and demonstrates relatively high quantity of clay content. However, the point counting results suggest the negligible amount of matrix (less than 0.5% on average) since most of the samples were taken from relatively clean intervals. Estimated average porosity within is facies is around 15%.

7.2.4.1 Porosity and Permeability

According to core plug data (Figure 6.12). It could be observed that facies belonging to the well 7324/7-2 (F-2 and F-3) demonstrate very good reservoir quality, owing to excellent porosity and permeability while in well 7321/9-1 (facies F-4 and F-5) the reservoir quality varies from fair to good. The reservoir quality of Stø Formation in well 7324/7-2 and 7321/9-1 has also been discussed based on matrix content and intergranular volume (IGV). According to the Figure 6.13, most of the samples in very good reservoir quality intervals have less than 5% matrix content and are belong to facies F-2 and F-3 while samples with 5-20 % and more matrix content are within facies F-4 and F-5. Although, some samples of the well 7321/9-1 contain minor amounts of the matrix (less than 5%) but still demonstrate poor reservoir quality which is due to the presence of high amounts of carbonate cements. The kaolinite constitutes 4% and 6% of the total rock volume of Stø Formation intervals of the wells 7324/7-2 and 7321/9-1, respectively. Kaolinite in these facies mostly concentrated as pore filling kaolinite and may have a minor effect on permeability. Based on the results it is evident that relatively high quantity of matrix content and cement, as well as moderate to high degree of bioturbation in facies F-4 and F-5, correspond to poor permeability and consequently lower reservoir quality in well 7321/9-1 compare to well 7324/7-2.

The petrophysical cut off for shale volume demonstrates almost all the samples below the V_{SH} threshold (Figure 6.11). From the Figure 6.15, it is obvious that most of the samples of the well 7324/7-2 have less than 50% water, whereas almost half of the samples of the well 7321/9-1 are above water saturation threshold and comprise of more than 50% water. Based on the petrophysical results it is evident that, well 7324/7-2 (Hanssen) with better reservoir quality has excellent potential for hydrocarbon discoveries while well 7321/7-2 with samples containing more than 50% water demonstrates poor reservoir quality and therefore could not act as hydrocarbon reservoir. Table 7.2 demonstrates the mineral composition, textural properties, and petrophysical cut off with resultant reservoir quality for facies F-2, F-3, F-4, and F-5.

Table 7.2: Mineral composition, textural properties and petrophysical cut off with resultant reservoir quality for facies F-2, F-3, F-4, and F-5.

	Properties	Facies				Effect on reservoir quality
		F-2	F-3	F-4	F-5	
Initial Composition	Quartz	87%	94%	86%	88%	• Framework grain
	Feldspar	1.95%	1.18%	1.70%	5.67%	• Framework grain • Early diagenetic dissolution and precipitation of kaolinite
	Rock Fragments	3.72%	0.46%	2.79%	1.19%	• Framework grain • Increase mechanical compaction • Samples with higher amount of rock fragments compact more readily compare to sand with less amount of rock fragments
	Matrix(allogenic clay)	3 %	0%	2%	0%	• Incrase mechanical compaction by filling the fraction between framework grains. • Reduces primary porosity.
Authigenic Minerals	Kaolinite	6.25%	0.37%	1.21%	0.51%	• Pore-filling mineral
	Carbonate cements Calcite/siderite	0/2.11%	4/0%	0/1%	0/4%	• Reduces porosity • Reduces permeability by creating vertical barriers • Reduces mechanical compaction
	Quartz cement	2.75%	3%	2.57%	2.26%	• Reduces porosity • 2-4% enough to shut down mechanical compaction
	Illite	pore-filling mineral in conjunction with kaolinite	pore-filling mineral in conjunction with kaolinite	pore-filling mineral in conjunction with kaolinite	pore-filling mineral in conjunction with kaolinite	• Pore-filling illite has a detrimental effect on reservoir quality by reducing the permeability
Texture	Grain size	Medium to very fine sand	Medium to fine sand	Medium to very fine sand	Medium to very fine sand	• Smaller grain size reduce mechanical compaction due to larger surface area
	Sorting	Mod. Well Sorted	Well Sorted	Well Sorted	Well Sorted	• Better sorting reduces mechanical compaction
	Avg. interganular volume (IGV)	26%	22.12%	25.74%	25%	• Volume between grains accupied by cement + depositional matrix + intergranular porosity
	Avg. Point counting porosity	15%	15%	12%	15%	• Porosity available for hydrocarbon storage
	Avg. Porosity fro m core plug data	25%	25%	20%	22%	• Porosity available for hydrocarbon storage
Cut Off	V_{sh} cut-off	0-10%	0-10%	0-20%	0-20%	• Less shale volume better= reservoir rock
	S_w Cut-off	0-5%	0-5%	50-52%	50-52%	• More than 50% water saturation = no hydrocarbon accumulation
Reservoir Quality		Very Good/oil bearing	Very Good/oil bearing	Good/ water-bearing	Good/water-bearing	

7.3 Phosphorite Conglomerate at the top of Stø Formation

Sedimentological and petrophysical analyses have been conducted on the condensed section at the top of Stø Formation in order to determine the origin and the depositional processes which have created this condensed section. Facies 6 consists of varying amount of quartz, light gray and moderately sorted pebbles, cobbles floating in a matrix of medium to coarse/grained sand. Facies F-6 units are correlated, meaning they occur at approximately the same time. Both cap a fluvial/deltaic below and covered by a fully marine environment. However, facies F-6 demonstrates sedimentary structures and petrographic characteristics which are entirely different in well 7324/7-2 from well 7321/9-1. Thus, this facies has been subdivided into facies F-6H in well 7324/7-2 and facies F-6f in well 7321/9-1. This facies is matrix loading comprises the medium sand to fine gravel fraction with changing admixture of quartz, chert pebbles, and glauconite which randomly oriented within the succession. One of the most significant diversity between the facies F-6H and F-6f is the presence of coarse-grained pebbly sized clasts (exotic clasts) which have been observed only in facies F-6f (Figure 7.10). The clasts are well rounded and predominantly accumulated at the top of facies F-6f. Based on the petrographical analysis, the mineral assembly of facies F-6 including calcite, siderite, kaolinite, muscovite, illite and trace amounts of plagioclase and K-feldspar, is almost the same in both wells. One of the observed difference in the mineral assembly is related to the presence of the fluorapatite (on average 10%) which is only found in Facies F-6f. Another difference between the mineral assembly of the facies F-6 is related to the total amount and type of rock fragments. The average amount of rock fragments within the facies F-6f is 10% while this amount reduces to 3% in its counterpart in well 7324/7-2. The textural analysis shows grain size variation between medium sand to find sand in Facies F-6H which is almost similar to grin size variation within the underlying facies. Whereas, facies F-6f mostly comprises pebble-sized particles and matrix of medium to fine-grained sand.

In the following section, the origin of the facies F-6 has been discussed based on matrix, phosphate and exotic clasts content.

7.3.1 Origin of the matrix

The matrix of the facies F-6 mostly comprises of medium to fine grain sand similar to underlying facies. Also, petrographic characteristics of the matrix within facies F-6 are comparable to the underlying facies of Stø Formation. Therefore, it could be interpreted that matrix of the facies F-6 is most likely only represent reworked material derived from Realgrunnen Subgroup (Tubåen, Nordmela, Fruholmen and Stø formations). The matrix of the facies F-6 possibly formed as results of regression during which underlying formations have been eroded, reworked and redeposited as matrix within the facies F-6.

7.3.2 Origin of phosphate

The most common type of the phosphate is apatite (Ca_5 $(PO_4)_3$(F, Cl, OH). Fluorapatite is the most common type of phosphate observed within the condensed section. Fluorapatite has been only observed within the facies F-6f. The marine fluorapatite is generally formed by the fossils with phosphatic skeletons (bone bed). Significant amounts of fluorapatite within the facies F-6f indicate the existence of a favorable condition for the preservation of the phosphate. There is a massive demand for phosphate in the marine environment. Thus preservation of this mineral requires the existence of certain conditions such as high organic productivity, nutrient-rich water, low or no input of clastic sediments (Bjørlykke and Jahren, 2015). Phosphate beds tend to from below the photic zone where the supply of the oxygen is limited, and organisms could not survive. The modern examples of phosphates indicate deposition on the continental shelf at a depth of 100 and 400 m (Bjørlykke and Jahren, 2015). However, it might not completely be rational to consider the defined depth as exact depth for phosphate minerals which were deposited in the past since some of the most important factors (sunlight, depth, nutrient) at the time of deposition are unknown. In this thesis, two theories about deposition of the phosphate at top of Stø are presented as follows:

Theory I. The deposition of the phosphate minerals in the area close to Stø Formation.

Theory II. Generation of the phosphate minerals has occurred directly at the top of Stø Formation. These phosphate minerals later eroded due to regression and formed phosphate nodules in the area.

Based on Theory I., there should have been high energy currents available which transferred the phosphate nodules from the site of deposition and redeposited it in the same environment at the top of the formation.

However, since there is no available information about energy currents and depositional environment at the time of deposition, therefore the second theory seems to be more realistic.

7.3.3 Origin of exotic clasts

The coarse-grained pebbly size clasts are only observed within the well 7321/9-1 in Fingurejupet Sub-basin and are absent in the other wells in the basin and also in Hoop Fault area. The frequency of the clasts shows increase towards the top of the succession of facies F-6f. One possible hypothesis for the source of the exotic clasts could be presented as follows:

The geographic position of well 7321/9-1 is close to Loppa High, which was uplifted and eroded during the Jurassic time. Therefore, Loppa High might be considered as a possible source for these exotic clasts in Fingerdjupet Sub-Basin. However, during the Triassic period, Loppa High mostly comprised of fine-grained particles which could not act as a source for

coarse-grain clastic sediment within facies F-6f. Consequently, this hypothesis would be correct provided that during the Jurassic time, Loppa High was eroded to the base. From the geological study, it is evident that during Jurassic time Loppa High has not been eroded to that depth at which these clasts are present. Accordingly, this hypothesis is discredited.

The exact source of these exotic clasts still is ambiguous and requires further work and more investigation in this area.

7.3.4 History/chronological evaluation of condensed section (Facies F-6)

The possible interpretation of the depositional process which led to formation of condensed section at the top of Stø Formation could be presented as follows:

The condensed section at the top of Stø Formation has been deposited as result of the transgression with minimal or no input of the clastic sediments. Stø Formation during the Jurassic time has been deposited as result of several episodes of transgression (Figure 7.11a). A new set of transgression probably started after deposition of Stø and reached to a maximum level (flooding surface) resulted in suitable conditions for preservation and accumulation of phosphatic minerals at the top of Stø Formation. The most common type of the phosphate within the facies F-6 is fluorapatite which is sourced from the organism's skeleton below the photic zone where the supply of the oxygen is limited, and the condition for the preservation of the phosphate is favorable. "Phosphate minerals are sensitive to erosion and as a result of even minor regression will be easily eroded" (Bjørlykke and Jahren, 2015). Presence of phosphate nodules indicates subsequent regression after transgression resulted in exposure and erosion of the phosphate layers and consequently the formation of phosphate nodules within the facies F-6 (Figure 7.11b). Also, glauconite and several traces of iron oxide have been observed within these intervals indicating the same marine regression which led to the exposure of the shelf thus dissolution of pyrite and precipitation of iron oxide within these intervals. Presence of iron oxide within the sediments is a sign of relatively prolonged subaerial exposure during relative sea level lowstand (Hwang and Heller, 2002). This marine regression also caused reworking of underlying sediments and redeposition of the sediments as matrix within the condensed section. The existence of a high quantity of rock fragment at the top of facies F-6f indicates the supply of the sediment from an external source which is still unknown. Final depositional process of the condensed section followed by subsequent transgression after a long period of regression which caused deposition of the Fuglen Formation at the top of Stø Formation.

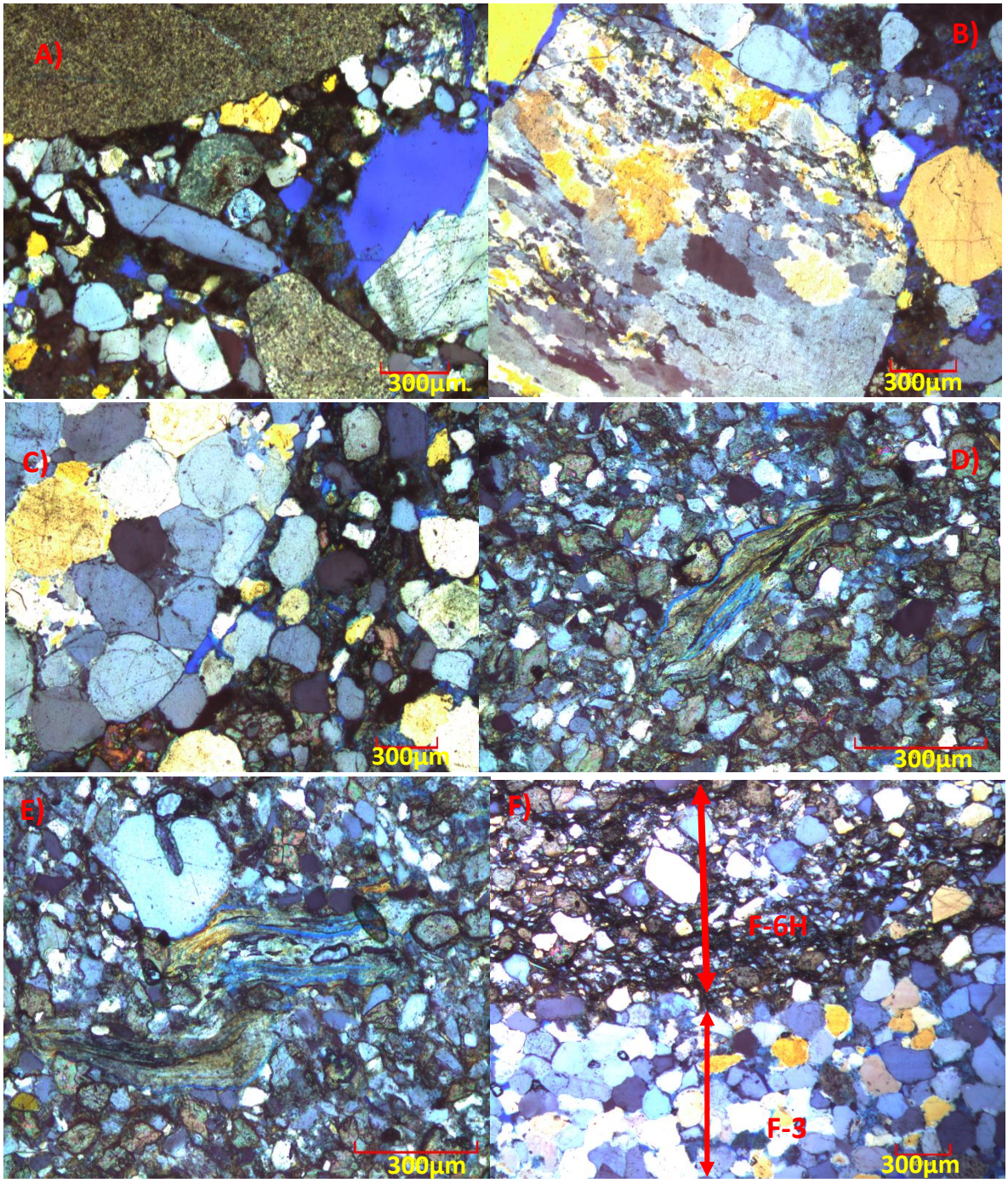

Figure 7.10) Pictures demonstrate the significant difference between petrographical characteristics of facies F-6 in wells 7324/7-2 and 7321/9-1.Pictures A, B, and C are from the samples of the facies F-6f (d= 1380 and 1379m). It is evident from the pictures that the facies F-6f comprises of more coarse-grained size particles compare to its counterpart in well 7324/7-2 (D, E and F, d= 713 and 712m). Picture F indicates the transition from Facies F-3 to Facies F-6H.

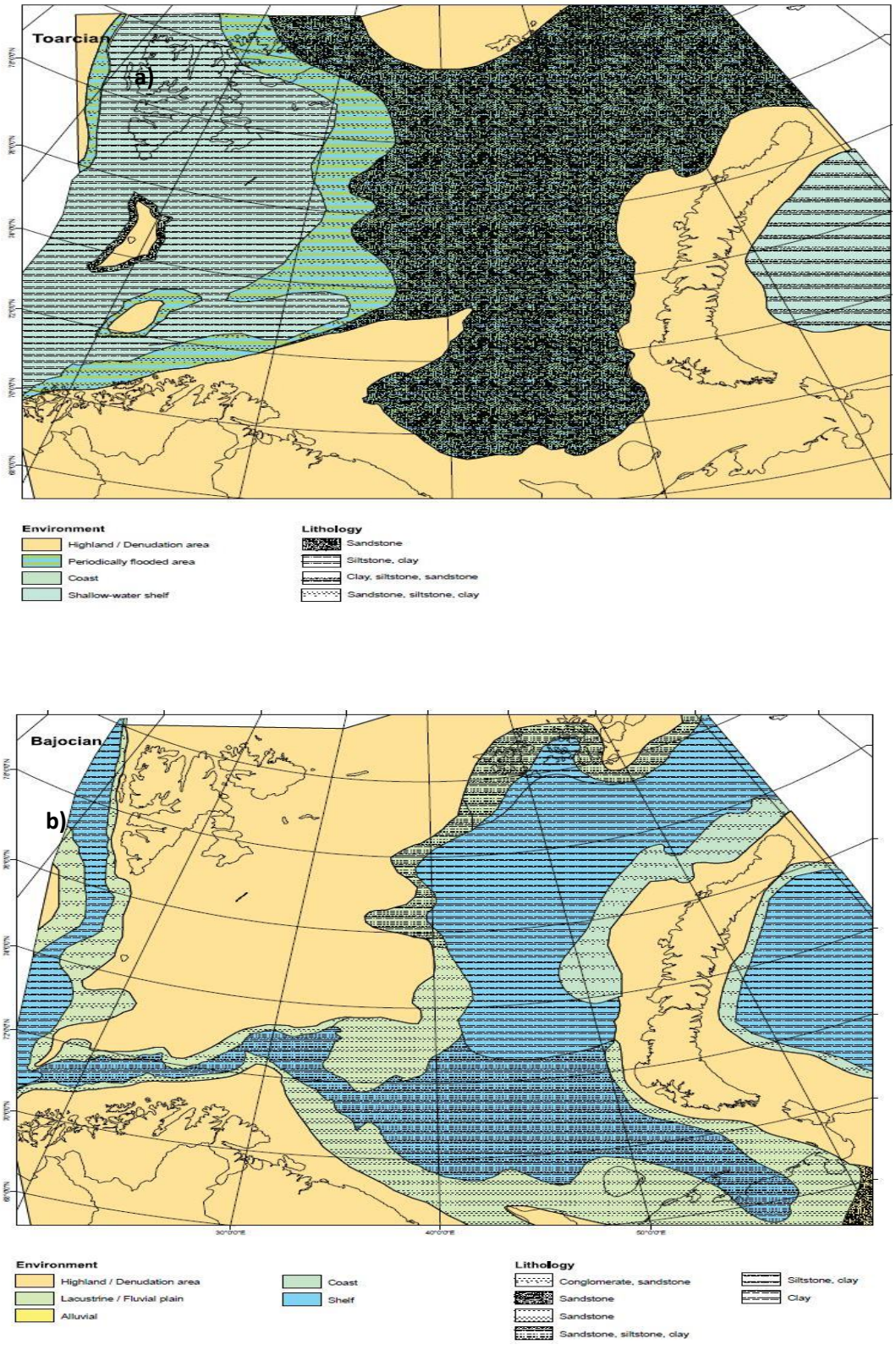

Figure 7.11: Stratigraphically development of the Barents Sea from Late Triassic to Late Jurassic (Smelror et al., 2009)

7.4 Offshore transition- offshore deposits and Facies Association 3

Facies F-7 is interpreted as offshore-transition to offshore deposits. Presence of very thin layers of sandstone between fine-grained intervals indicates the influence of storms within the offshore transition shelf environment (Clifton, 1973, Reading, 1996, Pemberton, 2001). Sedimentary characteristic of facies F-7 display deposition below fair-weather wave base thus have been subjected to a great storm event and higher sedimentation rate resulted in inter-bedding of sandstone and mudstone. An intense degree of bioturbation along with the occurrence of marine fossils suggest nutritious and oxygenated waters which provided a favorable environment for organisms to colonize and consequently destroy the primary sedimentary structures (MacEachern and Bann, 2008). The decrease proportion of interbedded, sandstone within siltstone and mudstone intervals toward the top of the succession, also indicates deposition from suspension in a calmer environment probably below the storm weather wave-base.

Chapter 8: Conclusion and Further work

8.1 Conclusions

- The mineral distribution classifies the Jurassic Stø Formation in the studied wells as Quartz arenites, Sublithic arenites, and lithic arenites. The difference in petrographic characteristic of Stø Formation is related to the different geographical position of the wells.

- Petrographic analysis suggests moderately to well sorted and mineralogically mature sandstone composition for Stø Formation. This maturation is related to the paleoclimate, provenance, and depositional environment which are critical factors, affecting the sandstone composition.

- The main early diagenesis reaction in studied samples is leaching of feldspar and muscovite and precipitation of pore filling authigenic kaolinite. Stø Formation intervals in wells 7324/7-2 and 7321/9-1 consist of the considerably low amount of feldspathic minerals due to an extensive reworking of underlying sediments, potentially together with the renewed input of the sediments source area containing less feldspathic minerals.

- Kaolinite has been found trace amounts in Stø Formation. Therefore, the effect of kaolinite on the reservoir quality is negligible. However, it might have some minor detrimental effect on permeability. Stø Formation intervals in well 7324/7-2 have consisted of a lower quantity of kaolinite (4%) compared to well 7321/9-1 with 6% kaolinite.
- The effective loss of porosity is caused by mechanical compaction prior to quartz cementation and reaches from an initial amount of (43%) in two wells to 21% and 20% in wells 7324/7-2 and 7321/9-1, respectively.

- Quartz cementation is initiated at approximately 70^0C. In clean sandstone, quartz cementation is the dominant porosity reducing parameter after the termination of the mechanical compaction. Therefore a subsequent amount of quartz cementation is expected in Stø Formation intervals in both wells. However, according to point counting result, only 2-3% quartz cement has been registered in Stø Formation intervals, suggesting additional cathodoluminescence in order to obtain more accurate results.

- Illite is found in trace amounts in almost all samples. The illicit clay is seen in Stø Formation probably deposited as parts of infiltrated material which later altered to illite due to the diagenetic reaction. At temperatures above 70^0C the smectite is no longer thermodynamically stable and is dissolved and replaced by illite which is considered as detrimental to reservoir quality (Bjørlykke and Jahren, 2015). However, illite is only

registered in small quantities mainly within facies F-6H (3%) and facies F-6f (1.17%). Typically, illite was found as a pore-filling mineral in conjunction with kaolinite within the facies.

- Stø Formation intervals in well 7324/7-2 have the best reservoir quality compare to well 7321/9-1, with low shale volume, relatively high effective porosity (up to 27%), less than 5% matrix content, less than 4% kaolinite and low bioturbation degree. The best reservoir quality intervals have been found in the fluvial deposits in this thesis (channel base and channel fill) which were responsible for the deposition of clean sands.

- Based on the results, it is evident that relatively high matrix content (between 5-20% and more), carbonate cement and moderate to high degree of bioturbation in facies F-4 and F-5 correspond to poor permeability and consequently lower reservoir quality in well 7321/9-1. Despite the fact that Stø Formation intervals in well 7321/9-1 demonstrate good reservoir quality but still could not be considered as a potential hydrocarbon reservoir due water saturation more than 50%.

- Relatively shallow depth of Stø Formation reservoir in Hoop area, despite significant exhumation of the study area, indicates that the formation has not experienced such high degree for diagenesis reactions.

- The condensed section at the top of Stø Formation comprises phosphate nodules, matrix and exotic clasts representing three different sources. The matrix of the facies F-6 possibly formed as result of regression during which underlying formations have been eroded, reworked and redeposited as matrix within the facies F6.

- Fluorapatite is the most commonly observed type of phosphate within the condensed section sourced from the fossils with phosphatic skeletons (bone bed). The Phosphate minerals directly deposited at the top of Stø Formation which later as result of the regression eroded and formed phosphate nodules at the top of the formation.

- The coarse-grained pebble-sized clasts are only observed within the well 7321/9-1 in Fingurejupet Sub-basin and are absent in the other wells in the basin and also in Hoop Fault area. Loppa High could not be considered as a possible source for these exotic clasts. Since it has not been eroded deep to the base during the Jurassic period. This indicates the disapproval of this hypothesis.

- Trangressive lags deposits have been formed as result of the rapid rise of sea level with minimum or limited input of the clastic sediments, providing a favorable condition for the preservation of the phosphate. Presence of a mixture of phosphate nodules and matrix (eroded material from the underlying facies) indicates a regression event subsequent to the transgression.The existence of the glauconite and trace of iron oxide indicate a relative

prolong period of the regression during which pyrite has been dissolved resulted in precipitation of iron oxide within the unit. In addition, observed coarse-grained pebbly size clasts at the top of the unit indicates supply of the sediment from another source which is not clear and require further investigation in this area. The final stage of the development of transgressive lag deposits followed by transgression which likely started by the end of the Jurassic period, which led to the deposition of the Fuglen Formation at the top.

8.2 Further work

In order to characterize and determine Stø Formation reservoir quality with greater accuracy in Hoop area and Fingerjupet Sub-Basin, several additional analyses are recommended.

- Clay XRD- analysis in order to determine a different type of clay minerals within the newly defined facies. Authigenic clay, especially illite are regarded as detrimental to reservoir quality thus further analysis would be beneficial.

- Since low quartz cement percentages observed within Stø Formation intervals, thereby additional cathodoluminescence analysis is recommended in order to determine intergranular volumes more accurately.

- Cathodoluminescence and detrital zircon analyses on quartz grains and matrix of the condensed section are highly recommended in order to determine the different types of the quartz within the succession and also to obtain more information about the provenance of the matrix material.

- Detailed petrographic analysis of rock fragments within the condensed section is also recommended in order to specify the exact types of rocks and consequently to find the possible source.

References

ADAMS, A. E., MACKENZIE, W. S. & GUILFORD, C. 1984. Atlas of sedimentary rocks under the microscope, Longman; Wiley.

AHLBERG, A., ARNDORFF, L. & GUY-OHLSON, D. 2002. Onshore climate change during the Late Triassic marine inundation of the Central European Basin. Terra Nova, 14**,** 241-248.

ALI, S. A., CLARK, W. J., MOORE, W. R. & DRIBUS, J. R. 2010. Diagenesis and reservoir quality. Oilfield Review, 22**,** 14-27.

ALLEN, J. 1970. A quantitative model of grain size and sedimentary structures in lateral deposits. Geological Journal, 7**,** 129-146.

ALLEN, J. R. L. The sedimentation and palaeogeography of the Old Red Sandstone of Anglesey, north Wales. Proceedings of the Yorkshire Geological and Polytechnic Society, 1965. Geological Society of London, 139-185.

ANDERTON, R. 1985. Clastic facies models and facies analysis. Geological Society, London, Special Publications, 18**,** 31-47.

BÄCKSTRÖM, S. A. & NAGY, J. 1985. Depositional history and fauna of a Jurassic phosphorite conglomerate (the Brentskardhaugen Bed) in Spitsbergen.

BAIG, I., FALEIDE, J. I., JAHREN, J. & MONDOL, N. H. 2016. Cenozoic exhumation on the southwestern Barents Shelf: Estimates and uncertainties constrained from compaction and thermal maturity analyses. Marine and Petroleum Geology, 73**,** 105-130.

BERGAN, M. & KNARUD, R. 1993. Apparent changes in clastic mineralogy of the Triassic–Jurassic succession, Norwegian Barents Sea: possible implications for palaeodrainage and subsidence. Arctic Geology and Petroleum Potential, Norwegian Petroleum Society (NPF), Special Publication, 2**,** 481-493.

BERGLUND, L., AUGUSTSON, J., FÆRSETH, R., GJELBERG, J. & RAMBERG-MOE, H. 1986. The evolution of the Hammerfest Basin. Habitat of Hydrocarbons on the Norwegian Continental Shelf. Graham & Trotman, London**,** 319-338.

BHATTACHARYA, H. & BHATTACHARYA, B. 2010. Soft-sediment deformation structures from an ice-marginal storm–tide interactive system, Permo-Carboniferous Talchir Formation, Talchir Coalbasin, India. Sedimentary Geology, 223**,** 380-389.

BJÆRKE, T. & DYPVIK, H. 1977. Sedimentological and palynological studies of Upper Triassic–Lower Jurassic sediments in Sassenfjorden, Spitsbergen. Norsk Polarinstitutt Årbok 1976**,** 131-150.

BJØRKUM, P. A., OELKERS, E. H., NADEAU, P. H., WALDERHAUG, O. & MURPHY, W. M. 1998. Porosity prediction in quartzose sandstones as a function of time, temperature, depth, stylolite frequency, and hydrocarbon saturation. AAPG bulletin, 82**,** 637-648.

BJØRLYKKE, K. 2010. Petroleum Geoscience: From Sedimentary Environments to Rock Physics., chap. Introduction to petroleum geology. Springer Science.

BJØRLYKKE, K., AAGAARD, P., DYPVIK, H., HASTINGS, D. & HARPER, A. 1986. Diagenesis and reservoir properties of Jurassic sandstones from the Haltenbanken area, offshore mid-Norway. Habitat of hydrocarbons on the Norwegian continental shelf**,** 275-286.

BJØRLYKKE, K. & JAHREN, J. 2010. Sandstones and sandstone reservoirs. Petroleum Geoscience. Springer.

BJØRLYKKE, K. & JAHREN, J. 2015. Sandstones and sandstone reservoirs. Petroleum Geoscience. Springer.

BLATT, H., TRACY, R. & OWENS, B. 2006. Petrology: igneous, sedimentary, and metamorphic, Macmillan.

BOGGS JR, S. & KRUMBEIN, W. 1996. Principles of Sedimentology and Stratigraphy. Sedimentary Geology, 105**,** 112-114.

BREKKE, H. & RIIS, F. 1987. Tectonics and basin evolution of the Norwegian shelf between 62 N and 72 N. Norsk Geologisk Tidsskrift, 67**,** 295-322.

BUATOIS, L. A., SANTIAGO, N., HERRERA, M., PLINK-BJÖRKLUND, P., STEEL, R., ESPIN, M. & PARRA, K. 2012. Sedimentological and ichnological signatures of changes in wave, river and tidal influence along a Neogene tropical deltaic shoreline. Sedimentology, 59**,** 1568-1612.

References

BUE, E. P. & ANDRESEN, A. 2014. Constraining depositional models in the Barents Sea region using detrital zircon U–Pb data from Mesozoic sediments in Svalbard. Geological Society, London, Special Publications, 386**,** 261-279.

BUSENBERG, E. & CLEMENCY, C. V. 1976. The dissolution kinetics of feldspars at 25 C and 1 atm CO2 partial pressure. Geochimica et Cosmochimica Acta, 40**,** 41-49.

CHERVEN, V. 1978. Fluvial and deltaic facies in the Sentinel Butte Formation, central Williston Basin. Journal of Sedimentary Research, 48.

CHUHAN, F. A., KJELDSTAD, A., BJØRLYKKE, K. & HØEG, K. 2002. Porosity loss in sand by grain crushing—Experimental evidence and relevance to reservoir quality. Marine and Petroleum Geology, 19**,** 39-53.

CHUHAN, F. A., KJELDSTAD, A., BJØRLYKKE, K. & HØEG, K. 2003. Experimental compression of loose sands: relevance to porosity reduction during burial in sedimentary basins. Canadian Geotechnical Journal, 40**,** 995-1011.

CLIFTON, H. E. 1973. Pebble segregation and bed lenticularity in wave-worked versus alluvial gravel. Sedimentology, 20**,** 173-187.

COLEMAN, J. M. & PRIOR, D. B. 1982. Deltaic environments of deposition.

COLLINSON, J. D. 1969. The sedimentology of the Grindslow Shales and the Kinderscout Grit: a deltaic complex in the Namurian of northern England. Journal of Sedimentary Research, 39.

DALLAND, A., WORSLEY, D. & OFSTAD, K. 1988. A lithostratigraphic scheme for the mesozoic and cenozoic and succession offshore mid-and northern norway, Oljedirektoratet.

DENGO, C. & RØSSLAND, K. 2013. Extensional tectonic history of the western Barents Sea. Structural and Tectonic Modelling and Its Application to Petroleum Geology, 1**,** 91-107.

DORÉ, A. 1995. Barents Sea geology, petroleum resources and commercial potential. Arctic**,** 207-221.

DOTT JR, R. H. 1964. Wacke, Graywacke and Matrix--What Approach to Immature Sandstone Classification? Journal of Sedimentary Research, 34.

DVORKIN, J. & NUR, A. 1996. Elasticity of high-porosity sandstones: Theory for two North Sea data sets. Geophysics, 61**,** 1363-1370.

EIDVIN, T. & RIIS, F. 1989. Nye dateringer av de tre vestligste borehullene i Barentshavet. Resultater og konsekvenser for den tertiære hevingen. Norwegian Petroleum Directorate Contribution, 27.

ELDHOLM, O., FALEIDE, J. I. & MYHRE, A. M. 1987. Continent-ocean transition at the western Barents Sea/Svalbard continental margin. Geology, 15**,** 1118-1122.

ELLIOTT, T. 1974. Interdistributary bay sequences and their genesis. Sedimentology, 21**,** 611-622.

ELLIOTT, T. 1976. The morphology, magnitude and regime of a Carboniferous fluvial-distributary channel. Journal of Sedimentary Research, 46.

ELLIOTT, T. 1986. Chapter 6. Deltas. Sedimentary Environments and Facies, 2nd Edition: Oxford, UK, Blackwell**,** 155-188.

ELLIS, D. V. & SINGER, J. M. 2007. Well logging for earth scientists, Springer.

EMERY, D. & MYERS, K. 1996, Sequence stratigraphy. Black Well Science Ltd.

FALEIDE, J. I., BJØRLYKKE, K. & GABRIELSEN, R. H. 2015. Geology of the Norwegian continental shelf. Petroleum Geoscience. Springer.

FALEIDE, J. I., GUDLAUGSSON, S. T. & JACQUART, G. 1984. Evolution of the western Barents Sea. Marine and Petroleum Geology, 1**,** 123IN1129IN5137-128IN4136IN8150.

FALEIDE, J. I., TSIKALAS, F., BREIVIK, A. J., MJELDE, R., RITZMANN, O., ENGEN, O., WILSON, J. & ELDHOLM, O. 2008. Structure and evolution of the continental margin off Norway and the Barents Sea. Episodes, 31**,** 82-91.

FALEIDE, J. I., VÅGNES, E. & GUDLAUGSSON, S. T. 1993. Late Mesozoic-Cenozoic evolution of the south-western Barents Sea in a regional rift-shear tectonic setting. Marine and Petroleum Geology, 10**,** 186-214.

FIELDING, C. 1984. Upper delta plain lacustrine and fluviolacustrine facies from the Westphalian of the Durham coalfield, NE England. Sedimentology, 31**,** 547-567.

FIELDING, C. 1986. Fluvial channel and overbank deposits from the Westphalian of the Durham coalfield, NE England. Sedimentology, 33**,** 119-140.

FIELDING, C. R. 1987. Coal depositional models for deltaic and alluvial plain sequences. Geology, 15**,** 661-664.

References

FIELDING, C. R. 2006. Upper flow regime sheets, lenses and scour fills: extending the range of architectural elements for fluvial sediment bodies. Sedimentary Geology, 190**,** 227-240.

FOLK, R. L. 1974. Petrology of sedimentary rocks, The university of Texas, Geology 370K, 383L, 383M, Hemphill.

FROSTICK, L., LINSEY, T. & REID, I. 1992. Tectonic and climatic control of Triassic sedimentation in the Beryl Basin, northern North Sea. Journal of the Geological Society, 149**,** 13-26.

GABRIELSEN, R. H., FAERSETH, R. B. & JENSEN, L. N. 1990. Structural Elements of the Norwegian Continental Shelf. Pt. 1. The Barents Sea Region, Norwegian Petroleum Directorate.

GHAWAR, B. M. B. & ELBURAS, F. S. 2015. Poisson's Ration, Deep Resistivity and Water Saturation Relationships for Shaly Sand Reservoir, SE Sirt, Murzuq and Gadames Basins, Libya (Case study). Journal of Geography and Geology, 7**,** 20.

GJELBERG, J., DREYER, T., HØIE, A., TJELLAND, T. & LILLENG, T. 1987. Late Triassic to Mid-Jurassic sandbody development on the Barents and Mid-Norwegian shelf. Petroleum Geology of North West Europe**,** 1105-1129.

GJELBERG, J. G. 1981. Upper Devonian (Famennian)-Middle Carboniferous succession of Bjørnøya: a study of ancient alluvial and coastal marine sedimentation.

GLØRSTAD-CLARK, E., FALEIDE, J. I., LUNDSCHIEN, B. A. & NYSTUEN, J. P. 2010. Triassic seismic sequence stratigraphy and paleogeography of the western Barents Sea area. Marine and Petroleum Geology, 27**,** 1448-1475.

GUDLAUGSSON, S., FALEIDE, J., JOHANSEN, S. & BREIVIK, A. 1998. Late Palaeozoic structural development of the south-western Barents Sea. Marine and Petroleum Geology, 15**,** 73-102.

HALLAM, A. 1985. A review of Mesozoic climates. Journal of the Geological Society, 142**,** 433-445.

HALLAND, E., MUJEZINOVIC, J. & RIIS, F. 2014. CO2 Storage Atlas: Norwegian Continental Shelf, Norwegian Petroleum Directorate, PO Box 600, NO-4003 Stavanger, Norway, 2014. URL http://www. npd. no/en/Publications/Reports/Compiled-CO2-atlas.

HALLAND, E., MUJEZINOVIĆ, J. & RIIS, F. 2013. CO2 torage atlas—Barents Sea: Norwegian Petroleum Directorate.

HARRELL, J. 1984. A visual comparator for degree of sorting in thin and plane sections. Journal of sedimentary research, 54.

HAY, J. 1978. Structural development in the northern North Sea. Journal of Petroleum Geology, 1**,** 65-77.

HENRIKSEN, E., RYSETH, A., LARSSEN, G., HEIDE, T., RØNNING, K., SOLLID, K. & STOUPAKOVA, A. 2011. Tectonostratigraphy of the greater Barents Sea: implications for petroleum systems. Geological Society, London, Memoirs, 35**,** 163-195.

HØY, T. & LUNDSCHIEN, B. 2011. Triassic deltaic sequences in the northern Barents Sea. Geological Society, London, Memoirs, 35**,** 249-260.

HWANG, I. G. & HELLER, P. L. 2002. Anatomy of a transgressive lag: Panther Tongue Sandstone, Star Point Formation, central Utah. Sedimentology, 49**,** 977-999.

KALANI, M., JAHREN, J., MONDOL, N. H. & FALEIDE, J. I. 2015. Compaction processes and rock properties in uplifted clay dominated units–the Egersund Basin, Norwegian North Sea. Marine and Petroleum Geology, 68**,** 596-613.

KJØLHAMAR, B. Hoop Basin—An integrated approach to 3D exploration in the Barents Sea: Presented at the Petroleum Potential of the Southwestern Barents Sea. NGS Conference, 2012.

KLAUSEN, T. G., MÜLLER, R., SLAMA, J. & HELLAND-HANSEN, W. 2017. Evidence for Late Triassic provenance areas and Early Jurassic sediment supply turnover in the Barents Sea Basin of northern Pangea. Lithosphere, 9**,** 14-28.

LANDRØ, M. 2011. Petroleum geoscience: From sedimentary environments to rock physics.

LEROY, N., BRES, E., JONES, D. & DOWNES, S. 2001. Structure and substitutions in fluorapatite. European Cells and Materials, 2**,** 36-48.

LI, W., BHATTACHARYA, J. P., ZHU, Y., GARZA, D. & BLANKENSHIP, E. 2011. Evaluating delta asymmetry using three-dimensional facies architecture and ichnological analysis, Ferron 'Notom Delta', Capital Reef, Utah, USA. Sedimentology, 58**,** 478-507.

References

LORD, G. S., SOLVI, K. H., KLAUSEN, T. G. & MØRK, A. 2014. Triassic channel bodies on Hopen, Svalbard: Their facies, stratigraphical significance and spatial distribution. Norwegian Petroleum Directorate Bulletin, 11**,** 41-59.

LUNDERGARD, P. 1992. Sandstone porosity loss. A ‘‘big picture’’view of the importance of Compactation. J Sediment Petrol, 62**,** 250-260.

LUNDSCHIEN, B. A., HØY, T. & MØRK, A. 2014. Triassic hydrocarbon potential in the Northern Barents Sea; integrating Svalbard and stratigraphic core data. Norwegian Petroleum Directorate Bulletin, 11**,** 3-20.

MAAST, T. E. 2013. Reservoir quality of deeply buried sandstones–a study of burial diagenesis from the North Sea.

MACEACHERN, J. & BANN, K. 2008. The role of ichnology in refining shallow marine facies models. Recent Advances in Models of siliciclastic shallow-marine stratigraphy: SEPM, Special Publication, 90**,** 73-116.

MAHER JR, H. D. 1989. A storm-related origin for the Jurassic Brentskardhaugen Bed of Spitsbergen, Norway. Polar Research, 7**,** 67-77.

MARCUSSEN, Ø., MAAST, T. E., MONDOL, N. H., JAHREN, J. & BJØRLYKKE, K. 2010. Changes in physical properties of a reservoir sandstone as a function of burial depth–The Etive Formation, northern North Sea. Marine and Petroleum Geology, 27**,** 1725-1735.

MIALL, A. D. 1985. Architectural-element analysis: a new method of facies analysis applied to fluvial deposits. Earth-Science Reviews, 22**,** 261-308.

MONDOL, N. H. 2009. Porosity and permeability development in mechanically compacted silt-kaolinite mixtures. SEG Technical Program Expanded Abstracts 2009. Society of Exploration Geophysicists.

MONDOL, N. H., BJØRLYKKE, K., JAHREN, J. & HØEG, K. 2007. Experimental mechanical compaction of clay mineral aggregates—Changes in physical properties of mudstones during burial. Marine and Petroleum Geology, 24**,** 289-311.

MONDOL, N. H., FAWAD, M., JAHREN, J. & BJORLYKKE, K. 2008. Synthetic mudstone compaction trends and their use in pore pressure prediction. first break, 26**,** 43-51.

MØRK, A., DALLMANN, W., DYPVIK, H., JOHANNESSEN, E., LARSSEN, G., NAGY, J., NØTTVEDT, A., OLAUSSEN, S., PCHELINA, T. & WORSLEY, D. 1999. Mesozoic lithostratigraphy. Lithostratigraphic lexicon of Svalbard. Upper Palaeozoic to Quaternary bedrock. Review and recommendations for nomenclature use**,** 127-214.

MORK, A., KNARUD, R. & WORSLEY, D. 1982. Depositional and diagenetic environments of the Triassic and Lower Jurassic succession of Svalbard.

MØRK, A., LORD, G., SOLVI, K. & DALLMANN, W. 2013. Geological map of Svalbard 1: 100 000, sheet G14G Hopen. Norsk Polarinstitutt Temakart No, 50.

MYHRE, A. M., ELDHOLM, O. & SUNDVOR, E. 1982. The margin between Senja and Spitsbergen fracture zones: implications from plate tectonics. Tectonophysics, 89**,** 33-50.

NALIVKIN, D. V. 1973. Geology of the USSR.

NICHOLS, G. 2009. Sedimentology and stratigraphy, John Wiley & Sons.

NYLAND, B., JENSEN, L., SKAGEN, J., SKARPNES, O. & VORREN, T. 1992. Tertiary uplift and erosion in the Barents Sea: magnitude, timing and consequences. Tectonic Modelling and Its Implication to Petroleum Geology; Larsen, RM, Brekke, H., Larsen, BT, Talleras, E., Eds**,** 153-162.

OLAUSSEN, S., DALLAND, A., GLOPPEN, T. & JOHANNESSEN, E. 1984. Depositional environment and diagenesis of Jurassic reservoir sandstones in the eastern part of Troms I area. Petroleum Geology of the North European Margin. Springer.

OLSEN, R. G. & HANSSEN, O. 1987. Part VIII—Hammerfest Basin 37 Askeladd. Geology of the Norwegian Oil and Gas Fields: An Atlas of Hydrocarbon Discoveries, Containing Full Descriptions of 37 of Norway's Major Oil and Gas Fields and Finds**,** 419.

PATERSON, N. W. & MANGERUD, G. 2015. Late Triassic (Carnian–Rhaetian) palynology of Hopen, Svalbard. Review of Palaeobotany and Palynology, 220**,** 98-119.

PATERSON, N. W., MANGERUD, G., CETEAN, C. G., MØRK, A., LORD, G. S., KLAUSEN, T. G. & MØRKVED, P. T. 2016. A multidisciplinary biofacies characterisation of the Late Triassic

References

(late Carnian–Rhaetian) Kapp Toscana Group on Hopen, Arctic Norway. Palaeogeography, Palaeoclimatology, Palaeoecology, 464**,** 16-42.

PAXTON, S., SZABO, J., AJDUKIEWICZ, J. & KLIMENTIDIS, R. 2002. Construction of an intergranular volume compaction curve for evaluating and predicting compaction and porosity loss in rigid-grain sandstone reservoirs. AAPG bulletin, 86**,** 2047-2067.

PEMBERTON, S. G. 2001. Ichnology & sedimentology of shallow to marginal marine systems. Geol. Assoc. Can., Short Course, 15**,** 343.

PITTMAN, E. D. & LARESE, R. E. 1991. Compaction of lithic sands: experimental results and applications (1). AAPG Bulletin, 75**,** 1279-1299.

POWERS, M. C. 1953. A new roundness scale for sedimentary particles. Journal of Sedimentary Research, 23.

RAMM, M. & BJØRLYKKE, K. 1994. Porosity/depth trends in reservoir sandstones: Assessing the quantitative effects of varying pore-pressure, temperature history and mineralogy, Norwegian Shelf data. Clay minerals, 29**,** 475-490.

READING, H. 1996. Sedimentary environments: Processes, facies and stratigraphy, John Wiley & Sons.

READING, H. G. 2009. Sedimentary environments: processes, facies and stratigraphy, John Wiley & Sons.

RIDER, M. H. 1986. The geological interpretation of well logs.

RIIS, F., LUNDSCHIEN, B. A., HØY, T., MØRK, A. & MØRK, M. B. E. 2008. Evolution of the Triassic shelf in the northern Barents Sea region. Polar Research, 27**,** 318-338.

RYSETH, A. 2014. Sedimentation at the Jurassic-Triassic boundary, south-west Barents Sea: indication of climate change. From Depositional Systems to Sedimentary Successions on the Norwegian Continental Margin, IAS Special publication, 46**,** 187-214.

SELLWOOD, B. W. & VALDES, P. J. 2006. Mesozoic climates: General circulation models and the rock record. Sedimentary geology, 190**,** 269-287.

SIDDIQUI, N. A., RAHMAN, A. H. A., SUM, C. W., YUSOFF, W. I. W. & ISMAIL, M. S. B. 2017. Shallow-marine Sandstone Reservoirs, Depositional Environments, Stratigraphic Characteristics and Facies Model: A Review. Journal of Applied Sciences, 17**,** 212-237.

SMELROR, M. 1994. Jurassic stratigraphy of the western Barents Sea region: A review. Geobios, 27**,** 441-451.

SMELROR, M., PETROV, O., LARSSEN, G. B. & WERNER, S. 2009. Geological history of the Barents Sea. Norges Geol. undersøkelse**,** 1-135.

SMITH, D., HARLAND, W., HUGHES, N. & PICKTON, C. 1976. The geology of Kong Karls Land, Svalbard. Geological Magazine, 113**,** 193-232.

SOLOMON, M. 1963. Counting and sampling errors in modal analysis by point counter. Journal of Petrology, 4**,** 367-382.

STEEL, R. J. & WORSLEY, D. 1984. Svalbard's post-Caledonian strata—an atlas of sedimentational patterns and palaeogeographic evolution. Petroleum geology of the North European margin. Springer.

STORVOLL, V., BJRLYKKE, K. & MONDOL, N. H. 2005. Velocity-depth trends in Mesozoic and Cenozoic sediments from the Norwegian Shelf. AAPG bulletin, 89**,** 359-381.

TALWANI, M. & ELDHOLM, O. 1977. Evolution of the Norwegian-Greenland sea. Geological Society of America Bulletin, 88**,** 969-999.

TAYLOR, A. & GOLDRING, R. 1993. Description and analysis of bioturbation and ichnofabric. Journal of the Geological Society, 150**,** 141-148.

TAYLOR, J. M. 1950. Pore-space reduction in sandstones. AAPG bulletin, 34**,** 701-716.

ULMER-SCHOLLE, D. S., SCHOLLE, P. A., SCHIEBER, J. & RAINE, R. J. 2014. A Color Guide to the Petrography of Sandstones, Siltstones, Shales and Associated Rocks, American Association of Petroleum Geologists.

WALDERHAUG, O. 1996. Kinetic modeling of quartz cementation and porosity loss in deeply buried sandstone reservoirs. AAPG bulletin, 80**,** 731-745.

WALDERHAUG, O. & RYKKJE, J. 2000. Some examples of the effect of crystallographic orientation on the cathodoluminescence colors of quartz. Journal of Sedimentary Research, 70.

WELTON, J. E. 1984. SEM petrology atlas.

References

WENTWORTH, C. K. 1922. A scale of grade and class terms for clastic sediments. The Journal of Geology, 30**,** 377-392.

WILSON, M. D. & PITTMAN, E. D. 1977. Authigenic clays in sandstones: recognition and influence on reservoir properties and paleoenvironmental analysis. Journal of Sedimentary Research, 47.

WORSLEY, D. 2008. The post-Caledonian development of Svalbard and the western Barents Sea. Polar Research, 27**,** 298-317.

WORSLEY, D., JOHANSEN, R. & KRISTENSEN, S. 1988. The mesozoic and cenozoic succession of Tromsøflaket. A lithostratigraphic scheme for the Mesozoic and Cenozoic succession offshore mid-and northern Norway. Norwegian Petroleum Directorate Bulletin, 4**,** 42-65.

WORTHINGTON, P. & COSENTINO, L. 2005. The Role of Cutoffs in Integrated Reservoir Studies. SPEREE 8 (4): 276-290. SPE-84387-PA. DOI: 10.2118/84387-PA.

WORTHINGTON, P. F. The Application of Cutoffs in Integrated Reservoir Studies. SPE Annual Technical Conference and Exhibition, 2005. Society of Petroleum Engineers.

XI, K., CAO, Y., JAHREN, J., ZHU, R., BJØRLYKKE, K., HAILE, B. G., ZHENG, L. & HELLEVANG, H. 2015. Diagenesis and reservoir quality of the Lower Cretaceous Quantou Formation tight sandstones in the southern Songliao Basin, China. Sedimentary Geology, 330**,** 90-107.

Appendix

Appendix **A: Petrophysical data**

Table 1: Summary of the well database used in this thesis from (www.npd.no)

Formation	Well	Core	Core sample-top depth	Core sample-bottom depth	Total length of Stø Fm (m)	Samples	Location
STØ	7324/7-2	3-5	710, 724, 739	723.5, 739.2, 757.4	24	13	Hoop Fault Complex
STØ	7321/9-1	1-2	1365, 1385.2	1384.1, 1398.1	38	17	Fingerdjupet Sub-basin

Table 2: Coordinates (degrees and UTM) for the well data base from (www.npd.no)

Well	Coordinates [Degrees]	Coordinates [UTM]	Location
7324/7-2	NS: 73° 29' 27.09'' N EW: 24° 14' 2.56'' E	NS: 8157493.85 EW: 412291.83	Hoop Fault Complex
7321/9-1	NS: 73° 16' 7.34'' N EW: 21° 41' 0.68'' E	NS: 8138267.66 EW: 329361.05	Fingerdjupet Sub-Basin

Table 3: Petrophysical data for calculation of geothermal gradient

well	Total depth [m MD]	Total depth [m TVD]	Water depth [m]	Bottom hole temperature [C^0]	Maximum inclination [^{0}]	Kelly bushing elevation [m]	Location
7324/7-2	1730.0	1719.9	417.5	51	14.3	40.0	Hoop Fault complex
7321/9-1	1800.0	1799.0	459.0	44	3.8	23.5	Fingerdjupet Sub.-basin

Appendix

Appendix B: Petrographic data

Table 5.1: Samples selected for petrographic analysis of Stø Formation. BX = Bulk XRD, PC = Point counting.

Well	samples	Depth [mD]	Facies	Petrographical investigations		
				BX	PC	SEM
7324/7-2	A24	730.84	F2	✓	✓	
	A25	730.39	F2	✓	✓	
	A26	727.75	F2	✓	✓	
	A27	725.87	F2	✓	✓	✓
	A28	724.88	F2	✓	✓	
	A29	723.38	F3	✓	✓	✓
	A30	721.78	F3	✓	✓	
	A31	719.61	F3	✓	✓	
	A32	714.48	F3	✓	✓	
	A33	715.61	F3	✓	✓	
	A34	713.17	F3	✓	✓	
	A35	712.96	F-6H	✓	✓	✓
	A36	712.60	F-6H	✓	✓	
	A3	711.63	F-7	✓		
	A38	673.44	F-7	✓		
	A39	580.57	F-7	✓		
	A40	579.62	F-7	✓		

Table 5.2: Samples selected for petrographic analysis of Stø Formation. BX = Bulk XRD, PC = Point counting.

Well	samples	Depth [mD]	Facies		Petrographical investigations		
					BX	PC	SEM
	F1	1397.25	F-4		✓	✓	
	F2	1396.5	F-4		✓	✓	✓
	F3	1395.5	F-4		✓	✓	
	F4	1393	F-4		✓	✓	✓
	F5	1392.93	F-4		✓	✓	
	F6	1390.5	F-4		✓	✓	
7321/9-1	F7	1391.35	F-4		✓	✓	
	F8	1388.75	F-4		✓	✓	
	F9	1387.75	F-4		✓	✓	
	F10	1385.75	F-4		✓	✓	
	F11	1383.5	F-5		✓	✓	
	F12	1382.75	F-5		✓	✓	
	F13	1380.48	F-6f		✓	✓	
	F14	1379.95	F-6f				
	F15	1379.85	F-6f				
	F16	1379.5	F-6f		✓	✓	
	F17	1379.15	F-6f		✓	✓	
	F18	1378.75	F-7		✓		
	F19	1378.50	F-7		✓		
	F20	1372.67	F-7		✓		

Appendix

Table 5.3: Point counting results for well 7324/7-2 (percentage).

Stø Formation			Quartz		Feldespar		Rock FR	Matrix						porosity	Phosphate
Facies	Samples	Depth	Quartz	Poly/quar	Plagioclas	K-feldspar	Rock FR	Matrix	Kaolinite	Illite	Siderite	Calcite	Quartz ce	porosity	Fluorapatite
F2	A24	730.84	58.50%	20.25%	0.75%	0.00%	2.00%	3.50%	0.50%	0.76%	0.00%	0.00%	2.75%	11.00%	0.00%
	A25	730.39	44.25%	22.75%	1.00%	0.50%	4.75%	6.00%	6.25%	3.00%	0.00%	0.00%	0.00%	11.50%	0.00%
	A26	727.75	52.31%	7.18%	0.51%	0.00%	0.51%	2.56%	4.87%	0.26%	10.00%	0.00%	0.00%	14.10%	7.69%
	A27	725.87	36.50%	37.00%	0.00%	0.50%	4.50%	0.50%	6.75%	0.75%	0.00%	0.00%	0.00%	13.50%	0.00%
	A28	724.88	58.50%	8.00%	0.50%	0.00%	6.75%	3.25%	1.00%	0.00%	0.00%	0.00%	2.75%	19.25%	0.00%
F3	A29	723.38	54.75%	17.25%	0.75%	0.00%	2.75%	0.00%	0.50%	1.50%	0.00%	0.00%	3.25%	19.25%	0.00%
	A30	721.78	60.25%	15.00%	0.00%	0.00%	1.25%	0.00%	0.75%	0.00%	0.00%	0.00%	2.50%	20.25%	0.00%
	A31	719.61	67.00%	14.25%	0.50%	0.00%	1.50%	0.50%	0.25%	0.25%	0.00%	0.00%	2.25%	13.50%	0.00%
	A32	715.61	63.00%	14.25%	0.50%	0.00%	1.50%	0.00%	1.50%	0.75%	0.00%	0.00%	4.00%	14.50%	0.00%
	A33	714.48	59.75%	20.00%	0.00%	0.00%	2.00%	0.00%	1.75%	0.25%	0.00%	0.00%	0.00%	16.25%	0.00%
	A34	713.17	62.75%	7.00%	0.25%	0.00%	0.00%	0.00%	0.00%	0.00%	0.00%	29.25%	0.00%	0.75%	0.00%
F-6H	A35	712.96	44.06%	19.18%	0.10%	0.00%	1.90%	19.11%	0.00%	0.00%	0.00%	15.65%	0.00%	0.00%	0.00%
	A36	712.6	37.35%	3.61%	0.00%	1.69%	6.02%	0.00%	16.05%	5.89%	19.76%	1.35%	0.00%	0.96%	0.00%

Table 5.4: Bulk XRD results from well 7324/7-2 (amount presented as fractions)

Facies	Depth	Samples	Quartz	Kaolinite	Illite	Muscovite	K-feldspar	Fluorapatite	Calcite	Siderite	Pyrite	Plagioclase
F2	730.84	A24	0.96	0.018	0	0.014	0	0	0	0	0	0
	730.39	A25	0.919	0.0128	0.0144	0.01355	0.0135	0	0	0	0.01043	0
	727.75	A26	0.7914	0.0391	0.00282	0		0.048	0	0.1047	0	0.014
	725.87	A27	0.882	0.0346	0.0158	0	0.0117	0	0	0	0	0.0557
	724.88	A28	0.781	0.206	0	0	0.00196	0	0	0	0	0
F3	723.38	A29	0.9653	0	0	0	0	0	0	0	0	0.0347
	721.78	A30	0.974	0.011	0	0.016	0	0	0	0	0	0
	719.61	A31	0.987	0	0	0	0	0	0	0	0	0.01342
	715.61	A32	0.981	0.00543	0	0.00211	0	0	0	0	0	0.01101
	714.48	A33	0.988	0	0	0	0	0	0	0	0	0.01159
	713.17	A34	0.727	0.00598	0	0	0	0	0.2647	0	0	0
F-6H	712.96	A35	0.11258452	0.02231932	0.00195671	0	0.00502893	0	0.00320023	0.00213349	0	0
	712.6	A36	0.4065	0.151	0.055	0.1155	0	0	0	0.1432	0	0
F7	711.63	A37	0.336	0.0861	0.0878	0.143	0.036	0	0	0.0116	0	0
	673.44	A38	0.04	0.8	0.003	0.03	0.00363	0	0	0	0.007	0
	580.57	A39	0.046	0.8295	0	0.067	0.0336	0.00642	0	0.0049	0	0
	579.62	A40	0.3300725	0.018	0	0.12939135	0	0	0	0	0	0

Appendix

Table. 5-5: Point counting results for well 7321/9-1 (percentage)

Stø Formation			Detrial Grains										Porosity	Other minerals	
			Quartz		Feldspar	Rock	Matrix	Kaolinite	calcite	siderite	Illite	Quartz			
Facies	Samples	Depth	Mono	Poly	Plagioclase	Fragment								Fluarapatite	
F4	F1	1397.25	61.17%	18.45%	0.00%	1.94%	1.46%	0.49%	0.00%	0.00%	0.49%	0.00%	16.02%	0.00%	
	F2	1396.5	67.25%	9.82%	0.00%	1.51%	9.07%	1.00%	0.00%	0.00%	0.25%	2.02%	9.07%	0.00%	
	F3	1395.5	59.40%	17.79%	0.25%	3.01%	3.76%	1.75%	0.00%	0.00%	3.76%	2.76%	7.52%	0.00%	
	F4	1393	41.16%	2.02%	0.25%	5.30%	0.00%	1.56%	0.00%	0.51%	0.00%	0.00%	2.53%	46.72%	
	F5	1392.93	55.92%	2.77%	0.00%	4.03%	0.00%	0.76%	0.00%	2.77%	1.26%	1.51%	11.34%	19.65%	
	F6	1390.5	64.34%	7.48%	0.00%	2.00%	0.00%	0.25%	0.00%	0.00%	10.48%	2.99%	12.47%	0.00%	
	F7	1391.35	66.50%	10.50%	0.25%	4.00%	0.75%	0.00%	0.00%	0.00%	2.75%	3.25%	12.00%	0.00%	
	F8	1388.75	62.00%	16.50%	0.25%	3.00%	0.75%	0.00%	0.00%	0.00%	0.75%	0.00%	16.75%	0.00%	
	F9	1387.75	58.50%	15.50%	0.00%	2.25%	1.50%	1.50%	0.00%	0.00%	2.75%	3.25%	14.75%	0.00%	
	F10	1385.75	67.33%	7.23%	0.00%	2.99%	0.50%	0.00%	0.00%	3.49%	1.25%	2.24%	14.96%	0.00%	
F5	F11	1383.5	64.32%	3.02%	0.00%	3.52%	0.00%	0.50%	0.00%	9.55%	1.26%	2.26%	15.58%	0.00%	
	F12	1382.75	65.25%	11.25%	0.00%	2.50%	0.00%	0.50%	2.75%	0.00%	0.75%	0.00%	16.50%	0.00%	
F6-f	F13	1380.48	73.49%	4.72%	0.00%	3.67%	0.79%	0.00%	0.00%	1.05%	0.00%	3.00%	12.34%	0.00%	
	F14	1379.95	49.00%	1.25%	0.00%	4.00%	0.00%	0.00%	39.50%	0.75%	4.00%	0.00%	0.50%	1.00%	
	F15	1379.85	16.40%	5.80%	0.00%	60.80%	4.40%	0.00%	0.00%	0.00%	2.60%	0.00%	2.60%	7.40%	
	F16	1379.5	21.23%	1.68%	0.00%	41.06%	0.00%	31.56%	0.00%	3.07%	1.12%	0.00%	0.28%	0.00%	
	F17	1379.15	15.48%	38.81%	0.00%	1.19%	4.05%	34.50%	0.48%	0.00%	1.90%	0.00%	4.05%	0.00%	

Table. 5-6: Bulk XRD results from well 7321/9-1 (amount presented as fractions).

Facies	Depth	Samples	Quartz	Kaolinite	Muscovite	Plagioclas	Fluorapati	Pyrite	Siderite	Ankerit	illite
F4	1397.25	F1	0.973	0	0.0269	0	0	0	0	0	0
	1396.5	F2	0.9014	0	0.0741	0	0	0	0	0	0.0155
	1395.5	F3	0.8337	0.066	0.0411	0.0592	0	0	0	0	0
	1393	F4	0.5148	0.0087	0.01097	0	0.4526	0	0	0.0129	0
	1392.93	F5	0.6172	0.0101	0.0353	0	0.1447	0	0.0842	0	0.0221
	1390.5	F6	0.9828	0	0.0172	0	0	0	0	0	0
	1391.35	F7	0.8327	0.0207	0.0169	0.0612	0	0.02651	0	0	0.0324
	1388.75	F8	0.99	0	0	0	0	0	0	0	0
	1387.75	F9	0.9677	0.0116	0	0	0	0	0	0	0.0207
	1385.75	F10	0.897	0.00247	0.0396	0.0478	0	0	0.0133	0	0
F5	1383.5	F11	0.8275	0	0	0.0585	0.0338	0	0.08025	0	0
	1382.75	F12	0.935	0.01015	0	0.055	0	0	0	0	0
F-6f	1380.48	F13	0.897	0.0299	0	0.0622	0	0	0.0109	0	0
	1379.95	F14	0.5237	0.0202	0	0	0.00246	0	0.05974	0.337	0
	1379.85	F15	0.4286	0.0037	0.0294	0	0.5072	0	0	0	0.0303
	1379.5	F16	0.324	0.44	0.027	0	0	0	0.146	0.052	0.014
	1379.15	F17	0.532	0.44	0.026	0	0	0.0085	0	0.0504	0.0146
F7	1378.75	F18	0.5499	0.0076	0.0987	0.0808	0	0.08977	0	0	0.0748
	1378.5	F19	0.3151	0.0324	0.0766	0.0158	0.0298	0.0295	0.4568	0.0135	0.0303
	1372.67	F20	0.5467	0.0291	0.1671	0.1299	0	0	0	0.0226	0.0487